

DISSERTATION

GENERALIZED PRESSURE DROP AND HEAT TRANSFER CORRELATIONS FOR JET
IMPINGEMENT COOLING WITH JET ADJACENT FLUID EXTRACTION

Submitted by

David Ryan Hobby

Department of Mechanical Engineering

In partial fulfillment of the requirements

For the Degree of Doctor of Philosophy

Colorado State University

Fort Collins, Colorado

Spring 2022

Doctoral Committee:

Advisor: Todd M. Bandhauer

Daniel B. Olsen

David Prawel

Karan Venayagamoorthy

Copyright David Ryan Hobby 2022

All Rights Reserved

ABSTRACT

GENERALIZED PRESSURE DROP AND HEAT TRANSFER CORRELATIONS FOR JET IMPINGEMENT COOLING WITH JET ADJACENT FLUID EXTRACTION

Jet impingement technologies offer a promising solution to thermal management challenges across multiple fields and applications. Single jets and conventional impinging arrays have been studied extensively and are broadly recognized for achieving extraordinary local heat transfer coefficients. This, in combination with the versatility of impinging arrays, has facilitated a steady incline in the popularity of jet impingement investigations. However, it is well documented that interactions between adjacent jets in an impinging array have a debilitating effect on thermal performance. Recently, in an attempt to mitigate the jet interference problem, a number of researchers have created innovative jet impingement solutions which eliminate crossflow effects by introducing fluid extraction ports interspersed throughout the impinging array. This novel adaptation on classical impinging arrays has been shown to produce dramatically improved thermal performance and offers an excellent opportunity for future high-performing thermal management devices.

The advent of jet-adjacent fluid extraction in impinging arrays presents a promising improvement to impingement cooling technologies. However, there have been very few investigations to quantify these effects. Notably, the current archive of literature is severely lacking in useful, predictive correlations for heat transfer and pressure drop which can reliably describe the performance of such impinging arrays.

Steady-state heat transfer and adiabatic pressure drop experiments were conducted using nine unique geometric configurations of a novel jet impingement device developed in this work.

This investigation proposes novel empirical correlations for Darcy friction factor and Nusselt number in an impingement array with interspersed fluid extraction ports. The correlations cover a broad range of geometric parameters, including non-dimensional jet array spacing (S/D_j) ranging from 2.7 to 9.1, and non-dimensional jet heights (H/D_j) ranging from 0.31 to 4.4. Experiments included jet Reynolds numbers ranging from 70 to 24,000, incorporating laminar and turbulent flow regimes. Multiple fluids were tested with Prandtl numbers ranging from 0.7 to 21. The correlations presented in this work are the most comprehensive to date for impinging jet arrays with interspersed fluid extraction.

Nusselt number was found to be correlated to impinging jet Reynolds number to the power of 0.57. The resulting correlation was able to predict 93% of experimental data within $\pm 25\%$. During adiabatic pressure drop experiments, multiple laminar-turbulent flow transition regions were identified at various stages in the complex jet impingement flow path. The proposed Darcy friction factor correlation was separated into laminar, turbulent, and transition regions and predicted experimental data with a mean absolute deviation of 20%.

The heat transfer and pressure drop correlations proposed in this investigation were used in a follow-on optimization study which targeted an exemplary impingement cooling application. The optimization study applied core experimental findings to a microchip cooling case study and evaluated the effects of geometry, flow, and heat load parameters on cooling efficiency and effectiveness. It was discovered that reducing non-dimensional jet height results in all-around improved cooling performance. Conversely, low non-dimensional jet spacing results in highly efficient but less effective solutions while high non-dimensional jet spacing results in effective but less efficient cooling.

ACKNOWLEDGEMENTS

There are a great many people that I wish to thank for playing some role—whether subtle or overt—in this journey. Of course, at the forefront of this catalog of names sits my advisor Dr. Todd Bandhauer. I would like to thank him for more than half a decade of challenge, guidance, and dedication. Beginning as an undergraduate in his heat transfer class, Dr. Bandhauer set me on a path (perhaps several) that I had yet to imagine, and which has proven to be equal parts challenging, cultivating, fascinating, and diverse. He has pushed me to succeed and has placed his faith in my technical capabilities countless times. I would be remised not to also acknowledge the shrimp boils, brewery visits, and other lab get-togethers which, I think, are critical for developing positive and cooperative lab culture.

I would like to thank all of the folks at Keysight, especially Chris Jacobsen, Dave Sherrer, Blake Vermeer, and Paul Carson. They not only provided funding for the root of this work, but also endless support. Working closely with Jake, Dave, and Blake has been a phenomenal experience and has certainly shaped the way that I think as an engineer. Jake has been an exceptional project manager, always with a remarkable ability to frame complex engineering problems. Dave has taught me so many “soft” lessons about engineering, that I often find myself passing on anecdotes I learned from him. Blake has saved more time for Zach and myself than I dare to imagine with his fingertip knowledge and technical support. Paul has always been a steadfast advocate for our work and a truly caring individual. I hope that I can carry the many lessons I have learned from these four gentlemen forward into all of my future endeavors.

I would also like to acknowledge the people at Lawrence Livermore National Lab. It is always a great pleasure to work with Jack Kotovsky and his team, whether it be for cutting-edge

laser diode cooling technologies, ventilators, or aerial-based system-level designs. Jack always seems to show great excitement for collaboration. I would like to thank Alex Rattner at Penn State University for his collaboration and expertise in computational fluid dynamics.

I must give a big thank you to everyone I have interacted with through the R2M program and Venture Validators. Steve Albers, Scott Shrake, Aaron Finch, Sarah Hibbs-Ship, Jim Brown, thank you for helping me expand my capabilities as an engineer with a market mindset and for giving me the opportunity to learn a truly valuable skillset through the various entrepreneurship programs.

I want to say thank you to the old I2P lab, especially Ray Huff and David Prawel, for all of the very early-stage assistance with fabricating the complex flow paths necessary for this work. Along the same theme, I want to thank my friends at the Rapid Prototyping Lab for all their help fabricating parts not only for the impingement cooling project but also for countless other projects. Thank you to John Mizia and Matt Willman for your enthusiasm for fabricating difficult and diverse components, and especially for fabricating the Gen II surrogate heater used in this work. Thank you to Labon Hillberry for figuring out all of the difficult solder and brazing joints.

I want to say a big thank you to Cliff Denson for believing in our technology and in our competence both as engineers and entrepreneurs. Thank you for jumping into this venture with us and fulfilling a crucial role in our team moving forward. And thank you for working so hard on your own time to find a path where Zach and I can finally get paid. I look forward to diving in full force.

I have had the incredible opportunity to work with so many remarkable individuals in the REACH Co-Lab, the former ITS lab, and the Powerhouse as a whole, I'm afraid I won't be able to list them all. So, thank you to everyone in the lab and everyone I have had the pleasure to work

with/near. I feel I have grown leagues simply by osmosis while in proximity with so many bright individuals, but here I will do my best to specifically acknowledge just a few. Thank you first to everyone who has interacted in some way directly with the Keysight project. Thank you, Kyle Forrester, Marie Dutton, and Tom Walker, for your aid and collaboration early on. Thank you to Torben Grumstrup for being my very first resource on the Keysight project. Thank you to Devin-Kyle-Bryce for the various help you have provided on many aspects of the Keysight project among others. Thank you to Roman for the help with system-level server testing. I want to say thanks to all of my friends at the Powerhouse with special thanks to the EISL which has provided a much-needed outlet for a long portion of my time there. Thank you to the EISL Commish, Chris Van Roekel. Thank you to Iman Babazadeh for always being ready to play soccer. Thank you to Derek Young and Shane Garland for your collaboration and friendship. Those guys are just so damned likable. A big thank you to all of my long-time friends in the dungeon. Jensen Hoke, Josh Richey, Bryan Burk, Caleb Anderson, thank you for tolerating all of the totally random conversations. To Josh, I specifically want to say you're welcome for allowing you to bask in my presence. To Jensen, thank you also for the collaboration on the SWaP work. Caleb, thank you also for collaboration on the latest LLNL work. I want to thank John Simon and Alex Grauberger for the fun times at lunch and for encouraging me to describe so many weird movies I apparently watch.

I want to give a special thanks to Katie Plese and Zach Gilvey. Katie contributed a great deal to this work, from helping build the test facility in my basement during quarantine to operating the facility for many long nights, collecting data. There have been many many hours of data collection that have gone into this work and Katie was the one sitting in the dungeon running those tests about 95% of the time. She has proven herself to be remarkably competent despite joining the lab nearly fresh out of high school. Katie, without a doubt, shows great promise as an engineer

(or law school, I guess – Lame!). Thank you, Katie, also for being such a great friend and for all of the fun times we have shared in and out of the lab.

Zach deserves so much of my gratitude not only for being a great friend with an endlessly positive attitude, but also for acting as a fitting complement to my own work style. Everyone has their many strengths and weaknesses and I have always felt that Zach's strengths and weaknesses complement my own in a way that allows us to accomplish truly great things when working together. Thank you for embarking on this journey with me and for just being such a damn entertaining guy. It has been a privilege to work alongside you and I look forward to our continued work together moving forward.

Now I would like to turn towards my friends and family to say thanks. I would like to specifically thank the late, great Choice City Crossfit for giving me a physical outlet over the past year and a half that is challenging, rewarding and fun. Thank you to Lauren Ollila and the many great people there. Of course, I must thank my family. Mom, Dad, Jason (and Madi), everything I have become all started with you and all the support, care, love, and laughter you have given me for the entirety of my life. Thank you and I love you all so much. I want to also give a dedication to Mike Knox who was a truly loving man whom we all miss dearly.

Finally, I must give my everlasting gratitude to the one person who was always there, through it all. Allison, you are the love of my life and everything that I could ever ask for in a partner and a best friend. Thank you for sticking by my side (if only just barely) from the very beginning through to the very end and for all the days hereafter which have yet to come. Everything I am has always been just for you, whether you like it or not. Thank you for pushing me. Thank you for comforting me. Thank you for feeding me. Thank you for laughing with me and traveling

with me. Thank you for fighting me and for loving me. I am so very lucky to have found you and convinced you to stay. I love you always.

I must also take a moment to acknowledge the journey itself, which has been so many things...

Today
I went for a walk
Down through the park, I walked
Through the grass and beneath the trees
Come to think of it, perhaps...
It was more of a stroll

Yes, a stroll
I could smell the flowers
Feel the sun warm against my face
As I cheerily hummed a tune
I waved hello to friendly faces
As I ran past

Ran?! That's right, I ran!
I remember now, I ran! Sprinted even!
The wind in my hair!
The pavement beneath my feet!
How they must envy my gait!
As I skipped along the path with ease!

More of a skip, really
Proud and fun and full of life
That's right, I recall thinking
How odd I must seem
Skipping joyously in the rain
As the mud pulled me down

As it devoured me
And I struggled against it
On the ground and nearly consumed
Slowly, I forced myself forward
Tired and afraid but crawling still
Crawling...

Is that right? Did I crawl?
But that seems quite odd?
Surely, I would remember such a thing?
Surely, someone would have seen?

Perhaps, simply
I went for a walk

TABLE OF CONTENTS

ABSTRACT.....	ii
ACKNOWLEDGEMENTS.....	iv
LIST OF TABLES.....	xi
LIST OF FIGURES.....	xiii
NOMENCLATURE.....	xxii
CHAPTER 1. Introduction.....	1
1.1. Motivation for Research.....	1
1.1.1. Challenges with conventional jet impingement.....	2
1.1.2. Advent of return jet impingement.....	4
1.2. Research Objectives.....	6
1.3. Thesis Organization.....	7
CHAPTER 2. Literature Review.....	8
2.1. Conventional Jet Impingement Cooling.....	8
2.2. Jet Impingement with Interspersed fluid extraction.....	12
2.3. Focus of Current Investigation.....	22
CHAPTER 3. Technology Development, Proof of Concept, and Preliminary Findings.....	24
3.1. POC Cooler Design and Fabrication.....	24
3.2. Experimental Setup/Methods.....	30
3.3. Heat Transfer Results.....	34
3.4. Pressure Drop Results.....	43
3.5. Challenges and Development of Robust Test Method.....	48
CHAPTER 4. Experimental Setup.....	53
4.1. Gen II Impingement Cooler Design and Fabrication.....	53
4.1.1. Cooler design and flow path.....	54
4.1.2. Key geometries and configurations.....	65
4.1.3. Fabrication and validation.....	74
4.2. Gen II Surrogate Heater.....	88
4.2.1. Design, functionality, and fabrication.....	89
4.2.2. Thermal uniformity.....	97
4.3. Test Facility.....	99
4.3.1. Instrumentation.....	103
4.4. Test Procedures.....	107
4.4.1. Heat transfer testing.....	107
4.4.2. Pressure drop testing.....	119
4.5. Uncertainty.....	125
4.5.1. Heat transfer uncertainty.....	125
4.5.2. Pressure drop uncertainty.....	131
CHAPTER 5. Heat Transfer Results, Discussion, and Correlation Development.....	136

5.1. Results.....	136
5.2. Correlation Development and Fit.....	146
CHAPTER 6. Pressure Drop Results, Discussion, and Correlation Development.....	160
6.1. Results.....	160
6.1.1. Manifold pressure drop contribution	167
6.2. Correlation Development and Fit.....	169
6.2.1. Constant k-factor evaluation	170
6.2.2. Reynolds number dependence	174
6.2.3. Geometric dependence.....	181
6.2.4. Goodness of fit.....	184
CHAPTER 7. Optimization Study.....	196
CHAPTER 8. Conclusions and Recommendations	216
8.1. Recommendations for Future Research	219
REFERENCES	223
APPENDICES	231

LIST OF TABLES

Table 2-1: Overview of impingement studies with jet-adjacent fluid extraction	23
Table 3-1: List of geometric, fluid, and flow parameters for preliminary study.	35
Table 3-2: Definition of pressure drop coefficients utilized by the ancillary pressure drop model; correlation numbers coincide with those shown in Figure 3-18	47
Table 4-1: Table of key geometric parameters	65
Table 4-2: As-designed geometric parameters for all impingement test section configurations..	73
Table 4-3: Impingement orifice diameter deviation	82
Table 4-4: Impingement height measurements	82
Table 4-5: Surrogate heater uniformity Taguchi thermal simulation results.....	99
Table 4-6: Count of all heat transfer tests conducted by part number and fluid type.....	119
Table 4-7: Number of adiabatic pressure tests performed by device configuration and fluid....	121
Table 4-8: Measurement contribution to propagated uncertainties for heat transfer tests.....	128
Table 4-9: Measurement contribution to propagated uncertainties for pressure drop tests	134
Table 5-1: Deviation between correlation predicted Nusselt number and experimental Nusselt number data.....	150
Table 6-1: Fraction of test section pressure drop attributed to impingement region for all test sections. The remainder of pressure drop is from inlet and outlet header sections.	169
Table 6-2: Best fit k-factors	173
Table 6-3: Best-fit values for f_G correlation fit parameter for all nine impingement geometries.	179

Table 6-4: Friction factor geometric parameter f_G for each impingement configuration as calculated by equation 6-12 189

Table 6-5: Overall fit statistics for the proposed pressure drop correlation against experimental data..... 189

Table 7-1: Optimal jet diameter values corresponding to Figure 7-4. 207

LIST OF FIGURES

Figure 1-1: Typical flow arrangement for a standard jet impingent cooling device with crossflow fluid extraction	2
Figure 1-2: Visual representation of the effect of cross flow on impinging jet formation and performance; adapted from Jing et al. [14]: a) Computational domain b) Side view of jet velocity contours c) Top view of heat transfer coefficient contours	3
Figure 1-3: (a) Typical flow arrangement for a jet impingent cooling device with distributed jet-adjacent fluid removal ports and (b) Solid model and flow description of quarter-jet repeating unit cell to serve as the solution domain for computational simulations.	5
Figure 2-1: The flow regions of an impinging jet [13].	9
Figure 2-2: Local Nusselt number of single impinging jet by Liu et al. [21].	10
Figure 2-3: Huber and Viskanta RJI experimental setup [20].	12
Figure 2-4: Rhee et al. RJI experimental setup [46].	13
Figure 2-5: Brunschwiler et al. RJI manifold architecture [6].	14
Figure 2-6: Sharma et al. impingement architecture with jets fully confined by microchannel structures [45].	16
Figure 2-7: RJI manifold architecture used by Onstad et al. and Hoberg et al. [40,41].	16
Figure 2-8: Primary RJI manifold architecture used by Wei et al. [47,48].	18
Figure 2-9: Secondary Wei et al. RJI manifold architecture (d) compared to primary architecture (a and b) [59].	20
Figure 2-10: Tertiary Wei et al. RJI manifold architecture (b and d) compared to primary architecture (a and c) [60].	21

Figure 3-1: Impingement device flow path (negative)	24
Figure 3-2: Solid model of the internal flow path of the impingent device, including fluid mounting sections where process measurements are made. (a) total flow path, (b) manifold (ancillary) flow regions, (c) jet impingement region with reference to the repeating unit cell.	26
Figure 3-3: Comparative print feature resolution of three additive manufacturing techniques viz., FDM, SLA, SLS [65].....	27
Figure 3-4: Autodesk Ember DLP printer [67].....	29
Figure 3-5: Microscope images of impinging array with optical measurements.....	29
Figure 3-6: Photograph of the 3D-printed jet impingent device used heat transfer and pressure testing, printed on the Kudo 3D Titan 2 printer.....	30
Figure 3-7: Process and flow diagram of the test facility for heat transfer and pressure drop measurement	31
Figure 3-8: Solid model of surrogate heater without insulation	33
Figure 3-9: Photograph of insulated test heater used for heat transfer experimentation of the impingement device. The impingement device is mounted to the square copper surface at the top of the heater. Lower right image shows the internal copper heater block with highlighted thermocouple mounting positions.....	34
Figure 3-10: Surface temperature differential under water impingement over range of heat loads	36
Figure 3-11: Measured heat transfer coefficient for a water jet impingement preliminary testing; note that vertical uncertainty bars are mostly obscured by the data markers	37
Figure 3-12: Comparison with Brunswiler et al. correlation	38
Figure 3-13: Comparison with correlations by Rattner, Hoberg et al., and Huber and Viskanta.	39

Figure 3-14: Rendering of simulation unit cell with representative computational mesh	41
Figure 3-15: Simulated and measured heat transfer results of the jet impingent device over the total range of flow rates	42
Figure 3-16: Pressure contours at (a) 200 mL min ⁻¹ and (b) 1000 mL min ⁻¹ total device flow rate	44
Figure 3-17: Computational (blue triangles) and experimental (green circles) pressure drop results with total predicted pressure drop (orange diamonds) presented as the aggregate of pressure drop in the impingement region (determined by CFD) and pressure drop in the manifold regions (determined by correlational-based analytical model).....	45
Figure 3-18: Simplified ancillary hydraulic resistance network for 3-by-3 three impingement array, broken into zones over which pressure drop correlations were applied; numbers indicate which correlations were used and coincide with those listed in Table 3-2	46
Figure 3-19: Proportional pressure drop in each individual flow section of the device as defined in Figure 3-2a.....	49
Figure 3-20: Model approximation of flow distribution by jet position in the impingement device	51
Figure 4-1: Gen II Impingement device. a) perspective view photograph of part C01 b) device C09 manifold negative (flow path) where blue represents inlet manifold and red represents outlet manifold c) device C09 inlet manifold negative, d) device C09 outlet manifold negative e) cross sectional view of C09 inflow manifold and jets shown in blue f) cross sectional view of C09 outflow manifold and fluid extraction orifices shown in red.....	55
Figure 4-2: Dimensioned photograph of impingement device configuration C01	57
Figure 4-3: Exploded view of surrogate heater and impingement cooler assembly.....	58

Figure 4-4: Impingement device C01 mounted to surrogate heater with process and measurement connections	59
Figure 4-5: Transparent solid model of C09 impingement device with key features. Instrumentation ports highlighted in red.....	61
Figure 4-6: Impingement part C01 hole array highlighting repeating unit cell.....	63
Figure 4-7: Typical thermal conductivity values of unfilled plastics [75].....	64
Figure 4-8: Diagram describing key geometric parameters of the impingement array.	65
Figure 4-9: Graphical representation of planned impingement geometric parameter ranges.....	71
Figure 4-10: Range of planned non-dimensional jet height and spacing by part	72
Figure 4-11: Perspective view of C01 thru C09 as-fabricated impingement test sections	75
Figure 4-12: Inlet view of C01 thru C09 as-fabricated impingement test sections	76
Figure 4-13: Impingement array view of C01 thru C09 as-fabricated impingement test sections	77
Figure 4-14: Sample image of C01 impingement array measured by Dino-Lite digital microscope	78
Figure 4-15: Histograms of jet and return orifice diameters for parts C01 thru C03	79
Figure 4-16: Histograms of jet and return orifice diameters for parts C04 thru C06	80
Figure 4-17: Histograms of jet and return orifice diameters for parts C07 thru C09	81
Figure 4-18: Impingement array height measurement locations	83
Figure 4-19: Surface plots of measured spatial impingement height for C01 thru C03 test sections.	84
Figure 4-20: Surface plots of measured spatial impingement height for C04 thru C06 test sections.	85

Figure 4-21: Surface plots of measured spatial impingement height for C07 thru C09 test sections.	86
Figure 4-22: As-designed and as-fabricated values for key geometric parameters (S/D_j , H/D_j)..	87
Figure 4-23: Partial cut-away solid model of Gen II surrogate heater.	88
Figure 4-24: Exploded view of Gen II surrogate heater	89
Figure 4-25: Cartridge heater specifications	91
Figure 4-26: Exploded view of Gen II surrogate heater and impingement device assemblies.....	93
Figure 4-27: Target block embedded thermocouples. a) solid model view, b) thermocouple locations and labels.	94
Figure 4-28: Fabricated, fully soldered surrogate heater (a) without insulation and (b) mounted, mostly insulated but without an impingement device.....	95
Figure 4-29: Mostly insulated surrogate heater assembly with C09 impingement test section mount on top	96
Figure 4-30: Exemplary thermal simulation results for surrogate heater uniformity study. a) Heat flux contour of the surrogate heater top surface for both SH01 and SH05. b) temperature profile of impingement target surface only.....	98
Figure 4-31: Overview of impingement test facility.....	100
Figure 4-32: Detailed process and instrumentation diagram of impingement test facility in liquid testing configuration	101
Figure 4-33: Detailed process and instrumentation diagram of impingement test facility in air testing configuration	103
Figure 4-34: Simplified test procedure process diagram for heat transfer testing	108

Figure 4-35: Complete set of flow and heat load conditions for heat transfer testing segregated by fluid type.	111
Figure 4-36: Complete set of flow and heat load conditions, segregated by fluid type and part number.	112
Figure 4-37: Exemplary temporal data set of six steady-state heat transfer tests at a single flow rate with air. Data shown are for C05 part configuration.	114
Figure 4-38: Histogram of steady state rate condition for all tests	116
Figure 4-39: Exemplary flow rate, power supply voltage, and temperature data for single test point. The same data is shown as in Figure 4-37, but magnified around point 3.	117
Figure 4-40: Range of Reynolds and Prandtl numbers tested by device number	118
Figure 4-41: Simplified test procedure for adiabatic pressure drop testing	120
Figure 4-42: Schematic of hysteresis during adiabatic pressure drop measurement.	123
Figure 4-43: Exemplary temporal pressure drop data for C09-water adiabatic pressure drop test.	124
Figure 5-1: Exemplary test data for water tests with the C02 impingement part at all nominal flow rates and heat loads. Prediction lines using Rattner’s correlation are provided for reference.	136
Figure 5-2: Exemplary steady-state heat transfer results for part C02 with water. a) heat transfer coefficient varying with standard flow rate. b) Nusselt number varying with Reynolds number.	139
Figure 5-3: Complete steady-state heat transfer data set with all nine geometry configurations and three working fluids. a) heat transfer coefficient vs. Reynolds number, b) Nusselt number vs. Reynolds number.	143

Figure 5-4: Comparison of typical heat transfer coefficient values [80] to experimental results from this study.....	145
Figure 5-5: Complete steady-state heat transfer dataset; correlation-predicted Nusselt number plotted against measured Nusselt number. a) Present study correlation; b) Rattner correlation [44]; c) Huber and Visaonta correlation [20].	149
Figure 5-6: Response surface of geometric parameters spacing (S/D_j) and height (H/D_j) on Nusselt geometry factor K_G	151
Figure 5-7: Steady-state heat transfer data: Colburn J factor vs Reynolds number for configurations C01, C02, C03.....	154
Figure 5-8: Steady-state heat transfer data: Colburn J factor vs Reynolds number for configurations C04, C05, C06.....	155
Figure 5-9: Steady-state heat transfer data: Colburn J factor vs Reynolds number for configurations C07, C08, C09.....	156
Figure 5-10: Colburn J factor correlation curves for each impingement geometry C01 thru C09	157
Figure 5-11: Complete heat transfer dataset; geometry-normalized Colburn J factor vs Reynolds Number	159
Figure 6-1: Exemplary pressure drop data for part C01 with water and air. a) linear plot of raw data b) log plot of raw data with excluded data shown in red	161
Figure 6-2: Exemplary adiabatic pressure drop data with error bars for part C01 with a) air and b) water.....	163
Figure 6-3: Pressure vs flow rate raw data for water and air with all part configurations.....	166

Figure 6-4: Exemplary header pressure drop fraction for part C08 with air, a) raw data with quadratic regression curves, b) stacked proportional pressure drop from regression curves.	168
Figure 6-5: Exemplary C01 pressure data. a) pressure drop vs kinetic energy, b) k-factor, c) Darcy friction factor	172
Figure 6-6: Laminar and turbulent flow regimes within C01 air pressure drop test data.....	175
Figure 6-7: Schematic of typical laminar-turbulent transition profile [83].	175
Figure 6-8: Schematic of potential laminar and turbulent regions within impingement flow pathway	177
Figure 6-9: Darcy friction factor with exemplary correlation curve fit for part C01	180
Figure 6-10: Regression goodness of fit for Darcy friction factor geometry coefficient f_G	182
Figure 6-11: Contour map of friction factor geometric coefficient f_G	183
Figure 6-12: Darcy friction factor experimental data with proposed correlation and Rattner correlation for C01, C02, C03.....	185
Figure 6-13: Darcy friction factor experimental data with proposed correlation and Rattner correlation for C04, C05, C06.....	186
Figure 6-14: Darcy friction factor experimental data with proposed correlation and Rattner correlation for C07, C08, C09.....	187
Figure 6-15: Correlation predicted pressure drop compared to experimental values for all datasets	188
Figure 6-16: Log-log plots of Darcy friction factor correlation at various impinging array geometries, a) nine test geometries, b) constant jet spacing and variable jet height, c) constant jet height and variable jet spacing.....	190
Figure 6-17: Predicted and experimental pressure drop for C01, C02, C03.....	193

Figure 6-18: Predicted and experimental pressure drop for C04, C05, C06.....	194
Figure 6-19: Predicted and experimental pressure drop for C07, C08, C09.....	195
Figure 7-1: Microchip package schematic	196
Figure 7-2: Contour maps of coefficient of performance (COP) and effectiveness for water and air at variable geometry configurations. Constant parameters: $D_j = 0.3$ mm, $dT = 50$ C. a) Air COP at 10 W/cm ² , b) air effectiveness at 10 W/cm ² , c) water COP at 500 W/cm ² , d) water effectiveness at 500 W/cm ²	201
Figure 7-3: Single impinging jet schematic.....	203
Figure 7-4: COP and effectiveness variation with jet diameter at $H/D_j = 0.5$ and variable S/D_j . a) air at 10 W/cm ² , b) water at 500 W/cm ²	206
Figure 7-5: Effect of heat flux on key performance parameters: Flow rate, pumping power, pressure drop, COP, and effectiveness. a) Air at 10 W cm ⁻² and $S/D_j = 2.5$, b) air at 10 W cm ⁻² and $S/D_j = 8$, c) water at 500 W cm ⁻² and $S/D_j = 2.5$, d) water at 500 W cm ⁻² and $S/D_j = 8$	209
Figure 7-6: Effect of flow rate on chip case temperature for constant geometry and heat load. a) air at 10 W cm ⁻² , b) water at 500 W cm ⁻²	214
Figure F-8-1: Percentage bilateral uncertainty for all heat transfer data points; a) Reynolds number, b) Nusselt number.....	240
Figure F-8-2: Nusselt vs Reynolds number data for all heat transfer tests with error bars.	241
Figure H-8-3: Heat transfer coefficient vs flow rate for all heat transfer tests segregated by part number and fluid type.....	245
Figure H-8-4: Nusselt number vs Reynolds number data for all heat transfer tests segregated by part number and fluid type.....	246

NOMENCLATURE

Variable	Description	SI Units
A	Area	m^2
COP	Coefficient of performance	
c_p	Specific heat	$J\ kg^{-1}\ K^{-1}$
D	Diameter	m
f	Darcy friction factor	
f_G	Geometry friction coefficient	
\dot{G}	Mass flux	$kg\ m^{-2}\ s^{-1}$
H	Jet height	m
h	Wall jet height	m
htc	Heat transfer coefficient	$W\ m^{-2}\ K^{-1}$
J	Colburn J factor	
k	Pressure loss coefficient (k-factor)	
k_f	Fluid thermal conductivity	
K_G	Heat transfer geometry coefficient	
L	Jet nozzle length	m
$LMTD$	Log mean temperature difference	K
MAD	Mean absolute deviation	
\dot{m}	Mass flow rate	$kg\ s^{-1}$
N_j	Jet array size	
Nu	Nusselt number	
P	pressure	Pa
POC	Proof of concept	
Pr	Prandtl number	
q	Heat load	W
q''	Heat flux	$W\ m^{-2}$
r	Radius	m
R	Thermal resistance	$K\ W^{-1}$
R^2	Coefficient of determination	
Re	Reynolds number	
Re_l	Laminar transition Reynolds number	
Re_t	Turbulent transition Reynolds number	
$RMSE$	Root mean square error	
S	Jet spacing	m
T	Temperature	K
t	Time	s
$\%T_{uni}$	Temperature uniformity	$\%$

<i>TDP</i>	Thermal design power	W
<i>th_{ch}</i>	Channel wall thickness	m
<i>U</i>	Uncertainty	
<i>v</i>	Velocity	m s ⁻¹
\dot{V}	Volume flow rate	m ³ s ⁻¹
<i>w_{ch}</i>	Channel width	m
<i>W_p</i>	Pumping power	W
<i>X</i>	spatial coordinate	m
<i>Y</i>	spatial coordinate	m
<i>Z</i>	spatial coordinate	m

Greek

α	Channel aspect ratio (≤ 1)	
ϵ	Surface roughness	m
ε	effectiveness	
μ	Dynamic viscosity	kg m ⁻¹ s ⁻¹
ρ	Density	kg m ⁻³
φ	Jet/return nozzle conical angle	rad

Subscripts

<i>a</i>	Actual
<i>adj</i>	Adjusted
<i>amb</i>	Ambient
<i>anc</i>	Ancillary
<i>app</i>	Applied
<i>c</i>	Case (IC lid)
<i>ch</i>	Channel
<i>CH</i>	Cartridge heater
<i>cl</i>	Critical lower
<i>cu</i>	Critical upper
<i>eq</i>	Equivalent
<i>exp</i>	Experimental
<i>f</i>	Fluid
<i>fr</i>	Frictional
<i>H</i>	Relating to jet height
<i>h</i>	Relating to wall jet height
<i>ideal</i>	Ideal
<i>imp</i>	Impingement
<i>in</i>	Inlet
<i>ins</i>	Insulation
<i>j</i>	Jet
<i>liq</i>	Liquid

<i>loc</i>	Local
<i>max</i>	Theoretical maximum
<i>mc</i>	Common (main) channel
<i>meas</i>	Measured
<i>min</i>	Theoretical minimum
<i>out</i>	Outlet
<i>pred</i>	Predicted
<i>r</i>	Return
<i>req</i>	Required
<i>s</i>	Target surface
<i>sc</i>	Side channel
<i>stp</i>	Standard temperature and pressure
<i>var</i>	Variation

CHAPTER 1. Introduction

1.1. Motivation for Research

Jet impingement cooling techniques are associated with high local heat transfer coefficients, making such cooling architectures very attractive for a variety of thermal management applications including turbine blade cooling [1], food freezing [2], compact heat exchanger design [3], and cooling of power electronics [4]. Similar to microchannel cooling techniques, by driving jet sizes down to the micro-scale, researchers have been able to demonstrate single-phase, liquid impingement heat transfer coefficients $>10,000 \text{ W m}^{-2} \text{ K}^{-1}$ [5–7]. This level of heat transfer performance makes jet impingement a viable option for many future high-heat flux cooling applications and a contender to some of the microchannel cooling structures in use today. While microchannel cooling methods provide many benefits including simplicity, ease of manufacturing and design, and surface area enhancement [8], impinging jet arrays offer distinct advantages within the realm of fluid delivery. Specifically, impinging jet arrays allow for fresh fluid of uniform inlet temperature to be delivered to a multitude of locations dispersed throughout the target surface. By contrast, in traditional microchannel architectures, fluid traverses the target surface and picks up heat along the relatively lengthy flow path. This leads to deteriorating cooling performance further downstream. Recently, some researchers have explored ways to mitigate this problem while still using microchannels by attaching a repeating array of microchannel sections to the target surface with a hierarchical flow delivery structure [9]. While a segmented microchannel approach is very promising, it also tends to add a great deal of complexity akin to jet impingement systems, thus somewhat reducing its advantage. The capability for highly selective fluid delivery, inherent with

jet impingement, even offers the possibility to selectively cool local hotspots present on the target surface, thus allowing for better flow utilization and more uniform surface temperatures.

Another advantage of jet impingement is that the fluid can be easily placed into direct contact with the target surface. This is an especially attractive attribute in the field of electronics cooling, where the total thermal resistance is often dominated by a thermal interface material (TIM) placed between an integrated circuit (IC) package and the heatsink [10]. The TIM layer can be completely omitted using a jet impingement cooler, significantly reducing overall thermal resistance. Microchannel coolers are typically mounted to the cooled surface with no direct fluid contact. Direct fluid contact also means that a jet impingement device can be constructed from non-thermally conducting materials, allowing for very low-cost cooling solutions.

1.1.1. Challenges with conventional jet impingement

The typical configuration of a jet impingement array (depicted in Figure 1-1) is a repeating pattern of impinging jets spaced uniformly above the target surface. Although single impinging jets have been investigated extensively in the literature [11,12], interactions between jets when in an array often mean that single jet characteristics cannot simply be scaled to describe those of an

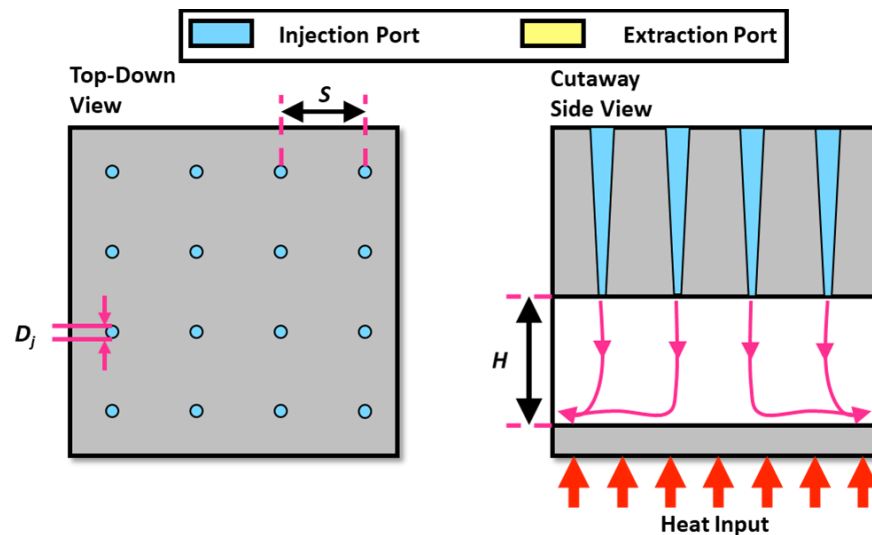


Figure 1-1: Typical flow arrangement for a standard jet impingement cooling device with crossflow fluid extraction

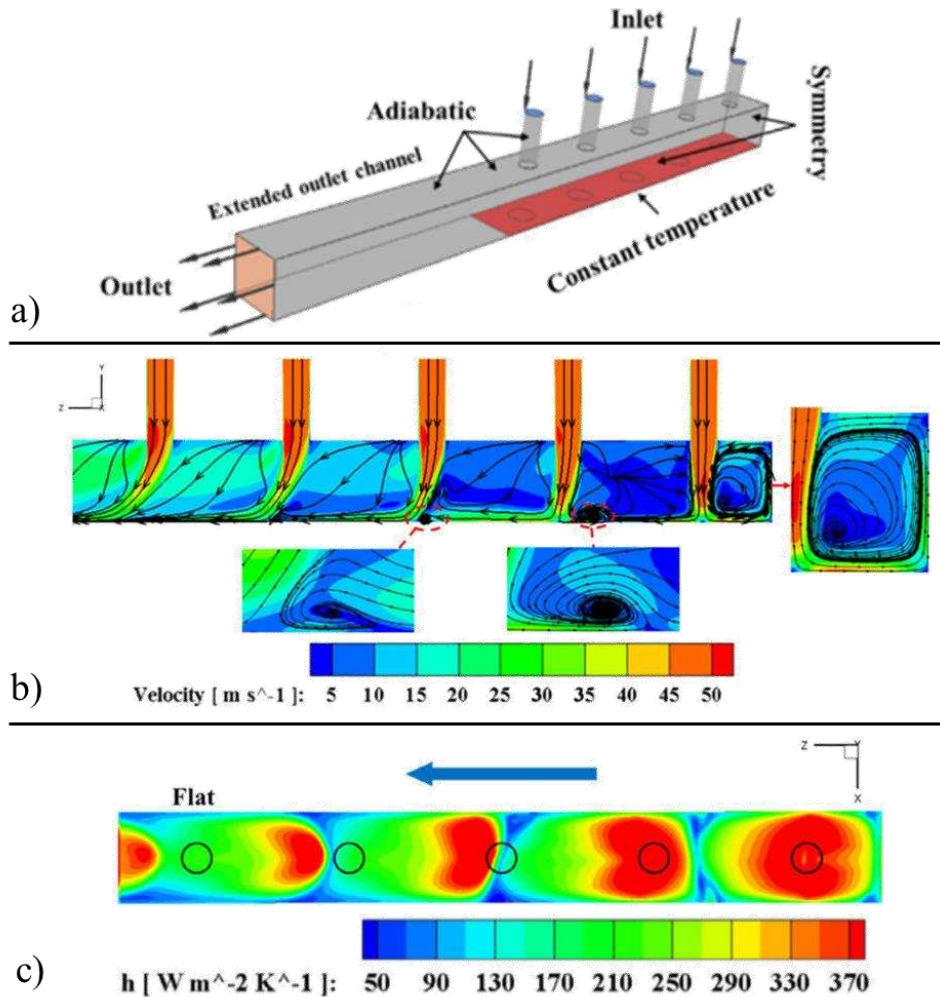


Figure 1-2: Visual representation of the effect of cross flow on impinging jet formation and performance; adapted from Jing et al. [14]: a) Computational domain b) Side view of jet velocity contours c) Top view of heat transfer coefficient contours

array. In an array, after impacting the target surface, the spent fluid continues past adjacent jets to the periphery for removal, resulting in crossflow interference. This causes degraded heat transfer performance as jets toward the periphery are swept away by the upstream fluid [13]. Jing et al. provides an excellent visual depiction (adapted in Figure 1-2) of cross flow effects on downstream jet formation [14]. Figure 1-2a outlines the computational domain of the study, where each successive jet is further from the center of the array. Figure 1-2b shows velocity contours of the five jets. While the jet nearest the center of the array (far-right) appears similar to a single-jet

profile, the peripheral jet (far-left) is clearly swept away by the spent flow. The effect on thermal performance is obvious from the heat transfer coefficient contours in Figure 1-2c which show diminishing regions of red (highest heat transfer coefficient) toward the periphery (left). The negative effect of crossflow interference is especially prevalent in arrays with high jet counts, thus limiting the scalability of jet impingement arrays to large surface areas and impacting cooling uniformity. Natarajan and Bejjani attempt to quantify this limitation by proposing that the average drain velocity should be kept below one-half of the average jet velocity to avoid significant degradation in cooling performance at the periphery of a conventional impingement array [15]. Therefore, it remains an important challenge for practical implementation of jet impingement cooling solutions to combat crossflow interference.

1.1.2. Advent of return jet impingement

Several approaches have been developed to moderate jet-to-jet interference. Some examples include using an angled confining wall [16], variable jet spacing [17], and hybrid microchannel-impingement concepts [18,19]. One promising technique, first introduced by Huber and Viskanta [20], involves interspersed fluid extraction, wherein fluid return ports are situated directly adjacent to each impinging jet. Figure 1-3a depicts an impingement flow concept with interspersed fluid extraction (here coined *return jet impingement*, or RJI). Figure 1-3a also outlines a quarter-jet unit cell that can be repeated to form a full array. A single unit cell is provided in Figure 1-3b as a solid model with indicators for the local flow path boundary conditions. A major advantage of return jet impingement over some other crossflow mitigation techniques is the inherent existence of a repeating unit cell. This allows for a consistent jet profile to be theoretically applied to any size array. Of similar importance, the application of a repeating unit cell greatly simplifies computational models, thereby allowing for lower cost and higher fidelity prediction.

Physical production of return jet impingement architectures, however, is challenging. The presence of many distinct flow pathways in close proximity to one another makes fluid routing difficult. Relatively complex manifolding structures are needed both upstream and downstream of the impingement region. Fabricating these flow structures often requires advanced manufacturing techniques and non-conventional design practices. Furthermore, while a return jet impingement

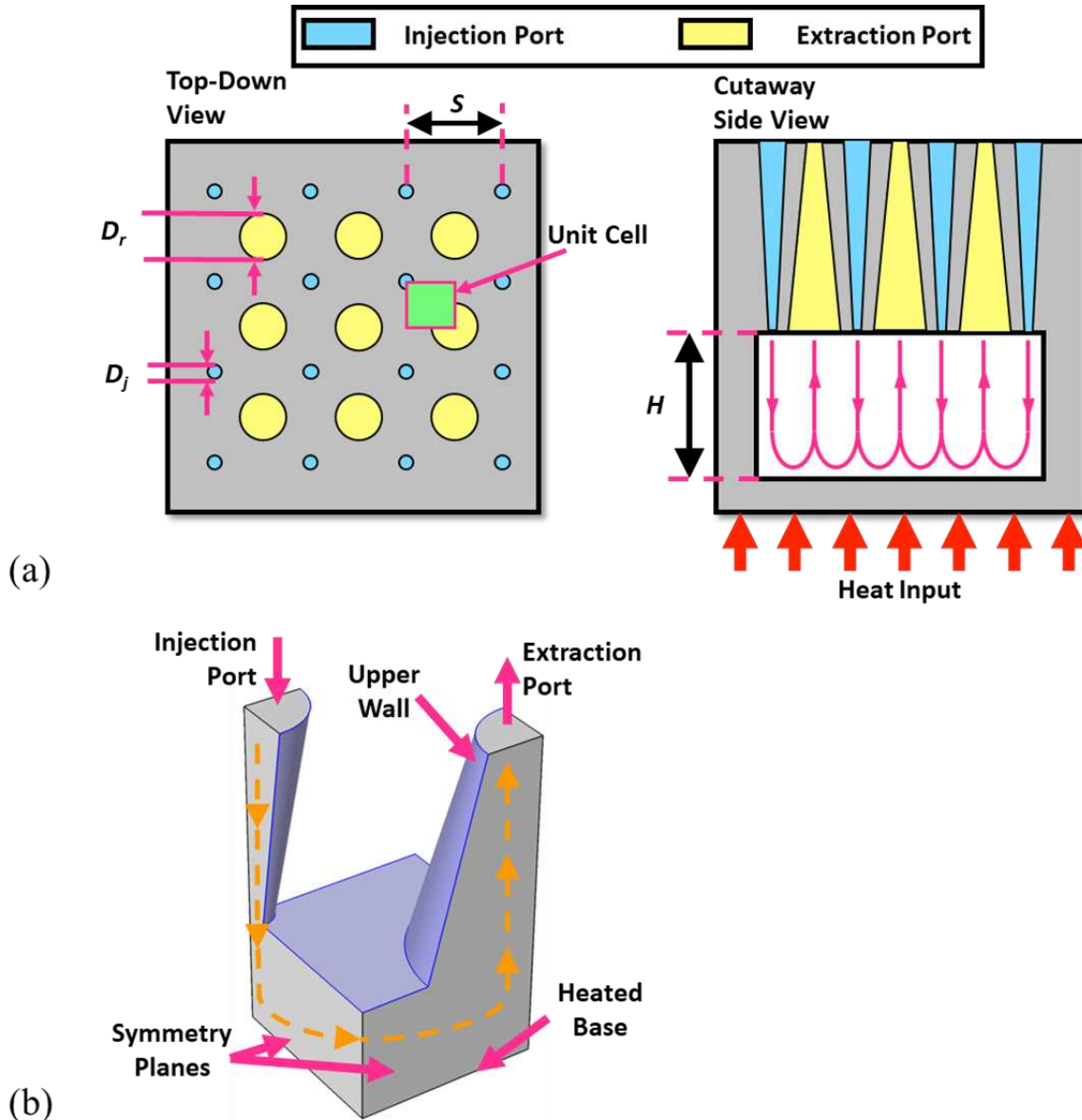


Figure 1-3: (a) Typical flow arrangement for a jet impingent cooling device with distributed jet-adjacent fluid removal ports and (b) Solid model and flow description of quarter-jet repeating unit cell to serve as the solution domain for computational simulations.

array may be modeled as a collection of repeating unit cells, this approximation relies on uniform inlet conditions provided to each jet, an assumption that is highly dependent on manifold geometry. Downstream uniformity conditions can also impact unit cell repeatability. In light of these challenges, to promote concurrence between prediction models and experiments, effort is needed to either mitigate, or account for, manifold effects on jet array performance. In short, return jet impingement offers unique and useful heat transfer capabilities while presenting a significant research challenge.

1.2. Research Objectives

Jet impingement cooling techniques offer a promising opportunity for many cooling applications. By introducing fluid extraction throughout an impinging array, the exceptional performance of single impinging jets can be applied over an extended surface without the typical degradation observed in large conventional arrays. Currently, there exists only a very small number of studies which investigate return jet impingement in any capacity, and even fewer studies propose useful correlation to aid design efforts. The breadth of these studies will be discussed further in the following chapter. The current work seeks to expand the existing body of literature on return jet impingement in an impactful way by proposing empirical heat transfer and pressure drop correlations. The proposed correlations shall be composed from carefully designed experiments which span a wide range of geometric, fluid, and flow parameters.

In summary, this study will:

- Design and fabricate a novel impingement device with interspersed fluid extraction
- Compose an experimental approach and associated facilities for evaluating the heat transfer and pressure drop performance of the novel impingement device

- Establish highly applicable predictive correlations for heat transfer and pressure drop in a generic return jet impingement array
- Evaluate core performance metrics for return jet impingement cooling and provide recommendations cooler design

1.3. Thesis Organization

This manuscript is constructed of eight chapters followed by supporting appendices. This chapter introduces the concept of return jet impingement and the significant value it holds as a cooling technique. Chapter 2 will present a succinct investigation of the relevant literature on jet impingement with a focus on studies which include interspersed fluid extraction. Upon evaluating the literature, Chapter 2 will also identify key research gaps and will propose a focus of the current investigation as it seeks to remedy those deficiencies. Chapter 3 will detail a preliminary, proof-of-concept investigation including technology development, experimental setup and results, and important discoveries which were crucial for constructing the expanded investigation described in Chapters 4 through 6. The experimental set up for the expanded investigation is examined in detail Chapter 4. Chapter 5 will present and discuss return jet impingement heat transfer experimental results and will propose a Nusselt correlation for predicting the thermal performance of such systems. Chapter 6 will provide similar examination but for pressure drop through the return jet impingement array; once again, proposing a predictive correlation. Chapter 7 will employ the experimental findings from chapters 5 and 6 in a case study analysis where the proposed empirical heat transfer and pressure drop correlations are applied towards cooling a theoretical electronics package. Key performance trends will be identified and discussed, and design recommendations will be made in Chapter 7. Finally, Chapter 8 will summarize this work, provide conclusions, and offer recommendations for future studies.

CHAPTER 2. Literature Review

An in-depth review of the open literature was conducted on return jet impingement technologies. There exists a vast body of literature on the broad subject of jet impingement techniques encompassing single jets and jet arrays, various jet shapes, mini- and micro-scale jets, free, submerged, and confined jets, surface area enhancement, local and average heat transfer, flow characteristics and more. Impingement studies are rich in both experiments and simulations conducted over more than seven decades. However, the subset of jet impingement investigations which consider interspersed fluid extraction techniques are remarkably limited, composing only a handful of studies since the concept was first introduced in 1994. This chapter will provide a comprehensive but succinct description of jet impingement studies involving interspersed fluid extraction alongside a very brief review of predecessor conventional impinging technologies.

2.1. Conventional Jet Impingement Cooling

Within the realm of conventional impingement studies, there are several concepts and discoveries which are of particular relevance to the current investigation, of which a few are highlighted here. Figure 2-1, adapted from Zuckerman and Lior [13], contains a schematic of a submerged impinging jet with descriptions of the various flow regions. As fluid exits the jet nozzle, a free jet is formed. This free jet region exists where the fluid is sufficiently far enough from the target surface that the flow, so far, is largely unaffected by downstream interactions with the target surface. Shearing between the impinging jet and surrounding fluid causes entrainment, raising the jet mass flow but reducing its velocity as it travels further from the nozzle exit. A potential core region at the center of the free jet maintains its initial velocity but degrades radially inward as more flow entrainment occurs along the axial length of the jet affecting the entire jet profile. The potential core region persists for approximately four to eight jet diameters away from the nozzle

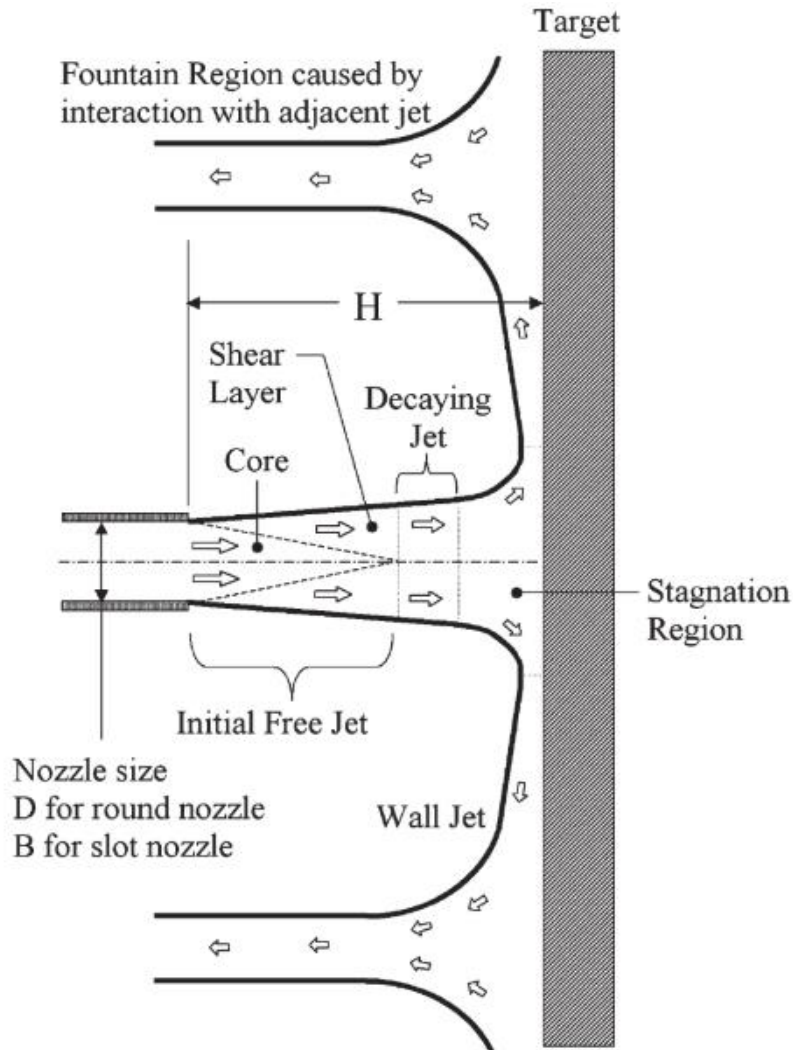


Figure 2-1: The flow regions of an impinging jet [13].

exit. The region after the core jet has fully dissipated is known as the decaying jet where the jet velocity has developed into a Gaussian profile which continues to decrease gradually in magnitude from the center to the edge of the jet. At a point approximately 1.2 jet diameters away from the target surface, fluid begins to interact with the wall, increasing static pressure and producing what is known as the stagnation region where flow turning occurs and the axial jet momentum is transferred radially outward. Zuckerman and Lior point out that if the jet nozzle is placed close enough to the target surface, the decaying jet region, or even the initial free jet region may not develop, as interaction with the wall occurs before those regions have a chance to form. For a non-

dimensional jet height, H/D_j , less than 8, the decaying jet may not occur, meaning that the potential core is still present when the jet begins to interact with the target. For very small values of H/D_j the free jet may not even form as the stagnation region begins immediately upon the nozzle exit. Following the stagnation region, a wall jet is formed radially outward along the target wall. The wall jet gradually thickens as it moves away from the jet centerline. In the case of an impinging array, the wall jet from one jet will inevitably interact with an adjacent jet, forming a fountain region. With relation to the present study, this ideal representation of an impinging jet is of critical importance because the goal of return jet impingement is to extend this behavior to large jet arrays independent of jet spacing, height, or position. In conventional arrays, the flow profile shown may be dramatically affected by crossflow effects.

Figure 2-2 presents another important concept from conventional jet impingement that plays a major role in this work. Liu et al. [21] provide experimental data matched by modeling for local Nusselt number produced by a single impinging jet. The x-axis represents radial distance away from the jet axis, normalized by jet diameter. Local Nusselt number is at a maximum at the

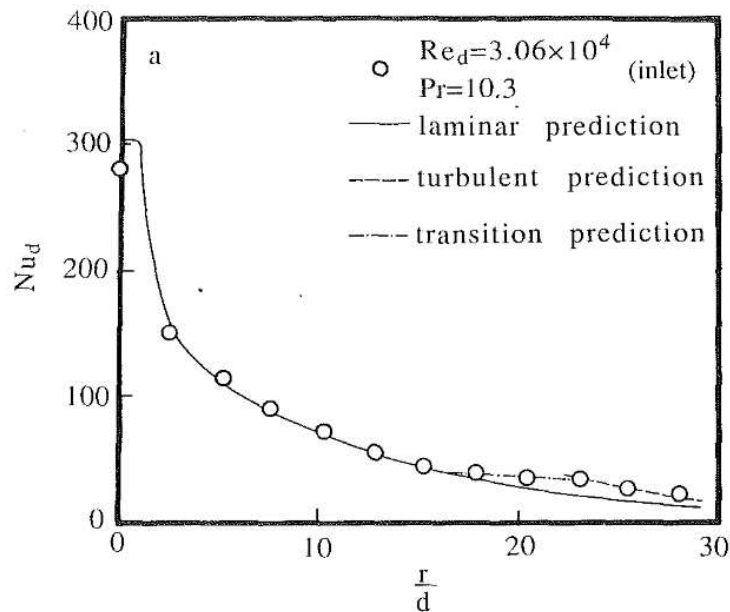


Figure 2-2: Local Nusselt number of single impinging jet by Liu et al. [21].

centerline of the impinging jet and rapidly declines radially outward from center. From this description of the local heat transfer behavior of an impinging jet, it is easy to see how jet spacing could play a critical role on the average heat transfer performance experience by an array of jets. Closely packed jets will theoretically produce a higher area averaged Nusselt number while also increasing the amount of interaction between jets. These factors compete with the net result of a reduction in overall performance when compared to the theoretical superposition of individual jets.

Notably, there have been several studies that present Nusselt number correlations for single impinging jets and conventional arrays [11,21–31]. Although these correlations vary greatly in their construction, each considered a power-law relationship of Nusselt number with Reynolds number. The Reynolds number exponent in these studies ranges from 0.46, to 0.78.

Beyond these specific examples, jet impingement cooling techniques have been an active area of research for many years. As such, both single jets and conventional impinging arrays have been investigated extensively in the literature. Seminal works by Martin [11], Zuckerman and Lior [13], and Webb and Ma [32] discuss the hydrodynamics of impinging flow in detail and provide guidance to develop appropriate correlations that account for the relevant physical parameters. Each of the authors compile works from a myriad of sources and touch on a variety of topics including round jets, slot jets, arrays, nozzle geometry and position, array configuration, impact angle, and target surface geometry. In 1992, a review paper by Jambunathan et al. [12] compiled twenty-seven independent studies on single round jets alone. A more recent (2017) review by Shukla and Dewan [33] identifies more than thirty important computational studies on jet impingement. Several studies have been directed at surface area enhancement under jet impingement [7,34–36]. Other studies have explored microjet conventional arrays [4,37–39].

Clearly, the archive of literature on jet impingement is thorough and extensive. Still, the contribution of academic investigation on return jet impingement remains limited.

2.2. Jet Impingement with Interspersed fluid extraction

Although investigations on return jet impingement are relatively sparse, there are still a number of previous researchers who have established the merits of jet-adjacent fluid extraction both experimentally [20,40,41], and computationally [15,42–45]. Moreover, a small number of studies have used a combination of computational and experimental methods to investigate impinging jet arrays with interspersed fluid extraction [6,46]. Very recently, one research group has contributed a series of return jet impingement investigations, including experimental and computational work as well as applied studies [47–60]. The following provides a synopsis of the complete body of return jet impingement studies.

As was previously mentioned, Huber and Viskanta [20] first introduced a return jet impingement flow concept in 1994. An illustration of their experimental setup is provided in Figure 2-3. They experimentally demonstrated consistently elevated local Nusselt numbers when compared to standard crossflow fluid removal. That study focused on large ($D = 6.35$ mm) air jets

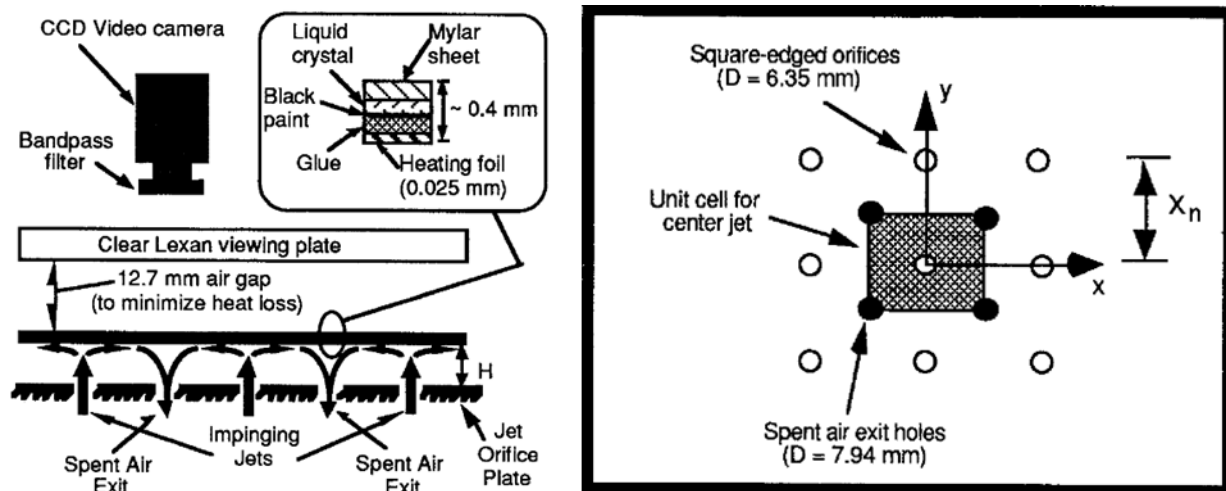


Figure 2-3: Huber and Viskanta RJI experimental setup [20].

in a small array and the impingement manifold geometry was not thoroughly described. Huber and Viskanta measured local heat transfer using a thermochromatic liquid crystal technique. They considered a range of non-dimensional jet heights and spacings for turbulent flow where $Re > 3,500$. That investigation proposed a Nusselt correlation with terms for Reynolds number, Prandtl number, jet height ($H/D_j = 0.2-6.0$), and jet spacing ($S/D_j = 4-8$). The Huber and Viskanta correlation represents the most comprehensive experimental correlation available in the prior literature. Notably, the Huber and Viskanta study fails to evaluate alternate fluids or laminar flow regimes.

Rhee et al. [46] were next to publish an investigation on return jet impingement. Their study involved both an experimental and a computational investigation of confined air jets with effusion holes interspersed throughout the impinging array. Figure 2-4 provides an illustration of the physical setup. They compared the thermal performance of an impinging array with and without interspersed fluid extraction for variable non-dimensional jet heights. Local heat transfer coefficients were observed using a naphthalene sublimation method. The study concludes that the inclusion of flow extraction orifices results in improved performance at low H/D_j ratios compared

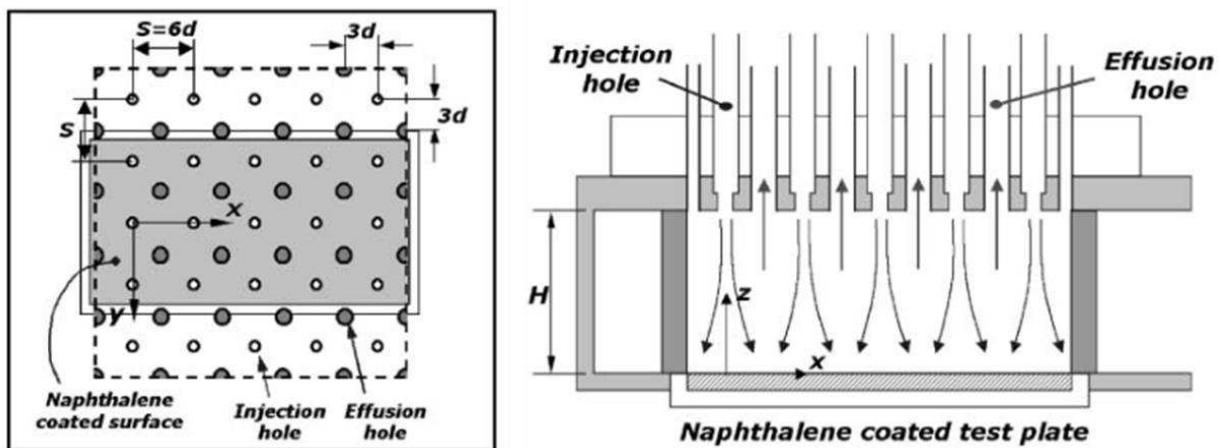


Figure 2-4: Rhee et al. RJI experimental setup [46].

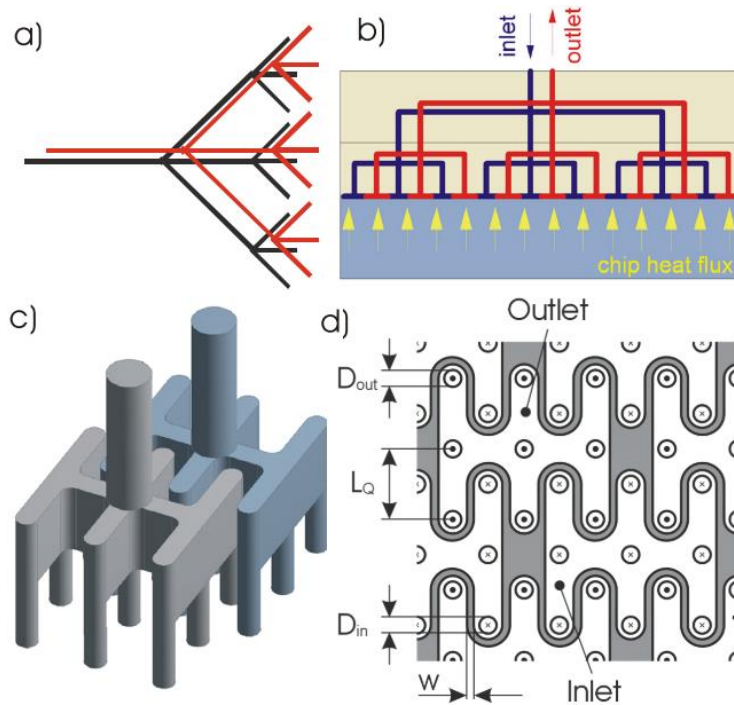


Figure 2-5: Brunschwiler et al. RJI manifold architecture [6].

to crossflow fluid removal. Heat transfer performance between the two methods was found to converge as H/D_j was increased. No correlations were produced.

In 2006, IBM researchers Brunschwiler et al. [6] conducted both an empirical and CFD study which used a multi-layered hierarchical geometry to create jet-adjacent returns for microelectronic applications. A schematic of their manifold architecture is shown in Figure 2-5. The study examined jet diameters from 31 - 126 μm which were fabricated into either a multilayer ceramic (MLC) or multilayer deep reactive ion etched (DRIE) silicon cooling structure. A single jet height of $H/D_j = 1.2$ was considered, with multiple jet spacings spanning $3.2 < S/D_j < 9.9$. Jet arrays for that investigation exceeded 45,000 jets and heat transfer coefficients in some arrangements were greater than $100 \text{ kW m}^{-2} \text{ K}^{-1}$. The work by Brunschwiler et al. was meaningful for demonstrating the tremendous heat transfer capabilities of the technology while identifying key drawbacks in the form of *thermal shortcut losses* – i.e., preheating the entering cooling fluid with heated outlet fluid – and manufacturing cost and complexity. Brunschwiler et al. proposed a

simple Nusselt correlation which accounts for Reynolds number dependence only, but no geometric effects. Pressure drop for the whole device was measured and guidance was provided for reducing flow losses through manifold design but no correlation for this effect was developed. They proposed a Reynolds exponent of 0.73. There have been two follow up numerical studies from IBM expanding on the initial study. In the first follow up study by Natarajan and Bezama [15], they expanded on the MLC impingement manifold through design and fabrication improvements. The new MLC cooler design was tested on a silicon chip and demonstrated a cooling heat flux of 250 W cm^{-2} at a pressure drop of less than 70 kPa. The study also provides very practical quantitative guidance for determining when impingement crossflow interactions begin to significantly reduce cooling performance. A second follow up study was conducted by Sharma et al. in 2015 [45]. Researchers evaluated a novel microchip cooling device of hybrid slot jet and microchannel construction. The geometry of the cooling device diverges greatly from other RJI architectures included in this literature review. Each jet is fully confined and entirely incapable of interacting with adjacent jets due to the included microchannel structure. However, it is mentioned here because of its affiliation with the two prior studies in combination with the fact that impinging jets and local fluid extraction are included in the design. The impingement architecture is provided in Figure 2-6.

Onstad et al. [40] and Hoberg et al. [41] fabricated impingement arrays with interspersed effusion holes for fluid extraction. The impingement structures were fabricated using a stereolithography (SLA) process in plastic with relatively large jet diameters (0.94 – 8.46 mm). These works present the first known return jet impingement architecture fabricated out of plastic as well as the first instance of a 3D-printed RJI device and the manifold design is depicted in Figure 2-7. The former study investigates a single impinging geometry while the latter study expands on

the former by including a range of geometries. Air was used as the working fluid for heat transfer experiments and Reynolds numbers ranged from 500 to 10,000. The Hoberg et al. study establishes a simple Nusselt number correlation in terms of Reynolds number only where Nusselt number was found to be proportional to Reynolds number to the power of 0.59.

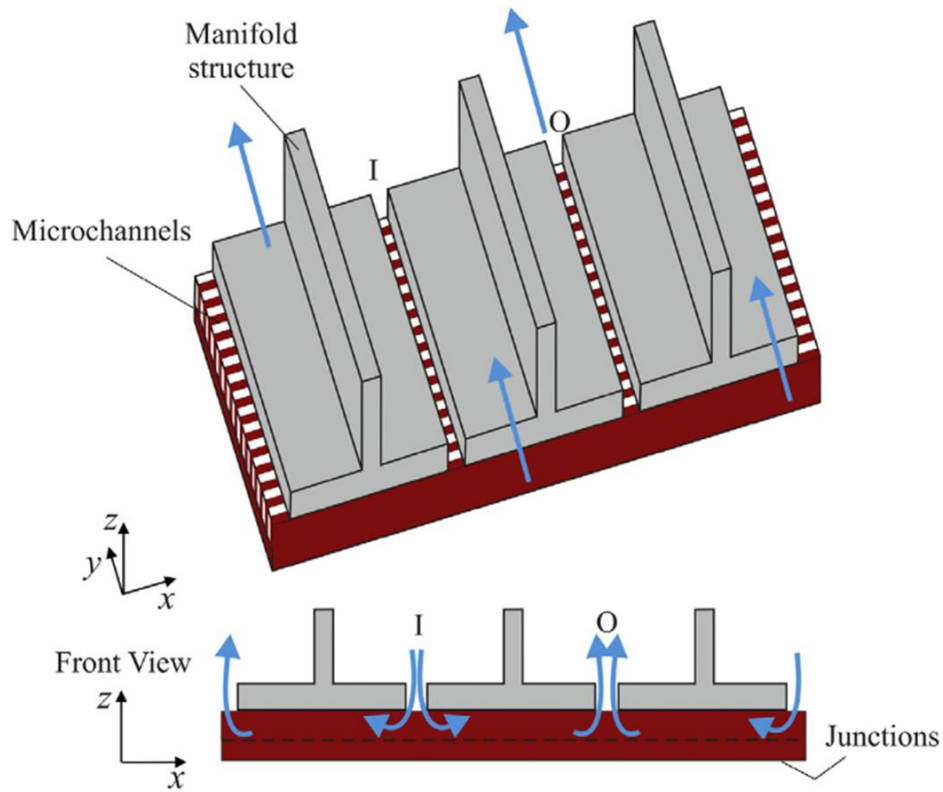


Figure 2-6: Sharma et al. impingement architecture with jets fully confined by microchannel structures [45].

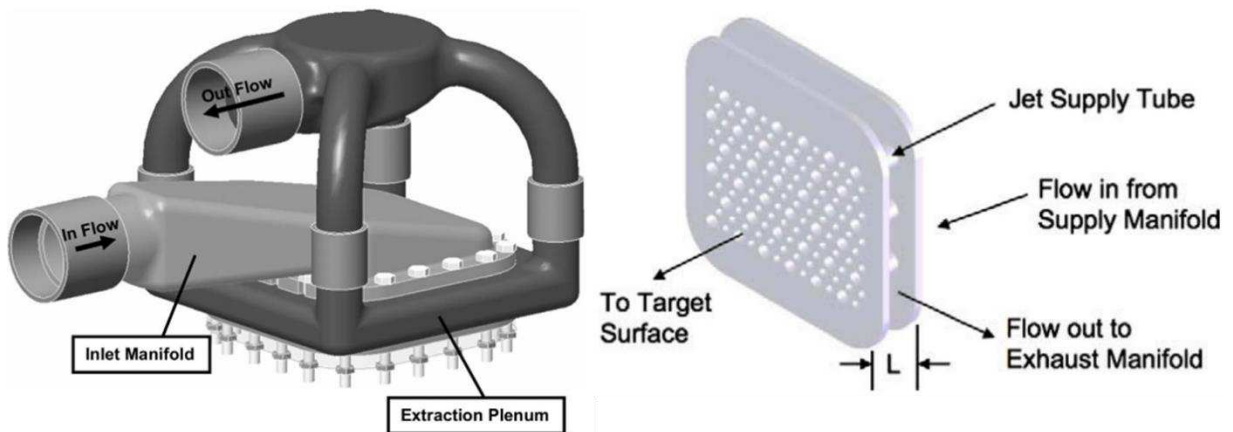


Figure 2-7: RJI manifold architecture used by Onstad et al. and Hoberg et al. [40,41].

In 2014, Han et al. [42] conducted a purely computational study on a hybrid impingement microchannel cooler which closely resembles return jet impingement. The cooler design incorporated round jet nozzles with slot-style fluid extraction ports. Han et al. experiment with frequency and size of return ports throughout the impingement array. Using this design, simulations predicted average heat transfer coefficients well in excess of $100 \text{ kW m}^{-2} \text{ K}^{-1}$ at pumping powers less than 1 W when applied towards a 350 W cm^{-2} heat flux. Pressure drop was found to be less than about 60 kPa for all configurations. Only the impingement region was simulated, and they did not include any manifold structure in their model. This study did not propose correlations for heat transfer or pressure drop.

Husain et al. [43] presents another fully computational study. In their study, a return jet impingement flow architecture was compared to a confined conventional impinging array and an unconfined conventional impinging array. Husain et al. found that the RJI configuration outperformed both conventional array configurations by yielding higher heat transfer coefficients. However, thermal improvements came at the cost of greater pressure drop. The manifold architecture was not simulated in this study. No correlations were proposed in this study.

In 2017, Rattner [44] conducted a numerical study which evaluated the thermal and hydraulic performance of jet impingement using jet-adjacent fluid extraction. A single unit cell was simulated to represent an infinite repeating array. The manifold architecture was not considered in this study. Rattner's simulations spanned a large range of cases which varied Reynolds number ($Re = 20-500$), Prandtl number ($Pr = 1-200$), jet height-to-diameter ratio ($H/D_j = 0.1-4.0$), and jet spacing-to-diameter ratio ($S/D_j = 1.8-7.1$). Using these computational results, Rattner presented a correlation for predicting jet impingement Nusselt number and loss coefficient for these conditions. The pressure loss correlation included terms for Reynolds number, jet

spacing, and jet height. The Nusselt correlation included all the same terms in addition to a Prandtl number term. The Rattner study incorporates a wide range of geometric parameters and Prandtl number. However, the study is very limited in terms of Reynolds number, only applying towards low Reynolds number laminar flow. Notably, Rattner acknowledged that developing mechanistically driven correlations which encompass the full scope of parameters was very difficult. Instead, Taylor series expansions were used for developing the proposed correlations.

Wei et al. conducted a series of studies beginning in 2017 [47–60]. They investigate multiple iterations of a return jet impingement cooling device using exclusively deionized water and applied towards integrated circuit cooling. They present both experimental and simulation results examining the thermal and hydrodynamic performance of the impingement device. The researchers evaluate the effects of various geometric parameters including jet spacing, jet height, nozzle length, and manifold construction. Wei et al. initially present a plastic 3D printed cooler (provided in Figure 2-8) fabricated using vat photopolymerization process [47,48]. They explore the effects of variable nozzle count and jet diameter. In one study [49], they produced a similar cooler using a micromachining process and compared its performance with the 3D printed variant. The performance was similar for both designs; however, the 3D printed design offered benefits to manufacturability and package size over the micromachined design. In a follow up computational

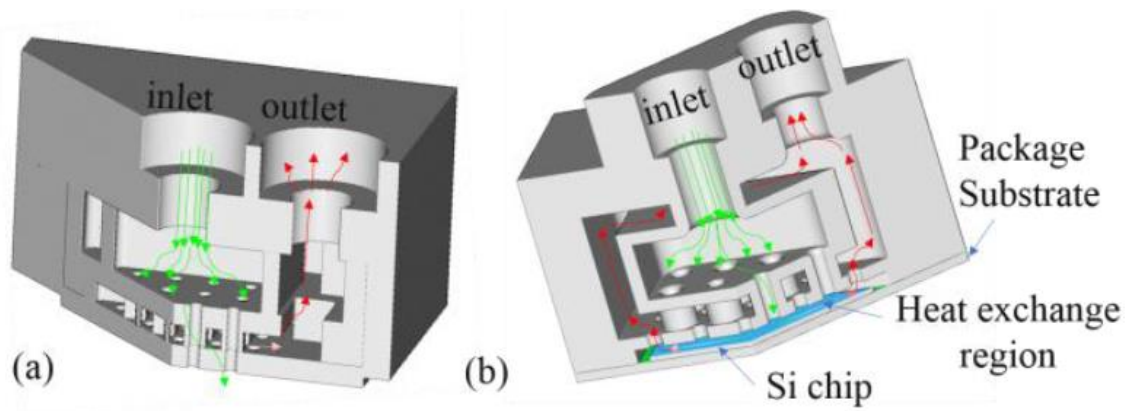


Figure 2-8: Primary RJI manifold architecture used by Wei et al. [47,48].

only study [50], Wei et al. further evaluated the thermal resistance and pumping power of impinging arrays over a range of jet spacings from 2.5 jet diameters up to 40 jet diameters. Among other things, they observe that cooling efficiency degrades with increasing nondimensional jet spacing. One study [51] applies the 3D printed cooler to a MOSFET device. They demonstrate a very low thermal resistance of $0.16 \text{ K cm}^2 \text{ W}^{-1}$ at a pumping power of less than 1 W cm^{-2} . Another study [52] compares the 3D printed cooler to a single impinging jet approach for cooling an integrated circuit with non-uniform heating. They observe superior temperature uniformity for the RJI design. This study also correlates return jet impingement Nusselt number to Reynolds number to the power of 0.57 with no considerations for geometry or fluid properties. In a follow on computational study [53], Wei et al. compared the fidelity of different CFD turbulence models applied toward RJI. They determined that both transition SST and $k-\omega$ SST models can provide accurate predictions when compared to an LES baseline.

In an application study [54], Wei et al. employed a single 3D printed impingement device to cool two integrated circuits in a single lidless package. They demonstrated improved thermal resistance by eliminating the thermal interface material for TIMs with poor thermal conductivity. However, they also showed that for high thermal conductivity TIMs, better cooling performance is achieved by retaining the TIM layer and utilizing heat spreading through the package lid. Another application study [55] uses the 3D printed RJI cooler with a non-uniform impinging array configuration to selectively cool hotspots on an integrated circuit. They show a reduction in maximum chip temperature with the hotspot targeted impingement array. Yet another application study [56] compares the 3D printed cooler to a standard air-cooled heatsink solution for cooling a 5.3 cm^2 chip with a thermal design power of 285W. The microfluidic water impingement cooler outperforms the standard air-cooled heatsink. Wei et al. revisit the hotspot cooling study from [55],

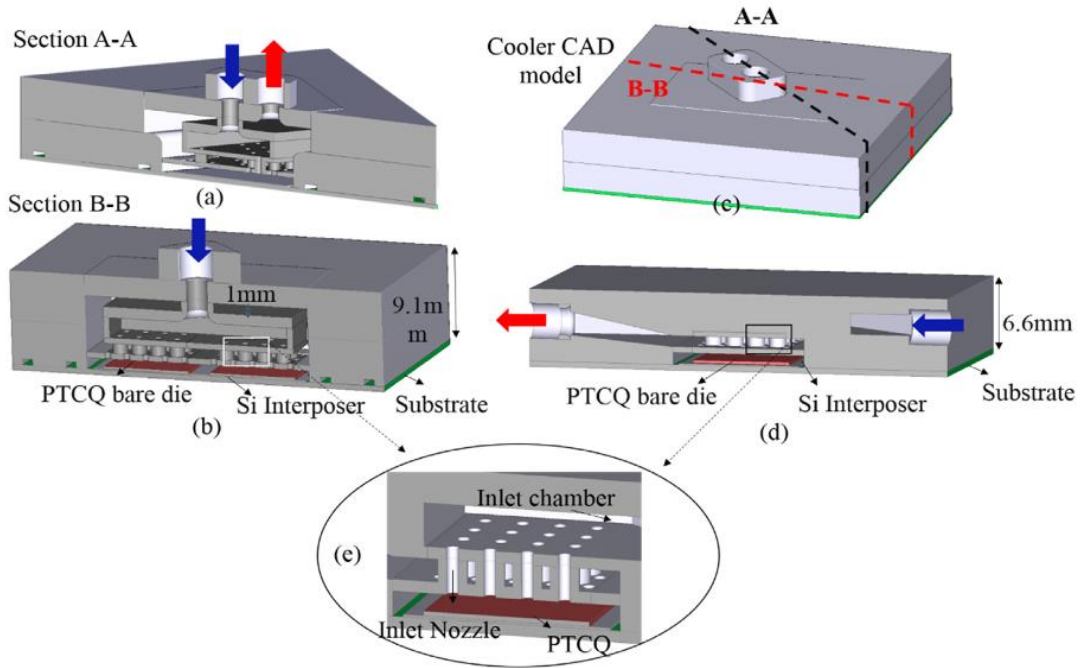


Figure 2-9: Secondary Wei et al. RJI manifold architecture (d) compared to primary architecture (a and b) [59].

in a follow up investigation [57]. This time they improve performance further by incorporating open return ports throughout the full array and jets only in the hotspot regions.

Wei et al. perform another scaling analysis in yet another study [58]. Here, they determine that an ideal nozzle density can be found which maximizes cooling efficiency, given other constant geometric and flow rate parameters. A further investigation [59] explores a new manifold architecture (shown in Figure 2-9) and compares it to the manifold architecture used in all prior studies. The new manifold offers an approximate 50% reduction in device pressure drop for similar cooling performance. Finally, in a 2021 study [60], another manifold strategy (depicted in Figure 2-10) is devised and compared to the original. In this case it was found that chip cooling uniformity could be improved with the new design. Although the works by Wei et al. present a significant contribution to the body of literature across these works, no generalized heat transfer or pressure drop correlations have yet to be formed.

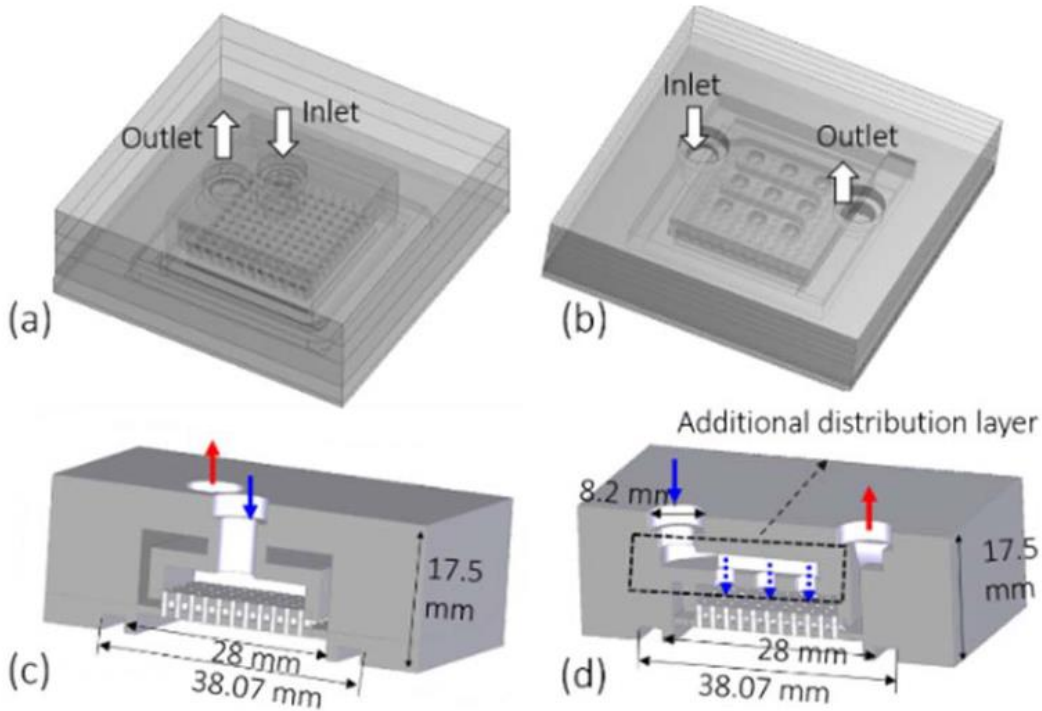


Figure 2-10: Tertiary Wei et al. RJ manifold architecture (b and d) compared to primary architecture (a and c) [60].

A synopsis of the relevant studies which have explored interspersed fluid extraction are presented in Table 2-1, segregated by institution. Excluding this work, eight distinct institutions have contributed to the body of publicly available return jet impingement research. Although there have been a respectable number of studies on the topic, very few have presented heat transfer or pressure drop correlations and all are included in Table 2-1. Engineers require practical prediction tools that correlate relevant parameters (i.e., geometry, fluid flow rates, and thermodynamic and transport properties) to performance to evaluate this technology against modern cooling challenges. While all of these studies provide valuable insight into the mechanics, capabilities, and limitations of return jet impingement, the development of predictive correlations is imperative for facilitating good design of productized cooling strategies. Of the available literature, only five studies [6,20,41,44,52] were found to provide a heat transfer correlation and only a single study by Rattner [44] provided a pressure drop correlation. The five correlations available on return jet

impingement heat transfer are relevant over only a small range of highly specific geometries and flow conditions. Four of the correlations [6,20,41,52] have each been developed using a single working fluid, limiting their applicability. The correlations by Brunswiler et al. [6], Hoberg et al. [41], and Wei et al. [52] are given in terms of Reynolds number only, meaning that differences in fluid and geometry cannot be accounted for by the end user. Rattner's correlation and Huber and Viskanta's correlation are perhaps the most general and may be applied over the greatest range of fluids, jet heights (H/D), and jet spacings (S/D). However, Rattner's correlation is limited to low Reynolds number laminar flow. Furthermore, having been developed using only computational methods, it also lacks experimental validation. Conversely, Huber and Viskanta's correlation is only validated for turbulent flows with air. Clearly, there still exists a major need for generalized heat transfer and pressure drop correlations for jet impingement with jet-adjacent fluid extraction to enable future designers to implement practical solutions.

2.3. Focus of Current Investigation

The current work seeks to address the gaps in the literature through development and testing of a new return jet impingement geometry with the main objective of developing generalized heat transfer and pressure drop correlations. Correlations resulting from this work should apply to a wide and practical range of impinging array geometries (i.e., S/D , H/D), fluids (i.e., Prandtl number), and flow regimes (laminar to turbulent). This work aspires to offer useful correlations that are independent of device manifold geometry and that have been compared and validated using the limited studies available on return jet impingement. This document will summarize preliminary efforts towards achieving these goals and discuss the future efforts needed for completion.

Table 2-1: Overview of impingement studies with jet-adjacent fluid extraction

Return Jet Impingement Studies					Correlation		Correlation Range			
Institution	Related Pubs.	Years	Primary Authors	Type	Heat Transfer	Pressure Loss	Re	S/D	H/D	Fluid
Purdue Univ.	[20]	1994	Huber and Viskanta	Exp.	$Nu = 0.285Re^{0.710} Pr^{0.33} \left(\frac{H}{D}\right)^{-0.123} \left(\frac{S}{D}\right)^{-0.725}$		3,500-20,400	4-8	0.25-6	air
Yonsei Univ.	[46]	2003	Rhee et al.	Exp./CFD						
IBM Corp.	[6,15,45]	2006, 2007, 2015	Brunschwiler et al., Natarajan and Bezama, Sharma et al.	Exp./CFD	$Nu = 0.78Re^{0.73}$		5-900	3.2-9.9	1.2	water
Stanford Univ.	[40,41]	2009, 2010	Onstad et al., Hoberg et al.	Exp.	$Nu = 0.36Re^{0.59}$		500-10,000	2.34	0.44-3.97	air
Singapore Inst. of Micro-electronics	[42]	2014	Han et al.	CFD						
Sultan Qaboos Univ.	[43]	2016	Husain et al.	CFD						
Pennsylvania State Univ.	[44]	2017	Rattner	CFD	$Nu = Pr^{0.29} \cdot 10^{\left\{ \sum_{j=1}^{20} a_j Re^{b_j} \left(\frac{S}{D}\right)^{c_j} \left(\frac{H}{D}\right)^{d_j} \right\}}$	$k = 10^{\left\{ \sum_{j=1}^{20} a_j Re^{b_j} \left(\frac{S}{D}\right)^{c_j} \left(\frac{H}{D}\right)^{d_j} \right\}}$	20-500	1.8-7.1	0.1-4.0	Pr = 1-200
IMEC Leuven, KU Leuven	[47-60]	2017-2021	Wei et al.	Exp./CFD	$Nu = 1.63Re^{0.57}$		20-2,300	4	0.6	water

CHAPTER 3. Technology Development, Proof of Concept, and Preliminary Findings

3.1. POC Cooler Design and Fabrication

To address the gaps in the literature, a proof-of-concept (POC) investigation was devised and executed. An initial single impingement geometry was selected, and a test facility was constructed for thermodynamic and hydrodynamic characterization. The POC manifold architecture contains interlocking channels rather than flow vias or hierarchical structures which were present in prior return jet impingement designs depicted in Figure 2-3 through Figure 2-10. This results in a very low-profile device, especially suited for spatially constrained electronics cooling applications. Figure 3-1 is a solid model of the flow path (a negative of the actual device), including the branched manifold sections and the impingement region. The blue regions indicate

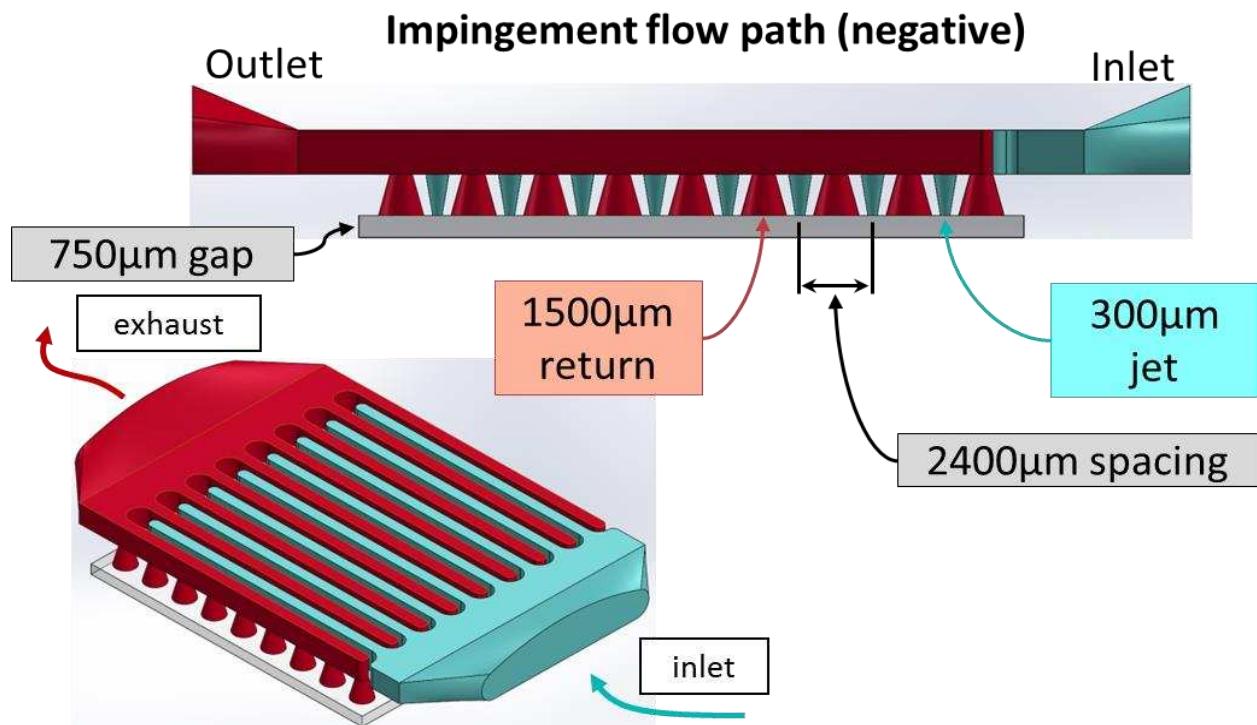


Figure 3-1: Impingement device flow path (negative)

flow upstream of impingement and the red regions indicate flow downstream of impingement. The semi-transparent gap is the open cavity above the impinged surface. Fluid enters a series of 8 parallel inlet channels (blue) from an upstream header. The channels are each 1500 μm tall by 750 μm wide and feed into 8 parallel jet nozzles for a total of 64 jets in the array. The jet nozzles taper from a diameter of 750 μm to 300 μm at the nozzle exit, allowing for smoother flow transition. The return flow path is similar to the inlet but with 9 parallel channels, each with 9 return nozzles for a total of 81 interspersed fluid returns. The return nozzles are tapered in the opposite direction with a 1500 μm inlet and 750 μm exit. The conical jet and return nozzle shapes were chosen to reduce impingement pressure losses by promoting more gradual flow acceleration from the supply channels to the jets. Prior jet nozzle shape studies support this, citing flow separation at the nozzle inlet as a significant contributor to pressure losses [61,62]. All jet and return nozzles are spaced uniformly 2.4 mm apart ($S/D = 8$) and are positioned at a height of 750 μm above the target surface ($H/D = 2.5$). The quarter-jet unit cell from Figure 1-3 provides a local view of the nozzle geometry. Figure 3-2 shows the flow path through the device header and mounting structures. The flow path is broken into sections in Figure 3-2b and Figure 3-2c denoted inlet header, inlet branches (channels), impingement region, outlet branches (channels), and outlet header. The header and branch sections cumulatively make up all device manifolding, while the impingement region is the area of greatest research interest.

After much consideration, the cooler was fabricated in one, continuous piece using a vat photopolymerization additive manufacturing (*3D printing*) process. A variety of other manufacturing methods were evaluated including micromachining and anisotropic etching techniques, as well as alternative 3D printing approaches like powder bed fusion and melt extrusion. The feasibility of machining the impingement device's complex, micro-scale features

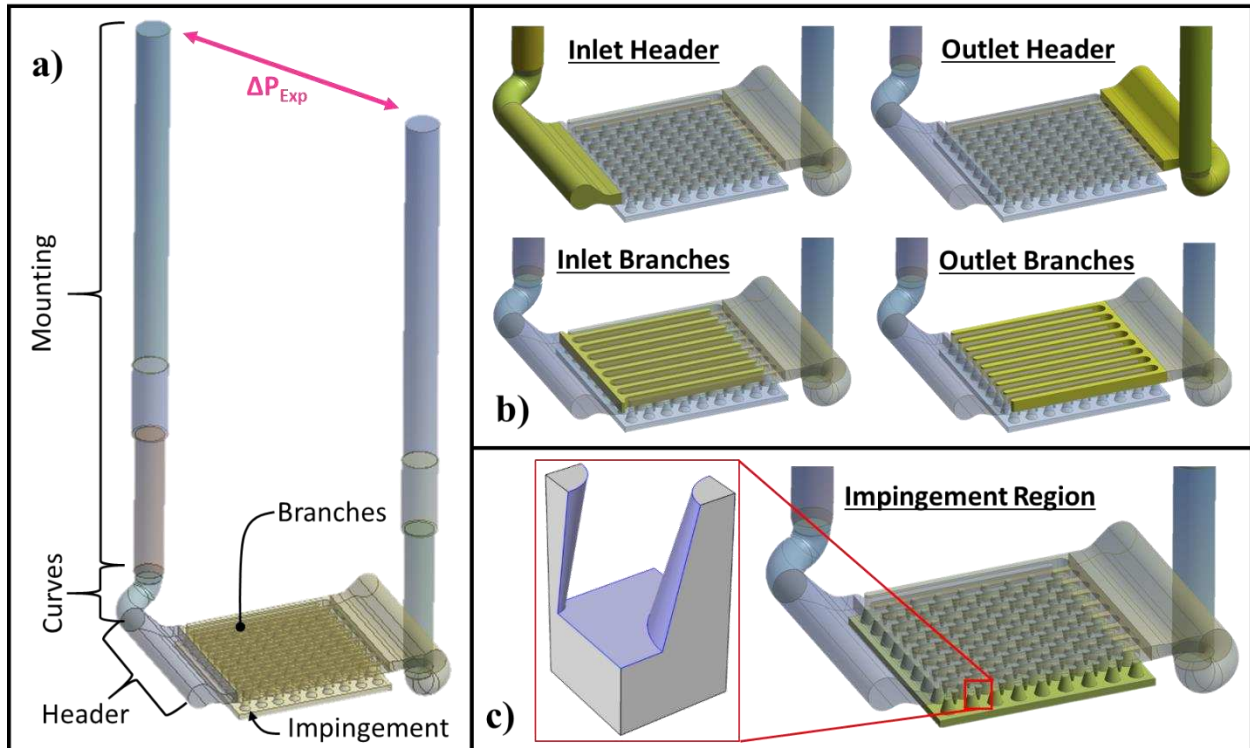


Figure 3-2: Solid model of the internal flow path of the impinging device, including fluid mounting sections where process measurements are made. (a) total flow path, (b) manifold (ancillary) flow regions, (c) jet impingement region with reference to the repeating unit cell.

is questionable at best and certain features—like the opposite-facing tapered nozzles—are likely unachievable. Assuming the device could be micromachined, the process would be costly and labor intensive making it prohibitive of design iteration. Etching techniques such as Deep Reactive Ion Etching (DRIE) could certainly produce the feature sizes needed. In fact, Brunschwiler et al. [6] enlisted a DRIE process for their design with hole diameters as small as 31 μm . However, DRIE is strictly a 2.5D fabrication process, meaning many stacked layers are required to realize a return jet impingement design and the use of tapered nozzles would be unachievable. Also, like micromachining, DRIE is much more expensive than most additive techniques at prototyping quantities.

Additive manufacturing offers several advantages. It is widely recognized as an ideal group

of processes for many prototype-phase applications and for high-complexity designs. The types of manifold geometries required for jet-adjacent fluid extraction are inherently quite complicated, making additive manufacturing a very simple and inexpensive solution when compared to other fabrication techniques. 3D printing allows for extremely problematic geometries like conical jets to be fabricated without any additional difficulty. It also enables for the full structure, including jets, manifold, and headers to be constructed as a single, continuous piece. This kind of flexibility is nearly impossible using other fabrication methods. For future research, this flexibility could even allow for experimental testing of optimal flow path designs which have been generated by topology optimization similar to the work by Dede [63].

Among the multitude of additive manufacturing processes, the most ubiquitous techniques of melt extrusion, vat photopolymerization, and powder bed fusion (PBF) were considered for this investigation. Melt extrusion printing—most commonly associated with fused deposition modeling (FDM)—is inexpensive and highly accessible; however, compared to the alternative 3d printing techniques, it offers drastically inferior resolution [64], making it nonideal for microfluidics. Figure 3-3 provides an exemplary photograph of three identical parts fabricated by



Figure 3-3: Comparative print feature resolution of three additive manufacturing techniques viz., FDM, SLA, SLS [65].

three different additive manufacturing techniques [65]. Here, the difference in resolution between melt extrusion (FDM) and alternate methods is apparent. Powder bed fusion includes printing techniques such as selective laser sintering (SLS), selective laser melting (SLM), and electron beam melting (EBM), among others. Vat photopolymerization printing techniques can generally be categorized as either stereolithography (SLA) printing or digital light projection (DLP) printing. Both techniques are similar in operation with the primary difference being that the photocuring light source is a laser for SLA and a digital projector for DLP. As a general rule, DLP systems are much less expensive than SLA systems because of the ubiquity of relatively low-cost digital projectors compared to the more complex laser management systems in SLA printers. PBF, SLA, and DLP processes all offer excellent resolution capable of realizing the return jet impingement geometry. Compared to SLA and DLP, PBF techniques can produce parts of superior structural performance; however, the mechanical advantages of PBF are unnecessary for the present application because minimal mechanical loads are imparted on the test sections. Vat photopolymerization printing is much less energy intensive and exceedingly available in low-cost prototyping platforms, making it the method of choice for this preliminary investigation. Furthermore, previous researchers have already demonstrated the usefulness of vat photopolymerization 3D printing in creating micro-fluidic devices [66].

The geometry tested in the preliminary study was initially printed on an Autodesk Ember DLP style printer using the standard PR48 resin which is an acrylate-based photopolymer. A rendered CAD image of the Ember is provided in Figure 3-4, courtesy of Autodesk's open source platform and 3DPrint.com [67]. Gong et al. [68] provide a detailed description of the curing properties of PR48. The printer's native x-y resolution is 50 μm . A z-direction resolution of 10 μm was used for the test section which printed in approximately nine hours, consuming less than 15

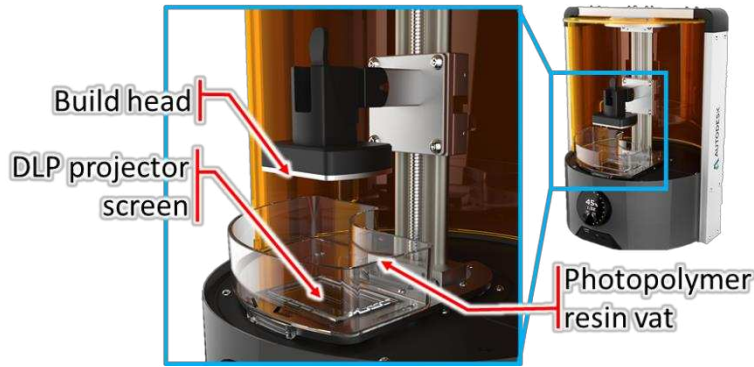


Figure 3-4: Autodesk Ember DLP printer [67]

grams of material (excluding waste). Subsequent parts have also been printed on alternative printers including an EnvisionTEC Micro Plus, Kudo3D Titan 2, and 3D Systems ProJet 5000. Key dimensions for the test section were confirmed optically. Representative images of the jet array and individual nozzles can be seen in Figure 3-5. Although the jet holes were slightly non-circular, they were generally found to be very close to the design size. Other larger geometries were found to be very closely held and any warpage that occurred as a result of the fabrication process was only apparent on non-critical features. Images of the fabricated device are provided in Figure 3-6.

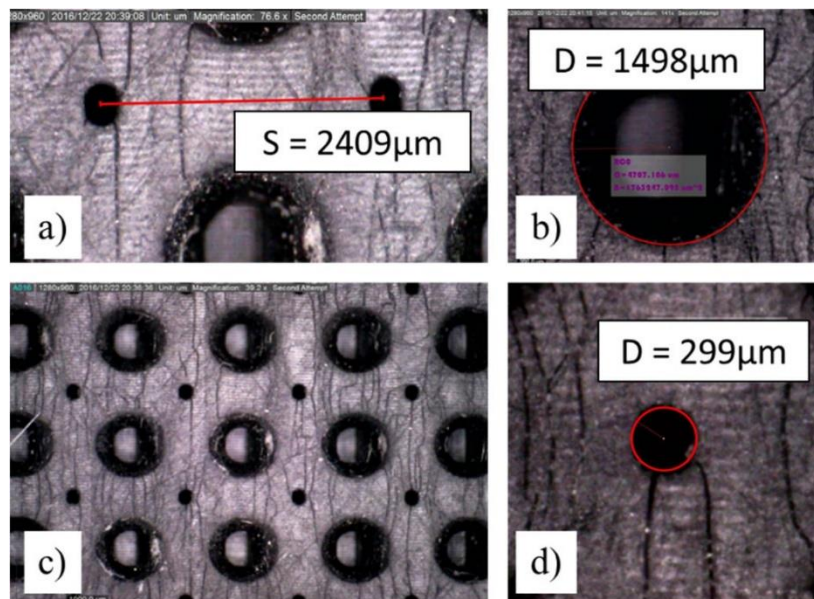


Figure 3-5: Microscope images of impinging array with optical measurements, printed on Kudo 3D Titan 2 printer

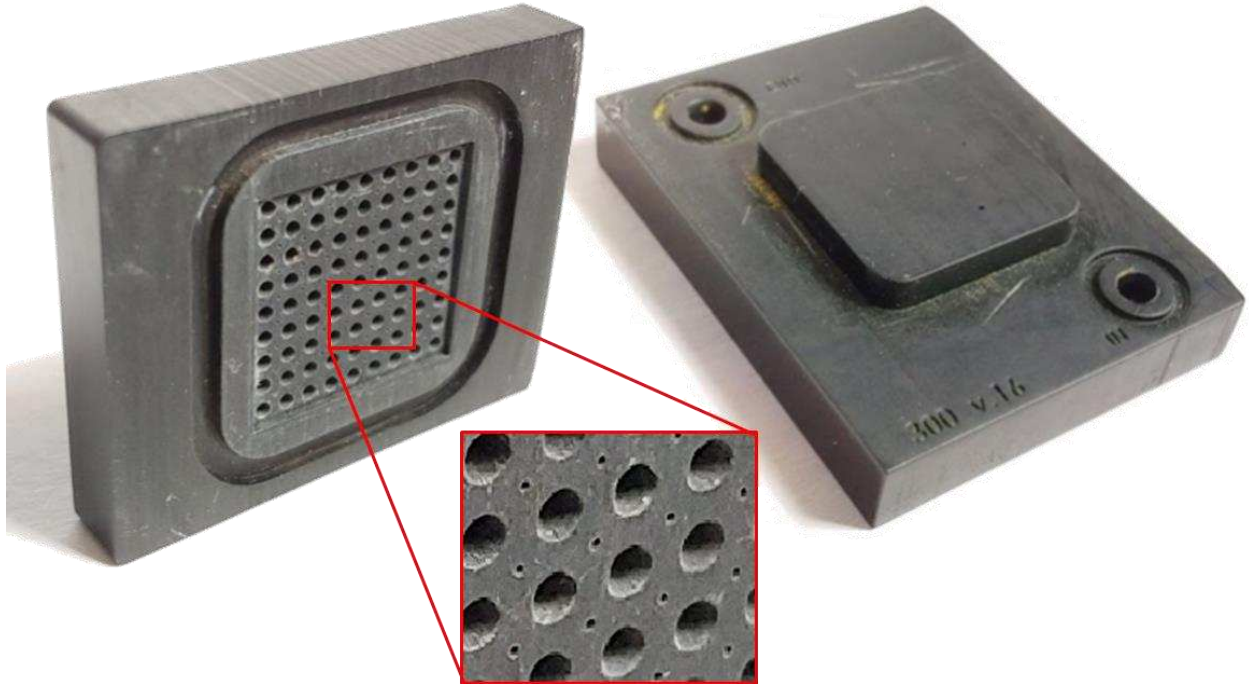


Figure 3-6: Photograph of the 3D-printed jet impingent device used heat transfer and pressure testing, printed on the Kudo 3D Titan 2 printer

One major advantage of using a plastic to fabricate the impingement device is the low thermal conductivity. A low thermal conductivity in the manifold reduces the previously mentioned thermal shortcut losses as described by Brunswiler et al. [6]. Although thermal conductivity for the photopolymer is not provided, it can be assumed to be at least 2-3 orders of magnitude lower than silicon which was used by Brunswiler et al.

3.2. Experimental Setup/Methods

A test facility was constructed to characterize the performance of the impingement cooler. The test station, shown in Figure 3-7, consisted primarily of a fluid loop and a heater loop. In the fluid loop, a pump supplied water to the impingement device. A 90 μm filter was positioned upstream of the impingement cooler to ensure that no large particulates would enter the device. Flow to the impingement device was controlled using a valve and a bypass loop. Upon exiting the device, the fluid was recirculated to the pump after passing through a standard air-cooled radiator

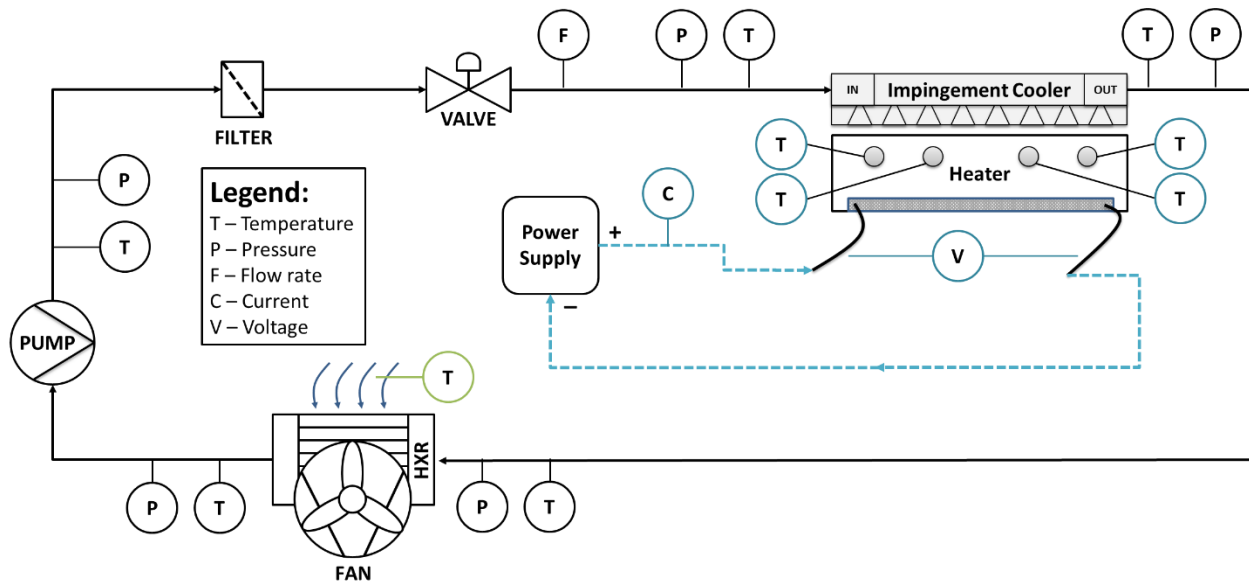


Figure 3-7: Process and flow diagram of the test facility for heat transfer and pressure drop measurement

where any heat picked up by the fluid was rejected to ambient air. Temperature and pressure measurements were taken at the impingement cooler entrance and exit, as well as throughout the rest of the fluid loop. The volumetric flow rate was measured just upstream of the impingement device. The fluid loop was evacuated prior to being filled with water for testing. This was done to minimize any air bubbles present in the system. Using this test facility, the flow rate could be reliably controlled from $0.2\text{-}1.0\text{ L min}^{-1}$ at a steady delivery pressure of up to $\sim 5.2\text{ bar}$. In the heater loop, a power supply provided current to a custom fabricated heater apparatus (*surrogate heater*) on which the impingement device was attached. The electrical input from the power supply to the heater was used to determine the heat dissipated by the test piece.

During testing, fluid and heater temperature measurements were taken using type J thermocouples which were calibrated against a high accuracy Fluke RTD ($\pm 0.0012^\circ\text{C}$) over a range from 0°C to 95°C . Post-calibration, all thermocouples had a bias uncertainty within $\pm 0.25^\circ\text{C}$. Actual calculated uncertainty values for each individual thermocouple were used for uncertainty propagation analysis. A Keysight N6700 programmable power supply was used to provide power

to the surrogate heater with milliwatt precision. A 10% uncertainty was applied to heat flux measurements to accommodate for any thermal losses through the surrogate heater insulation. Flow rate measurements were taken using a manual rotameter with $\pm 2\%$ full scale accuracy (40 mL min^{-1}). However, due to slight flow variations over time, it was assumed that flow rate could only be reliably measured to within 50 mL min^{-1} by the observer. Inlet and outlet fluid pressure was measured using uncalibrated Omega PX309 absolute pressure transducers with an uncertainty of 6.9 kPa. These low-accuracy absolute pressure sensors were used to ascertain fluid properties only. Meanwhile, pressure drop data was measured using a more accurate Omega PX409 differential pressure transducer which had a bias uncertainty of 1.7 kPa. While jet dimensions were confirmed optically, only a few select jets in the array were measured. To compensate for jet size and shape variations, an assumption was made that all jets fall within 20% ($\pm 30 \text{ }\mu\text{m}$) of the $300 \text{ }\mu\text{m}$ design size. Uncertainty propagation analysis was carried out in Engineering Equation Solver using all of these uncertainty values to calculate error bars for experimental values shown in the results section.

A surrogate heater was constructed to provide the thermal load for heat transfer characterization. This heater (see Figure 3-8) was fabricated out of copper and provides the top $2 \text{ cm} \times 2 \text{ cm}$ square surface with a uniform heat flux. Copper was chosen for its high thermal conductivity, which improves heat spreading. The copper portion of the heater is divided into two sections. The lower section houses a standard cartridge heater which was attached to the power supply and would generate heat. For the initial investigation, the heat load was varied between 1.75 and 165 W (i.e., 0.44 to 41.3 W cm^{-2} at the impingement surface). The maximum load of 165 W was dictated by the maximum voltage rating on the power supply, and reconfiguration of the test facility can allow even higher heat fluxes to be tested. The lower copper piece was made long

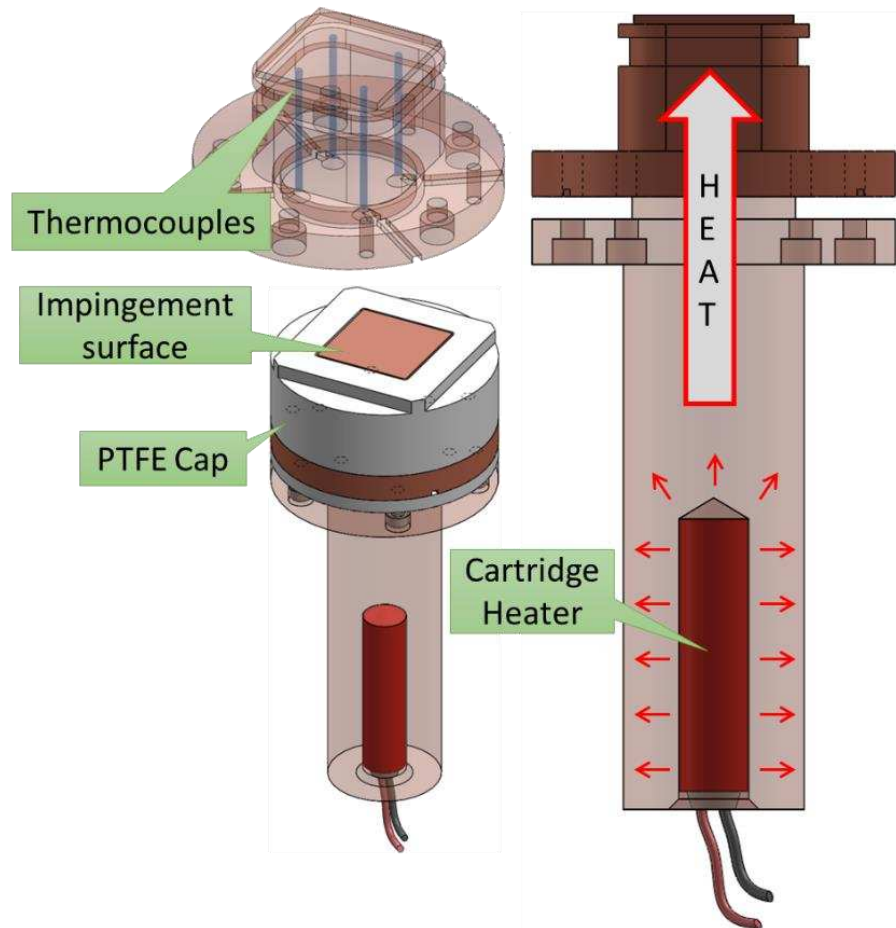


Figure 3-8: Solid model of surrogate heater without insulation

enough to facilitate sufficient heat spreading prior to contacting the upper copper piece. Four thermocouples were embedded deep into the bottom side of the upper copper piece so that each thermocouple tip was approximately 0.127 mm beneath the impingement surface. This allowed for accurate measurement of the cooled face without disrupting the flow path of impinging jets. The four thermocouples are spaced 12 mm apart evenly about the center axis of the heater. A PTFE cap is fixed and sealed to the upper copper piece, which serves as the sealing surface for the impingement device while insulating it from direct contact with the hot copper block. PTFE was selected for its relatively high operating temperature and for having a similar coefficient of thermal expansion (CTE) to copper. Because the jet height is referenced with respect to the PTFE sealing surface rather than the copper impingement surface, the full top face (PTFE and copper) was milled

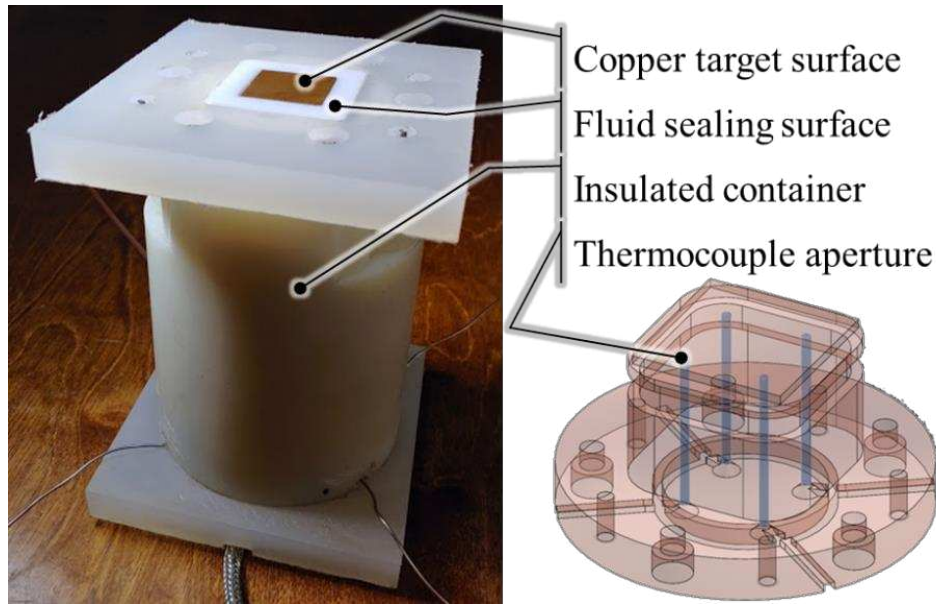


Figure 3-9: Photograph of insulated test heater used for heat transfer experimentation of the impingement device. The impingement device is mounted to the square copper surface at the top of the heater. Lower right image shows the internal copper heater block with highlighted thermocouple mounting positions.

flush together after assembly. The fully assembled surrogate heater can be seen in Figure 3-9. Heat loss to the ambient for the fully insulated assembly was estimated to be at most 2% of the total heat load [5]. Furthermore, heat flux uniformity in the surrogate heater was validated using a thermal FEA model in Ansys. The model predicted minimal temperature drift across the heater surface under conditions of uniform convective heat transfer.

3.3. Heat Transfer Results

Initial heat transfer tests were performed for six flow rates ranging nominally from 200–1000 mL min⁻¹ and heat loads from 1.75–165 W. A summary of major geometric, fluid, and flow parameters are cataloged in Table 3-1. The impingement surface temperature and fluid inlet temperatures were measured for each case and are displayed in Figure 3-10. The surface temperature measurement is an average of the four thermocouples which were calibrated to a bias uncertainty within $\pm 0.25^{\circ}\text{C}$. The same calibration procedure was followed as described in section

Table 3-1: List of geometric, fluid, and flow parameters for preliminary study.

Geometric Parameter	Definition	Units	Value/ Range
D_j	Jet nozzle diameter	mm	0.3
D_r	Return orifice diameter	mm	1.5
D_r/D_j		[dim]	5
H	Jet nozzle height from target surface	mm	0.75
H/D_j		[dim]	2.5
S	Jet to jet spacing	mm	2.4
S/D_j		[dim]	8
L	Jet nozzle length	mm	1.5
L/D_j		[dim]	5
ϕ_j	Jet nozzle conical angle	rad	0.30
ϕ_r	Return port conical angle	rad	0.49
N_j	Jet array size i.e., sqrt(total jets)	#	8
Fluid/Flow Parameter	Definition	Units	Value/ Range
Re	Jet Reynolds number	[dim]	300-1500
Pr	Prandtl number	[dim]	4.5-5.0

4.3.1. The four measurement locations did reveal a slight spatial temperature distribution across the target surface, suggesting cooling non-uniformity. However, in all cases, the variation in temperature across the different thermocouples was within $\pm 1^\circ\text{C}$ of the mean. Thus, it is sufficient to assume that the flow and heat transfer profiles were reasonably uniform and likely have only a minor impact on calculation of heat transfer coefficients. This is an important finding because it demonstrates that any flow maldistribution present in the impingement array was not significant enough to markedly diminish overall cooling performance. Still, the presence and significance of flow maldistributions cannot be dismissed entirely and may warrant further investigation.

As expected, the temperature differential between heater surface and fluid inlet exhibits a linear trend with heat load. This suggests a constant heat transfer coefficient at any of the flow rates tested that is independent of heat flux. A minimum thermal resistance of $0.33 \text{ K cm}^2 \text{ W}^{-1}$ was

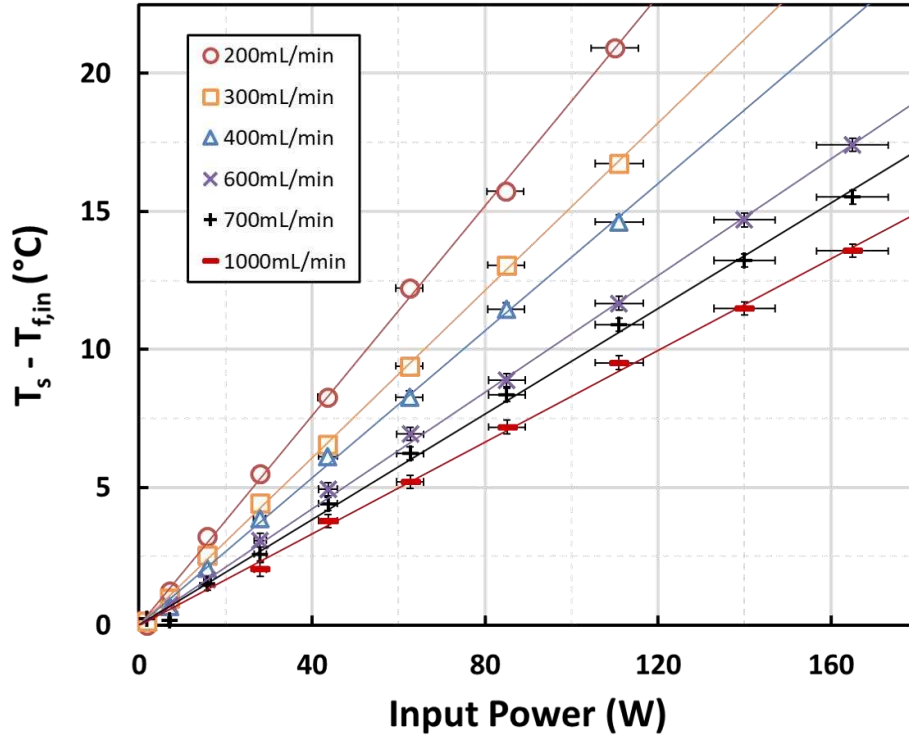


Figure 3-10: Surface temperature differential under water impingement over range of heat loads

demonstrated at the highest flow rate of 1 L min^{-1} . The temperature-heat load data were used to determine average heat transfer coefficients at each of the six flow rates. This was done using linear regressions of the data shown in Figure 3-10. Each regression was taken with the constant term set to zero; thus, the slope of each regression represents the reciprocal of heat transfer coefficient. Log mean temperature difference (LMTD) was not used for computing heat transfer coefficient in the POC study; however, LMTD was used in the follow-on investigation. The resulting heat transfer coefficients are plotted against flow rate in Figure 3-11. The black line in Figure 3-11 represents a power law curve fit to the dataset. When nondimensionalized, the impingement heat transfer exhibits the following Nusselt number trend:

$$Nu = 0.32Re^{0.54}$$

3-1

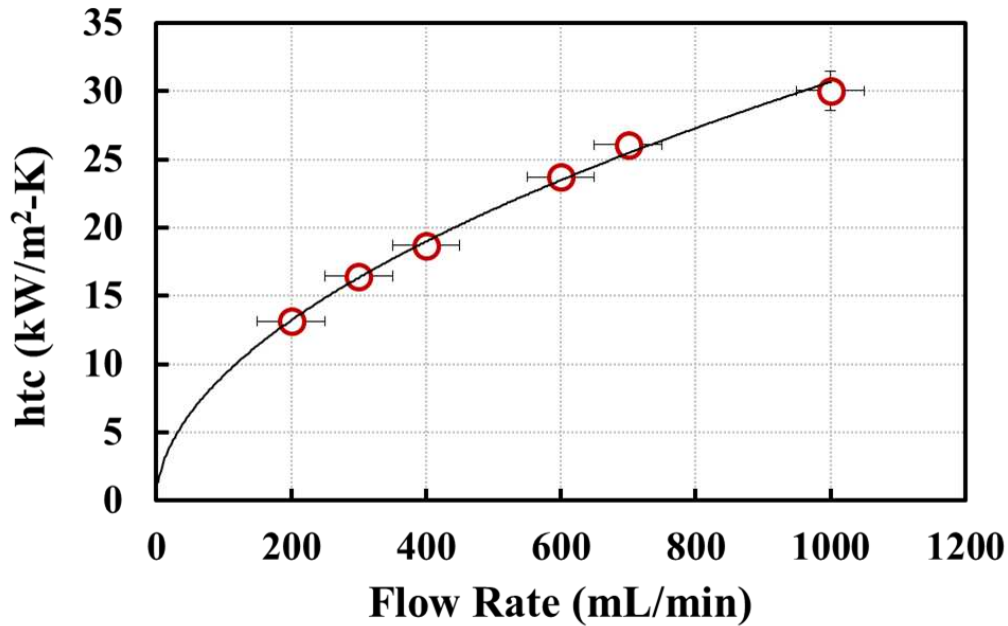


Figure 3-11: Measured heat transfer coefficient for a water jet impingement preliminary testing; note that vertical uncertainty bars are mostly obscured by the data markers

The lowest flow rate of 200 mL min^{-1} yielded a heat transfer coefficient of $13,200 \text{ W m}^{-2} \text{ K}^{-1}$ at an average jet velocity of 0.74 m s^{-1} and a Reynolds number of 310. The highest heat transfer coefficient demonstrated was $30,000 \text{ W m}^{-2} \text{ K}^{-1}$, which was achieved at a flow rate of 1 L min^{-1} , an average velocity of 3.7 m s^{-1} , and a jet Reynolds number of 1500.

Heat Transfer Comparison to Prior Works

As was previously discussed, Rattner [44], Huber and Viskanta [20], Brunswiler et al. [6], and Hoberg et al. [41] each provide a correlation relating Nusselt number to Reynolds number for jet impingement geometries with interspersed fluid returns. Each of these four correlations were compared to the data presented in the preliminary study (Figure 3-12 and Figure 3-13). The correlation by Wei et al. [52] was not compared here because it was formulated using only a single

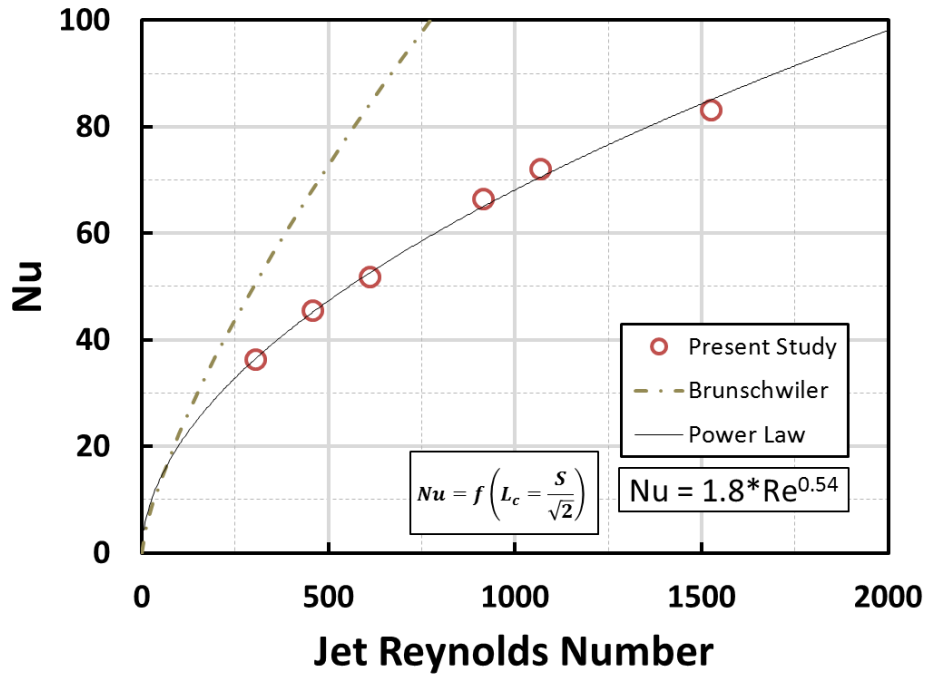


Figure 3-12: Comparison with Brunswiler et al. correlation

impingement geometry and was not available when this data was taken. The Brunswiler et al. correlation is as follows:

$$Nu = 0.78 Re^{0.73} \quad 3-2$$

This correlation was developed for geometries with $H/D = 1.2$, $S/D = 3.2-9.9$, and for water with a Reynolds number of $Re = 5-900$. This preliminary investigation comprises a larger H/D parameter and exceeds the Reynolds number range for the Brunswiler et al. correlation.

The characteristic length scale for the Reynolds number is defined as the jet diameter and the characteristic length used for Nusselt number is defined as the distance from a jet to the nearest fluid return ($L_c = S/1.414$). For consistency, the same length scale convention was used for generating the Nusselt values in Figure 3-12. The Brunswiler et al. correlation exhibits poor agreement with the data from this investigation. This is not surprising considering that the correlation does not account for geometric parameters like H/D or S/D . The overprediction by the

Brunschwiler et al. correlation might be attributed to the difference in the H/D parameter which has been shown to result in increased Nusselt number as H/D is decreased.

The other correlations were plotted separately from the Brunschwiler et al. correlation in Figure 3-13 because they each use jet diameter as the characteristic length scale for Nusselt number. The Hoberg et al. correlation is given in equation 3-3 and was developed for air impingement where $H/D = 0.44-3.97$, $S/D = 2.34$, and $Re = 500-10,000$. The present investigation lies well outside of the S/D parameter and at the bottom end of the Reynolds number range for the Hoberg et al. correlation:

$$Nu = 0.36Re^{0.59} \quad 3-3$$

The Huber and Viskanta correlation was also developed for air impingement. The relevant parameters are $H/D = 0.25-6$, $S/D = 4-8$, and $Re = 3,500-20,400$. The present investigation lies

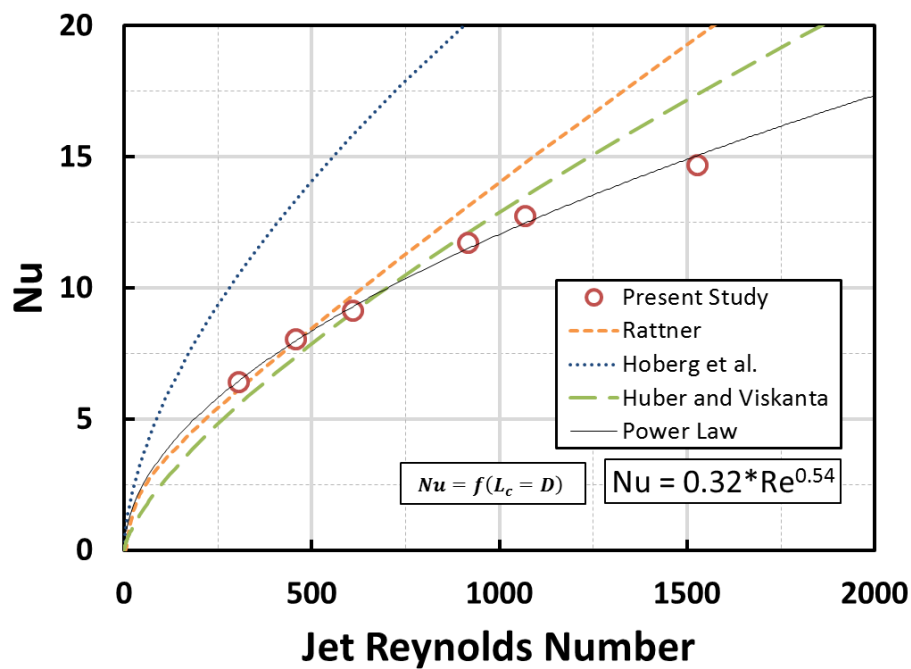


Figure 3-13: Comparison with correlations by Rattner, Hoberg et al., and Huber and Viskanta

well below the Reynolds number range. The Huber and Viskanta correlation is provided in equation 3-4. An average Prandtl number of 4.9 was used for the correlation, corresponding to water at roughly 35°C.

$$Nu = 0.285 Re^{0.710} Pr^{0.33} (H/D)^{-0.123} (S/D)^{-0.725} \quad 3-4$$

Rattner's correlation is provided in equation 3-5 and is dependent upon an array of coefficients (a_j , b_j , c_j , d_j) which are not provided here. The correlation was developed numerically for $H/D = 0.1-4.0$, $S/D = 1.8-7.1$, $Re = 20-500$, and $Pr = 1-200$. The current study lies just outside the S/D parameter and exceeds the Reynolds number range. Again, an average Prandtl number of 4.9 was used for the Rattner correlation.

$$Nu = Pr^{0.29} \cdot 10^{\wedge} \left\{ \sum_{j=1}^{20} a_j Re^{b_j} (S/D)^{c_j} (H/D)^{d_j} \right\} \quad 3-5$$

The Hoberg et al. correlation (dotted line in Figure 3-13) provided a poor fit to the present study, overpredicting the Nusselt number like the Brunschwiler et al. correlation. This was to be expected because the correlation was developed for air jets and does not include Prandtl number dependence to help adjust for different fluids. It is also important to note the much smaller jet spacing-to-diameter ratio in the Hoberg et al. study may account, in part, for the overprediction.

The final two correlations managed to predict the data from this experiment reasonably well. The Rattner correlation, shown in Figure 3-13 as the short-dashed line, achieves strong agreement at the low Reynolds numbers for which it was established (i.e., 20-500). As Reynolds number is further increased, Rattner's correlation overpredicts the data. The Huber and Viskanta correlation (long-dashed line in Figure 3-13) produced the best fit of the data in the current investigation. This was a surprising development because the correlation was developed for air

jets at much higher Reynolds number. Regardless, the Huber and Viskanta correlation exhibited strong low-Reynolds number agreement with the data and similarly began to overpredict as Reynolds number increased. Both correlations diverge rapidly from experiment at high Reynolds numbers and, upon closer investigation, provide inconsistent agreement with each other at varying geometric parameters.

As a result of comparing the preliminary heat transfer data to available return jet impingement correlations in the open literature, it is clear that existing correlations provide poor or inconsistent agreement with one another and with the data in this study. This finding highlights the need for more expansive correlational development.

Heat Transfer Comparison to CFD

In an effort to validate and expand upon the preliminary experimental investigation, a collaborative CFD study with Rattner was conducted using the impingement geometry [69]. The

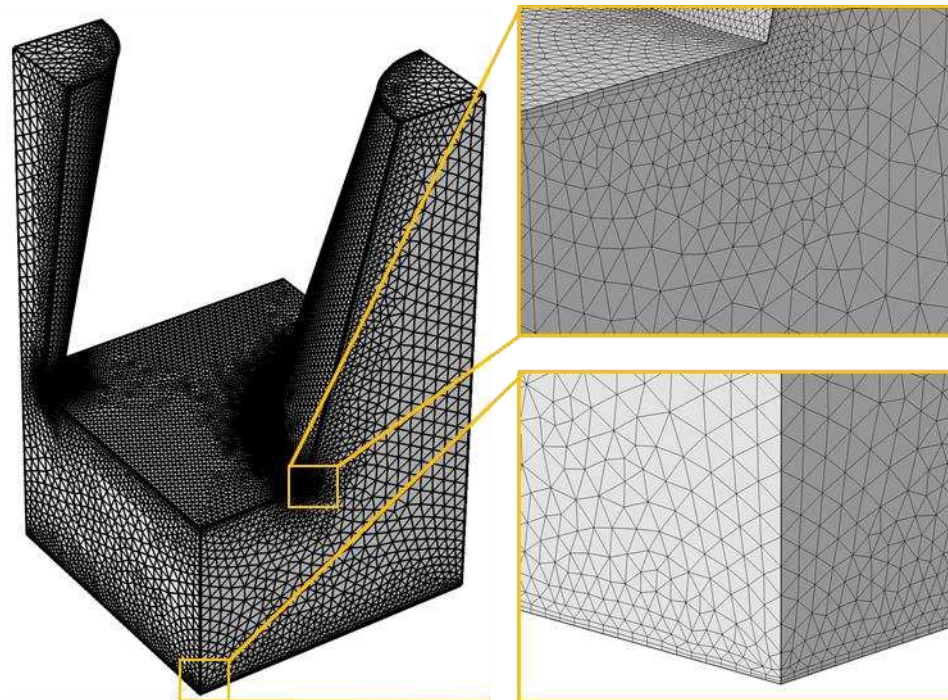


Figure 3-14: Rendering of simulation unit cell with representative computational mesh

unit cell in Figure 1-3 presents the computational domain and the associated boundary conditions, while Figure 3-14 provides a representative computational mesh. Computational simulations were performed by a collaborator at Pennsylvania State University using COMSOL Multiphysics 5.2a [70] at the same nominal conditions as those tested in the preliminary investigation. A brief description of the computational methods is provided in Appendix A. The red circles in Figure 3-15 represent the CFD Nusselt number results alongside the preliminary experimental data. Slight differences in Reynolds number are attributed to the divergence of real test conditions from nominal conditions used for simulations. The computational and experimental results are similar in magnitude but show very different trends. This discrepancy is highlighted by the power law trendlines fit to each data set. Simulation results indicate a Reynolds dependency to the 0.87 power; substantially higher than the 0.54 power indicated by the experimental data. If CFD simulation

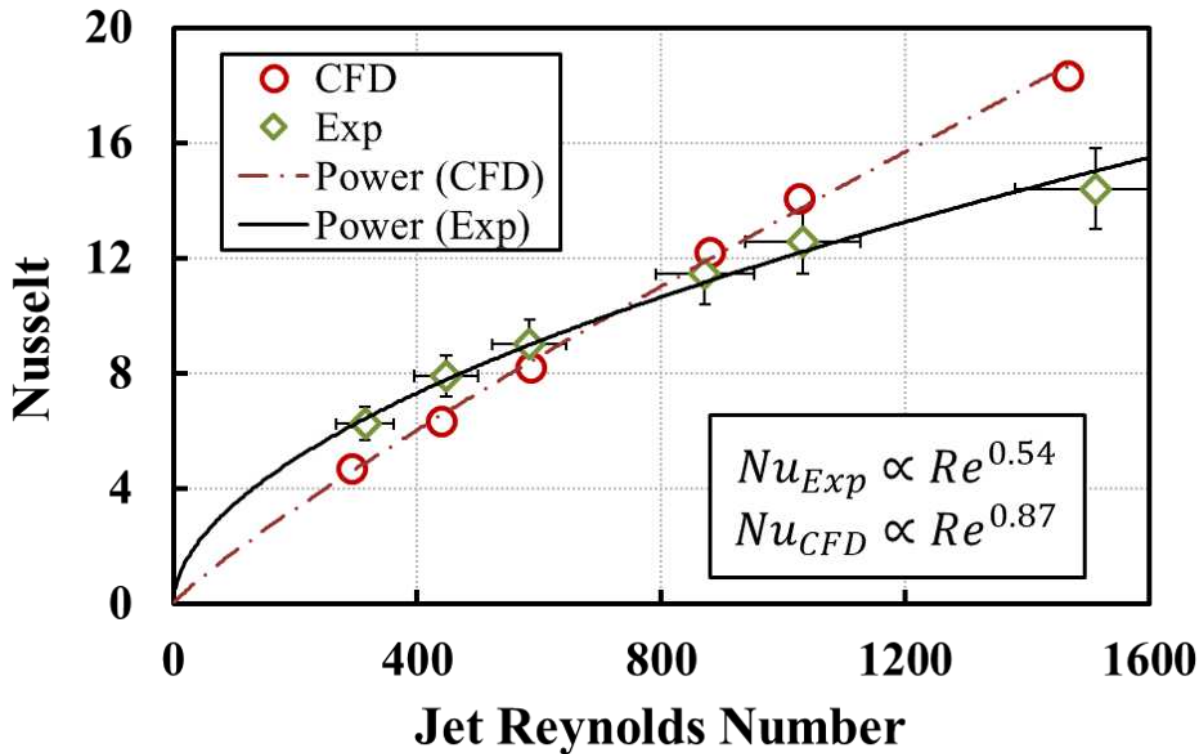


Figure 3-15: Simulated and measured heat transfer results of the jet impingent device over the total range of flow rates

results are to be used for correlational development, then much better experimental agreement is required.

There are several possible explanations for the discrepancy between simulation and experimental results. For example, the model assumes constant fluid properties, uniform flow, and unidirectional flow at the jet nozzle inlet. It also neglects thermal shortcut losses, conjugate heat transfer effects, and target surface roughness. Appendix B provides a brief discussion on other possible causes for the discrepancy between experiment and simulation. Regardless of the specific causes, it is imperative that they be identified and accounted for—by model or experiment—before the developing generic and reliable heat transfer correlations.

3.4. Pressure Drop Results

Pressure drop measurements were also taken for the return jet impingement device under adiabatic conditions. As with the heat transfer results, a CFD simulation was performed to compare with experimental pressure drop results. Figure 3-16 provides static pressure contours and velocity contours at the highest (1000 mL min^{-1}) and lowest (200 mL min^{-1}) simulated flow rates. As is expected, each contour shows a dramatic reduction in pressure in the jet nozzle as the fluid accelerates through the nozzle orifice. The stagnation region directly below the jet is clearly visible where the pressure spikes against the target wall. The high-velocity free jet is distinguishable in red in the velocity contours with a visible wall jet forming against the target impingement surface.

The blue triangles in Figure 3-17 show the total simulated pressure drop from jet nozzle inlet to return nozzle outlet. The highest flow rate corresponds to a jet Reynolds number of 1470 and yielded a total pressure drop of 8.7 kPa. The green circles in Figure 3-17 give the measured pressure drop across the full device between the measurement points indicated in Figure 3-2a. At the highest flow rate, the measured pressure drop was nearly 26.6 kPa at a jet Reynolds number of

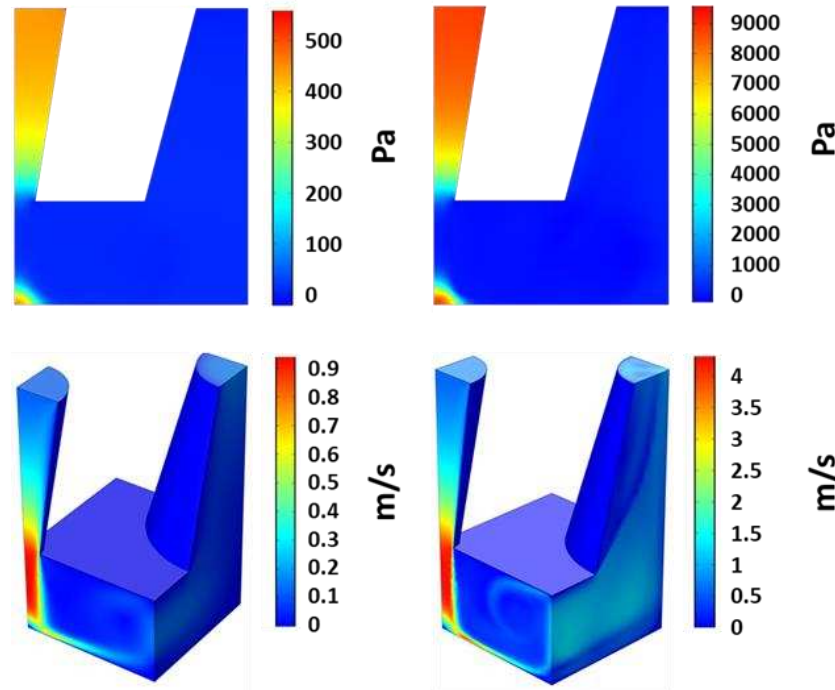


Figure 3-16: Pressure contours at (a) 200 mL min⁻¹ and (b) 1000 mL min⁻¹ total device flow rate

1490. This represents a pumping power of only 0.44 W, or 0.11 W cm⁻². Once again, the slight difference in Reynolds number is the result of minor variations in experimental flow conditions from the nominal simulation conditions. From the large discrepancy between measured and simulated pressure drop, it is clear that ancillary pressure drop in the manifold structures accounts for a significant portion of the total flow restriction and, thus, measured pressure drops cannot be used to directly approximate impingement flow restriction in this experiment.

An attempt was made, in this work, to account for the ancillary pressure drop using a reduced-order model that relies on a hydraulic resistance network and correlational pressure drop estimates rather than on CFD simulation. This ancillary pressure drop model was formed in Engineering Equation Solver (EES) [71] and approximates the total flow path shown in Figure 3-2 as a network of discretized flow segments consisting of elbows, bends, tees, round and rectangular straight channels, expansions, and contractions. The restriction of each flow element was

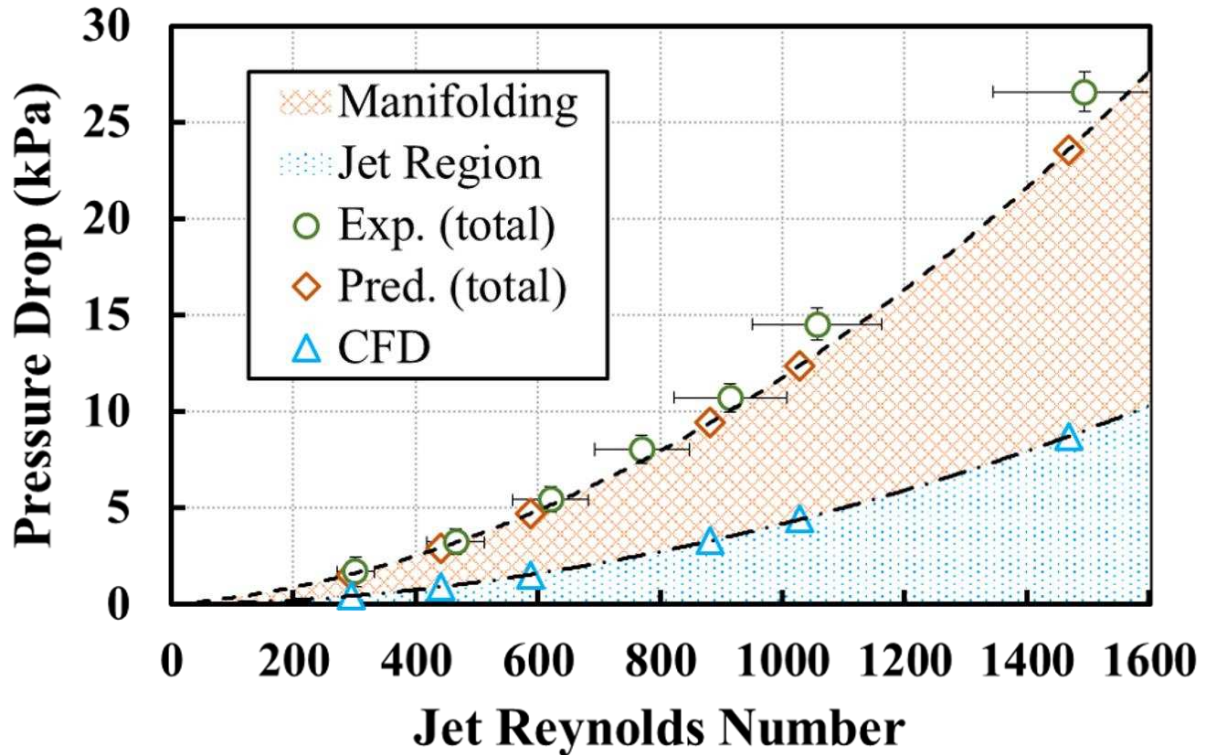


Figure 3-17: Computational (blue triangles) and experimental (green circles) pressure drop results with total predicted pressure drop (orange diamonds) presented as the aggregate of pressure drop in the impingement region (determined by CFD) and pressure drop in the manifold regions (determined by correlational-based analytical model)

calculated using common and well-established correlations from the open literature [72–74]. Figure 3-18 provides a simplified version of the hydraulic flow path broken into zones where each correlation is applied. Solid circles represent impinging jet locations and dotted circles represent extraction port locations. Each of the ancillary pressure drop correlations used are numbered and equations for Darcy friction factor or K-factor are provided in Table 3-2. The model assumes that all jets receive the exact same flow rate regardless of position in the array. The same assumption is made for each return nozzle. The resulting ancillary pressure drop was added to the computational results to give the total predicted device pressure drop presented as diamonds in Figure 3-17. By combining CFD results and the ancillary pressure drop model, very close

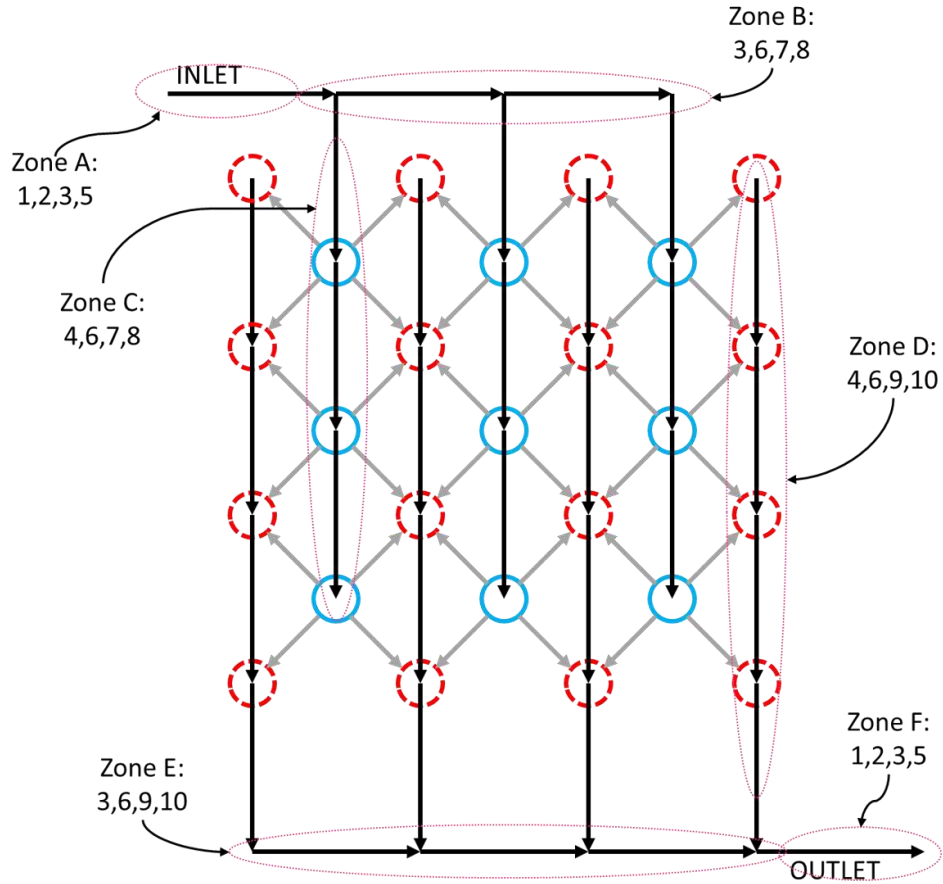


Figure 3-18: Simplified ancillary hydraulic resistance network for 3-by-3 three impingement array, broken into zones over which pressure drop correlations were applied; numbers indicate which correlations were used and coincide with those listed in Table 3-2

agreement was achieved to the experimental results, indicating a promising prediction model. The cross-hatched region on Figure 3-17 represents the share of total predicted pressure drop attributed to ancillary flow regions. Meanwhile, the dotted area represents the portion attributed to the impingement region only. Figure 3-18 breaks down the flow restriction in each region of the device by percentage for each simulated flow rate. Generally, the impingement region accounts for approximately one-third of device pressure drop. This proportion increases gradually with flow rate. The inlet and outlet manifold regions account for approximately equal portions of the total device pressure drop.

Table 3-2: Definition of pressure drop coefficients utilized by the ancillary pressure drop model; correlation numbers coincide with those shown in Figure 3-18

Corr. No.	Description	Definition	Ref.
1	Sudden expansion	$k = \left(1 - \frac{D_{small}^2}{D_{large}^2}\right)^2$	[73]
2	Sudden contraction	$k = 0.5 \left(1 - \frac{D_{small}^2}{D_{large}^2}\right)$	
3	Round tube	$f = 8 \left[\left(\frac{8}{Re}\right)^{12} + \frac{1}{(C_1 + C_2)^{1.5}} \right]^{1/12}$ $C_1 = \left[2.457 \ln \left(\frac{1}{\left(\frac{7}{Re}\right)^{0.9} + 0.27 \frac{\epsilon}{D}} \right) \right]^{16}$ $C_2 = \left(\frac{37530}{Re} \right)^{16}$	[74]
4	Rectangular channel	$f = \exp \left[\left(\frac{\ln(Re) - \ln(2000)}{\ln(4000) - \ln(2000)} \right) \cdot (\ln(f_{cu}) - \ln(f_{cl})) + \ln(f_{cu}) \right]$ $f_{cu} = \frac{0.3164}{4000^{0.25}} \cdot (1.0875 - 0.1125\alpha)$ $f_{cl} = \frac{96}{2000} \cdot (1 - 1.3553\alpha + 1.9469\alpha^2 - 1.7012\alpha^3 + 0.9564\alpha^4 - 0.2537\alpha^5)$	
5	Smooth bend	$k = k_{loc} + k_{fr} + \frac{3000}{Re}$ $k_{loc} = 0.9 \sin \left(\frac{\pi}{2} \right) \cdot 0.21 \left(\frac{r_{bend}}{D} \right)^{-2.5}$ $k_{fr} = 0.0175 \left(\frac{\pi}{2} \right) \cdot \lambda \frac{r_{bend}}{D}$ $\lambda = 0.11 \left(\frac{\epsilon}{D} + \frac{68}{Re} \right)^{0.25}$	[72]
6	Sharp 90° elbow	$k = 1.2(0.97 - 0.13 \ln(\alpha))$	
7	Diverging 90° wye (side branch)	$k = 1 + \left[\frac{v_{sc}}{v_{mc}} \right]^2$	
8	Diverging 90° wye (straight branch)	$k = C \frac{v_{sc}}{v_{mc}}; C = \begin{cases} 0.4 & \text{for } \frac{A_{sc}}{A_{mc}} \leq 0.4, \text{ any } \frac{v_{sc}}{v_{mc}} \\ 2 \left(2 \frac{v_{sc}}{v_{mc}} - 1 \right) & \text{for } \frac{A_{sc}}{A_{mc}} > 0.4, \frac{v_{sc}}{v_{mc}} \leq 0.5 \\ 0.3 \left(2 \frac{v_{sc}}{v_{mc}} - 1 \right) & \text{for } \frac{A_{sc}}{A_{mc}} > 0.4, \frac{v_{sc}}{v_{mc}} > 0.5 \end{cases}$	
9	Converging 90° wye (side branch)	$k = C \left[1 + \left(\frac{v_{sc}}{v_{mc}} \right)^2 - 2 \left(1 - \frac{v_{sc}}{v_{mc}} \right) \right]^2$ $C = \begin{cases} 1 & \text{for } \frac{A_{sc}}{A_{mc}} \leq 0.35, \text{ any } \frac{v_{sc}}{v_{mc}} \\ 0.9 \left(1 - \frac{v_{sc}}{v_{mc}} \right) & \text{for } \frac{A_{sc}}{A_{mc}} > 0.35, \frac{v_{sc}}{v_{mc}} \leq 0.4 \\ 0.55 & \text{for } \frac{A_{sc}}{A_{mc}} > 0.35, \frac{v_{sc}}{v_{mc}} > 0.4 \end{cases}$	
10	Converging 90° wye (straight branch)	$k = 1.55 \frac{v_{sc}}{v_{mc}} - \left(\frac{v_{sc}}{v_{mc}} \right)^2$	

Overall, excellent agreement was found between model prediction and experimental pressure drop. This indicates that the ancillary pressure drop model can serve as a useful means for bridging the gap between impingement region pressure drop and device level pressure drop. However, for the purpose of correlational development, estimating impingement region pressure drop from the calculated ancillary pressure drop relies much too heavily on the accuracy of the

ancillary pressure drop model. A sample calculation provided in Appendix C illustrates this issue by showing that ancillary model accuracy dominates impingement region pressure drop uncertainty. As a result, accurate and reliable predictions of impingement region pressure drop are not possible as long as the ancillary pressure drop accounts for the majority of total device pressure drop and pressure drop across the impingement array cannot be measured directly. Furthermore, flow distribution uniformity may be promoted through device manifold design which produces dominant pressure drop in the impingement region.

To develop an accurate pressure drop correlation, it will be necessary to adjust impingement manifold design to minimize the impact of ancillary pressure drop regions. The existing ancillary pressure drop model can be used to guide simple, yet impactful design changes. This and other research challenges are discussed in the following section.

3.5. Challenges and Development of Robust Test Method

Challenges with the Current Approach

Contributions by the manifold structure prevent reliable measurement of thermal and hydraulic phenomena in the impingement region. As such, manifold independence is imperative for developing generalized correlations. Still, so far, no previous researchers have established or justified manifold independence. This work attempts to form generalized correlations for return jet impingement. However, this preliminary investigation has demonstrated multiple challenges with the experimental approach that prevents manifold-independent results from being attained. Here, three manifold-attributed challenges are identified which may skew experimental results: (1) manifold restriction (2) flow uniformity (3) conduction pathways.

The first performance modifier is flow restriction in the manifold which, if unaccounted for, would result in overprediction of impinging pressure drop that is heavily dependent on manifold geometry. The ancillary pressure drop model presented in the preliminary work was used to calculate the relative contributions of each flow section on total measured pressure drop. These contributions are presented for each flow rate in Figure 3-19 which indicates that nominally one-third of the measured pressure drop may be attributed to the impingement region. The ancillary pressure drop model accurately predicts the remaining two-thirds of measured pressure drop over the test conditions. However, as with any prediction model, the ancillary model must be validated against experimental data and should provide agreement within some level of accuracy. Unfortunately, because the ancillary pressure drop contribution is roughly twice as large as in the impingement region, the propagation of uncertainty causes any model inaccuracy to result in double the impingement pressure drop uncertainty. For example, if the ancillary model were shown to be accurate within $\pm 25\%$, the calculated impingement region pressure drop could only be, at

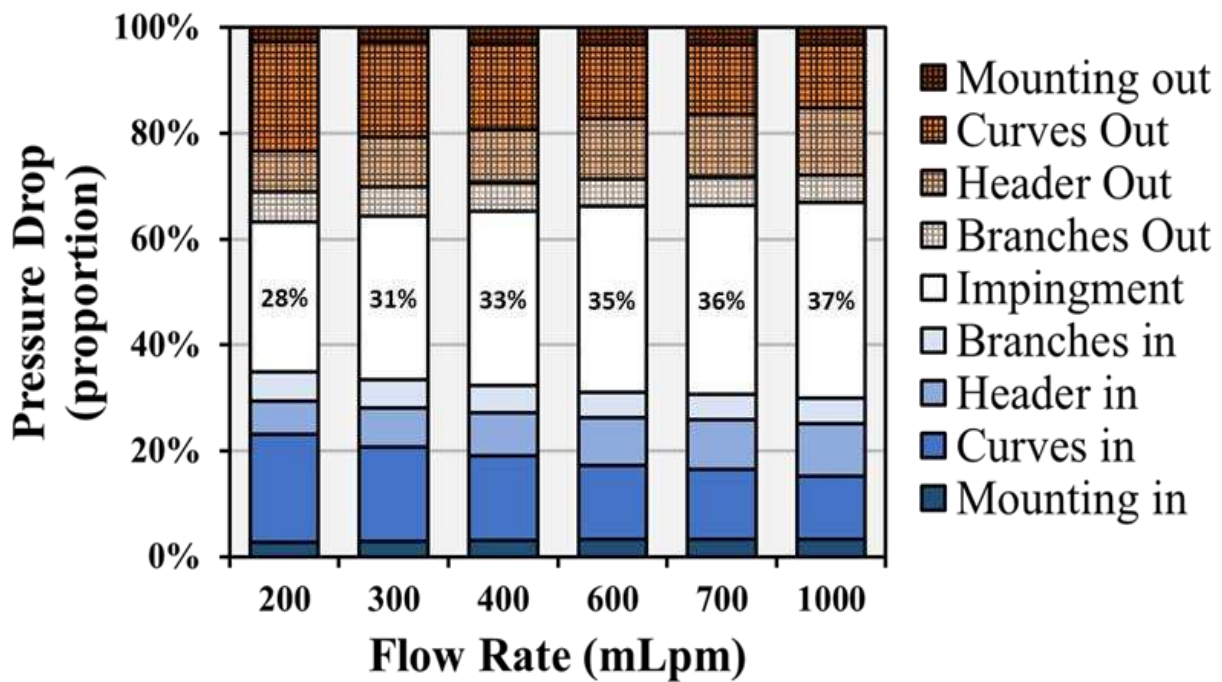


Figure 3-19: Proportional pressure drop in each individual flow section of the device as defined in Figure 3-2a

best, within $\pm 50\%$, which is unacceptable for correlation development, especially when combined with measurement uncertainties. Conversely, if manifold restriction only contributed half as much pressure drop as the impingement region, the impingement region uncertainty would be diminished to $\pm 12.5\%$ (at best) after propagation. Clearly, as the contribution of ancillary flow restriction is reduced, prediction inaccuracy caused by modeling error will be likewise diminished.

The second possible manifold-caused performance modifier involves flow uniformity. Heat transfer and pressure drop in the jet array is evaluated under the assumption that every impinging jet delivers equal flow. In reality, some jets supply more or less flow than others based on position in the array and upstream/downstream flow restrictions in the manifold. To estimate the prevalence of flow maldistribution, a modified version of the ancillary pressure drop model was used to calculate the relative flow to each jet in the 8 by 8 array tested under water impingement conditions in the proof-of-concept investigation. In this model, the same hydraulic resistance network is used but flow rates are allowed to vary from jet to jet such that the pressure drop from any two parallel flow paths is made to coincide. Figure 3-20 provides a visual representation of the resulting model-predicted flow uniformity at the 1 L min^{-1} flow case. The X and Y axes mark jet location in the impinging array while the Z axis displays average jet velocity at each location (m s^{-1}). Clearly, jets towards one corner of the array (position 0,0) receive substantially less flow than those at the opposing corner (position 8,8). In the most extreme case, the highest flow jet is expected to receive roughly 3.5 times more flow than the lowest flow jet location. This non-uniform flow distribution has a potentially significant effect on hydraulic and thermal performance which is currently unquantified.

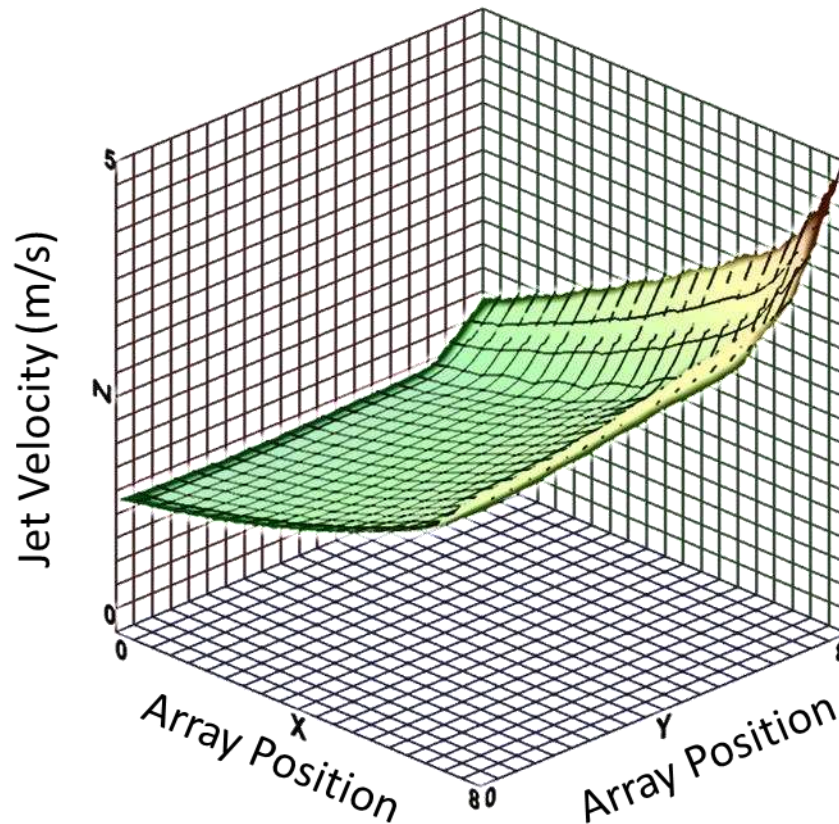


Figure 3-20: Model approximation of flow distribution by jet position in the impingement device

Conduction pathways within the manifold present a third measurement challenge. Brunschwiler et al. explain how the cool inlet fluid passing in close proximity to the warm exhaust fluid in the device manifold allows for heat to pass from the exhaust fluid into the inlet fluid. This causes pre-heating of the jets prior to impingement and diminishes the overall thermal performance. In a return jet impingement architecture, regardless of the specific flow routing strategy, exhaust flow paths must be interspersed throughout inlet flow paths, creating a manifold geometry reminiscent of a heat exchanger. Thus, the role of conduction pathways within the manifold are amplified in comparison to typical cooling technologies. Fortunately, by using a non-thermally conducting plastic to fabricate the manifold, the impact of thermal shortcut losses can be dramatically reduced. Appendix D provides a simplified approximation for thermal shortcut

losses present in the preliminary investigation which are predicted to have little effect on measurements. Still, it is important for measurement fidelity to provide a reliable estimate of these losses and to design a manifold which minimizes their role.

In summary, the proof-of-concept study established manufacturing viability of the cooling solution using desktop-style vat photopolymerization additive manufacturing technologies and resulted in several important lessons learned which are used to inform and improve the remainder of this investigation. Key discoveries included:

- A 3D printed microfluidic return jet impingement device was designed, constructed, and tested for thermal and hydraulic performance with water
- Heat transfer coefficients exceeding $30,000 \text{ W m}^{-2} \text{ K}^{-1}$ were demonstrated with single phase water
- A 41 W cm^{-2} heat flux was dissipated over a 13°C temperature differential using only 0.11 W cm^{-2} of pumping power
- Prior existing heat transfer correlations were found to misalign with each other and with the preliminary data from this study
- Impingement array pressure drop measurement was found to be dominated by ancillary pressure drop in the manifold structures, a point not addressed in prior works
- For accurate correlational development, it was determined that manifold effects must be isolated or mitigated in the form of:
 - Flow distribution nonuniformity
 - Thermal shortcut losses
 - Relative contribution to measured pressure drop

CHAPTER 4. Experimental Setup

Based on the findings in the preliminary proof-of-concept study described in Chapter 3, an improved test methodology was developed to facilitate robust heat transfer and pressure drop testing. New jet impingement cooler geometries and an improved surrogate heater device capable of accommodating the new impingement designs were developed. Similarly, a new test apparatus was constructed for delivering controlled and measured flow to the new impingement test sections. The following sections will discuss the updated test methodology and will provide detail on the design and construction of all hardware involved.

The improved experimental setup described in these sections seeks to accomplish the following core objectives:

- Investigate a diverse and relevant set of impingement array geometries while minimizing impingement device count.
- Minimize the contribution of manifold geometry on measured impingement array thermal and hydrodynamic performance through the following means:
 - Maximize flow uniformity about the impinging array
 - Minimize manifold flow restriction
 - Minimize conduction pathways within the manifold
 - Perform pressure measurements substantially close the impingement array
- Investigate a diverse and relevant set of fluid and flow parameters.

4.1. Gen II Impingement Cooler Design and Fabrication

A total of 9 distinct impingement devices were designed and fabricated, improving upon the POC design. Each device follows a consistent basic design but offers a variable configuration

of key parameters (e.g., S/D_j , H/D_j) selected for consideration in this study. Each device configuration was allotted a designation from C01 to C09. All devices were again fabricated in a photopolymer material via a stereolithography additive manufacturing (3D printing) process. The following sections will describe, in detail, the design of the impingement device including the flow path, key features, and all configurations. Device fabrication and measurement of key physical parameters will also be discussed.

4.1.1. Cooler design and flow path

Description of flow path:

A single configuration of the Gen II impingement cooler is provided in Figure 4-1. Figure 4-1a is a perspective view photograph of a manufactured (3D printed) part while Figure 4-1b-f are CAD generated images for representing the flow path through the device. In all figure views, fluid enters the right side of the device, passes through the impinging array, and exits from the left side of the device. An arrow printed into the anterior face (with the word “Flow” embedded) of the fabricated device (Figure 4-1a), designates the direction of bulk flow. Figure 4-1b depicts a negative of the impingement device manifold. As such, only the fluid is shown rather than actual printed material. Figure 4-1c and d show individual negatives of the inlet and outlet manifolds respectively. Note that the jet and return arrays are not shown in Figure 4-1b-d. Figure 4-1e and f provide cross-sectional views of the impingement device. The plane visible in Figure a bisects the device along the central outlet channel, providing a reference for the cross-sectional view shown in Figure 4-1f. The cross-sectional plane for Figure 4-1e is parallel to the Figure 4-1f plane, bisecting an inlet channel instead.

Arrows in Figure 4-1b-f denote the direction of flow. Colors (blue and red) represent the condition of the fluid (fresh/spent) with respect to the point of impingement where blue indicates

cool, inlet fluid upstream of the impingement region and red indicates hot, outlet fluid downstream of the impingement region. For brevity, the term “fresh” will be used to describe the former and the term “spent” will be used to describe the latter.

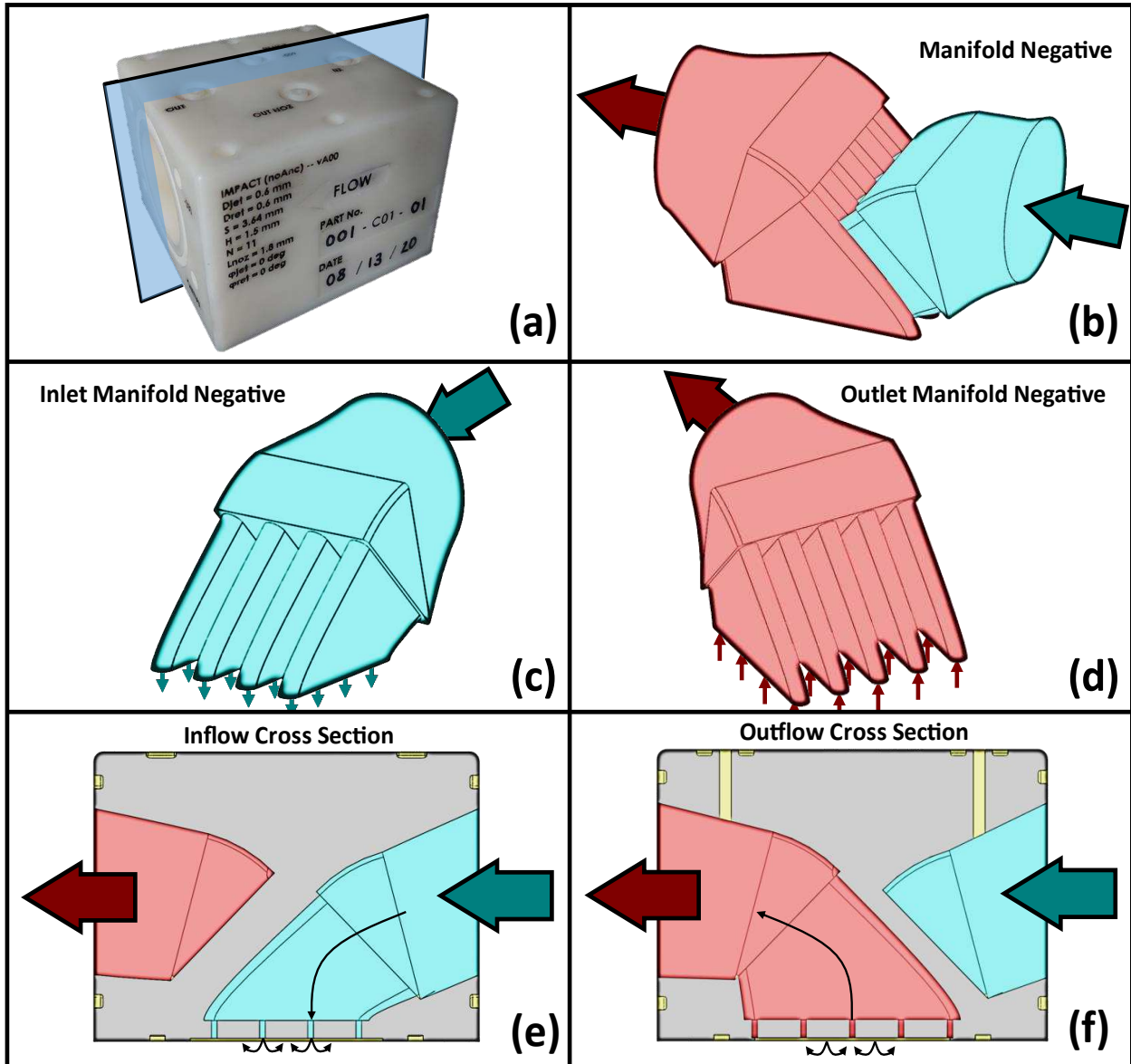


Figure 4-1: Gen II Impingement device. a) perspective view photograph of part C01 b) device C09 manifold negative (flow path) where blue represents inlet manifold and red represents outlet manifold c) device C09 inlet manifold negative, d) device C09 outlet manifold negative e) cross sectional view of C09 inflow manifold and jets shown in blue f) cross sectional view of C09 outflow manifold and fluid extraction orifices shown in red.

Fresh fluid, driven by a pumping mechanism elsewhere in the system, enters the impingement device via the circular 1.5-inch diameter orifice at the inlet (right side) of the device. That fresh flow continues thru the inlet header down a series of sloped parallel channels. For the particular device configuration shown in Figure 4-1b-f, four inlet channels are clearly shown in Figure 4-1c. The exact number of fresh fluid channels (N_{ch}) varies throughout the multiple device configurations tested. Each inlet channel delivers fresh fluid to a series of N_{jet} impinging jets shown at the bottom of the channel where N_j always equals N_{ch} , thus producing a square $N_j \times N_j$ array of impinging jets. Fresh fluid passes thru each jet, impinging upon a flat target surface (not shown) situated directly below the impingement device. After impacting and flowing along the target surface, the spent fluid turns vertically and passes thru an $(N_j + 1) \times (N_j + 1)$ array of fluid extraction ports shown in Figure 4-1f. Five extraction ports are shown in the exemplary configuration. From the extraction ports, spent fluid enters the outlet manifold thru a series of $N_{ch} + 1$ outlet channels. The spent flow channels run parallel to and are interlocked with the fresh flow channels but are sloped in the opposite direction. Spent fluid passes thru the outlet channels thru the outlet header and out of the device via the circular 1.5-inch orifice at the outlet (left side) of the device.

Mechanical/fluidic connections:

Figure 4-2 presents a dimensioned perspective view of a manufactured impingement device, showing the top, inlet, and posterior sides of the device. Some features have been outlined to enhance visibility. The impingement device is 58 mm tall with a square 80 mm by 80 mm base. External dimensions were chosen to be as large as necessary to accomplish mounting and fluidic connections while limiting total part volume to reduce fabrication cost. In contrast to the POC impingement design (Chapter 3), this variation employs excessive volume to mitigate manifold

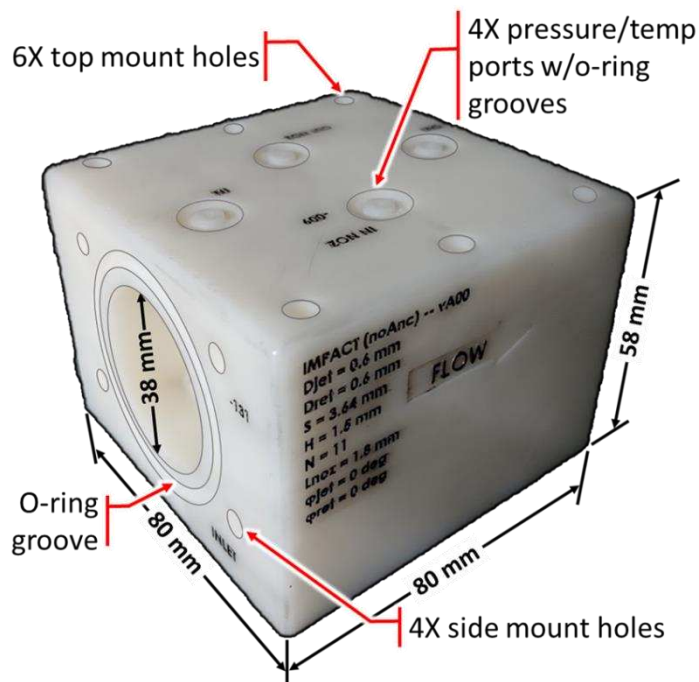


Figure 4-2: Dimensioned photograph of impingement device configuration C01

pressure drop. The inlet and outlet orifices to the device are circular and 1.5 inches (~38.1 mm) in diameter. The impingement device is secured to a surrogate heater (which will be discussed in detail in Section 4.2) via a top mounting plate and six 10-32 mounting screws. A size -036 o-ring forms the seal between the impingement device and the surrogate heater. An exploded view schematic of the mechanical mounting and process attachment assembly can be seen in Figure 4-3 and a photograph of the assembly is shown in Figure 4-4. The inlet and outlet fluid connections consist of a stainless steel tri-clover fitting welded to a stainless steel custom fabricated mounting plate. A consistent inner diameter of 1.5 inches is maintained throughout the entire process connection assembly. A size -131 o-ring is situated into a groove printed into the RJI device and forms the fluidic seal between the inlet and outlet mounting plates and the impingement device. The inlet and outlet fluid connections are attached to the test facility using a tri-clover clamping

system. On the top side, four size -009 o-rings are used to form the seal around pressure and temperature measurement ports printed into the device. Instrumentation ports are used to measure pressure at four distinct locations and temperature at two distinct locations in the impingement device.

Fluid connection accessories, including the top mount plate, inlet mount plate, and outlet mount plate were fabricated by the Rapid Prototyping Lab located at the Powerhouse Energy Campus at CSU.

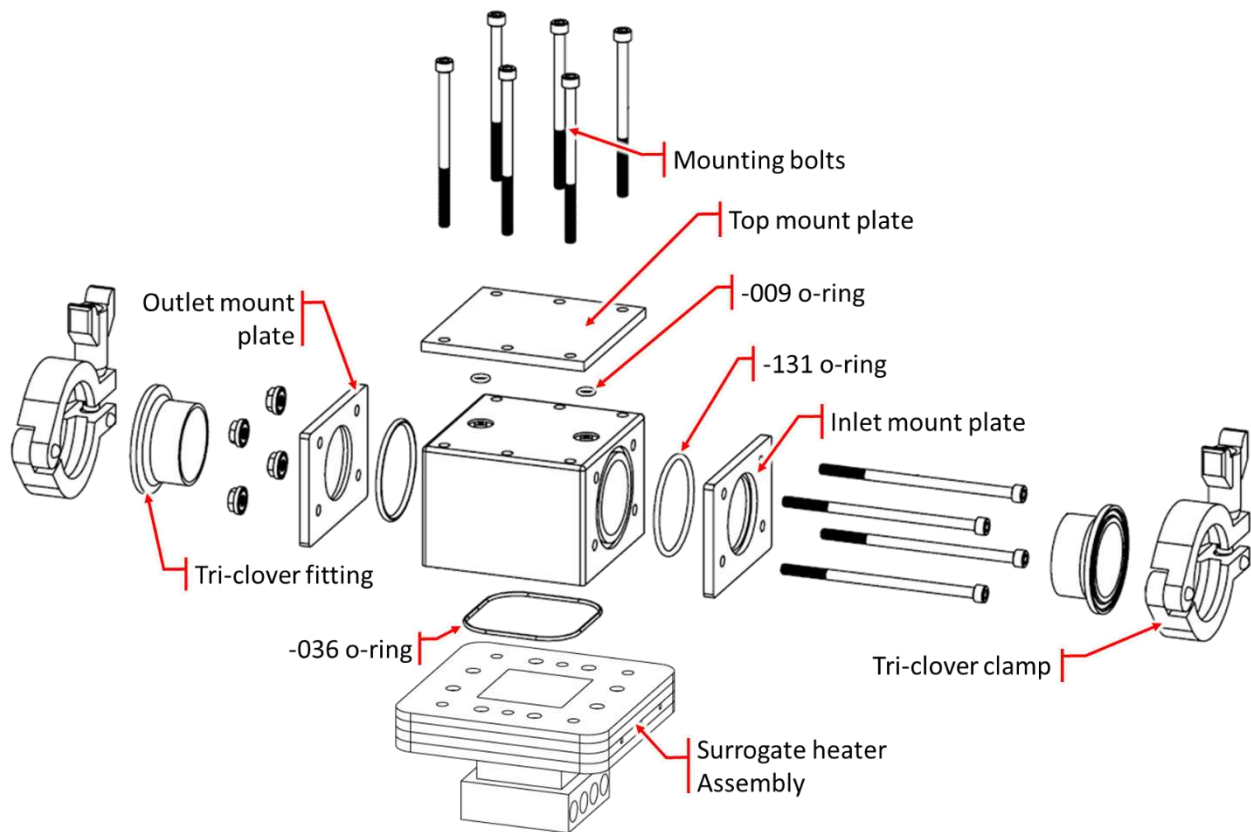


Figure 4-3: Exploded view of surrogate heater and impingement cooler assembly

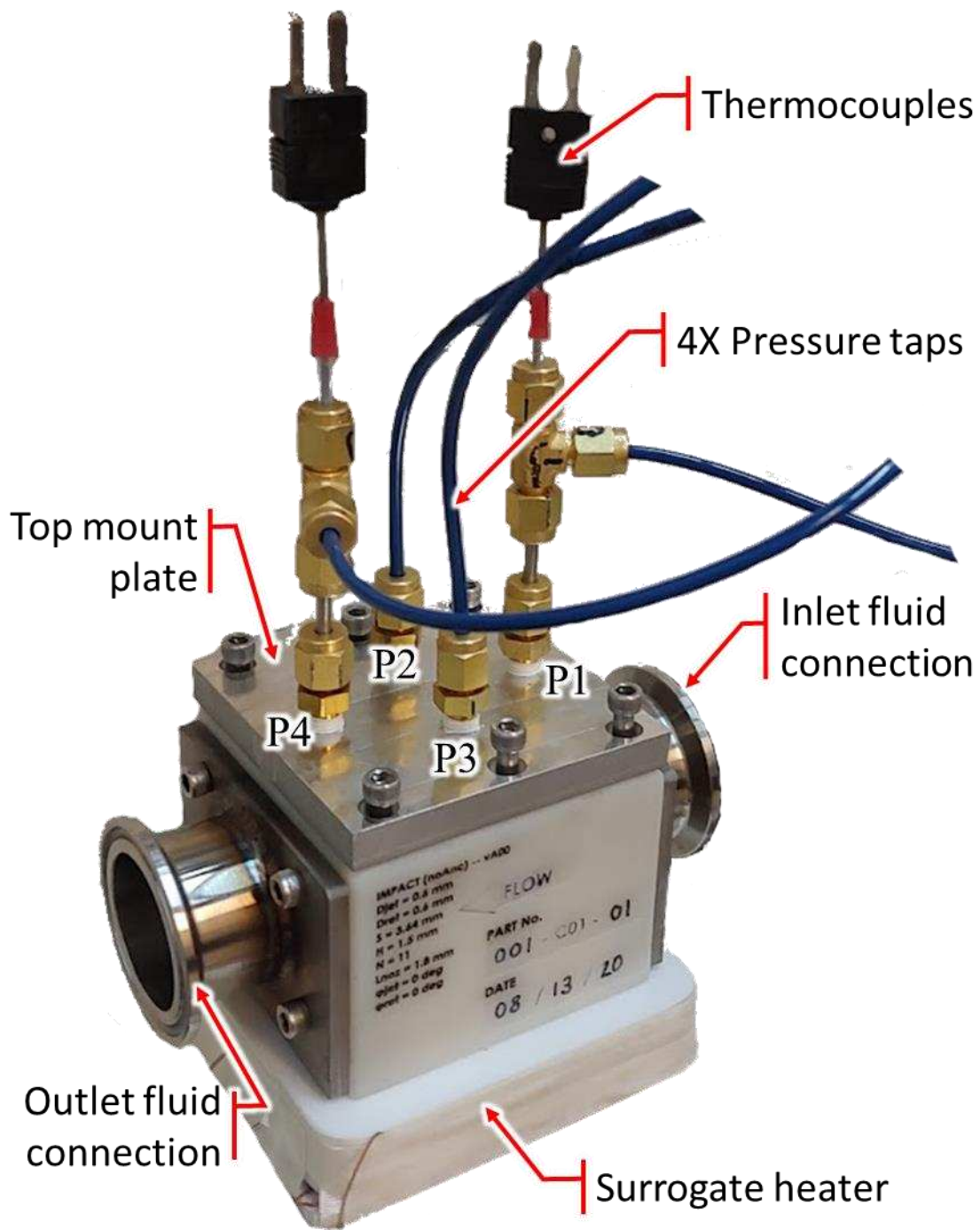


Figure 4-4: Impingement device C01 mounted to surrogate heater with process and measurement connections

Key design features:

As was previously discussed, the impingement test section was designed in an effort to minimize the effect of the manifold geometry, thus isolating experimental findings to be contributed predominantly by the impingement array. The following will discuss key design features, why they were selected, and how they contribute towards accomplishing this goal. The following is a list of some key features that will be discussed:

- Large inlet and outlet headers
- Gradual flow turning
- Wide open channels
- Short flow path length
- Instrumentation ports
- Repeatable unit-cell jet array
- Plastic construction

The large, open inlet and outlet headers serve to provide flow delivery to the attached channels while imparting minimal pressure drop. The cross-sectional flow area in the header regions (nominally 1140 mm²) was designed to be significantly larger than that of the combined impinging jet array. Nominal impinging array cross sectional areas ranged from 18 mm² (C03 and C09) up to 137 mm² (C08); thus, the inlet and outlet header areas were always between 8.3 and 63 times larger than the total impinging array area. Furthermore, the in-line orientation of the headers and channels promotes evenly distributed flow to each channel by not acting against the fluid's preexisting momentum upon entering the device. That is to say that although some flow turning is necessary to deliver fluid from the horizontally oriented inlet and outlet headers to the vertically

oriented jet array, additional, unnecessary flow turning is avoided in this design. Necessary flow turning is accomplished gradually rather than using a hard 90° angle. Figure 4-1e and f clearly illustrate the gradually turning pathway.

The flow channels which deliver fluid between the inlet/outlet headers and the impingement array are also kept as wide and open as could be achieved while maintaining a printable wall thickness. Channel wall thickness was constrained to a minimum of 0.5 mm and a maximum of 0.7 mm. The channel widths across all nine parts were held to be at least one jet diameter but were made much wider (up to 3.6 jet diameters) whenever maintaining the minimum wall thickness was still achievable. Channel lengths were kept short as well as wide, with a typical mean-line path length of approximately 23 mm, allowing for minimal pressure drop to be contributed by the manifold sections.

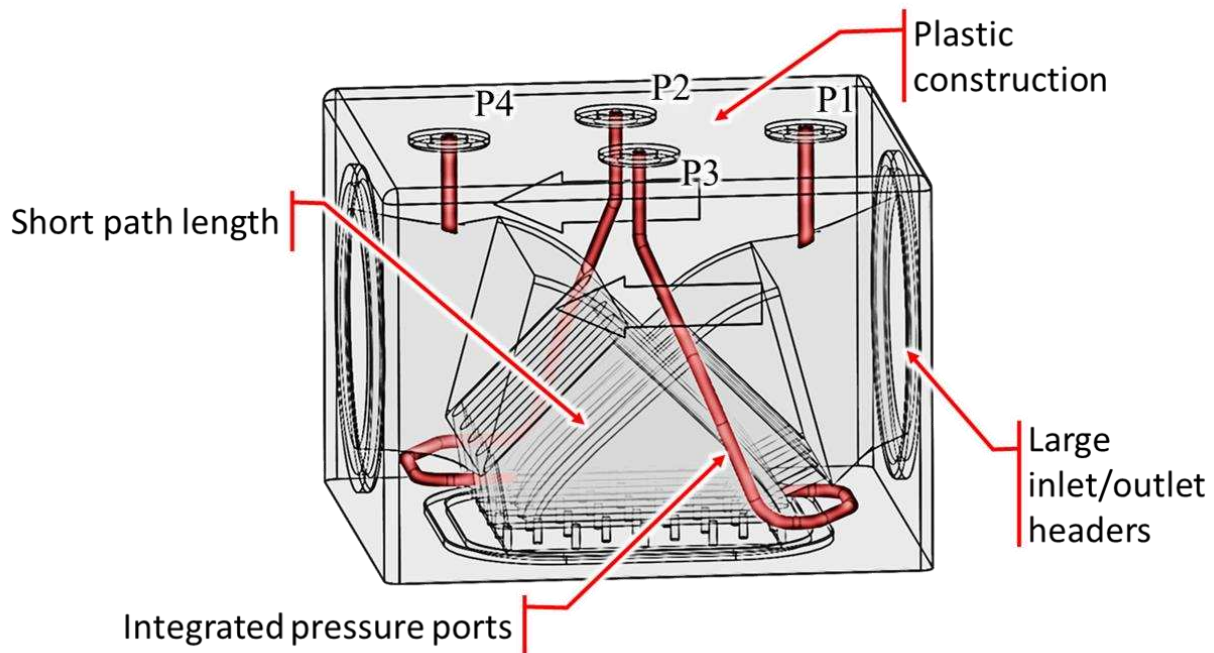


Figure 4-5: Transparent solid model of C09 impingement device with key features. Instrumentation ports highlighted in red.

An additional key feature of the Gen II impingement design—made possible only through the employment of additive manufacturing techniques—is the integration of complex-path instrumentation ports. Integrated instrumentation ports are highlighted in red in Figure 4-5. Some features, including decals and mounting holes are omitted from Figure 4-5 for clarity. Instrumentation ports are labeled as P1 thru P4 and correspond to those given in Figure 4-4. Port P1 is connected to the device inlet header, P2 is connected to the inlet to the impinging array, P3, is located at the outlet of the impinging array, and P4 is connected to the device outlet header. Thermocouples are inserted into ports P1 and P4 to measure inlet and outlet fluid temperature. An absolute pressure transducer is attached to port P1 for determining fluid property information at the inlet of the device. Differential pressure transducers are placed between ports P1 and P2 (inlet header pressure drop), P2 and P3 (impingement array pressure drop), and P3 and P4 (outlet header pressure drop). Ports P2 and P3 are routed through the impingement device to attach to a single inlet and single outlet channel just above the impingement jet/return orifices. If manifolding pressure drop accounts for a small proportion of the total device pressure drop, then the direct pressure measurement between P2 and P3 will represent a good approximation for actual jet array pressure drop.

Another design attribute which contributes towards creating a broadly applicable test section is the incorporation of a repeating unit cell jet array. In all design configurations, the impingement array extends to the very edge of the 40 mm by 40 mm target region and return holes at the periphery of the array are truncated in an attempt to most closely approximate an infinite repeating array. This design attribute becomes less important as the jet count increases and more important as the jet count is reduced. For example, the C09 configuration contains only 16 repeating jet unit cells (4 by 4 jet array) and 12 of those are at the periphery. Figure 4-6 depicts the

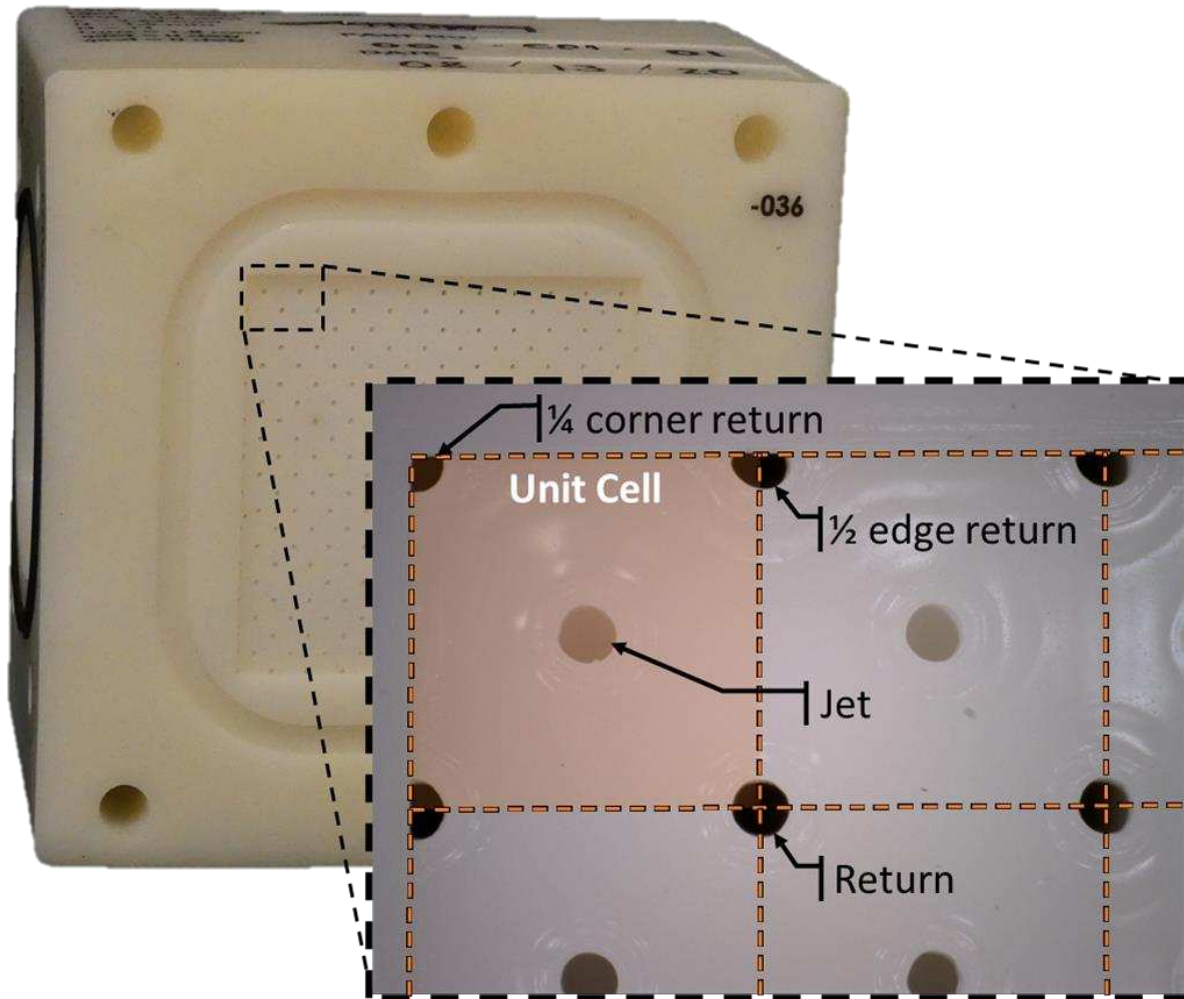


Figure 4-6: Impingement part C01 hole array highlighting repeating unit cell.

unit cell using photographs of the C01 impingement array. The truncated edge and corner return ports can be clearly seen.

Finally, the impingement test sections were fabricated from a thermally insulating polymer material. This is very important for reducing thermal shortcut losses in the manifold which may affect the apparent heat transfer performance of the impingement array. These thermal shortcut losses have been discussed in further detail in appendix D. The nine impingement test sections were fabricated from a proprietary 3D Systems photopolymer (Accura® Xtreme™ White 200). The thermal conductivity of the photopolymer is not provided by the manufacturer however, as

with most plastics, it is assumed that the thermal conductivity is near $0.2 \text{ W m}^{-2} \text{ K}^{-1}$. Typical thermal conductivity values for a wide variety of unfilled plastics are provided in Figure 4-7 [75]. In opposition to the POC study, test sections for this extended investigation were fabricated by a third-party manufacturer, Xometry, rather than internally using the REACH CoLab printing facilities.

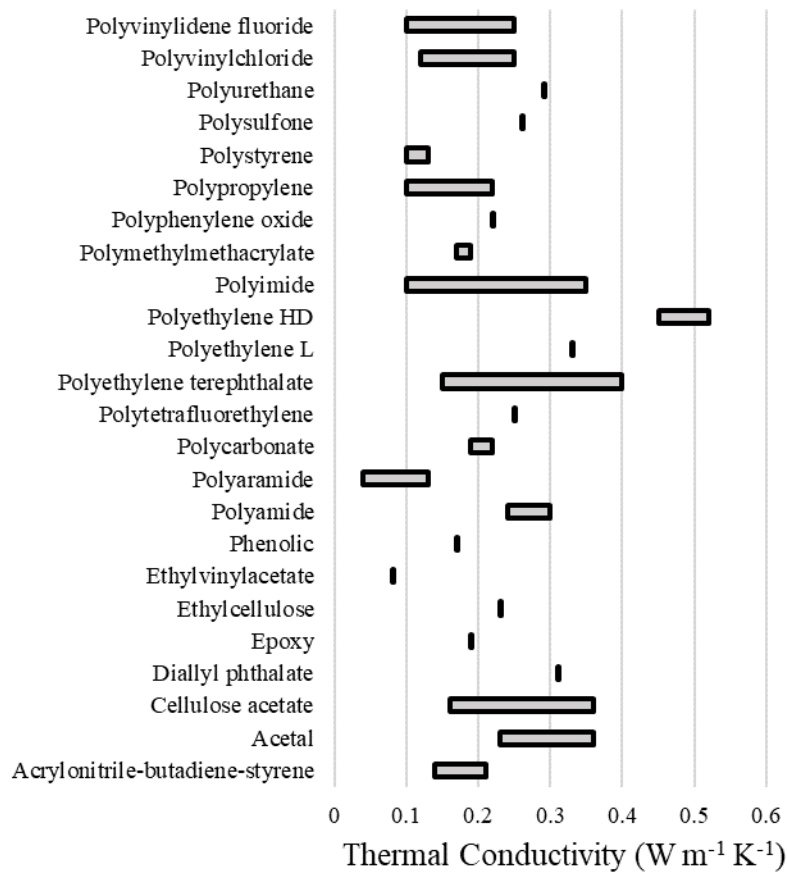


Figure 4-7: Typical thermal conductivity values of unfilled plastics [75].

4.1.2. Key geometries and configurations

Discounting the impingement device manifold geometry, there are several important geometric parameters relating to the impinging array that were identified and controlled during this investigation. Table 4-1 in cooperation with Figure 4-8 provides a list of definitions and ranges for each of these parameters. Six distinct non-dimensional parameters were selected and controlled to describe the impinging array. Those are the non-dimensional return orifice diameter (D_r/D_j),

Table 4-1: Table of key geometric parameters

Geometric Parameter	Definition	Units	Range
D_j	Jet nozzle diameter	mm	0.6 – 1.2
D_r	Return orifice diameter	mm	0.6 – 1.2
D_r/D_j		[dim]	1
H	Jet nozzle height from target surface	mm	0.6 – 4
H/D_j		[dim]	0.5 – 4
S	Jet to jet spacing	mm	3.1 – 10
S/D_j		[dim]	3.0 – 8.3
L	Jet nozzle length	mm	1.8 – 3.6
L/D_j		[dim]	3
ϕ_j	Jet nozzle conical angle	rad	0
ϕ_r	Return port conical angle	rad	0
N_j	Jet array size, i.e. sqrt(total jets)	#	4 – 13

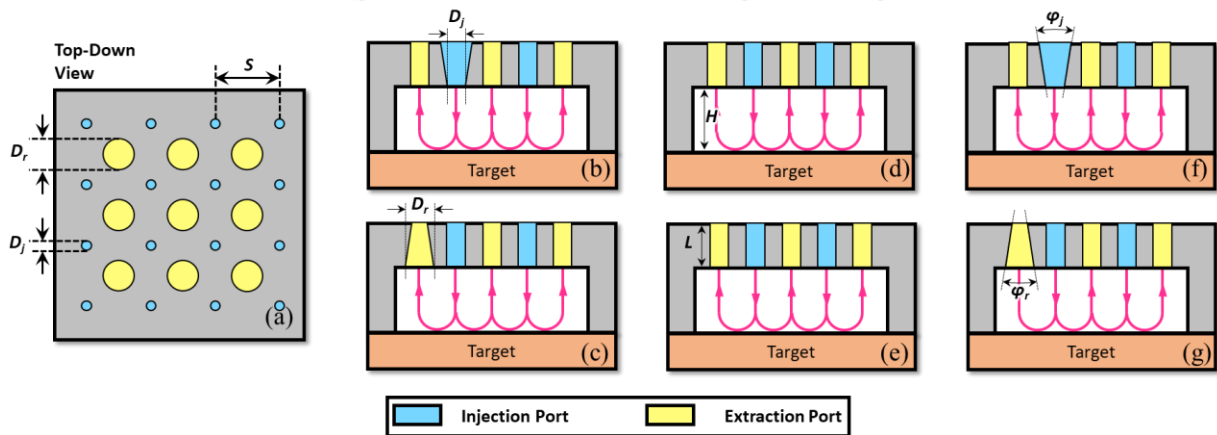


Figure 4-8: Diagram describing key geometric parameters of the impingement array.

non-dimensional jet height (H/D_j), non-dimensional jet spacing (S/D_j), non-dimensional jet nozzle length (L/D_j), and jet/return nozzle cone angles (ϕ_j , ϕ_r). Naturally, many other geometric parameters could be contrived to further alter the impingement array. For example, the ratio of return orifice count to jet orifice count, impact angle of the impinging jet onto the target surface, jet nozzle shape, and the ratio of jet height to return orifice height could all be varied. However, alterations beyond the six parameters listed would result in complicated changes to the basic impingement array structure of which there could be boundless diverse configurations. In the interest of investigating a simple, broadly applicable impingement geometry while minimizing the test geometries, parameters beyond those listed were not considered. Furthermore, of the six core parameters listed, most were held constant for this investigation for the same purpose. Of the six core parameters, the two most important parameters (S/D_j , H/D_j) were selected to vary while the remaining parameters were held constant. Non-dimensional jet spacing and non-dimensional jet height have been identified repeatedly in the open literature as important geometric parameters for characterizing impinging arrays and, as such, varying these offers the greatest opportunity for contribution to the current body of literature and to engineers seeking to design jet impingement cooling devices [11,13,76]. With the fundamental testing framework and manifold design in place, the remaining parameters may be subject to continued investigation beyond the scope of this study.

Nine test section configurations were devised with consideration to the impingement array geometric parameters discussed. Core geometric parameters—return orifice diameter (D_r/D_j) and jet nozzle length (L/D_j)—were held constant at 1 and 3 respectively. Jets and return ports were made cylindrical (i.e., $\phi_j = 0$, $\phi_r = 0$). Jet height (H/D_j) and jet spacing (S/D_j) were varied with attention to physical limitations to form a diverse geometry set. Dimensional parameters varied as

necessary to meet the prescribed non-dimensional design points. The range over which each geometric parameter was varied can be seen in Table 4-1.

The limits for each core geometric parameter were selected carefully with consideration for manufacturability and usefulness. Here, some of the reasoning behind those selections will be discussed.

A return orifice diameter (D_r/D_j) of 1 was selected to represent the most likely condition for impingement cooling devices with interspersed fluid extraction. Incorporating return ports smaller than the jet nozzles would likely result in greater pressure drop without posing any intuitively obvious benefit to heat transfer performance, making it unlikely to be preferable in most applications. Increasing the return orifice diameter to be greater than the jet diameter may produce performance benefits in the form of reduced pressure drop; however, once again, the effect on heat transfer is non-obvious. Furthermore, selecting a return-to-jet diameter ratio of unity allows for the fresh-flow and spent flow channels to be easily designed at the same width for all configurations. It also makes smaller S/D_j ratios possible than would be with larger return ports, making a unity condition the simplest and most applicable place to start while offering an interesting space for potential improvements by employing alternate values for D_r/D_j .

Selecting cylindrical jet and return nozzles was an obvious choice for this study. Although altering jet shape is likely to improve performance of the impinging array, cylindrical holes provide the simplest and most widely applicable jet geometry.

Jet nozzle length was selected to be constant at 3 jet diameters. This constraint was set mostly for manufacturing purposes. Given an L/D_j of 3, the impingement floor thickness varied from 1.8 mm up to 3.6 mm. Increasing the floor thickness much beyond this point would have required excessive material, driving up part cost. It also possibly would have required increasing

the overall height of the part to accommodate the extra floor thickness. On the low end, it was desirable that the impingement floor be sufficiently thick to resist bowing or warpage which may compromise the geometry of the impinging array. While wall thicknesses as low as 0.5 mm were prescribed, warpage or alteration in those areas would not result in significant changes to core geometric parameters under investigation, and so are tolerated.

For the jet diameter parameter (D_j) a minimum was set at 0.6 mm. This limit was selected after inspection of previous sample parts printed with varying orifice sizes. While orifices as small as 0.3 mm were successfully fabricated, as the hole size is reduced, tolerances become relatively larger, and the hole shape becomes less reliably circular. Furthermore, the transition from in-house printing improved print reliability, reduced labor, and increased the available print volume; however, print resolution was somewhat reduced. Sample prints from the in-house printing facilities and the third-party manufacturer were used to inform design. It was determined that clean, circular 0.6 mm holes were very reliably and repeatably produced by Xometry, eliminating any concern of hole shape effecting experimental results. There is still considerable variation in hole diameter (to be quantified in Section 4.1.3) at a 0.6 mm design size, but the holes were measured to compensate. The upper bound for jet diameter of 1.2 mm was allowed to vary as necessary to fulfill other geometry constraints.

Jet height was constrained dimensionally from 0.6 to 4 mm and non-dimensionally from 0.5 to 4 jet diameters. The upper non-dimensional constraint of $4D_j$ was selected to form a broad, but interesting range of geometries. It has been well established in the literature that increasing jet height results in reduced heat transfer performance, making lower values of H/D_j more applicable than higher ones. Furthermore, as H/D_j is increased, the implementation of interspersed fluid extraction becomes less impactful as spent fluid has more space to flow past adjacent jets. For

these reasons a modest range of H/D_j was chosen that falls in line with previous studies [6,20,41,44] but focuses on lower values which are of greater interest. The lower 0.6 mm limit was set with consideration for manufacturing constraints. Similar to the jet diameter limit, as H is reduced, tolerances become more proportionally significant. Maintaining a minimum jet height of 0.6 mm allows the impingement array to be positioned above the target surface with reasonable accuracy. The lower non-dimensional limit was constrained primarily by the 0.6 mm physical limit. Lower H/D_j values are of interest but constructing them in this design set would have been difficult to achieve without sacrificing the range of other parameters. The upper dimensional limit of 4 mm was allowed to vary as needed.

Jet spacing spanned nominally from 3 to 8 jet diameters (3.1 to 10 mm). Jet spacing was determined in large part by the jet count (N_j) and the impingement target area size. The impingement target was a flat 40 mm by 40 mm square surface. In order to completely fill the target array with a whole number of repeating impingement unit cells, jets were distributed evenly across the surface at whatever spacing was required to accomplish that. As such, the jet spacing, S , was defined as 40 mm divided by N_j . The lower limit was constrained by manufacturability. The necessity to maintain reasonable channel widths and wall thicknesses limited how closely the jets could be positioned together. The upper limit was constrained in part by achieving a reasonable whole number of jets and in part by a desire to focus on a useful range. Similar to H/D_j , heat transfer performance and extraction port efficacy each degrade as S/D_j is increased and an upper limit of 8 was in range for other studies in the literature [6,20,41,44]. The design configuration with the least number of jets contains a 4 by 4 array and has the maximum jet spacing. Reducing the jet count further would allow for higher jet spacings to be achieved, but would also detract from the application towards an infinite repeating array.

A final parameter which played an important role in geometry selection was Reynolds number. Impingement array geometries were chosen to provide experimental data over a robust range of Reynolds number. Given the final geometries, tested using both air and water across flow ranges achievable by the test apparatus (see Section 0), it was predicted that Reynolds numbers as low as 50 and up to 20,000 would be achieved during testing. Reynolds number predictions were calculated as:

$$Re = \frac{\rho_f V_j D_j}{\mu_f} \quad 4-1$$

where, nominal values were selected for fluid density (ρ_f) and fluid viscosity (μ_f) at 20°C and 1 atm for air and water. Mean jet velocities (V_j) were calculated from nominal volume flow rates given the expected range of test conditions (0.3 – 5 LPM for liquids, and 10 – 300 LPM for air).

The design ranges for all six core non-dimensional geometric parameters (D_r/D_j , H/D_j , S/D_j , L/D_j , ϕ_j , ϕ_r) as well as jet diameter (D_j), jet count (N_j), and Reynolds number can be seen graphically in Figure 4-9. Reynolds number is plotted on the secondary y-axis while all other parameters are plotted on the primary y-axis. All values are dimensionless besides D_j , which is expressed in millimeters. Filled and unfilled Reynolds number data points represents water and air predictions respectively. Note that not all tests are considered, only the predicted upper and lower range for each of the nine parts. As will be discussed in the following section, the actual range of geometries and flow conditions varies from the planned/predicted values presented in this section.

Given all of the design considerations and constraints discussed above, nine design configurations were contrived and labeled sequentially from C01 to C09. Figure 4-10 shows the two main parameters of interest (H/D_j and S/D_j) and how they were assigned for each part. The nine configurations fulfill the four corner points, four edge points and single center point of the H/D_j , S/D_j design space. All key geometric values for each part are provided in Table 4-2.

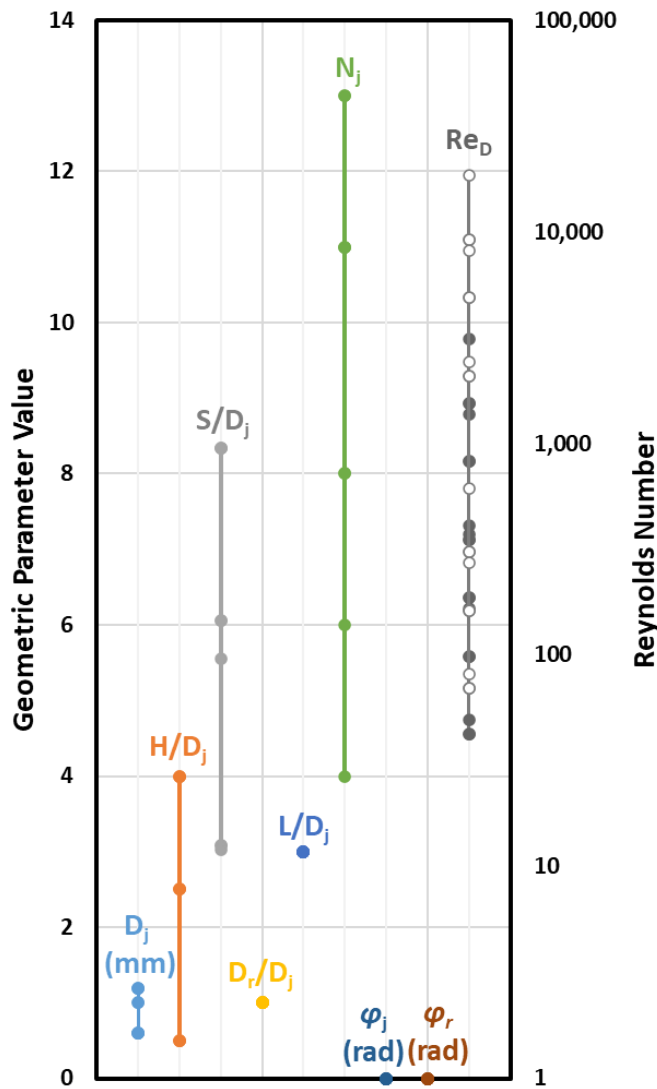


Figure 4-9: Graphical representation of planned impingement geometric parameter ranges

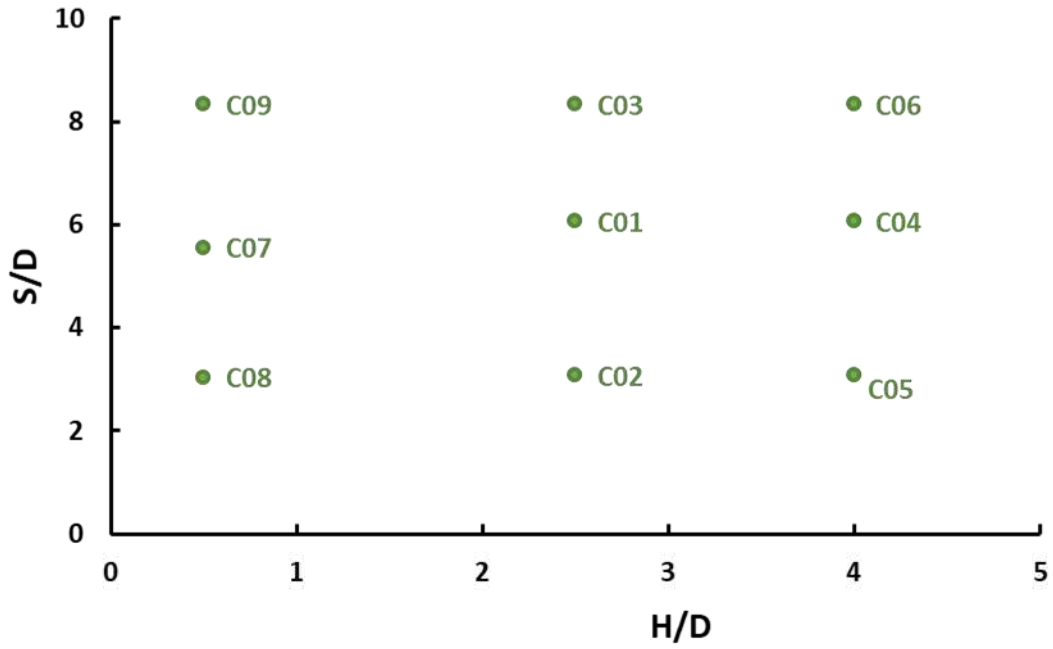


Figure 4-10: Range of planned non-dimensional jet height and spacing by part

Table 4-2: As-designed geometric parameters for all impingement test section configurations.

Geometric Parameter	Definition	Units	C01	C02	C03	C04	C05	C06	C07	C08	C09
D_j	Jet nozzle diameter	mm	0.6	1	0.6	0.6	1	0.6	1.2	1.2	1.2
D_r	Return orifice diameter	mm	0.6	1	0.6	0.6	1	0.6	1.2	1.2	1.2
D_r/D_j		[dim]	1	1	1	1	1	1	1	1	1
H	Jet nozzle height from target surface	mm	1.5	2.5	1.5	2.4	4	2.4	0.6	0.6	0.6
H/D_j		[dim]	2.5	2.5	2.5	4	4	4	0.5	0.5	0.5
S	Jet to jet spacing	mm	3.64	3.08	5	3.64	3.08	5	6.67	3.64	10
S/D_j		[dim]	6.06	3.08	8.33	6.06	3.08	8.33	5.56	3.03	8.33
L	Jet nozzle length	mm	1.8	3	1.8	1.8	3	1.8	3.6	3.6	3.6
L/D_j		[dim]	3	3	3	3	3	3	3	3	3
ϕ_j	Jet nozzle conical angle	rad	0	0	0	0	0	0	0	0	0
ϕ_r	Return port conical angle	rad	0	0	0	0	0	0	0	0	0
N_j	Jet array size i.e., sqrt(total jets)	#	11	13	8	11	13	8	6	11	4
w_{ch}	Channel width	mm	1.12	1	1.8	1.12	1	1.8	2.63	1.2	4.3
th_{ch}	Channel wall thickness	mm	0.7	0.54	0.7	0.7	0.54	0.7	0.7	0.62	0.7

4.1.3. Fabrication and validation

An exterior perspective view photograph of all nine fabricated part configurations can be seen in Figure 4-11. Outwardly, from this view, all nine parts appear to be mostly identical with the exception of varying decals which indicate key as-designed geometries. Figure 4-12 and Figure 4-13 respectively depict the inlet face (with inlet channels) and the impingement array for all nine fabricated parts. From these two figures, it is easy to visualize some of the key differences between the various part configurations.

As was briefly mentioned, the impingement test sections were fabricated by a third-party manufacturer, Xometry. All parts were fabricated by a vat photopolymerization process using a 3D Systems ProJet series printer. The exact printer model was not disclosed. The printing material was 3D Systems' Accura Xtreme white 200. Material information can be found in the material data sheet provided by 3D Systems [77].

As was discussed in Section 3.1, previous impingement cooler designs were fabricated in-house using small-scale desktop photopolymer printers including the Kudo3D Titan 2. The transition from the previous fabrication approach to the most recent was driven by a combination of rapid technology advancements in the field of additive manufacturing and various tradeoffs between the production methods. Over the last several years, additive manufacturing technologies have progressed at a remarkable pace, enabling the low-cost and reliable commercial production of geometries such as these. The desktop printing method used to fabricate Gen 1 impingement coolers offers excellent spatial resolution at extremely low cost. Clean, round jet geometries less than 300 μm in diameter have been printed in-house on the Kudo3D platform for only the cost of material, which amounts to only a few dollars per part. However, this method has proven to be extraordinarily laborious, requiring many hours of troubleshooting and maintenance with

countless failed prints to produce even a single functional part. Furthermore, the total print volume was severely limited. At its highest resolution—which was needed to achieve the micro-scale geometries used—the Kudo3D platform offered less than a 50 mm by 30 mm print area which could only be fully utilized at the cost of a precipitous reduction in print quality and reliability. Third party fabrication through Xometry, by contrast, offered a simple hands-off solution for

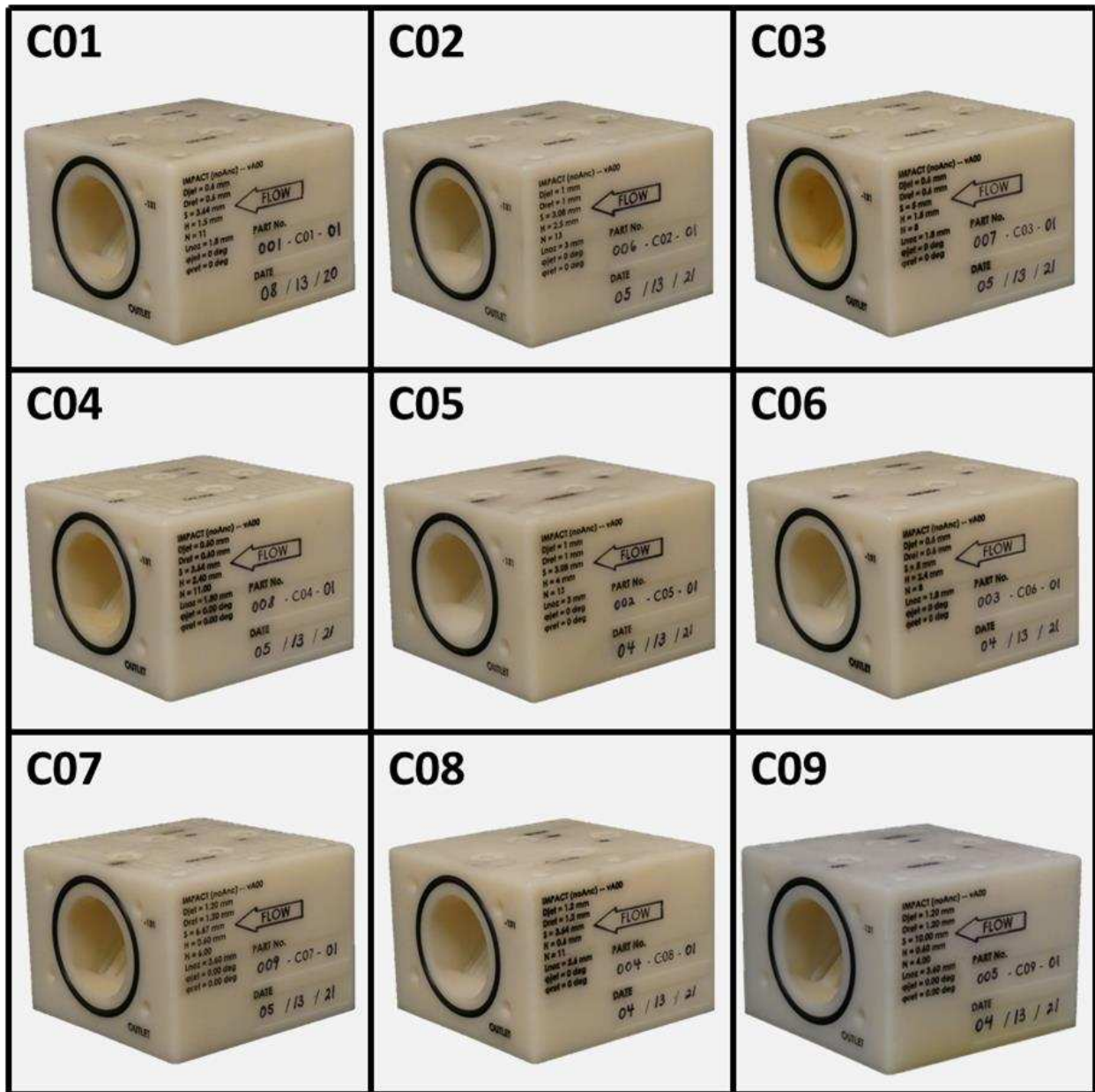


Figure 4-11: Perspective view of C01 thru C09 as-fabricated impingement test sections

producing impingement parts in a timely manner with guaranteed results. This method also offered greatly increased print volume, which was necessary for producing the large manifold structures. As a tradeoff, the minimum jet diameter was increased to 0.6 mm and the dollar cost per part was significantly increased by approximately two orders of magnitude. Due to the rapid advancements in additive manufacturing, the additional cost was still very affordable, even when producing

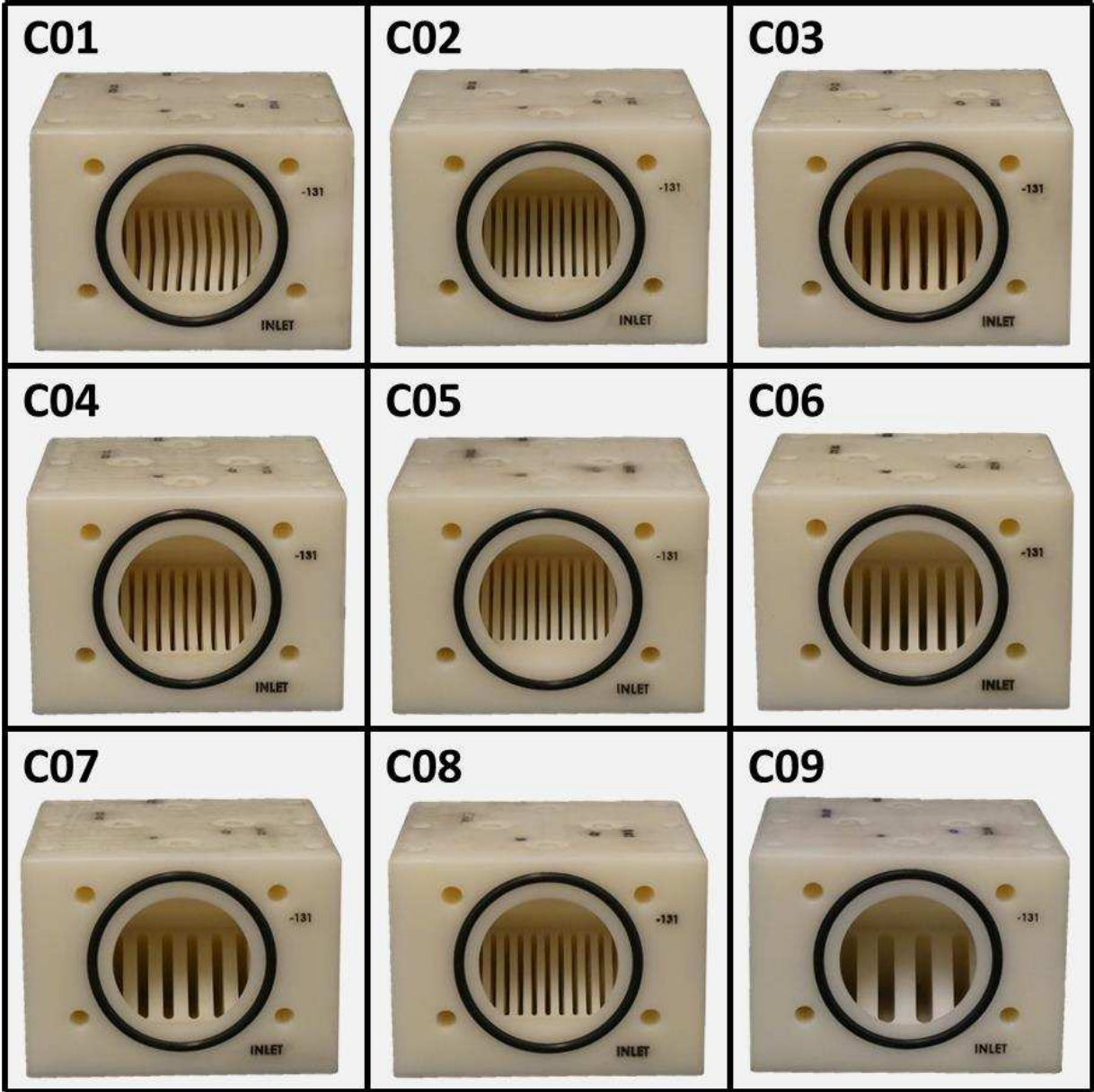


Figure 4-12: Inlet view of C01 thru C09 as-fabricated impingement test sections

several different part configurations. With all of these considerations, third party fabrication became the obvious choice for manufacturing the parts used in this investigation.

After fabricating each of the impingement designs, it was important to validate the key geometries. Each part was inspected, and jet diameters and jet heights were measured. Jet diameters were measured optically using a Dino-Lite AM7815MZT digital microscope. A sample image of the part C01 impingement array as measured by the digital microscope is provided in

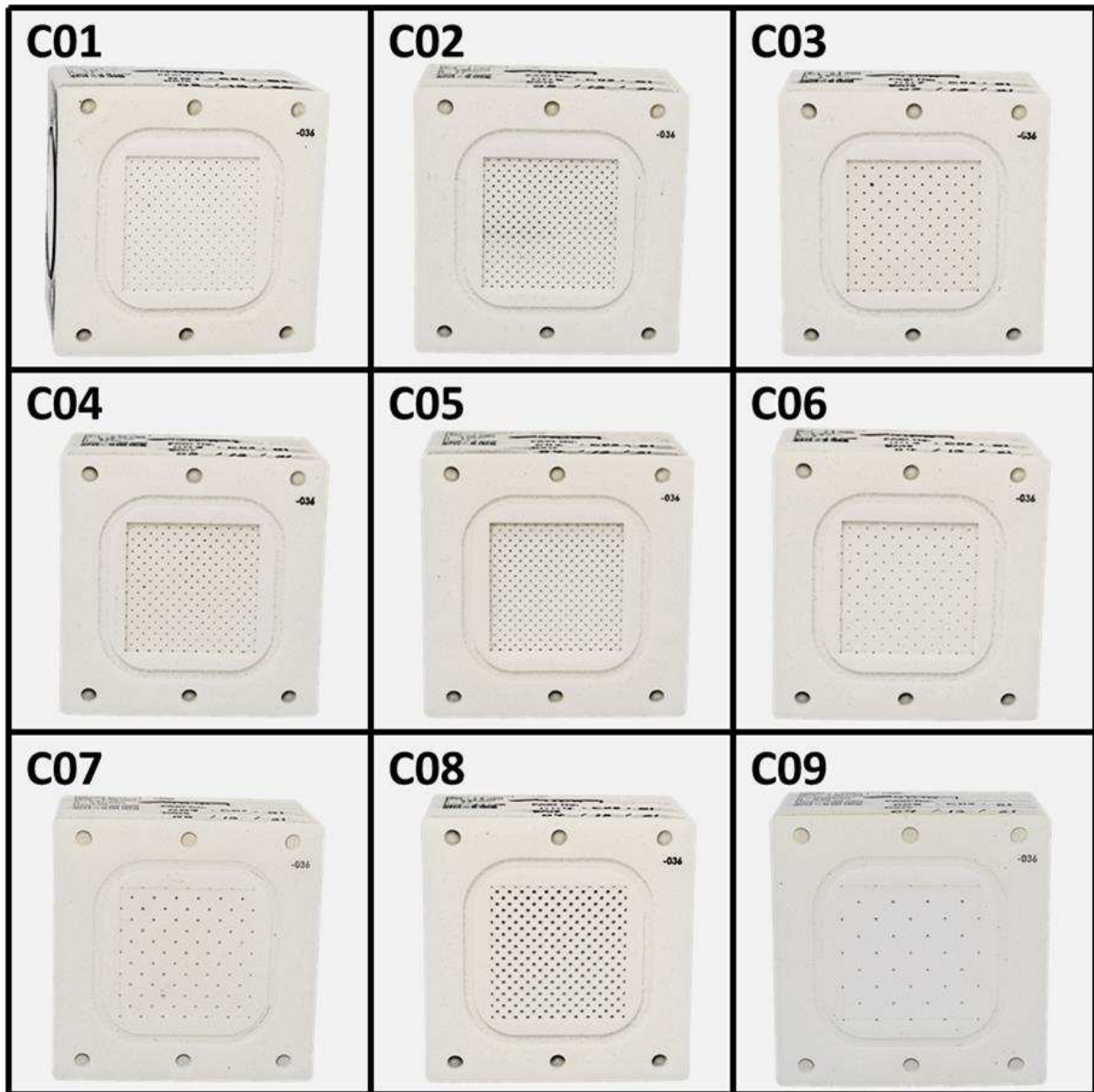


Figure 4-13: Impingement array view of C01 thru C09 as-fabricated impingement test sections

Figure 4-14. A large sample of both jet and return orifices were measured for each part and those values were catalogued for determining actual as-fabricated hole sizes. The complete body of measured impingement orifices has been compiled into a series of histograms shown in Figure 4-15 through Figure 4-17. Each histogram includes all measured jet and return orifices as well as a normal distribution curve overlain on top of the data. Average hole diameters and standard deviations are provided in each figure along with the as-designed diameter for reference.

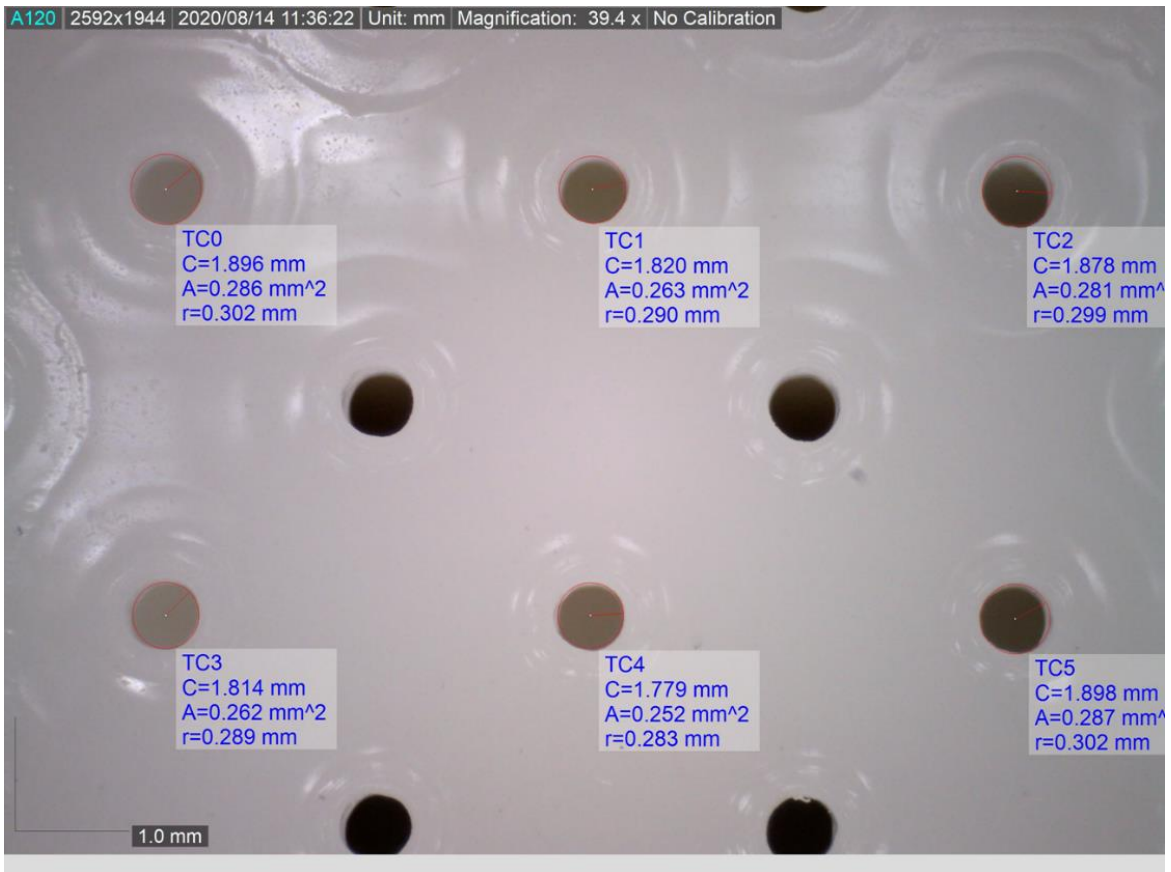


Figure 4-14: Sample image of C01 impingement array measured by Dino-Lite digital microscope

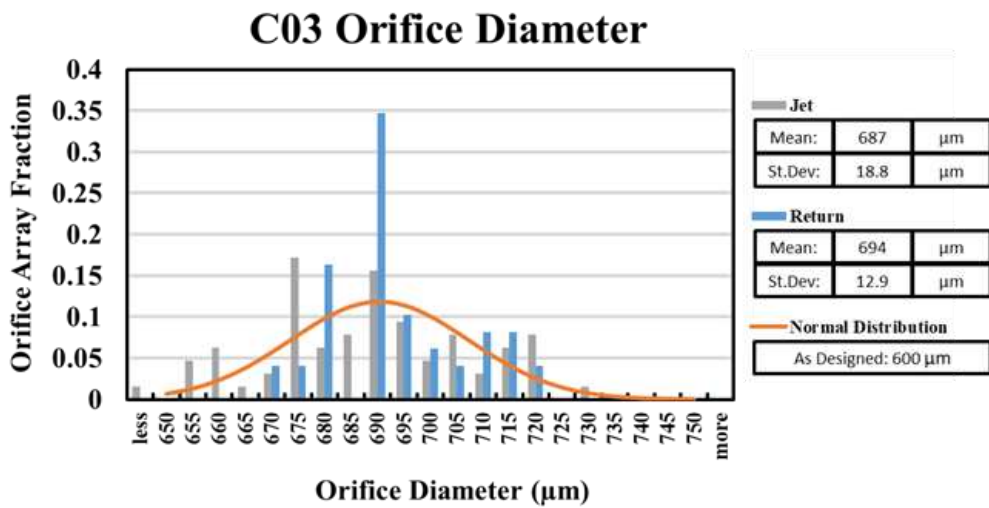
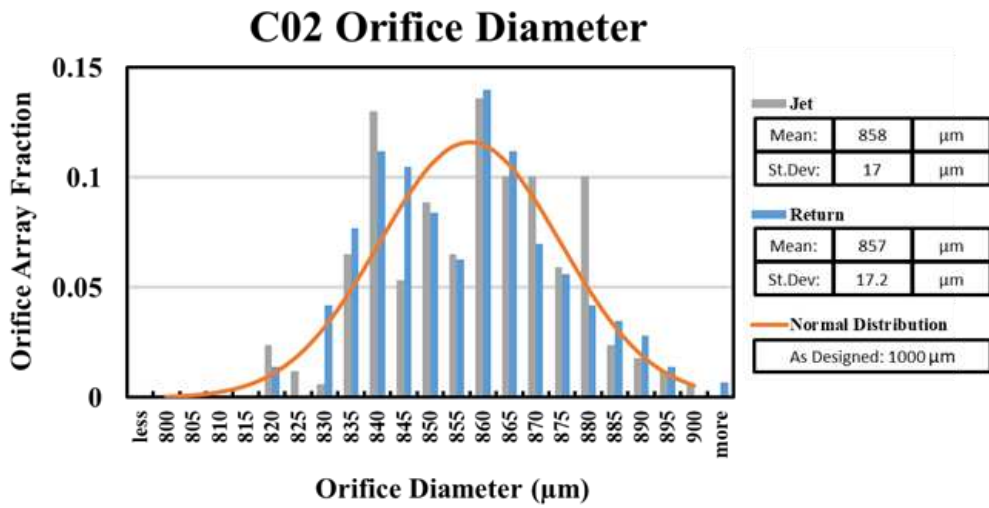
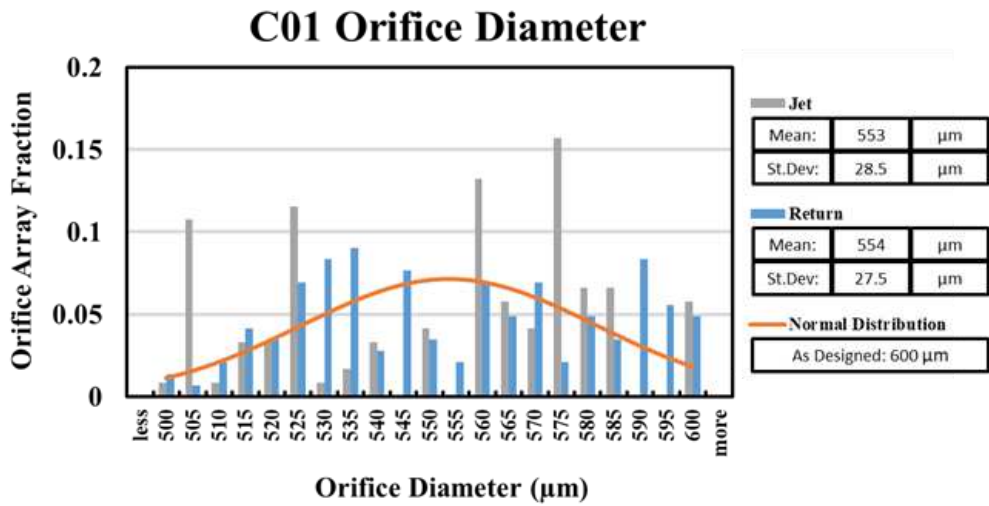


Figure 4-15: Histograms of jet and return orifice diameters for parts C01 thru C03

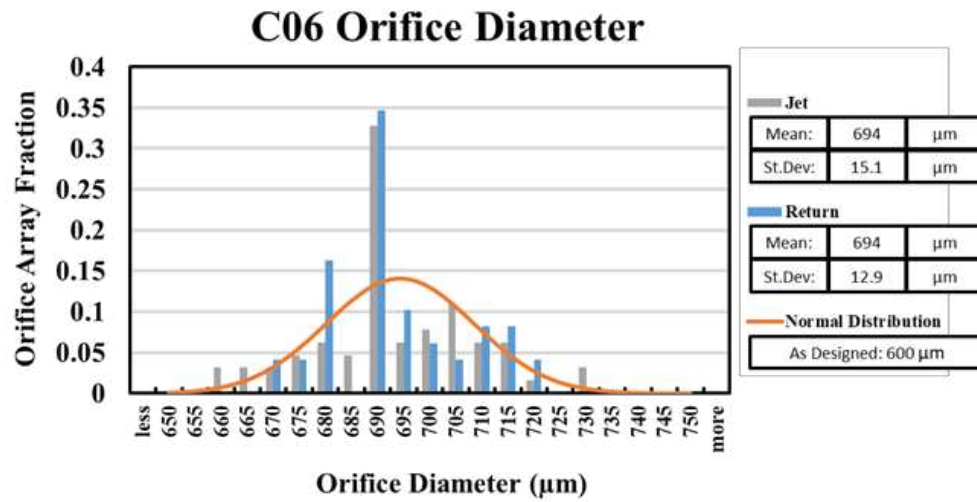
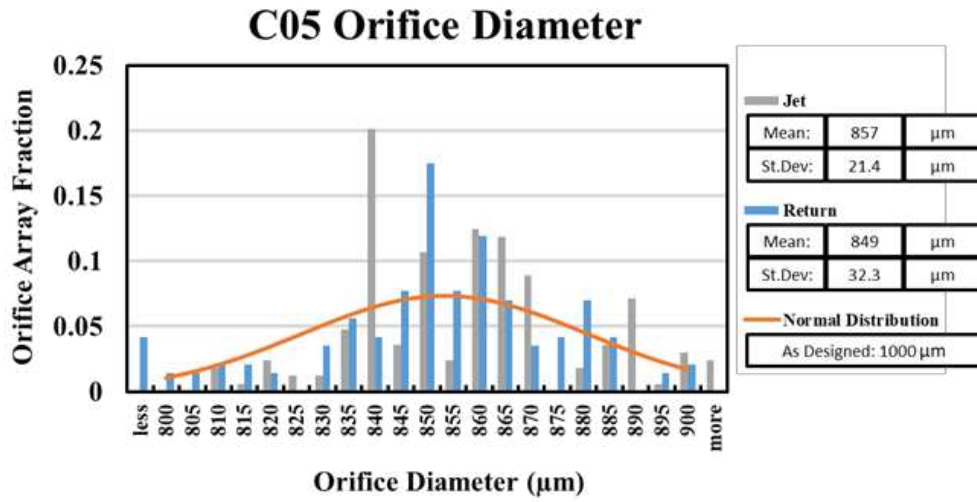
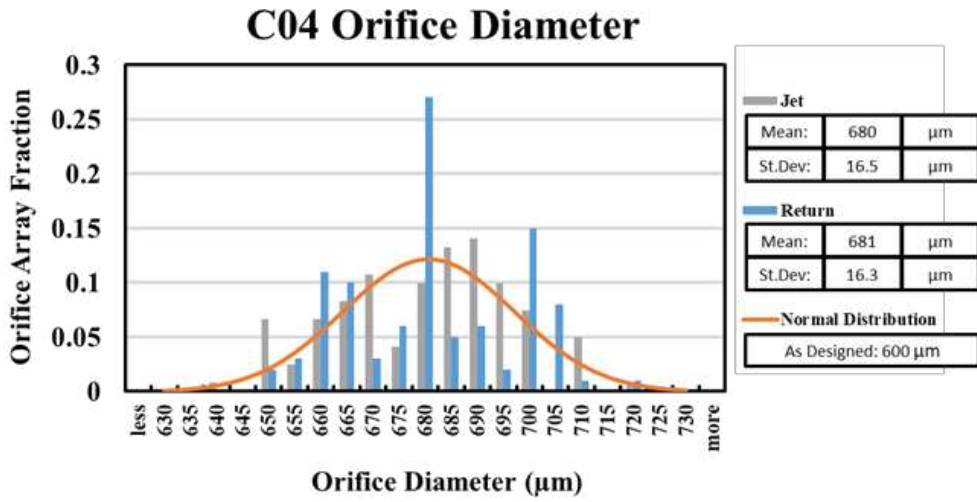


Figure 4-16: Histograms of jet and return orifice diameters for parts C04 thru C06

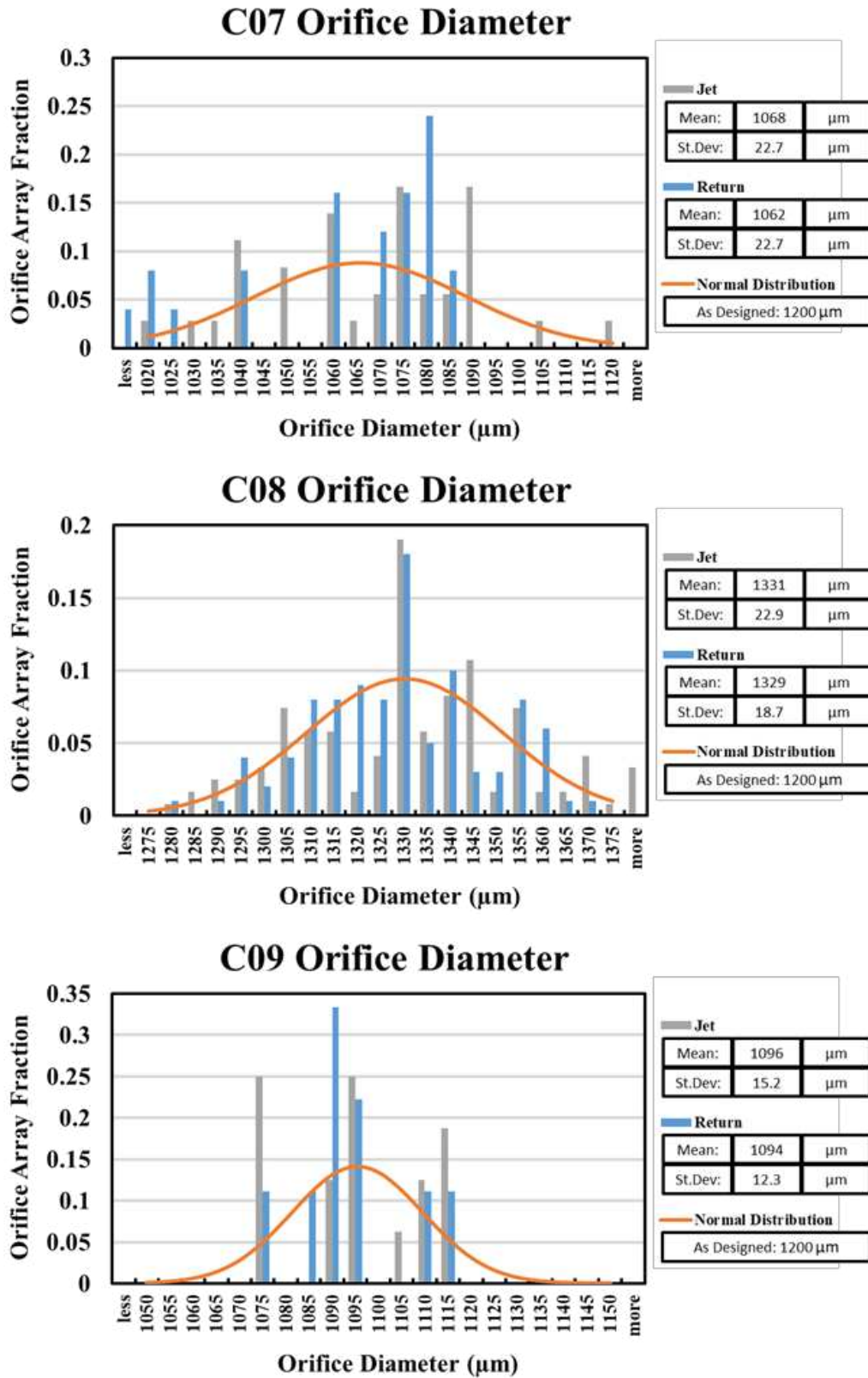


Figure 4-17: Histograms of jet and return orifice diameters for parts C07 thru C09

As can be seen in Figure 4-15 through Figure 4-17, impingement orifice diameters were close to normally distributed and varied notably from the design sizes. Furthermore, the hole size variation was not uniformly in one direction. In other words, some fabricated holes were, on average, smaller than the design size while others were larger than the design size. Mean orifice diameters deviated by as much as 14% smaller (part C02) to 16% larger (part C06) than their design points. Parts C01 and C05 contained the greatest hole size variation within a single geometry configuration. Mean jet diameters and their deviation from design sizes are compiled in Table 4-3.

Impingement height (H) was measured using a depth micrometer. Measurements were taken at eight distinct positions across the impingement array and each measurement was repeated three times. Figure 4-18 marks the approximate height measurement locations on the C04 part configuration, labeled A thru H. Height measurements were done by hand in the pattern shown; the exact measurement locations were not strictly controlled. All as-designed and actual measured heights are provided in Table 4-4. From impingement height measurements, it is apparent that all nine device configurations were fabricated with a smaller average height than was designed. Actual mean jet heights ranged from 5% less than the design parameter (part C05) to 36% less in

Table 4-3: Impingement orifice diameter deviation

Part Config	Design Jet Dia. (mm)	Mean Jet Dia. (mm)	Dev (%)
C01	0.6	0.554	-8%
C02	1	0.858	-14%
C03	0.6	0.690	15%
C04	0.6	0.681	13%
C05	1	0.853	-15%
C06	0.6	0.694	16%
C07	1.2	1.066	-11%
C08	1.2	1.330	11%
C09	1.2	1.095	-9%

Table 4-4: Impingement height measurements

Part Config	Design Height (mm)	Mean Height (mm)	MAD (mm)	Dev (%)
C01	1.5	0.960	0.093	-36%
C02	2.5	2.270	0.032	-9%
C03	1.5	1.370	0.024	-9%
C04	2.4	2.220	0.025	-7%
C05	4	3.810	0.036	-5%
C06	2.4	2.080	0.051	-13%
C07	0.6	0.530	0.039	-12%
C08	0.6	0.410	0.046	-32%
C09	0.6	0.500	0.055	-17%



Figure 4-18: Impingement array height measurement locations

the case of part C01. There was also variation in jet height spatially across the impingement array. This variation is represented by the Mean Absolute Deviation (MAD) of height measurements across all 8 measurement locations on a single test section. Part C01 had the greatest variation with a MAD of $93\ \mu\text{m}$, while part C03 had the least variation with a MAD of only $24\ \mu\text{m}$. Surface plots provided in Figure 4-19 thru Figure 4-21 give an approximation of the spatial height of the impingement array for all nine device configurations. Measured height data are shown by red circles on each plot while the surface is of a bi-quadratic regression fit through the measured height data. The curvature shown in the impingement surfaces is visually exaggerated by the height axis being disproportionately large compared to the x and y positional axes. Also, interpolation and extrapolation between and beyond the eight measurement locations is not expected to be highly accurate. However, these graphics serve to demonstrate the importance of limiting the lower boundary of the height parameter. To highlight this, part C05 and part C07 have nearly the same mean absolute deviation across their surfaces ($36\ \mu\text{m}$ and $39\ \mu\text{m}$, respectively); however, the relative variation of C07 is dramatically more apparent due to the smaller H value. This type of variation presents a challenge for testing low H/D_j geometries in this study and in studies which have come before it.

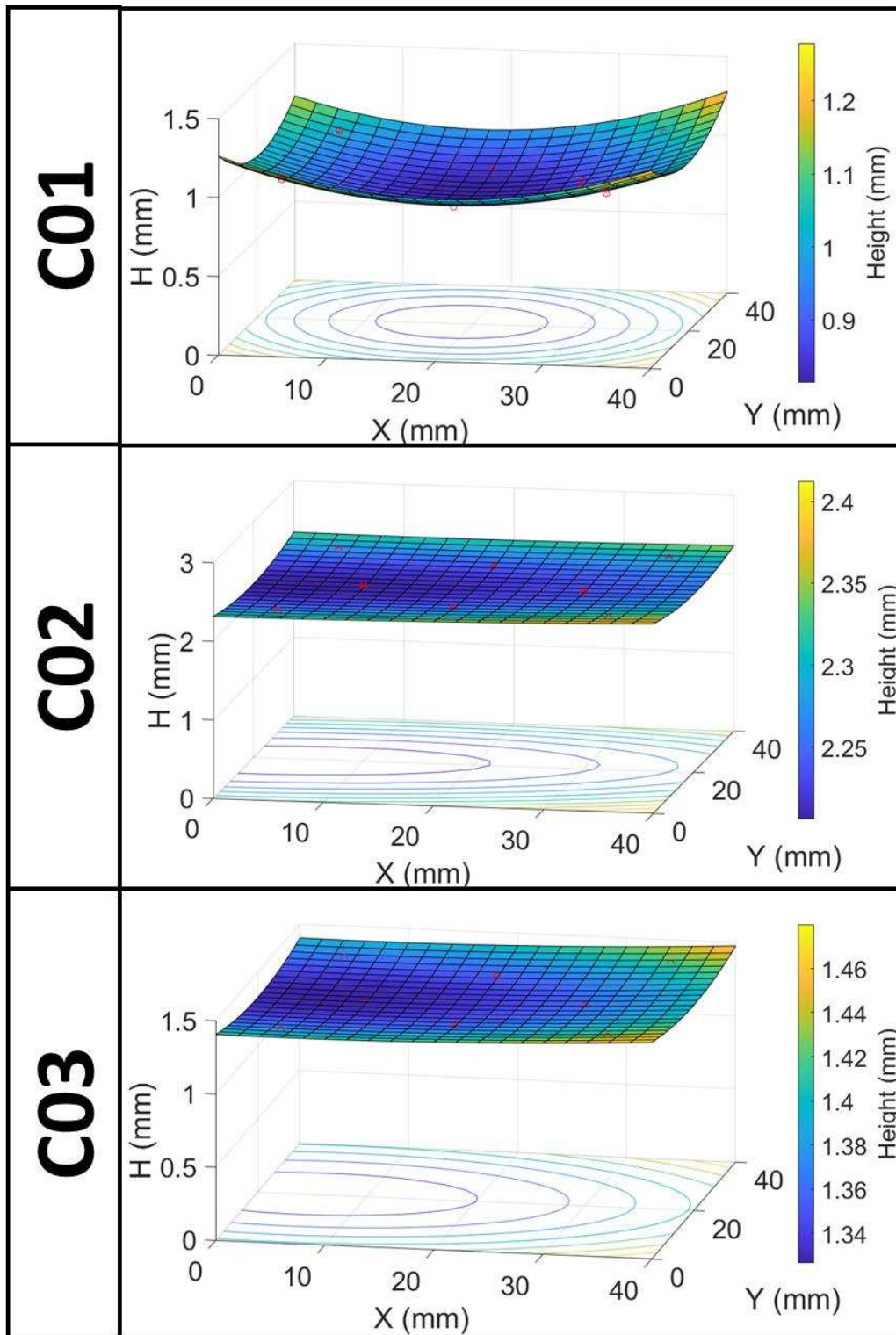


Figure 4-19: Surface plots of measured spatial impingement height for C01 thru C03 test sections.

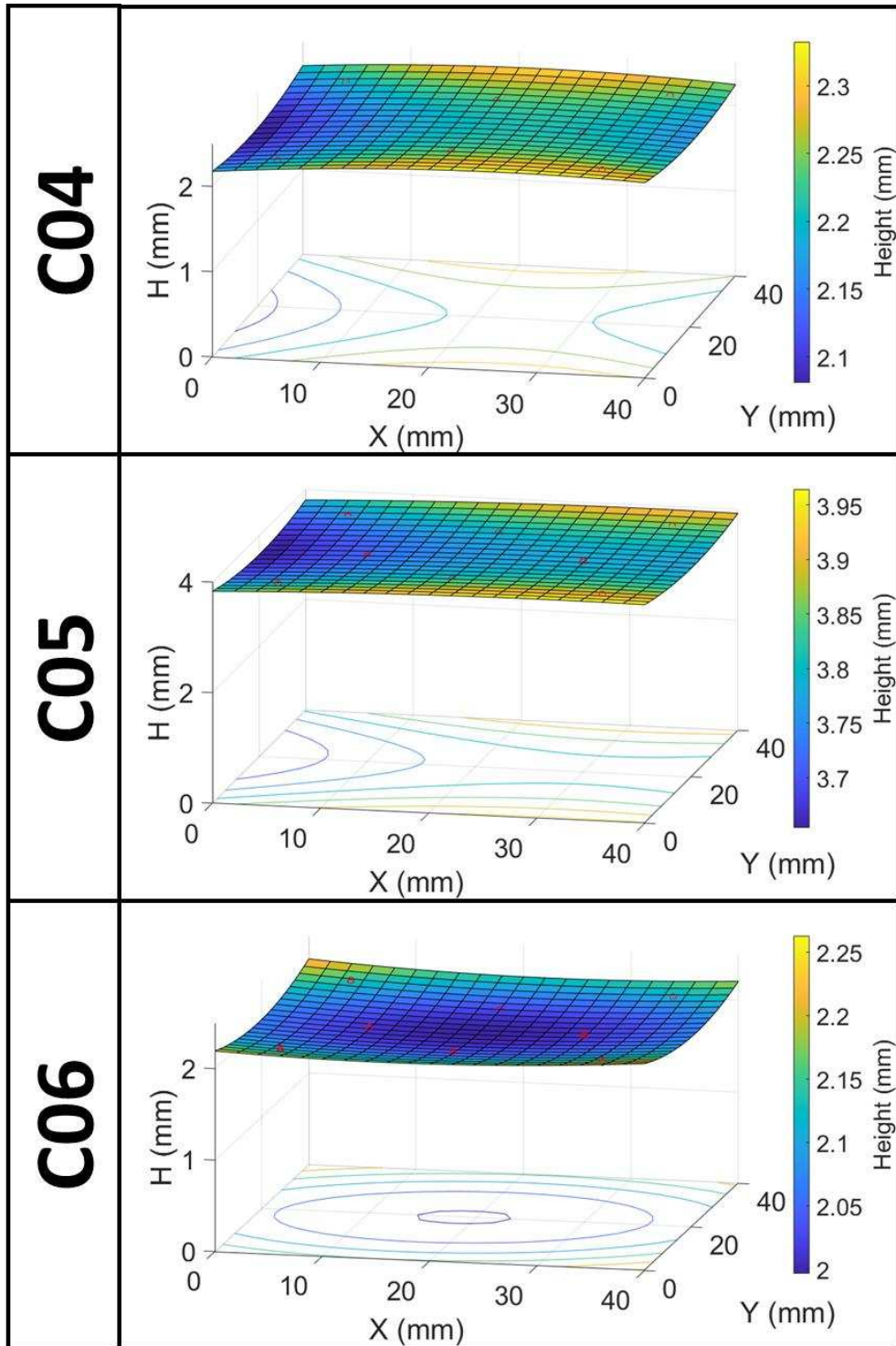


Figure 4-20: Surface plots of measured spatial impingement height for C04 thru C06 test sections.

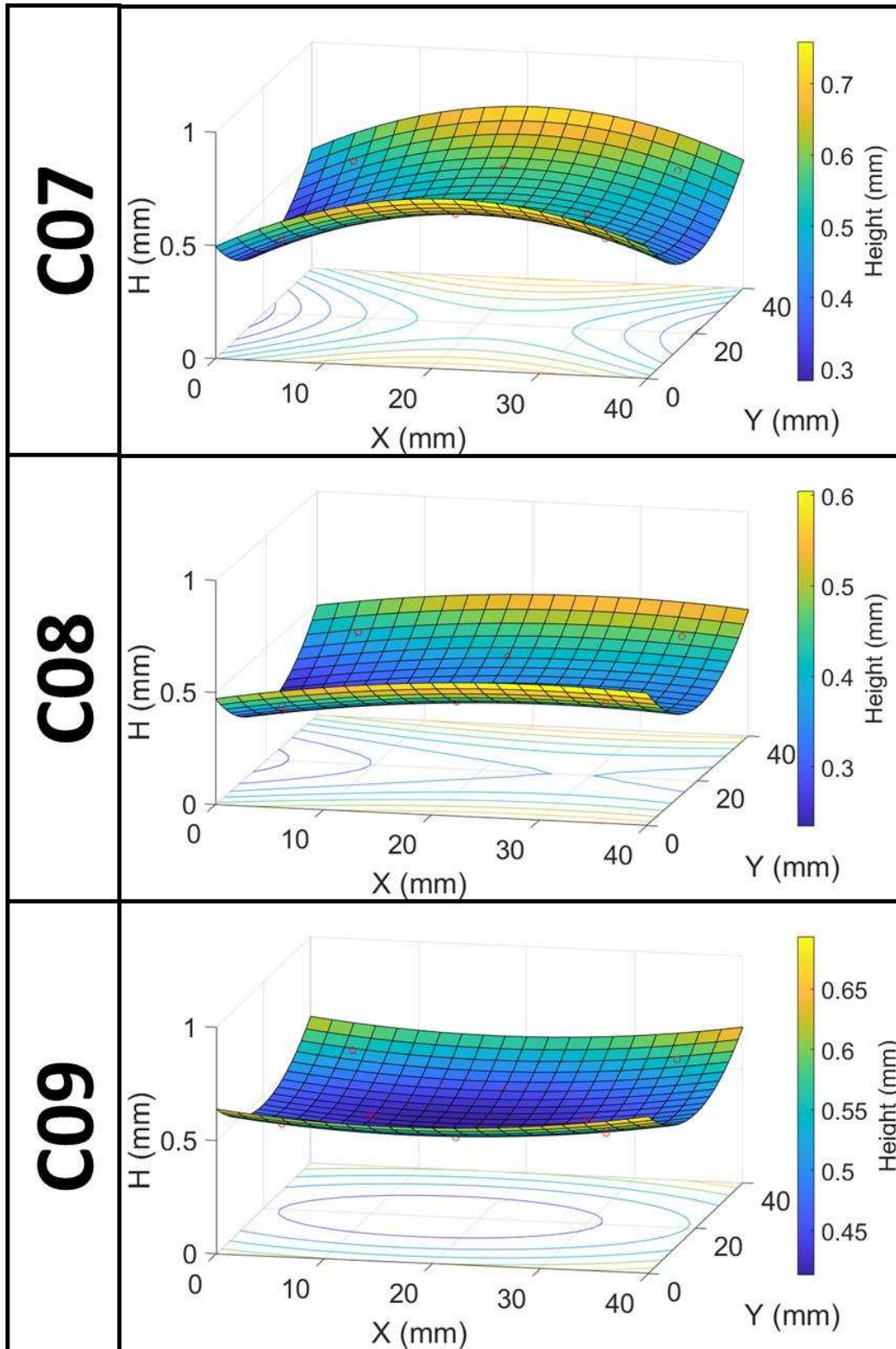


Figure 4-21: Surface plots of measured spatial impingement height for C07 thru C09 test sections.

All measured height (H) and jet and return orifice diameters (D_j , D_r) have been utilized to determine “as-fabricated” key geometric parameters S/D_j and H/D_j . Note that hole spacing was not measured for each fabricated part. This is because the average hole spacing can be defined as the impingement target surface area divided by the total number of jets. The target surface area is well controlled (CNC machined to tight tolerances) and constant for each part. From this definition, clearly even if local jet-to-jet spacing varies, the average jet spacing across the full array will definitionally be equal to the as-designed spacing, within the tolerances of the machined target surface. Thus, hole spacing measurement was determined to be unnecessary for establishing core parameter values.

As-designed and as-fabricated non-dimensional spacing and non-dimensional height values are provided for all nine configurations in Figure 4-22. Some as-fabricated configurations are geometrically quite different from their prescribed state, thus highlighting the importance of

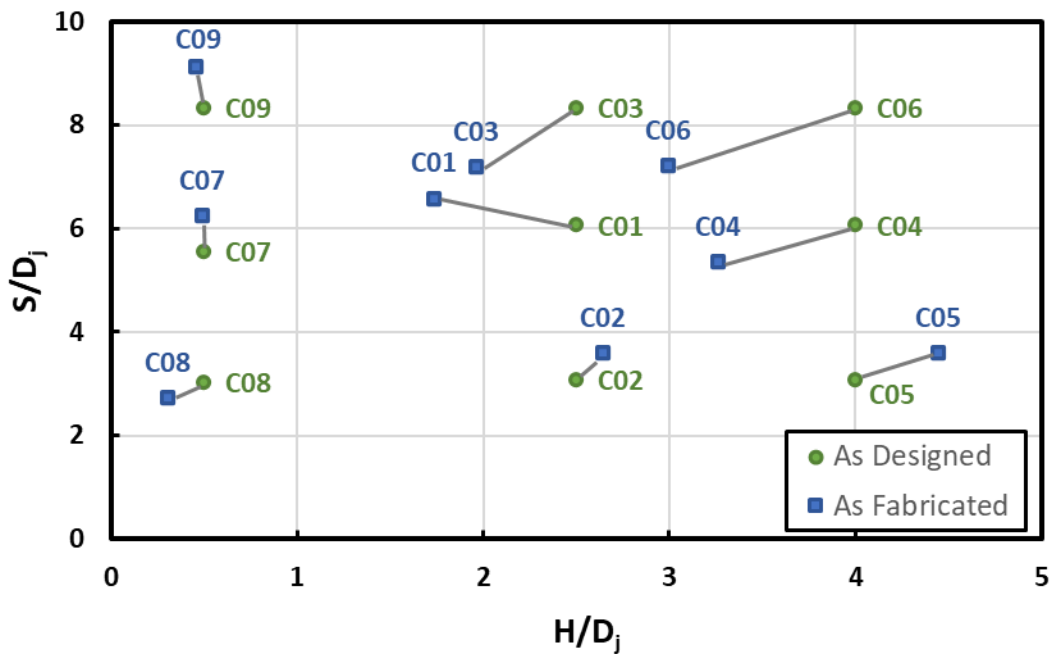


Figure 4-22: As-designed and as-fabricated values for key geometric parameters (S/D_j , H/D_j)

conducting post-production geometric validation. Overall, the as-fabricated geometry set covers a similar range of S/D_j and H/D_j parameters as was designed. A slightly wider range of H/D_j is accommodated from a minimum of 0.31 (part C08) to a maximum of 4.4 (part C05). Similarly, the S/D_j range has been extended slightly, now spanning from 2.7 (part C08) up to 9.1 (part C09). The geometry region including both high H/D_j and high S/D_j values was contracted somewhat from the design state. As planned, the nine as-fabricated impingement test sections cover a broad and diverse range of jet spacing and jet height parameters.

4.2. Gen II Surrogate Heater

To accommodate the second-generation impingement device, a complementary Gen II surrogate heater was constructed. The function of the Gen II surrogate heater is the same as that of the Gen I surrogate heater described in Chapter 3. The device serves as a target surface for the jet impingement cooling test sections. It must be capable of delivering a controlled and uniform heat

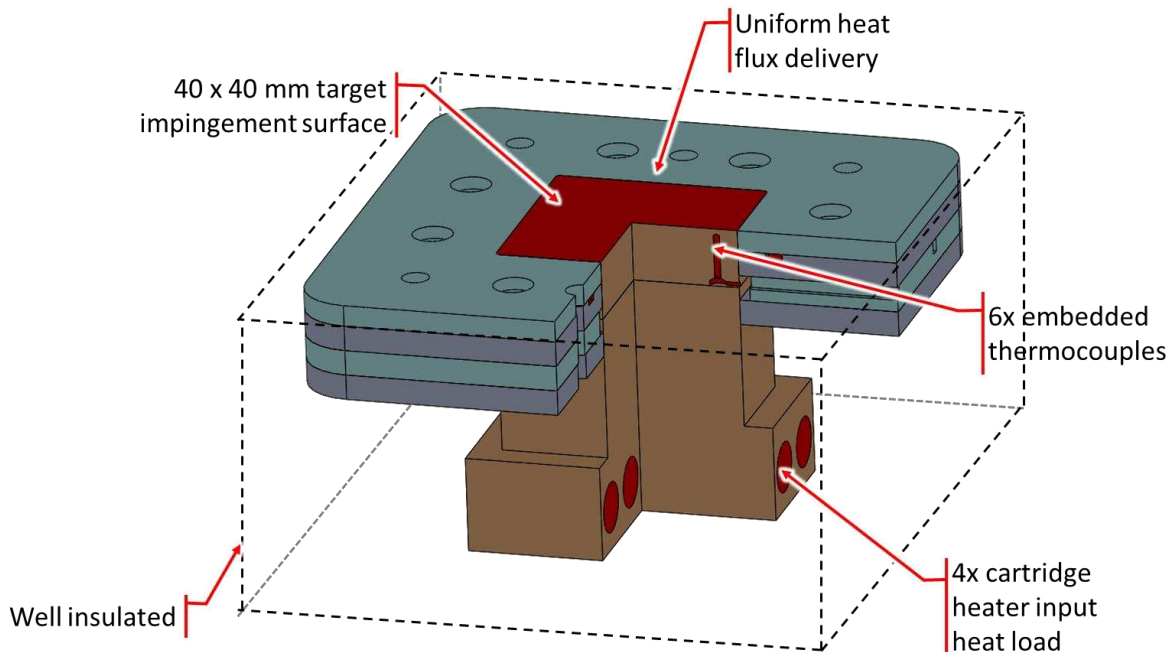
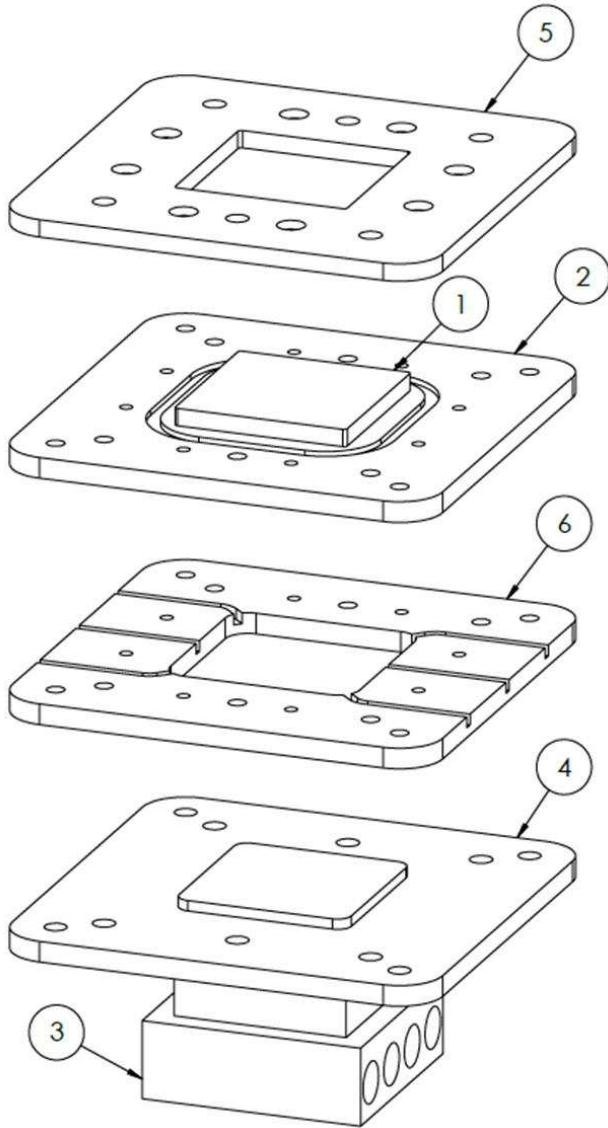


Figure 4-23: Partial cut-away solid model of Gen II surrogate heater.



Part	Description	Material
SH01	Target block	110 Cu
SH02	Upper mounting flange	316 SS
SH03	Heater block	110 Cu
SH04	Lower mounting flange	316 SS
SH05	Top plate	PTFE
SH06	Flange washer	PTFE

Figure 4-24: Exploded view of Gen II surrogate heater

flux while maintaining a fluidic seal. In this section, the generation II surrogate heater design and functionality will be described in detail.

4.2.1. Design, functionality, and fabrication

A 3D model of the Gen II surrogate heater is provided in Figure 4-23 with several key features highlighted. The second-generation surrogate heater consists of six separate pieces which are shown and labeled in the exploded view in Figure 4-24. The top square surface, shown in red

in Figure 4-23, is the impingement target cooling surface. It is a 40 mm by 40 mm surface at the top of part SH01 and is made of copper. The primary function of the surrogate heater is to deliver a uniform heat load to that surface. Four cartridge heaters are inserted into the four cavities highlighted in red at the bottom of part SH03. These cartridge heaters are driven in parallel by an external power supply, thus producing a heat load to the surrogate heater device. The primary conduction pathway is from the four cartridge heaters, upwards through the copper heater block (SH03), through the copper target block (SH01) and to the target surface. The cartridge heaters are custom made by Nordic Sensors. Each one contains an embedded type J thermocouple and is rated for 350 W at 40V. Thus, with a properly sized power supply, the Gen II surrogate heater is capable of delivering 1400 W of heat to the target surface. Specifications for the cartridge heater can be found in Figure 4-25.

The upper mounting flange (SH02) serves primarily as a rigid attachment point for mounting the impingement test section to the surrogate heater surface. The six 10-32 top mounting screws shown in Figure 4-3 are threaded directly into six tapped holes in part SH02. The lower mounting flange (SH04) served to temporarily mount and align the heater block (SH03) with the target block (SH01) during the fabrication process. Both mounting flanges are made of 316 stainless-steel and are plated in nickel. 316 stainless-steel was selected because it is rigid (allowing for reliable test section mounting without deflection), corrosion resistant, metallic, and much less thermally conductive than copper. Components SH01 and SH02 could have been machined as a unitary component out of a single piece of copper (same as with SH03 and SH04), however, the high thermal conductivity of copper would allow for increased heat spreading outward through the flange, which is undesirable. Instead, 316 stainless-steel has approximately one order of magnitude lower thermal conductivity than copper, thus limiting heat spreading through the flange. Of course,

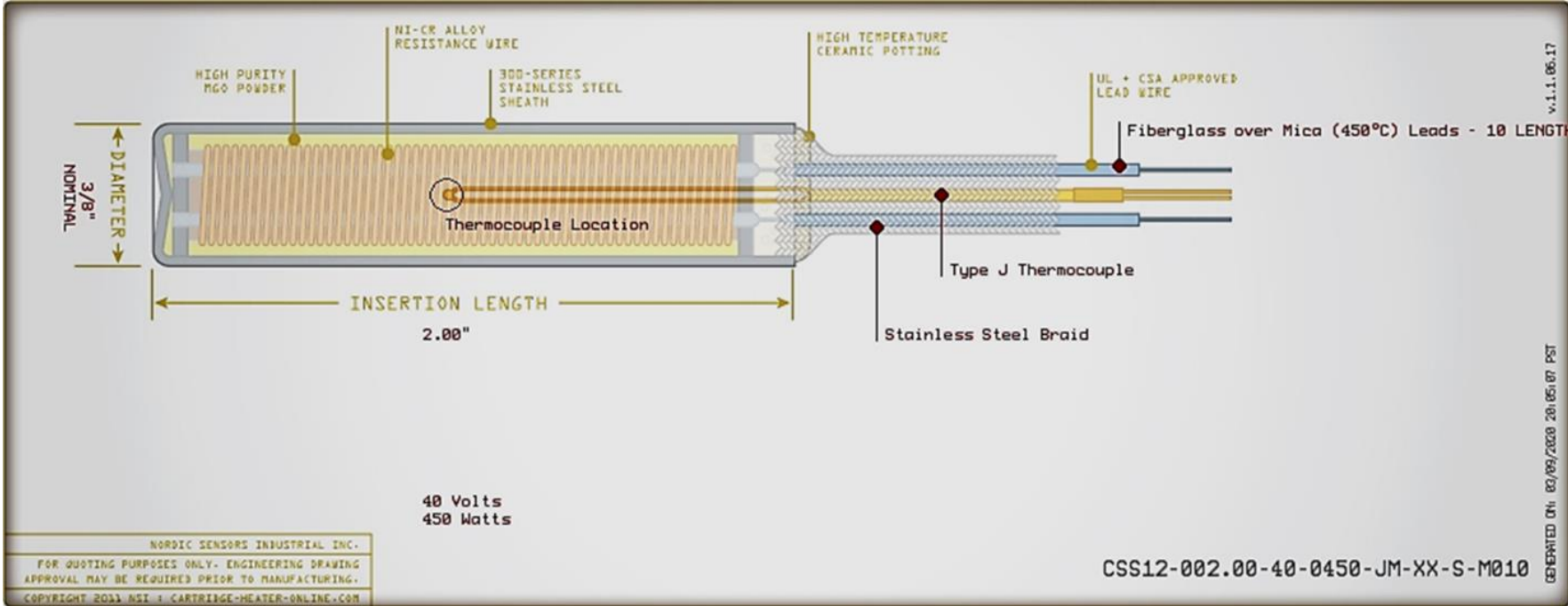


Figure 4-25: Cartridge heater specifications

a plastic or ceramic flange could have reduced heat spreading even further but plastic would be far less rigid, and ceramics are difficult to machine and present a risk of fracture. Furthermore, using a metallic material offers the opportunity to use soldering and brazing techniques for attachment. By nickel plating the stainless-steel pieces, they could be securely and hermetically joined to their respective copper pieces by brazing, without the need for any gaskets or complicated fastening. Part SH02 was brazed directly to part SH01 and part SH04 was brazed directly to part SH03. Clamping force was applied between the impingement test sections and the target block (SH01) by six 10-32 screws which passed through the impingement test section and were threaded into complementary holes in the upper mounting flange (SH02) which is rigidly attached to the target block (SH01) through the aforementioned brazed joint.

The top plate (SH05) was machined from PTFE and serves two main functions. The first is to act as an insulation layer between the upper mounting flange (SH02) and the impingement device/ambient. PTFE, being easy to machine, having a high melting point, and having a low thermal conductivity (more than three orders of magnitude less than copper), serves as a good insulating structural material for this application. The second main function of part SH05 is to serve as a sealing face for the impingement test section. The impingement cooler is sealed onto the top plate by a -036 O-ring seated into an O-ring groove in the bottom side of the impingement device. The square window in SH05 is tightly fit around the target block (SH01) and SH05 is mounted to SH02 via eight 4-40 screws which sit fully below the top surface of the PTFE plate. A second -036 O-ring is seated into the groove in SH02, forming a hermetic seal between the parts. The PTFE flange washer (SH06) simply serves as an insulation layer between the two stainless-steel flanges. It is loosely fit with various machined pathways and thru-holes to avoid interference

with thermocouples and fasteners. Part SH06 is bisected (not shown) so that it can be inserted or removed after final assembly. A more elaborate exploded view of the full combined surrogate heater and impingement cooler assembly can be seen in Figure 4-26.

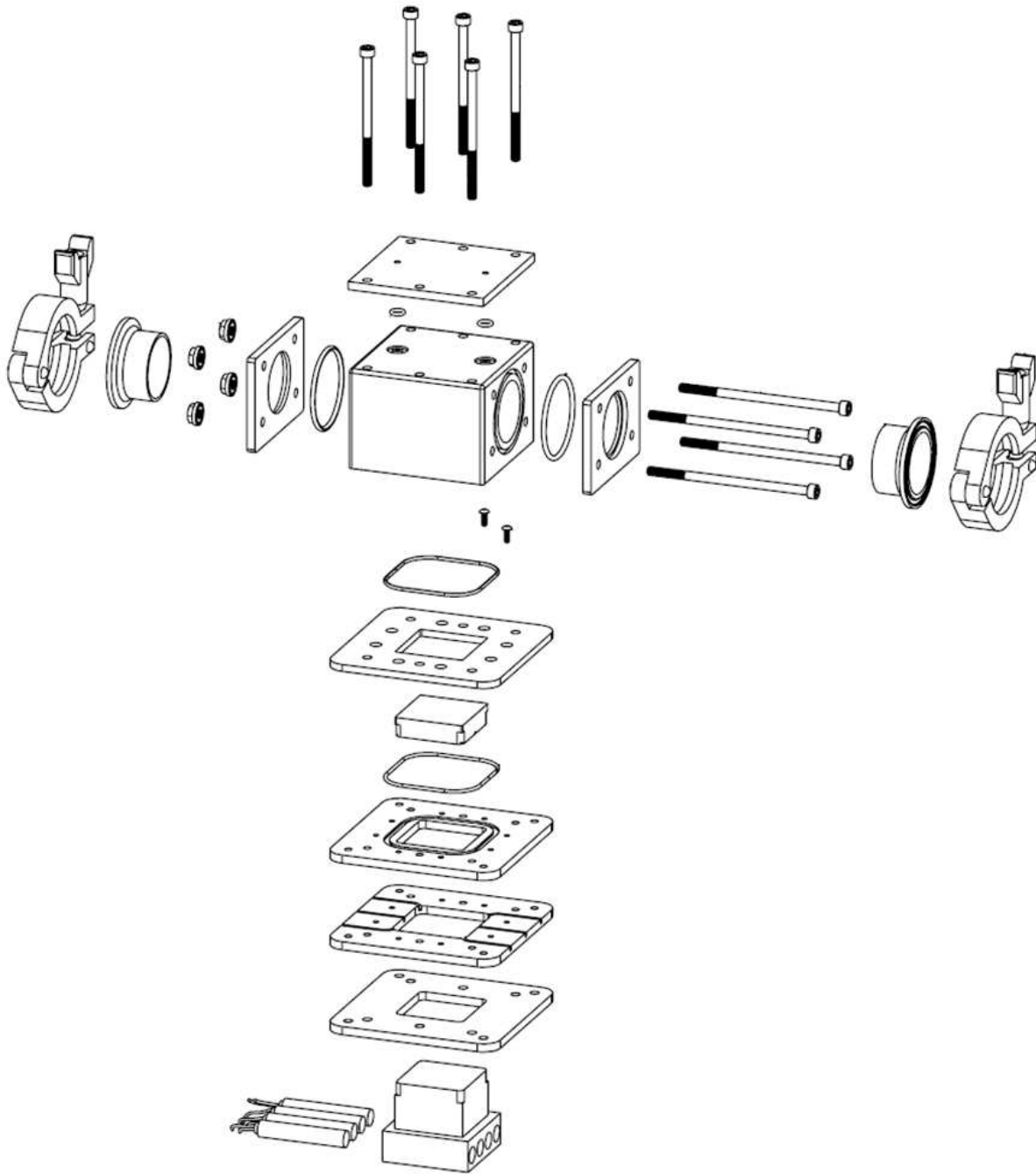


Figure 4-26: Exploded view of Gen II surrogate heater and impingement device assemblies

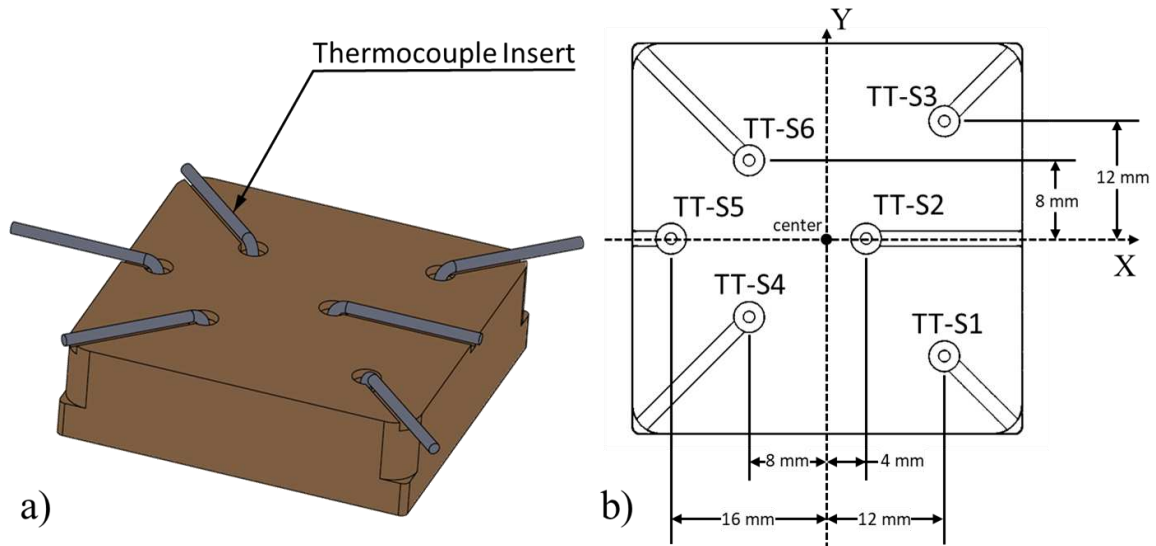


Figure 4-27: Target block embedded thermocouples. a) solid model view, b) thermocouple locations and labels.

Six type J thermocouples are embedded into the bottom side of the target block (SH01). A cut-away view of one thermocouple cavity is highlighted in red in Figure 4-23. Figure 4-27 provides another view of the surrogate heater target block. In a) a solid model is shown of the bottom side of the target block (SH01) with six bent thermocouples protruding out of the six probe holes. The thermocouples were labeled as TT-S1 thru TT-S6 and their locations are given in b). The thermocouples are shielded, 1 mm diameter type J probes from Omega Engineering. They are mounted at a depth of 0.9 mm below the target surface. To improve thermal contact between the thermocouples and the copper, they were nickel-plated and soldered into place. Solder paste was used to fill the entire thermocouple cavity and was heated in a reflow oven to make the bond. The thermocouples were ordered with ceramic connectors rather than plastic ones so that they could withstand the soldering process. All six thermocouples were calibrated in their assembled positions after complete fabrication of the Gen II surrogate heater.

The heater block (SH03) was soldered directly to the target block (SH01) to provide excellent thermal contact and mechanical attachment between the two components. All four

cartridge heaters were similarly soldered into place after being nickel plated. The Gen II surrogate heater device was fabricated by the Rapid Prototyping and Applied Engineering Lab (RPL) at the Powerhouse Energy Campus at Colorado State University. A photograph of the fabricated heater with no insulation is provided in Figure 4-28a.

After being fabricated, the surrogate heater was thoroughly insulated to prevent heat from leaving via secondary thermal pathways besides the impingement target surface which is actively cooled by an impingement device during testing. All surfaces of the surrogate heater, with the exception of the top surface where the impingement part is mounted, were covered by fiberglass

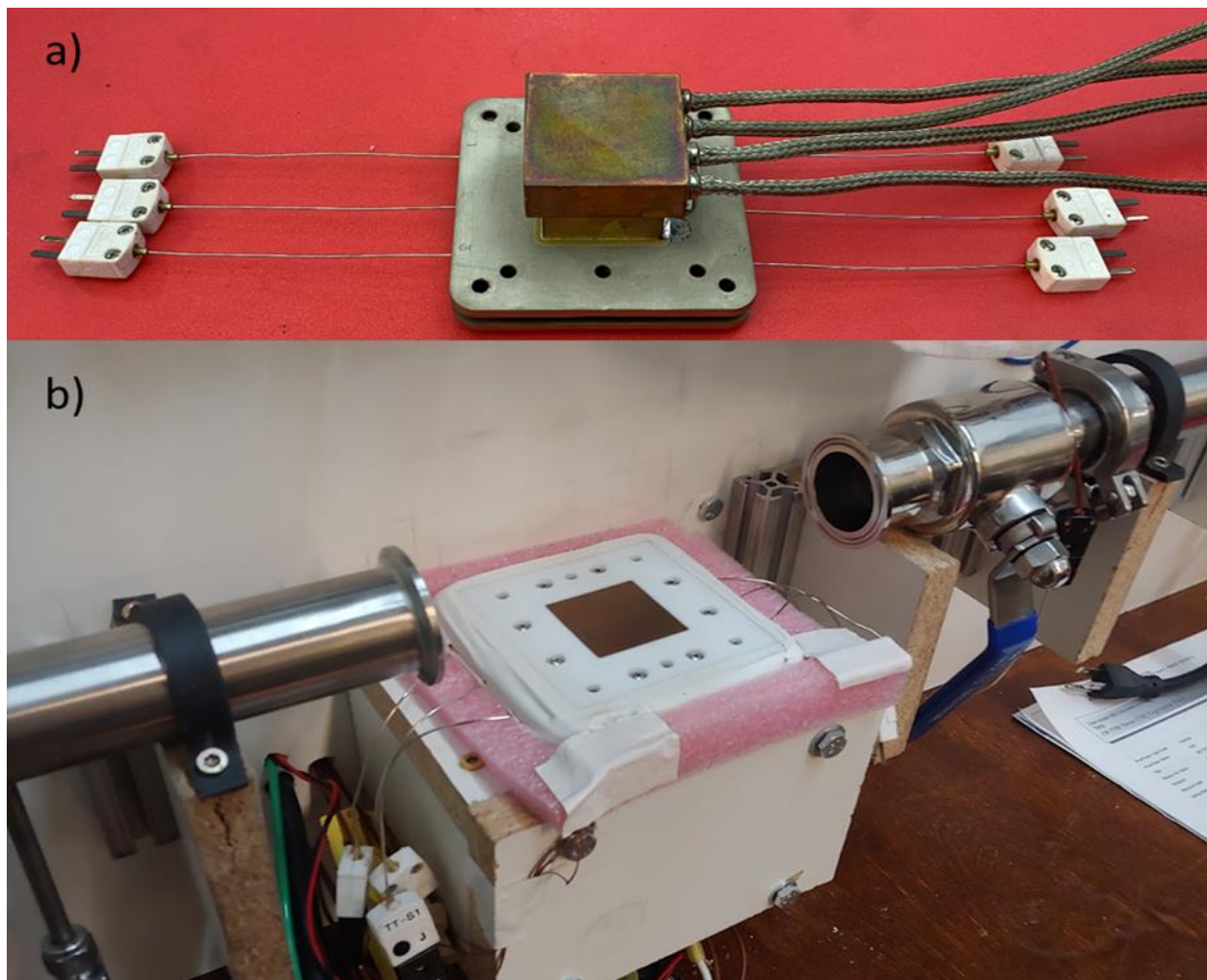


Figure 4-28: Fabricated, fully soldered surrogate heater (a) without insulation and (b) mounted, mostly insulated but without an impingement device.

tape and a layer of nominally 3/16” thick fiberglass reinforced Aerogel insulation with a reported R-value of $1.23 \text{ K m}^2 \text{ W}^{-1}$ [78]. A single layer of the Aerogel insulation is sufficient on its own to provide a thermal resistance of roughly 80 K W^{-1} . Where space allowed, a second layer of Aerogel insulation was applied. The insulation was held in place by an additional layer of fiberglass tape. A box was constructed of 3/4” thick melamine fiberboard and the surrogate heater was placed inside along with loosely packed mineral wool insulation material. After each impingement test section

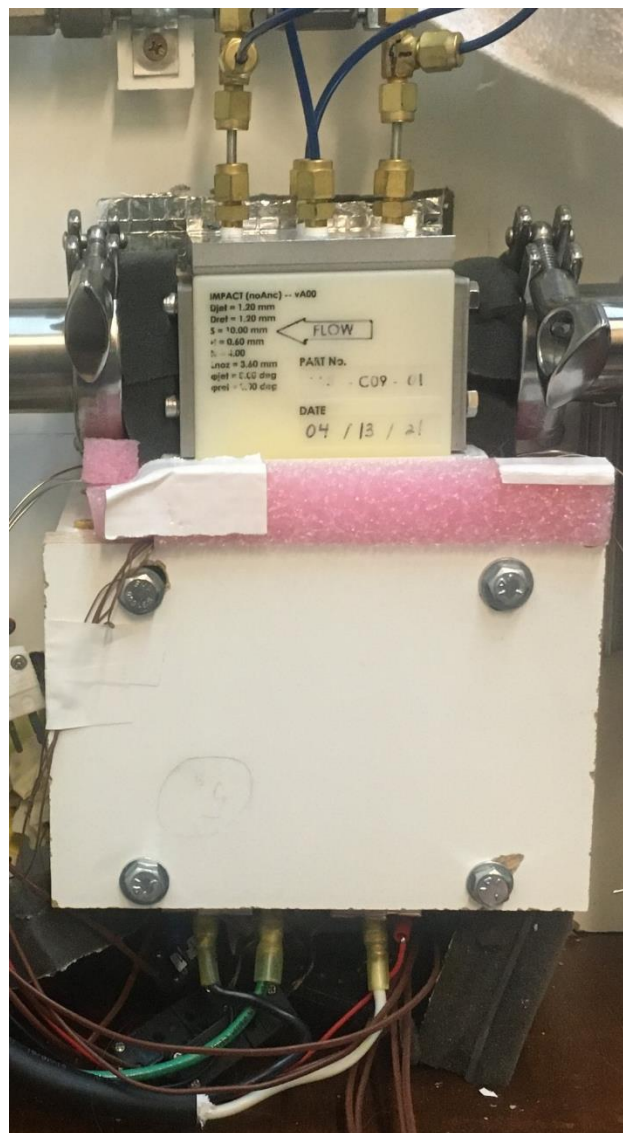


Figure 4-29: Mostly insulated surrogate heater assembly with C09 impingement test section mount on top

was mounted, the entire assembly was surrounded by additional insulation material. Figure 4-28b depicts the surrogate heater mounted in place and mostly insulated. Figure 4-29 shows the same with an impingement test section mounted onto the surrogate heater. Some insulation across the front and top of the assembly, surrounding the impingement device, are missing in the photograph.

4.2.2. Thermal uniformity

Similar to the first-generation surrogate heater described in Section 3.2, it was important for the Gen II surrogate heater to provide a uniform heat load to the target surface. Care was taken during the design process to ensure that this would be the case. A steady state thermal FEA model of the Gen II surrogate heater was set up in Ansys Fluent prior to fabrication. The model was constructed such that a heat load would be applied to the device via the cartridge heater cavities and a constant heat transfer coefficient was applied to the 40 mm by 40 mm target surface. Additionally, a modest heat transfer coefficient was applied to the remaining surfaces with modest insulation applied. In order to investigate the effect of varying fluid temperatures, impingement heat transfer coefficients, total applied heat loads, and differences in heat load applied by each distinct cartridge heater (e.g., the four cartridge heaters might supply 11, 9, 12, and 8 W for a total of 40 W), a parametric study was carried out in which each of the parameters was varied and the target surface thermal profile was calculated. A Taguchi design of experiments [79] was employed to investigate a wide range of parameters while maintaining a reasonable number of simulations. Five levels were applied to each variable with heater power ranging logarithmically from 14 W up to 1400W, variation between heaters ranging linearly from 0% up to 20%, heat transfer coefficient ranging logarithmically from $400 \text{ W m}^2 \text{ K}^{-1}$ up to $40000 \text{ W m}^2 \text{ K}^{-1}$, and fluid temperature ranging linearly from 15°C up to 85°C . Twenty-five distinct cases were simulated in accordance with the Taguchi design and key uniformity metrics were reported.

Graphical results of a single exemplary case are provided in Figure 4-30. The surface heat flux contour in a) distinctly shows that the heat flux through target surface in this case is several orders of magnitude greater than the heat flux passing through the PTFE top plate. The temperature profile in b) provides more granularity over the target surface. In this case the difference between the minimum and maximum temperatures on the target surface is less than 0.1 °C. Across all 25 cases which were simulated, the total variation in temperature across the target surface never exceeded 0.2% of the average absolute surface temperature. Table 4-5 provides temperature uniformity results for all 25 simulated cases. Conditional formatting has been applied to the simulation input variables to better highlight the combination of values dictated by the Taguchi design. Given this result, it was determined that the surrogate heater design would produce substantially uniform heating over a wide range of conditions. Thus, the design was approved and deployed.

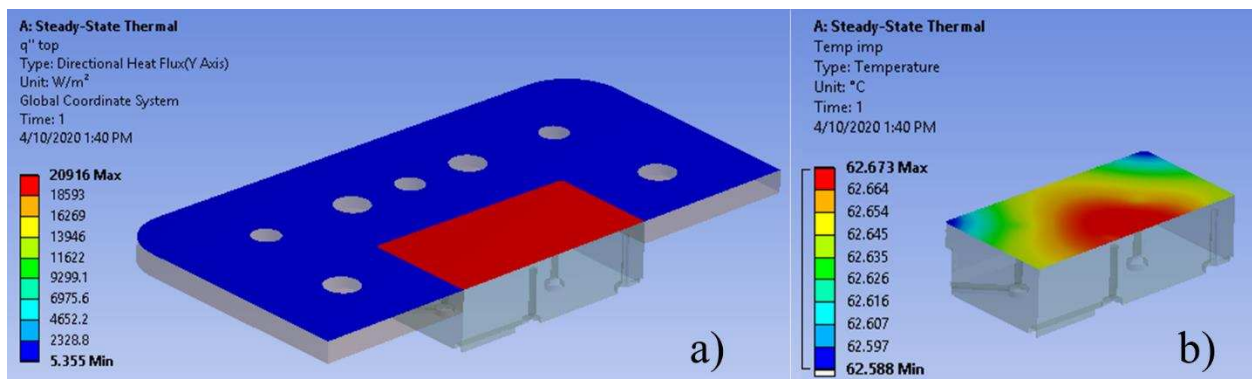


Figure 4-30: Exemplary thermal simulation results for surrogate heater uniformity study. a) Heat flux contour of the surrogate heater top surface for both SH01 and SH05. b) temperature profile of impingement target surface only.

Table 4-5: Surrogate heater uniformity Taguchi thermal simulation results.

Sim num (-)	Taguchi simulation input variables				Simulation outputs			
	Heat load (W)	Heater variance (%)	Applied HTC (W/m ² K)	Fluid inlet temp (K)	Target surface temp			
					min (K)	max (K)	ave (K)	var (%)
1	14.0	0.0%	400	288.2	307.1	307.1	307.1	0.01%
2	13.9	5.4%	1265	305.7	311.2	311.3	311.3	0.01%
3	13.7	12.9%	4000	323.2	324.6	324.6	324.6	0.01%
4	14.4	21.1%	12649	340.7	341.0	341.0	341.0	0.02%
5	12.7	19.1%	40000	358.2	358.2	358.2	358.2	0.02%
6	44.3	0.0%	1265	323.2	341.4	341.5	341.4	0.02%
7	42.8	6.4%	4000	340.7	346.0	346.1	346.1	0.02%
8	49.8	19.8%	12649	358.2	360.1	360.1	360.1	0.02%
9	41.1	12.1%	40000	288.2	288.8	288.8	288.8	0.00%
10	38.8	19.5%	400	305.7	352.4	352.5	352.4	0.03%
11	140.0	0.0%	4000	358.2	377.8	378.0	377.9	0.04%
12	133.2	2.0%	12649	288.2	294.7	294.7	294.7	0.02%
13	128.9	16.1%	40000	305.7	307.6	307.6	307.6	0.02%
14	126.6	15.0%	400	323.2	476.8	477.1	477.0	0.06%
15	137.5	19.9%	1265	340.7	400.2	400.4	400.3	0.04%
16	442.7	0.0%	12649	305.7	327.0	327.2	327.1	0.06%
17	448.6	6.2%	40000	323.2	329.9	330.1	330.0	0.05%
18	430.2	11.9%	400	340.7	872.2	873.1	872.7	0.10%
19	456.7	4.6%	1265	358.2	562.3	562.7	562.6	0.09%
20	449.3	25.3%	4000	288.2	356.3	356.7	356.5	0.12%
21	1400.0	0.0%	40000	340.7	361.9	362.4	362.2	0.13%
22	1406.5	8.0%	400	358.2	2112.5	2115.2	2114.1	0.13%
23	1424.7	7.2%	1265	288.2	939.1	940.4	939.9	0.14%
24	1427.0	8.3%	4000	305.7	521.4	522.3	521.9	0.16%
25	1523.0	12.5%	12649	323.2	396.7	397.5	397.2	0.20%

4.3. Test Facility

A new test facility was constructed to accommodate the new impingement devices and new surrogate heater. Figure 4-31 provides an overview of the test facility. In the upper right, a very simplified process and instrumentation diagram describes the basic functionality of the test apparatus. An impingement device test section is mounted to the surrogate heater and fluid is delivered to the impingement device via some fluid delivery mechanism (a pump for liquids and a compressor for air). Upon exiting the impingement device, the fluid is exhausted in which case it either recirculates or, in the case of air, is dumped to ambient. Fluid flow rate is measured upstream of the impingement test section. Inlet fluid temperature and absolute pressure are measured at the device inlet via the P1 instrumentation port shown in Figure 4-4. Temperature of the spent fluid is measured on the downstream side of the test section via the P4 instrumentation port. Differential

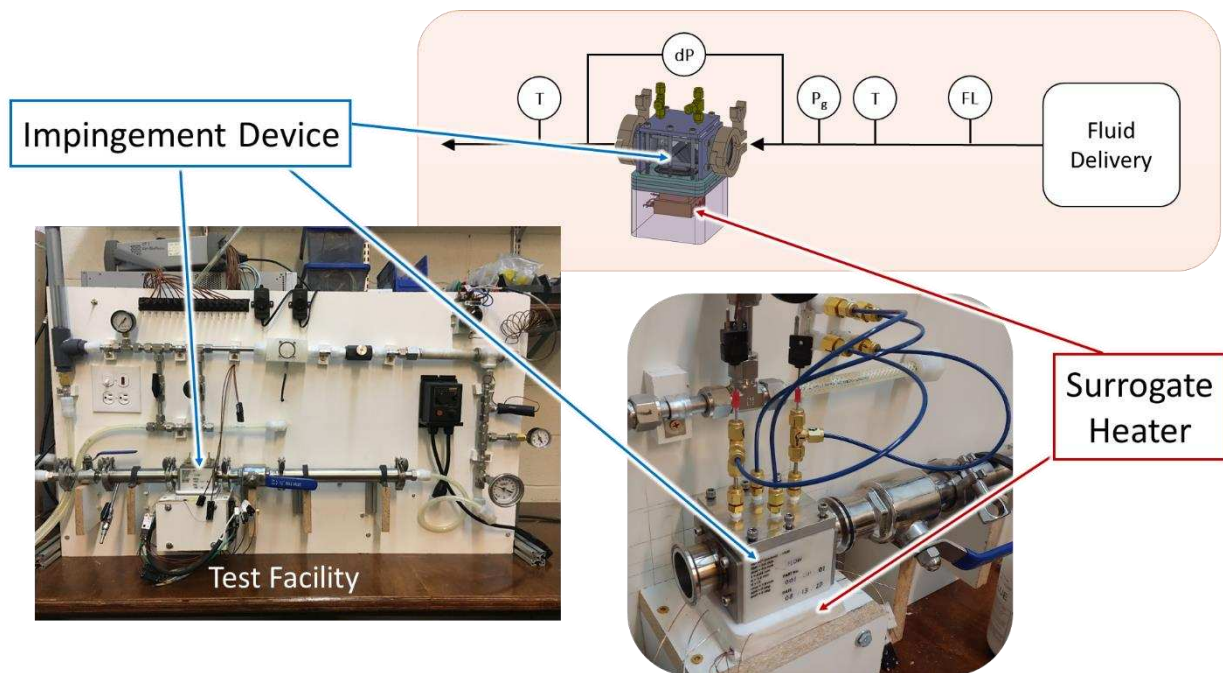


Figure 4-31: Overview of impingement test facility

pressure is measured across the impingement device via all four embedded instrumentation ports in the arrangement described in Section 4.1.1. The photograph in the lower left of Figure 4-31 displays the constructed test facility as configured for liquid testing and the photograph in the lower right provides a close-up view of the impingement test section mounted in place. Not shown in this figure is a centrifugal pump, which sits below the test facility, an in-line 5 μm filter attached downstream of the pump, and a radiator situated onto the backside of the mounting board. The process and flow diagram in Figure 4-32 provides a more detailed account of components in the test facility in the liquid test configuration. Note that the majority of instrumentation is attached directly to the impingement test section and the surrogate heater including multiple pressure,

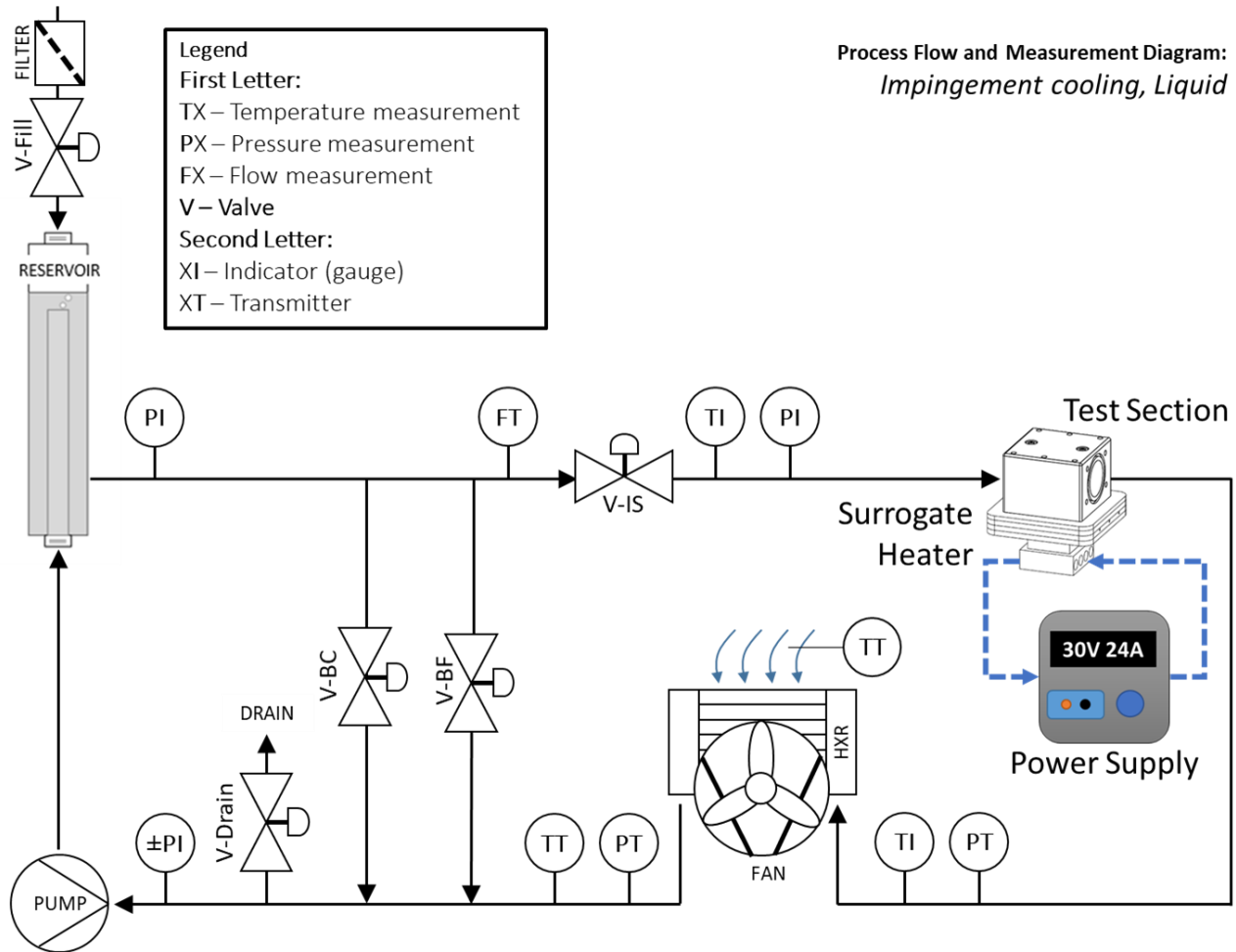


Figure 4-32: Detailed process and instrumentation diagram of impingement test facility in liquid testing configuration

temperature, and voltage measurements, as discussed in sections 4.1 and 4.2. The surrounding test facility serves only as means of providing controlled power and flow to the central test section and surrogate heater components. Before operation, the complete facility is evacuated and filled with the working fluid. The working fluid is drawn through a 3 μm filter as it enters the system through the top of the liquid reservoir. The reservoir serves dually as a bubble trap for any air that is leftover or inadvertently enters the system.

Because almost all key instrumentation is connected directly to the impingement test section and the surrogate heater, the liquid test facility can be easily reconfigured to accommodate air as the working fluid. The impingement piece is simply detached from the rest of the liquid test section and connected to a shop air compressor line with a separate flow meter. A process diagram of the air testing configuration of the test facility is provided in Figure 4-33. In this configuration, there is no need to recirculate the air, so it is exhausted directly to ambient.

In both the liquid and air testing configuration, a key attribute of the impingement test section is how flow is managed immediately upstream and immediately downstream of the test section. The impingement device offers a circular 1.5" inlet and outlet for fluid attachment. Tri-clover fittings and piping connected to either end of the surrogate heater provide a straight continuous section of 1.5" flow diameter for more than 10 pipe diameters upstream and more than 4.5 pipe diameters downstream of the test section. This ensures that the flow entering the test device is uniform, fully developed, and slow moving compared to the impinging jets and thus, does not impact flow distribution to the impinging array.

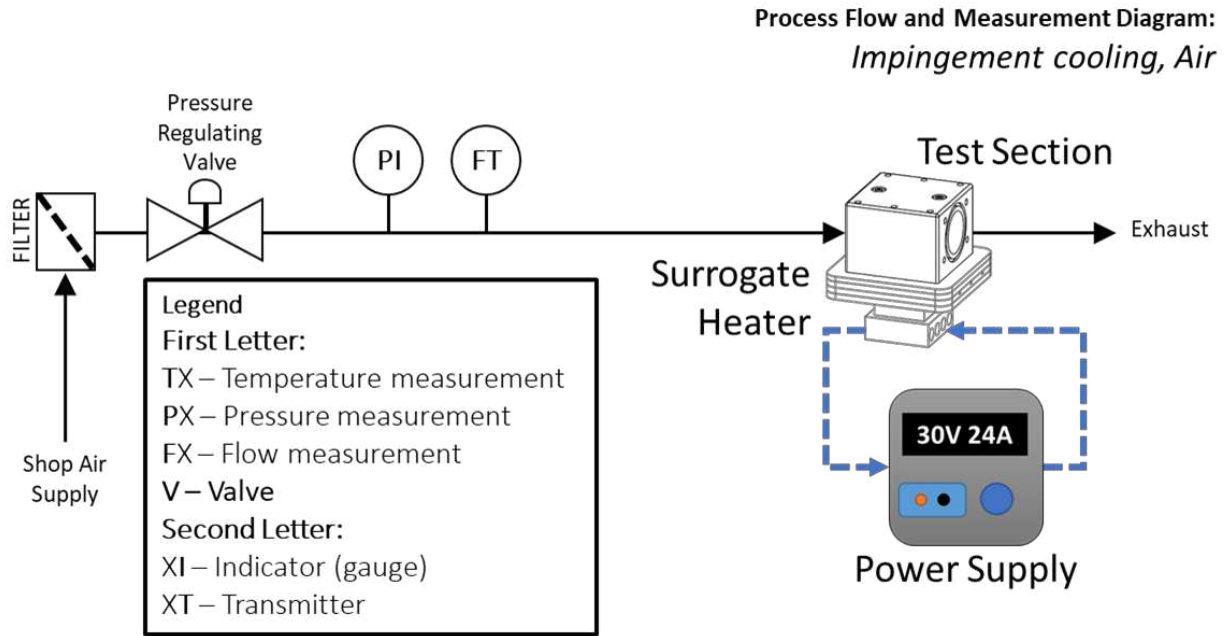


Figure 4-33: Detailed process and instrumentation diagram of impingement test facility in air testing configuration

4.3.1. Instrumentation

All pertinent instrumentation will be discussed in this section. Instrumentation can be classified into power delivery, fluid flow rate, fluid state (temperature and pressure), and surrogate heater temperature state categories. All measurements were logged using a Keysight 34972A data acquisition unit outfitted with two 34901A 20-channel multiplexers.

Power delivery:

Power was delivered to the Gen II surrogate heater device using a high accuracy Keysight N6972A power supply. The N6972A has a maximum output of 40 V and 50 A with a total maximum output power of 2 kW. A software safety feature limits the power output to only 700 W when the supply is connected to a standard 115 VAC circuit, with the full 2 kW capability available only when connected to a 230 VAC circuit. In this setup, the power supply was connected to a 115 VAC circuit, effectively limiting power output to 700 W.

Surrogate heater power was calculated as $q_{app} = IV$, where the power supply output current, I , was set programmatically by the N6972A. The N6972A is capable of maintaining an output current set point with an accuracy of 15 mA plus 0.1% of the set point value. This current was taken directly for calculating heater power. The surrogate heater voltage, V , was measured using the 34972A DAQ directly across the cartridge heater terminals to minimize error due to line losses between the power supply and the surrogate heater. The voltage measurement accuracy is range dependent and can be found in the 34972A technical documentation. Over the full range of measurements, the voltage measurement uncertainty was always less than 0.01% of the voltage reading. By propagating uncertainty for both voltage and current measurements, it was determined that power delivery uncertainty was always less than 0.6% ($\pm 0.3\%$) of the calculated power. Power delivery uncertainty could be reasonably approximated between 10 and 1000 W using a power law regression such that $\frac{U_q}{q} \times 100\% = 1.082q^{-0.294}$.

Fluid flow:

For liquid experiments, an FPR301-038 paddle wheel volumetric flow meter was used from Omega Engineering. The flow meter had a range from 0.07 to 5 GPM (0.26 to 19 LPM) with a published accuracy of 1% of the full-scale measurement. Ten diameters of straight pipe was provided upstream of the flow meter with five diameters of straight pipe downstream to ensure a uniform flow profile. For air testing, mass flow rate was measured using a digital mass flow meter from Kelly Pneumatics. The flow meter can measure from 0 up to 300 sLPM with a published accuracy of 2% of the reading or 0.05 sLPM, whichever is greater. Straight pipe was provided for 20 diameters upstream and 10 diameters downstream of the flow meter to maintain uniform flow.

Fluid state:

Fluid temperature was measured at the inlet and outlet of the impingement test section using shielded type J thermocouples. The thermocouples were calibrated against a Fluke platinum RTD standard. Thermocouple calibration took place using a submerged water bath. The water bath was initially filled with ice water and placed on a hot plate with a stir bar which provided continuous fluid mixing throughout the calibration procedure. Thermocouples and the Fluke RTD standard were submerged very closely together within the water bath. The bath was then heated slowly from 0 °C until boiling occurred at approximately 95 °C. At this point, the heating source was turned off the water bath system was allowed to cool down gradually. Data from the thermocouples and the Fluke standard were logged continuously throughout the calibration procedure at regular 30 second intervals. Heating and cooling were done very gradually to avoid measurement hysteresis caused by the differing response rates. The full calibration procedure was conducted over approximately a 16-hour time period with an average heating rate of 0.25 °C min⁻¹ and an average cooling rate of -0.12 °C min⁻¹. The Fluke standard error was 0.024 °C (±0.012 °C) and calibrated thermocouple bias error could be calculated as ±0.038 °C and ±0.046 °C for the test section inlet and outlet thermocouples, respectively.

Other thermocouples were used for reference measurements throughout the liquid process loop. However, none of those measurements were used for subsequent calculations, thus calibration for those instruments was deemed unnecessary.

Absolute fluid pressure was measured immediately upstream of the impingement test section using a PX309-50AI pressure transmitter from Omega Engineering. The PX309 has a 4-20 mA output signal and a 0-50 psia measurement range. The measurement accuracy is ±0.25% (±0.125 psi) of full scale. Device inlet absolute pressure measurements were used exclusively for calculating fluid properties, and not for pressure drop measurements across the impingement

device. Thus, the accuracy of the PX309 was suitable for its function. Other pressure transducers were included throughout the process loop for safety and reference measurements; however, they were not used for calculations and are thus omitted here.

Pressure drop across the P1 to P2, P2 to P3, and P3 to P4 test section embedded instrumentation ports were measured using a total of five Honeywell 24PC series differential pressure transducers. Three different 24PC transducer variations were utilized in three different measurement ranges: 0-0.5 psid (24PCEFA6D), 0-1 psid (24PCAFA6D), and 0-5 psid (24PCBFA6D). Inlet header pressure drop (P1 to P2) was measured using a single 0-0.5 psid 24PC series transmitter. Outlet header pressure drop (P3 to P4) was measured using a single 0-1 psid sensor. Impingement array pressure drop was measured using three pressure transducers (one of each range) situated in parallel. This was done to take advantage of the improved measurement accuracy of the low-range pressure transducers while allowing for the extended range provided by the 0-5 psid transducer. Pressure drop measurements were simultaneously recorded by all three sensors and a single value was extracted based on the most appropriate range for any particular point. All three pressure transducer models have a published maximum best fit straight line uncertainty of $\pm 1\%$ of full scale ($\pm 0.2\%$ typical).

Surrogate heater state:

Temperatures were measured at several locations throughout the surrogate heater. Type J and type K thermocouple were used for all measurements. As was previously mentioned, six type J thermocouples were embedded into the surrogate heater near the target surface. All of these thermocouples were calibrated in place after being fully integrated into the surrogate heater device. The same calibration procedure, as described above, was followed as with the impingement inlet and outlet fluid thermocouples. In this case, the full surrogate heater was submerged in the

calibration bath. Once again, heating and cooling was done gradually over roughly a 16-hour period. The resulting bias error ranged from ± 0.056 to ± 0.065 °C across all six thermocouples. For simplicity, the worst-case uncertainty of ± 0.065 °C may be assumed for all six.

Other thermocouples were situated in various locations in and on the surrogate heater including one thermocouple embedded into each of the four cartridge heaters. These temperature measurements were used primarily for monitoring safety limits as well as for estimating heat losses to ambient through the surrogate heater insulation. Therefore, the standard thermocouple accuracy of ± 2.2 °C was allowable and no calibration was necessary.

4.4. Test Procedures

The following sections describe the test procedures used in this investigation for evaluating heat transfer and pressure drop performance of the return jet impingement test sections.

4.4.1. Heat transfer testing

A simple test procedure was established for heat transfer testing and is summarized visually into five simple steps in Figure 4-34.

1. **Install test section:** An impingement device was selected and installed into the test apparatus.
2. **Set condition:** The test facility was configured to supply a set flow rate of the working fluid to the impingement device and a set heat load to the surrogate heater.
3. **Wait for steady state:** After the conditions were set, they were held until a steady state condition was reached.
4. **Collect data:** Flow, temperature, pressure, and power data were collected at the steady state condition.

5. **Repeat/complete:** Finally, a new flow and heat load set point was selected. This process repeated for several flow rate and heat load conditions, each test section, and for both water and air.

Naturally, the full test procedure is more nuanced than the simplified description given above. Each step of the procedure will be described in further detail here.

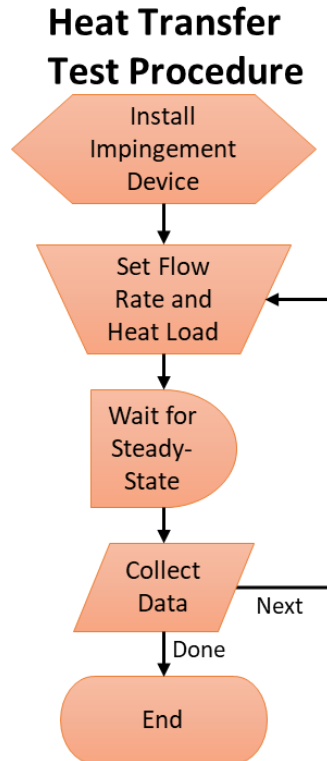


Figure 4-34: Simplified test procedure process diagram for heat transfer testing

Step 1 – Install test section:

The fluid medium was first selected for a particular test as either air, water, or Fluorinert FC3283 dielectric fluid. These three fluids were selected because of their diverse fluid properties and their application towards electronics thermal management. Electronics cooling offers a promising use case for RJI technologies; thus, selecting representative cooling media for that application was deemed appropriate. Air is ubiquitous in electronic cooling and has a low Prandtl

number of nominally 0.7. Water has a Prandtl number of nominally 7 and has seen rapidly growing adoption for electronics cooling. Dielectric fluids have also become increasingly popular because they do not pose a risk of damaging electronic components. Fluorinert FC3283 has a moderate Prandtl number of nominally 23 and a favorable boiling temperature for conducting single phase heat transfer experiments. FC3283 has a boiling point at one atmosphere of 128°C, meaning that phase change during testing was not a risk over the desired range of conditions.

For air testing, the impingement test facility was configured as shown in Figure 4-33 and for liquids it was configured as seen in Figure 4-32. The test section was mounted to the surrogate heater and fluid connections were made to the test facility. In the case of liquid testing, the test section was then evacuated via the drain port and filled with the working fluid. Additional liquid would be added to the system from an external reservoir to replace the volume used to fill the impingement device and nearby attached piping. The system was then operated with no heat load over the full range of flow rates to test for leaks or any other anomalies.

Changing out parts, particularly in the case of liquid testing, or when switching between fluids, could be quite laborious. To alleviate this hassle, whenever a particular test section was installed, it was tested at all prescribed flow rate and heat load conditions before moving on to another part. Similarly, testing was conducted first with air using all test geometries, then with liquids using all test geometries to avoid repeatedly reconfiguring the test facility.

Step 2 – Set condition:

During each test, the flow rate was set at some prescribed value, followed by the heat load. Due to the programmable nature of the N6700 series power supply used to drive the surrogate heater, the heat load could be changed programmatically without real-time human engagement. Flow rate, by contrast, could only be changed manually. To expedite testing, then, a single flow

rate was selected and multiple data points at varying heat loads were collected at that constant flow rate before changing the flow rate and repeating the process. This technique offered the advantage of only requiring direct human interaction with the system occasionally, and not in between every individual test. The system could be set at a single flow rate and programmed to apply several different heat loads then could be passively monitored until completion. This served to dramatically reduce the amount of labor required to produce the hundreds of test points present in this investigation.

Several distinct flow rates were selected for testing; they were nominally 0.3, 0.6, 1.2, 2.4, and 4.8 LPM for liquid testing and 10, 20, 40, 80, 160, and 300 sLPM for air testing. Actual test flow rates deviated marginally from prescribed values. Once a flow rate was set, that system condition would then be held and monitored for several tests at varying heat loads. The number of heat loads applied at each nominal flow rate was not constant and ranged from a single point up to more than a dozen points depending on the part configuration, fluid medium and particular flow rate. Typically, approximately eight heat loads were tested at any prescribed nominal flow rate.

The complete set of flow rate and heat load test conditions is provided in Figure 4-35, segregated by fluid type. The same data is further segregated by impingement part number in Figure 4-36. Heat loads varied depending on fluid medium, part configuration, and flow rate and are well distributed. Air tests were conducted with heat loads ranging nominally from 1 W to 100 W. Liquid tests covered a range of heat loads from approximately 30 W to 700 W. The prescribed air and liquid flow rates are easily distinguishable in Figure 4-35 and Figure 4-36 as distinct rows, evenly spaced on a logarithmic scale. The maximum heat load tested for any particular flow rate was limited to maintain the system below certain maximum safety operating conditions. There were three conditions which limited the maximum operating power: target surface temperature,

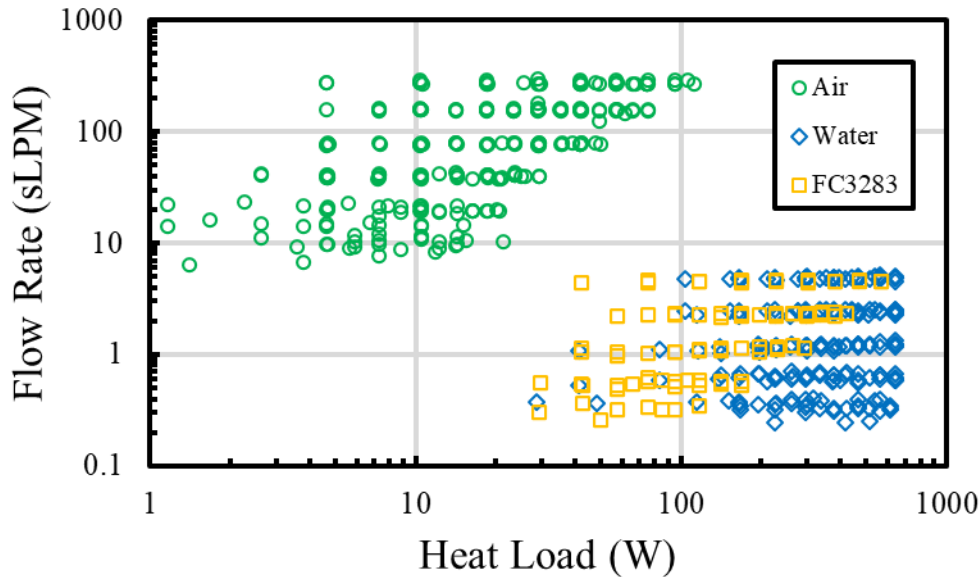


Figure 4-35: Complete set of flow and heat load conditions for heat transfer testing segregated by fluid type.

cartridge heater temperature, and the power supply delivery limit. The target surface temperature was controlled not to exceed 90 °C. This limit was set to avoid any potential phase change in the liquid or thermal damage to the impingement test sections and was often the limiting factor on maximum heat load. The cartridge heaters embedded in the surrogate heater were controlled to not exceed 160°C to avoid reflow of any of the solder joints. The minimum solder melting temperature (multiple different solders were used for different joints) was 181 °C. This limit sometimes confined the maximum heat load. The final limitation was the delivery power of the N6700 series power supply which was set at 700 W. This factor often limited the heat load during water tests, indicated by the right-most points in each row (flow rate) of water data in Figure 4-35 which all reach approximately the same heat load. By contrast, the right-most points in each row of air and FC3283 data reach progressively higher heat loads as flow rate is increased, indicating where temperature limits were reached. With consideration to these limitations, test heat loads were chosen arbitrarily to cover a diverse range within the safe and measurable operating envelope.

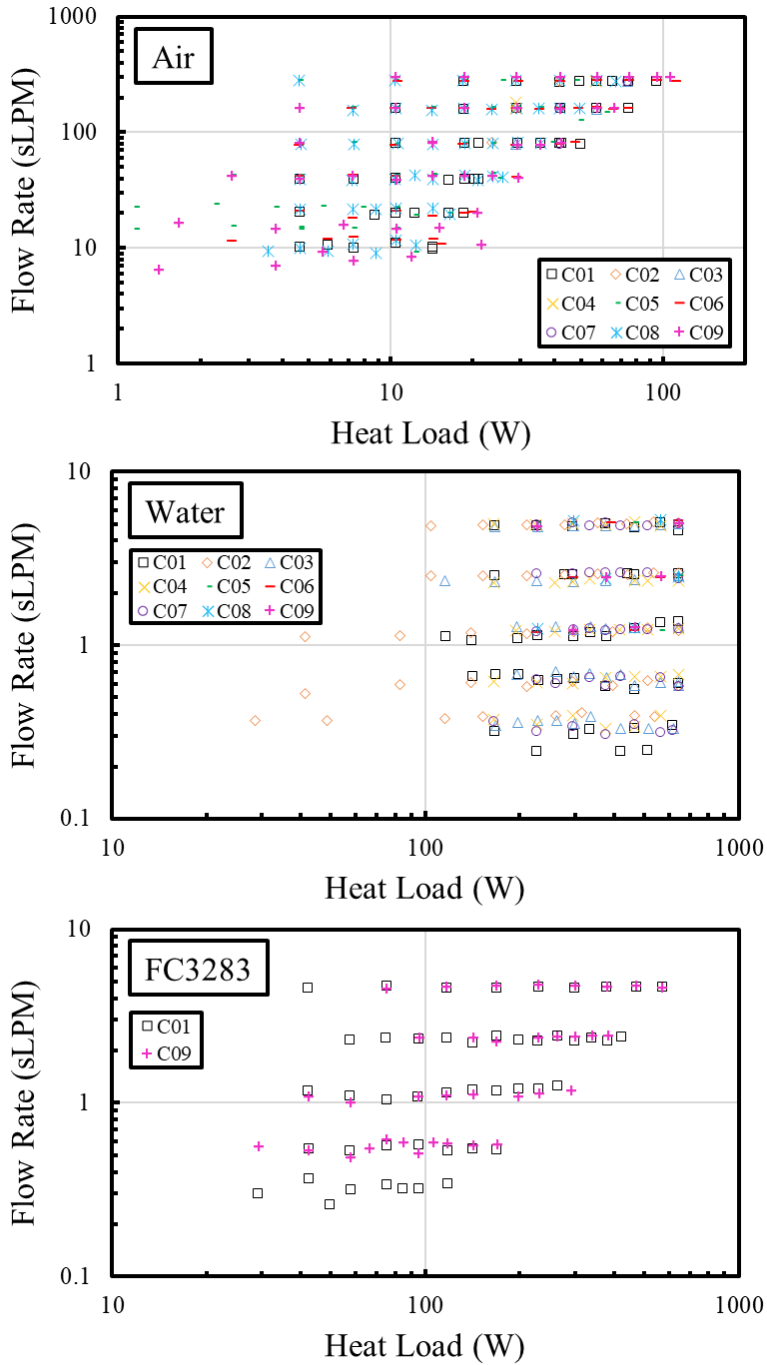


Figure 4-36: Complete set of flow and heat load conditions, segregated by fluid type and part number.

In order to better capture, the steady state condition, the direction of approach was varied throughout all of the tests. During roughly half of the tests, the heater temperature would begin at less than the steady state temperature and would approach from below and for roughly half of the

tests the heater temperature would begin at greater than the steady state temperature, thus approaching from above. Of course, a steady-state condition can only truly be reached after infinite time has passed. So, by approaching the steady-state condition from both directions, a better representation of true steady state could be characterized. This test method was executed programmatically by controlling the order of tested heat loads. For example, consider a hypothetical test condition at a single flow rate on a single impingement part. Consider that 6 heat loads are hypothetically tested from 15 W up to 90 W. The power supply could be programmed to deliver these heat loads in an order such that half are ascending, and half are descending (e.g., 30, 60, 90, 75, 45, 15). The effect of alternating the temperature approach direction is further described in step 3 below.

Step 3 – Wait for steady state:

After flow and heat load conditions were set, those conditions were held until the system reached steady state. Of course, a true steady state can only be reached after infinite time, so a determination must be made for when steady state was considered functionally achieved.

The difference between the average surrogate heater surface temperature and the fluid inlet temperature $\left(\frac{dT_{s-in}}{dt}\right)$ was selected to be the key metric for determining steady state. During testing, an attempt was made to ensure that each steady state data point was collected when the temperature rate of change $\left(\frac{dT_{s-in}}{dt}\right)$ was less than $0.2 \text{ }^\circ\text{C min}^{-1}$. Practically, the easiest way to achieve this steady state condition was by prescribing a set waiting period to each experiment. After the flow rate test condition had been set, next the heat load was set programmatically using the “Test Flow” capabilities in the Keysight Benchvue data acquisition software which would interface with the power supply and all measurement equipment. The Benchvue program would set the power supply load and then would be instructed to wait while continuously collecting data for a predetermined

period of time. The waiting period varied depending on part configuration, fluid, and flow rate; it ranged from only 15 minutes up to 90 minutes for a single test. Water tests reached steady state significantly quicker than air tests. The chosen waiting period was informed by experience with manually waiting for steady state at some of test conditions across various part configurations, fluids, and flow rates.

An exemplary data set is provided in Figure 4-37 which shows the temporal behavior of power supply voltage, flow rate, and surface temperature throughout six sequential tests at a single flow rate. All data shown in Figure 4-37 are from real testing and data points were taken at 30 second intervals. The data shown represent six of the 233 air test points taken during this investigation, labeled sequentially in the figure. For this test set, the steady state waiting period was set to 60 minutes and the air flow rate was set at approximately 280 sLPM, visible as a blue dotted line. The voltage supplied to the surrogate heater by the power supply is shown by the red

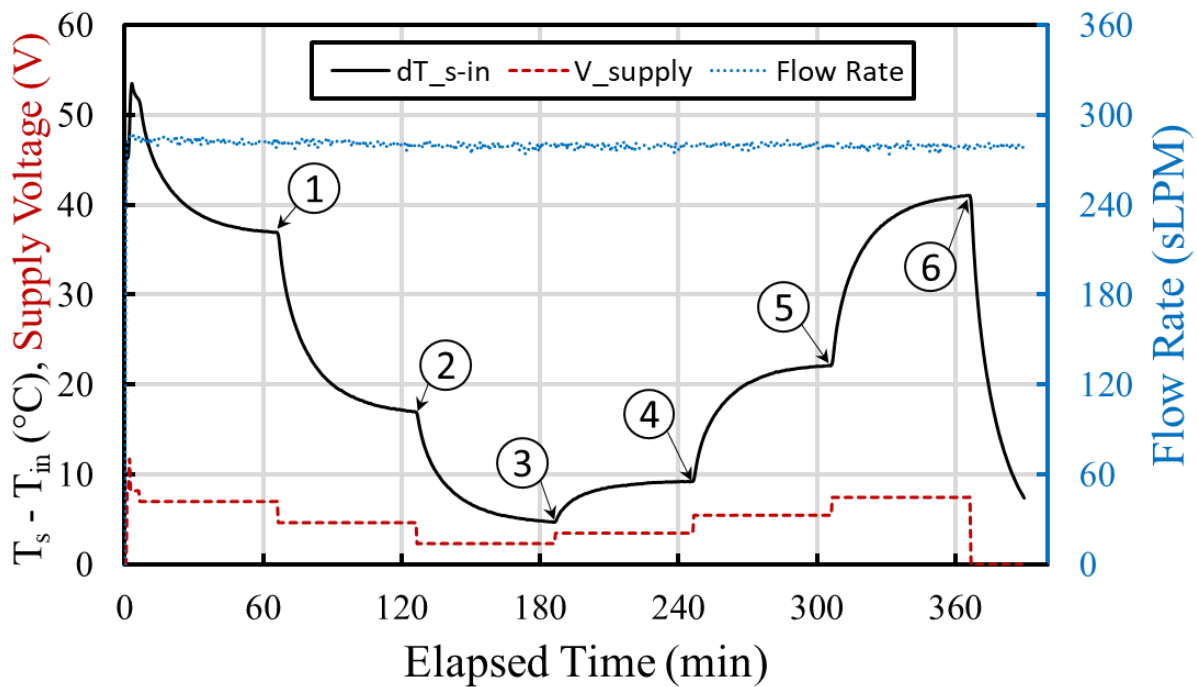


Figure 4-37: Exemplary temporal data set of six steady-state heat transfer tests at a single flow rate with air. Data shown are for C05 part configuration.

dashed line. This voltage directly controls the heat load of each test. The supply voltage was held at six distinct constant levels throughout data collection, changing regularly at steady 60-minute intervals until all six tests were complete. After the sixth test terminated, the power supply load was shut off entirely, as indicated by the voltage dropping to zero at approximately 367 minutes. Prior to beginning the test, the system was heated to above the steady state temperature of the first prescribed power load. This was done so that the first point would be a descending one. The solid black line represents the temperature difference between the target surface of the surrogate heater, T_s , and the fluid inlet, T_{in} . The temperature differential is shown to level off towards the end of each test, i.e., the slope approaches zero before the power supply voltage is changed, thus setting a new test condition. Note that, of the six data points taken, three approach the steady state condition from above and three approach it from below, as was discussed in step 2 of this test procedure.

The data shown in Figure 4-37 represent a typical test scenario. Among all six points shown, point 2 had the greatest slope at steady state, i.e., it was the furthest from reaching a true steady state condition. At point two, the slope $\left(\frac{dT_{s-in}}{dt}\right)$ was $-0.03 \text{ }^\circ\text{C min}^{-1}$. A similar steady state criteria was typically met across all heat transfer tests, as is demonstrated in Figure 4-38. Figure 4-38 provides a histogram of the rate of change of the surface-to-inlet temperature differential for the complete collection heat transfer tests. The histogram bars outside of the ± 0.15 bounds are overflow bins, representing all data outside of that range. 98.5% of all tests had a temperature slope within $\pm 0.2 \text{ }^\circ\text{C min}^{-1}$, 94.1% within $\pm 0.1 \text{ }^\circ\text{C min}^{-1}$, and 79.8% within $\pm 0.05 \text{ }^\circ\text{C min}^{-1}$. As was previously stated, roughly half of the data were taken by approaching the steady state temperature from above (46%) and the remainder by approaching from below.

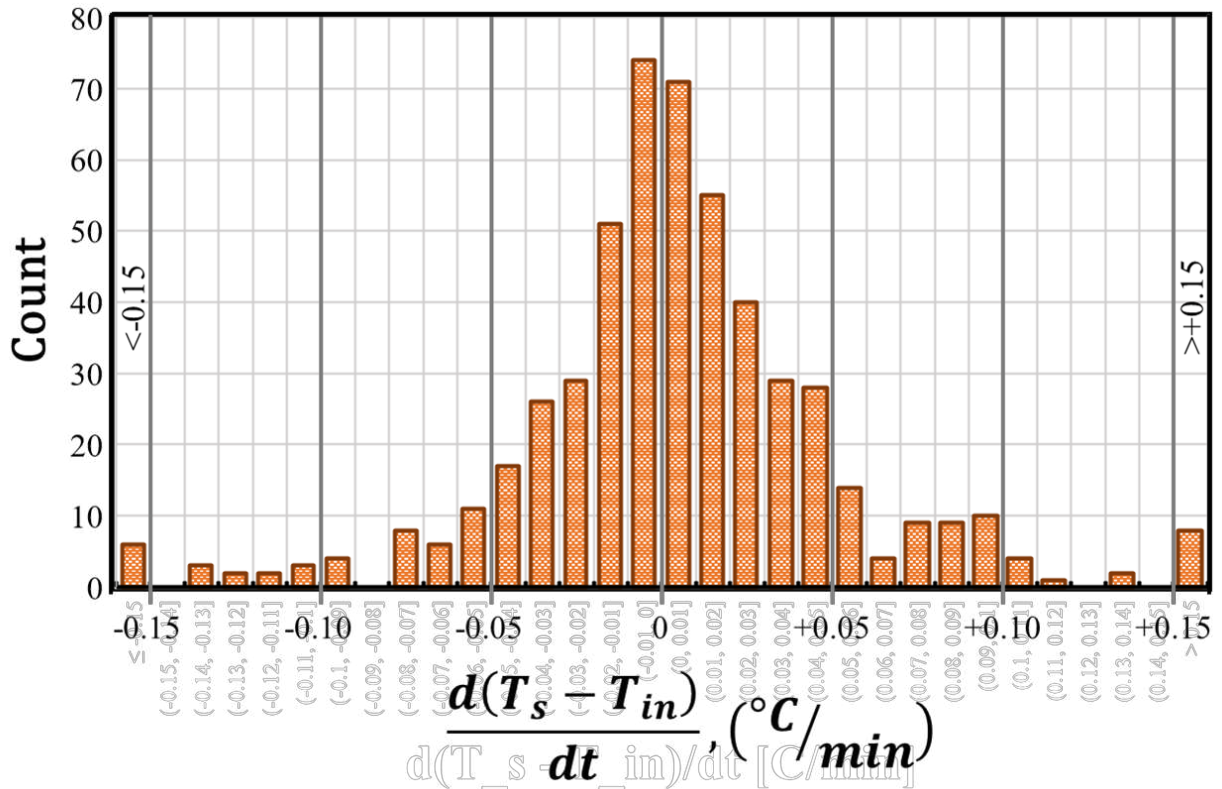


Figure 4-38: Histogram of steady state rate condition for all tests

Step 4 – Collect data:

Temperature, pressure, power, flow, and other measurements were taken continuously throughout the heat transfer tests at regular intervals. The sampling rate ranged from 12 Hz (1 point per 5 seconds) down to 2Hz (1 point per 30 seconds) and was determined intuitively in tandem with the steady state waiting period. For long waiting periods, a lower sampling frequency was selected simply to reduce the size of the data set where more points were unnecessary. After the prescribed waiting period (i.e., steady state had been met), the final eleven data points of all measurements were taken and averaged to form a single steady state data point which was representative of that test. This averaging technique was done to reduce the effects of measurement noise on the data. Figure 4-39 provides a visual description of some exemplary “steady state” data for a single test point. The data shown in Figure 4-39 are identical to that shown in Figure 4-37,

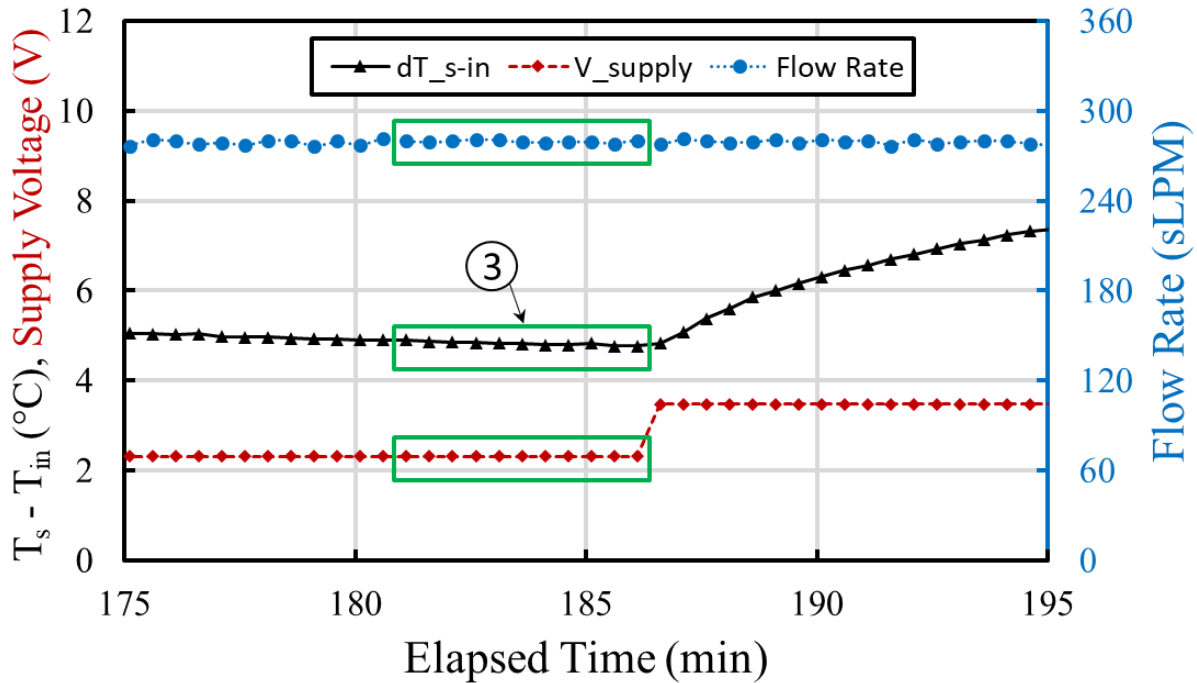


Figure 4-39: Exemplary flow rate, power supply voltage, and temperature data for single test point. The same data is shown as in Figure 4-37, but magnified around point 3.

but zoomed in on the 20-minute time period surrounding test point 3. The data highlighted within the three green rectangles were averaged to form the singular values which would represent the steady state flow rate, voltage, and surface-to-inlet temperature difference. All other test measurements not shown were averaged in the same way.

Step 5 – Repeat/complete:

Finally, this full process was repeated at each scheduled heat load for a single flow rate, at each scheduled flow rate for a single part configuration, for each scheduled part configuration for a single fluid, and for each fluid tested. In order to reduce the number of tests, some parts were tested more extensively with air than water and other parts were tested more extensively with water than air. Parts C01, C05, C06, C08, and C09 (the center point and four corner points in Figure 4-22) were tested extensively with air, but only sporadically with water. By contrast, parts C01, C02, C03, C04, and C07 (the center point and for edge points in Figure 4-22) were tested

extensively with water and only sporadically with air. A further reduced number of tests were conducted with FC3283. Table 4-6 quantifies the exact number of heat transfer tests conducted for each part configuration and for each fluid. Figure 4-40 provides a description of the range of Reynolds numbers and Prandtl numbers that were tested across all nine parts. A wide range of Reynolds numbers were tested with all three working fluids. Prandtl number varied mildly amongst different tests using the same working fluid due to changes in fluid temperature; this variation was not substantial.

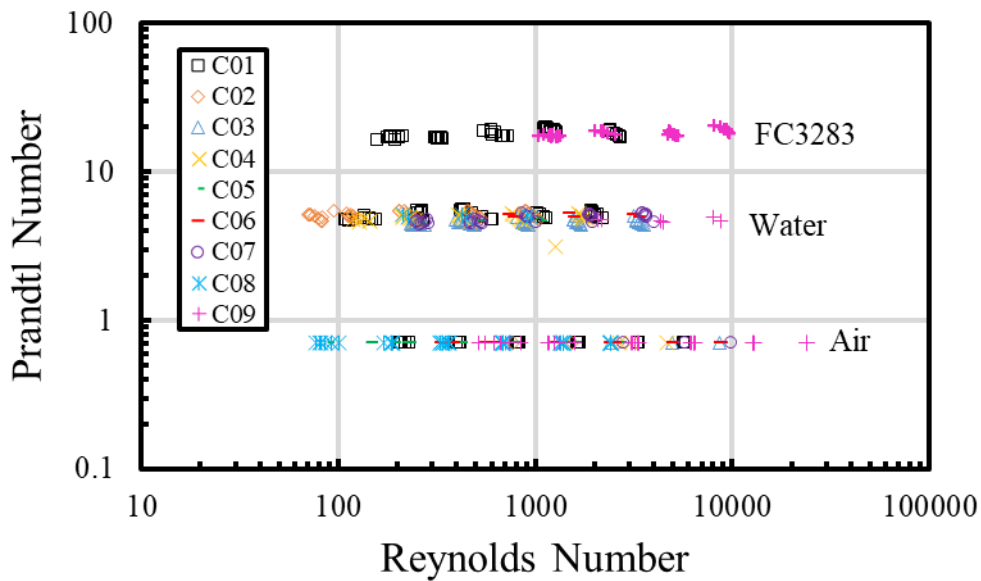


Figure 4-40: Range of Reynolds and Prandtl numbers tested by device number

Table 4-6: Count of all heat transfer tests conducted by part number and fluid type

Part	Numer of Tests Conducted			Total
	Air	Water	FC3283	
C01	42	40	47	129
C02	3	40	0	43
C03	3	40	0	43
C04	3	32	0	35
C05	47	6	0	53
C06	45	6	0	51
C07	3	35	0	38
C08	46	6	0	52
C09	41	6	35	82
Tot	233	211	82	526

4.4.2. Pressure drop testing

Pressure drop experiments were undergone using both water and air for all nine device configurations. These were conducted in tandem with the heat transfer experiments which were discussed in the section 4.4.1. A simple test procedure was established and is summarized in a process diagram in Figure 4-41. Each step in the test procedure is detailed below.

1. **Install test section**
2. **Initiate data collection**
3. **Ramp flow rate**
4. **End data collection**
5. **Repeat/complete**

Step 1 – Install test section:

As with the heat transfer tests, a device configuration was selected and installed into the test facility which would be configured for the particular test fluid. In fact, adiabatic pressure tests were conducted in tandem with heat transfer tests. Impingement parts were mounted onto the same

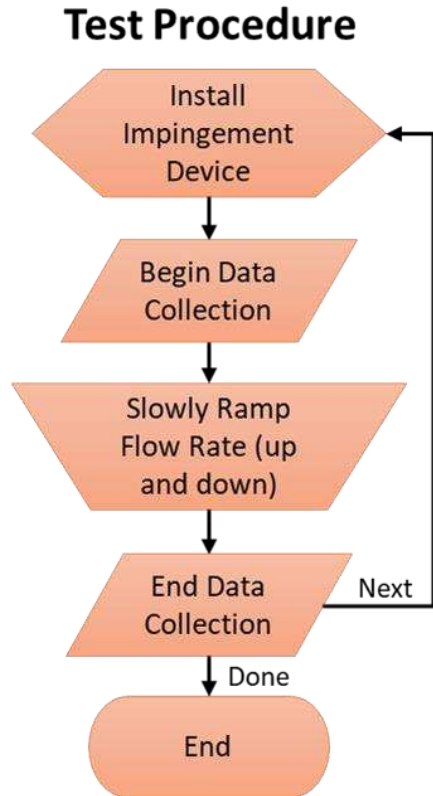


Figure 4-41: Simplified test procedure for adiabatic pressure drop testing

surrogate heater as with heat transfer testing; however, no heat load was applied. Once an impingement device was mounted into the test facility, an adiabatic pressure drop test would be completed prior to heat transfer testing on the same part. After heat transfer experiments were completed for that geometry/fluid configuration, another adiabatic pressure drop test would be performed before the part was dismounted. Pre and post heat transfer test data were taken as a way of accounting for possible changes in part geometry that could possibly occur during heat transfer testing. Jet hole erosion or thermally induced warpage could hypothetically change the impingement geometries enough to impact part performance in a measurable way. Note that some impingement part configurations were tested with only water, and some were tested with only air. For impingement parts that were tested with multiple fluids, often only a single adiabatic pressure

test was conducted with the secondary fluid and two (pre and post) tests were conducted with the primary fluid. Two impingement parts were also tested using the dielectric FC3283 fluid however, due to the dramatic pressure fluctuations which occurred during those tests, the adiabatic pressure drop data was unusable.

Table 4-7 summarizes all adiabatic pressure tests which were conducted as a part of this investigation by geometry configuration and fluid type. The table also indicates the number of independent pressure tests conducted for each.

Table 4-7: Number of adiabatic pressure tests performed by device configuration and fluid.

Part	Adiabatic Pressure Tests			Total
	Air	Water	FC3283	
C01	2	2	1	5
C02	1	2	0	3
C03	1	2	0	3
C04	1	2	0	3
C05	2	0	0	2
C06	2	1	0	3
C07	1	2	0	3
C08	2	0	0	2
C09	2	1	1	4
Tot	14	11	2	27

Step 2 – Initiate data collection:

Each test began with no flow passing through the impingement test section. The data acquisition system was initiated and set to collect all data (pressures, temperatures, flow rate, etc.) continuously at a sampling frequency of 0.2-0.5 Hz.

Step 3 – Ramp flow rate:

The system was held for several seconds with no supplied flow rate. After this, the flow rate was increased slowly as the data were collected. For air testing, the flow rate was controlled by manually adjusting the pressure regulator valve at the air supply shown in Figure 4-33. Flow

rate and pressure drop were monitored throughout to ensure that the system remained within suitable operating limits. The flow rate was elevated to approximately 300 sLPM of air for each test, the maximum measurement limit of the Kelly Pneumatic gas mass flow meter. After reaching the maximum desired flow rate, the air flow was then gradually, manually reduced until it ceased entirely. For liquid tests, the flow rate was controlled using three manual flow control valves (V-BC, V-BF, and V-IS in Figure 4-32) with the pump operating at the same condition throughout. The flow control valves consisted of a coarsely adjusted flow bypass valve (V-BC), a finely adjusted flow bypass valve (V-BF), and a finely adjusted impingement test section supply valve (V-IS). Each valve is labeled in Figure 4-32. The two bypass valves allow liquid to bypass the test section and return directly to the pump. The impingement supply valve is in line with the test section. Once again, the test was initiated with no flow through the part, the V-IS valve was fully closed and both flow bypass valves (V-BC, V-BF) were fully opened. To increase flow rate, first the V-IS valve was gradually opened. After V-IS had been fully opened, the bypass valves, V-BC and V-BF were gradually closed to further increase flow rate. With both bypass valves fully closed and the impingement supply valve fully open, the system was typically able to supply approximately 5 sLPM of liquid flow through the test section. This was well within the measurement range of the liquid volume flow meter. Upon reaching the maximum flow rate, the flow control valves would be used in a similar manner to gradually reduce the flow rate until it was stopped entirely.

Maintaining a slow ramp rate when adjusting the system flow rate is important for avoiding imposed hysteresis in the test data and for ensuring steady-state pressure drop measurement. Changes made to the system state (e.g., changing a valve position) take some period of time to propagate and for a new system steady state to be reached. System transience in the adiabatic case

can be primarily attributed to flow/pressure propagation and instrument response time. Naturally, flow and pressure fluctuations propagate through the system at the speed of sound in the flow medium. However, the wave speed may be significantly slower and reflections from such pressure fluctuations can reverberate through the system, possibly further delaying steady state for an extended period of time. For this system, it was observed that flow rate would lead pressure drop during system adjustments regardless of the direction of flow change (i.e., increasing or decreasing). This is illustrated using a simple schematic in Figure 4-42 which qualitatively describes the current system. As flow ramp rate is reduced, the quasi-steady-state observed data will converge towards the true steady-state line. Importantly, because observed flow rate changes always led observed pressure drop changes, the true steady-state condition was necessarily positioned between ascending and descending quasi-steady-state measurements. Thus, if no or little measurement hysteresis is observable, the collected quasi-steady-state data may then be considered as representative of the true steady-state condition. It was observed that if a rapid and substantial system change was made, a new steady-state condition was reached fairly quickly, within

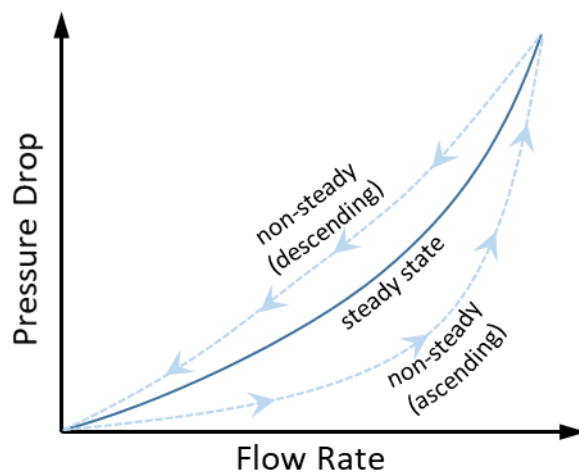


Figure 4-42: Schematic of hysteresis during adiabatic pressure drop measurement.

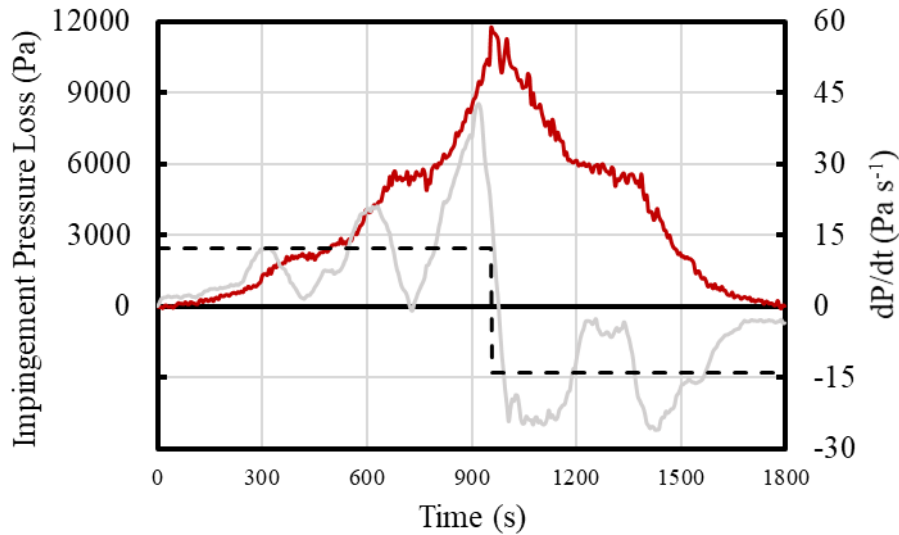


Figure 4-43: Exemplary temporal pressure drop data for C09-water adiabatic pressure drop test.

only a few seconds at most. This meant that a quality quasi-steady-state condition was achievable without requiring a tediously slow ramp rate.

Exemplary temporal pressure loss data is provided in Figure 4-43 for impingement part C09 with water. The solid red line represents the temporal pressure drop across the impingement device. The full test lasted approximately 30 minutes over which a maximum pressure drop of approximately 12 kPa was recorded. The light grey line represents the time derivative, or ramp rate, of the measured impingement pressure drop throughout the test. The derivative of the pressure drop data was taken as the slope of a 21-point linear regression centered about each data point to smooth the resulting curve which is otherwise chaotic due to signal noise and small pressure fluctuations. Generally, for the first half of the test, the ramp rate was held positive and, for the second half, it was held negative; however, it was not constant throughout the entire test. The dashed black line in Figure 4-43 depicts the average ramp rate during the increasing and decreasing test stages. On average, for the C09-water test, the pressure was increased at a ramp rate of 12.3 Pa s⁻¹ and was decreased at a ramp rate of -14.0 Pa s⁻¹.

Across all 25 air and water adiabatic pressure tests, the average ramp rate was $\pm 30 \text{ Pa s}^{-1}$. The highest absolute average ramp rate was 202 Pa s^{-1} , which occurred on part C03 with air. Some hysteresis was observed on certain adiabatic pressure tests however, where observable, the effects of hysteresis were minor. Later, in section 6.2.4, the water data collected for the C07 test section in Figure 6-19 provides a good example of minor, but observable hysteresis

Step 4 – End data collection:

Upon the completion of flow rate ramping, the test was ended, and data acquisition was terminated.

Step 5 – Repeat/complete:

Adiabatic pressure tests were repeated for each impingement part congruent with heat transfer tests. Thus, pressure tests were repeated in the same order as heat transfer tests.

4.5. Uncertainty

4.5.1. Heat transfer uncertainty

Propagation of uncertainty was conducted for all heat transfer tests to evaluate Reynolds number and Nusselt number measurement uncertainty. Reynolds number can be related to directly experimentally measured values by the following expressions:

$$Re_{air} = \frac{4\rho_{stp}}{\pi N_j^2} \cdot \frac{\dot{V}_{stp}}{\mu_f(T, P)D_j} \quad 4-2$$

$$Re_{liq} = \frac{4}{\pi N_j^2} \cdot \frac{\dot{V}\rho_f(T, P)}{\mu_f(T, P)D_j} \quad 4-3$$

Where the leading term in each equation represents constants. The subscript, *stp*, indicates standard temperature and pressure conditions. The Reynolds number expression is slightly different for air experiments than for liquid experiments because air flow rate is measured as standard volume flow

while liquid flow rate is measured as true volumetric flow. Dynamic viscosity and fluid density were taken from property tables within Engineering Equation Solver. Pressure can be effectively eliminated from the equations because viscosity is only a very weak function of pressure and the same is true for density in the case of the incompressible liquids. Thus, Reynolds number uncertainty may be approximated by considering only flow rate, fluid temperature, and jet diameter measurements using the following expression:

$$U_{Re}^2 = U_V^2 \left(\frac{\partial Re}{\partial \dot{V}} \right)^2 + U_{D_j}^2 \left(\frac{\partial Re}{\partial D_j} \right)^2 + U_T^2 \left(\frac{\partial Re}{\partial T} \right)^2 \quad 4-4$$

Where, U represents the uncertainty of the subscripted variable. In this case, fluid temperature T, was taken as the inlet fluid temperature. Uncertainties of all parameters were accounted for during actual propagation analysis, but had little effect downstream uncertainty. Nusselt number uncertainty can be similarly evaluated. The following expression describes Nusselt number in terms of directly measured and primary calculated parameters:

$$Nu = \frac{D_j \left(q_{app} - \left(\frac{T_{CH} - T_{amb}}{R_{ins}} \right) \right)}{A_s k_f(T, P) LMTD} \quad 4-5$$

$$LMTD = \frac{(T_s - T_{in}) - (T_s - T_{out})}{\ln \left(\frac{(T_s - T_{in})}{(T_s - T_{out})} \right)} \quad 4-6$$

Where, q_{app} represents the applied heat load as calculated by the product of heater voltage and current. The log mean temperature difference is calculated from surface temperature (T_s) and inlet (T_{in}) and outlet (T_{out}) fluid temperatures. The term $\left(\frac{T_{CH} - T_{amb}}{R_{ins}} \right)$ accounts for heat loss through the surrogate heater insulation where T_H is the maximum surrogate heater temperature at the heat

source. T_{amb} is the ambient temperature of the test environment. R_{ins} is the combined thermal resistance in $K W^{-1}$ of the insulation surrounding the surrogate heater and convection to ambient. The value for insulation thermal resistance was approximated to be $100 K W^{-1}$ with extremely generous uncertainty applied of $\pm 98 K W^{-1}$. Once again, pressure can be largely neglected from the uncertainty analysis because it has a weak effect on thermal conductivity over the applicable range. Thus, Nusselt number uncertainty can be expressed in terms of measured jet diameter, applied heat load, various temperatures (viz. target surface, ambient, heater maximum, fluid inlet, fluid outlet), and the surrogate heater secondary pathway thermal resistance (R_{ins}). Nusselt number uncertainty can be expressed as follows:

$$\begin{aligned}
 U_{Nu}^2 = & U_{D_j}^2 \left(\frac{\partial Nu}{\partial D_j} \right)^2 + U_{q_{app}}^2 \left(\frac{\partial Nu}{\partial q_{app}} \right)^2 + U_{R_{ins}}^2 \left(\frac{\partial Nu}{\partial R_{ins}} \right)^2 \\
 & + U_{T_s}^2 \left(\frac{\partial Nu}{\partial T_s} \right)^2 + U_{T_H}^2 \left(\frac{\partial Nu}{\partial T_H} \right)^2 + U_{T_{amb}}^2 \left(\frac{\partial Nu}{\partial T_{amb}} \right)^2 \\
 & + U_{T_{in}}^2 \left(\frac{\partial Nu}{\partial T_{in}} \right)^2 + U_{T_{out}}^2 \left(\frac{\partial Nu}{\partial T_{out}} \right)^2
 \end{aligned} \tag{4-7}$$

Uncertainty propagation was performed in Engineering Equation Solver using the built-in uncertainty tools. All partial derivatives were automatically computed numerically by the program. This was especially convenient for evaluating thermophysical properties which were based on embedded property tables. Broadly, it was found that Reynolds number uncertainty was dominated by jet diameter measurements for air data. For liquid data, Reynolds number uncertainty was dominated by both jet diameter and flow measurement uncertainty, with flow measurement playing a larger role for low flow. Air Reynolds number uncertainty remained below $\pm 5.5\%$ across all data. By contrast, liquid Reynolds number uncertainty varied more dramatically and was approximately ± 100 (absolute, not %) on average. This means that for low Reynolds number water

and FC3283 data, uncertainty reached as high as $\pm 78\%$ of the calculated value in the worst case. On average, Reynolds number uncertainty was $\pm 3.3\%$ for air, $\pm 22\%$ for water, and $\pm 20\%$ for FC3283. Nusselt number uncertainty was broadly held below $\pm 10\%$ across all fluid types with an average uncertainty of $\pm 4.8\%$. Nusselt uncertainty was chiefly dominated by impinging jet diameter measurement error. Despite the very generous uncertainty applied toward heat losses through the insulation (R_{ins}), that uncertainty did not have a dramatic impact on Nusselt number uncertainty due to the impingement thermal pathway being overwhelmingly dominant. This supports that exact calculation of thermal losses through insulation was unnecessary for maintaining experimental fidelity. Error bars have been included for a representative subset of the data in section 5.1 and additional uncertainty results are provided in appendix F.

The relative contributions of different measurements on downstream propagated uncertainty for heat transfer tests are detailed in Table 4-8. Relative uncertainty contributions are shown for both Reynolds number and Nusselt number calculations. All measurements not included in Table 4-8 had a negligible effect on calculated uncertainties ($\ll 0.1\%$). The percentage values provided in Table 4-8 are averaged across all parts and test conditions to provide a single representative value for each fluid and contributing measurement category. Each measurement category accounts for the combined uncertainty contributions of multiple distinct measurements. For example the temperature measurement category in Table 4-8 includes uncertainties for inlet and outlet fluid temperatures, ambient air temperature measurements, and surrogate heater surface

Table 4-8: Measurement contribution to propagated uncertainties for heat transfer tests

Measurement	Relative Contribution to Uncertainty					
	Reynolds Number			Nusselt Number		
	Air	Water	FC3283	Air	Water	FC3283
Flow Rate	44.5%	89.8%	85.5%			
Geometry (D_j , H)	55.4%	9.7%	14.2%	35.5%	49.3%	69.8%
Temps (T_s , T_{inv} , T_{out} , T_{amb})	0.1%	0.5%	0.3%	27.2%	49.7%	17.2%
Heat Flux (q , R_{ins})				37.4%	1.0%	14.3%

temperature with all biases accounted for. Reynolds number uncertainty was dominated by the uncertainty of flow rate measurements for liquid tests, contributing 90% and 86% for water and FC3283 respectively. This indicates that improved liquid flow measurement hardware would have had a significant impact on improving overall measurement fidelity. Geometric uncertainty had only a modest impact on the Reynolds number for liquid tests. The liquid flow meter provided the greatest source of error in this work. Air testing showed comparable contributions for flow rate measurement and jet geometry on Reynolds number uncertainty. This may be attributed to the improved measurement accuracy of the air mass flow meter when compared to the liquid flow meter used in the test facility. Improved manufacturing consistency of the 3D printing fabrication process could further reduce the uncertainty of Reynolds number computations with air.

Nusselt number uncertainty for air heat transfer tests was fairly evenly contributed by geometry, temperature, and heat flux measurement effects. Heat flux played a much larger role in air heat transfer uncertainty than for water and Fluorinert because of the relatively higher impingement thermal resistance achieved by air tests. Liquid tests achieved lower thermal resistance along the primary thermal pathway (through the impingement device), meaning that less heat would be lost through the surrogate heater insulation. Overall, device geometry had the greatest effect on Nusselt number uncertainty, contributing 36%, 49%, and 70% of uncertainty for air, water, and Fluorinert respectively. Once again, improved 3D printing consistency would allow for better Nusselt number measurement fidelity.

Surface temperature measurements were calculated as a weighted average of the multiple individual thermocouples embedded near the target surface. Unfortunately, three of the six embedded thermocouples were damaged during mounting but after calibration. Therefore, only the thermocouples in positions TT-S1, TT-S3, and TT-S4 in accordance with Figure 4-27b were

operational during testing. Flow moves from left to right in Figure 4-27b, therefore one thermocouple (TT-S4) was positioned upstream of the centerline and two thermocouples (TT-S1, TT-S3) were positioned downstream. The three temperature probes are not evenly distributed across the target surface, so to account for spatial temperature disparities, a geometric weighted average was taken rather than a simple unweighted average of the three measurements. Using all three temperature measurements and their associated cartesian coordinates relative to the center point, a plane could be constructed to approximate the temperature everywhere on the target surface. The center point location of that plane, then represents the geometric average temperature which was used for all calculations. The procedure for calculating spatially averaged surface temperature measurements is discussed in appendix G. Surface temperature uniformity may be quantitatively approximated by a single, simple metric. The following equation expresses the magnitude of the gradient of the spatial-temperature plane formed by the three measurement points:

$$\|\nabla T_s(X, Y)\| = \sqrt{\left(\frac{dT_s}{dX}\right)^2 + \left(\frac{dT_s}{dY}\right)^2} \quad 4-8$$

where, the temperature gradients (K cm^{-1}) in the X and Y directions can be found for the spatial-temperature plane formed by the three temperature measurements. This temperature gradient can then be multiplied by the length of the target surface (4 cm) to approximate the maximum temperature difference across the target surface:

$$\Delta T_{s,var} \approx \sqrt{A_s} * \|\nabla T_s(X, Y)\| = 4 \text{ cm} * \sqrt{\left(\frac{dT_s}{dX}\right)^2 + \left(\frac{dT_s}{dY}\right)^2} \quad 4-9$$

Finally, this surface temperature variation can be expressed as a percentage of the absolute average surface temperature (T_s) in Kelvin to produce a simple metric for surface temperature uniformity:

$$\%T_{uni} = \sqrt{A_s} \frac{\sqrt{\left(\frac{dT}{dX}\right)^2 + \left(\frac{dT}{dY}\right)^2}}{T_s} * 100\% \quad 4-10$$

Recall that a comparable metric was used in section 4.2.2 and Table 4-5 to evaluate predicted surface uniformity in the surrogate heater computational model. Mild temperature non-uniformity was observed during heat transfer testing. For air, the average temperature uniformity was 0.06%, while the average $\%T_{uni}$ was 0.38% for water, both similar to, but slightly higher than the predicted variations presented in Table 4-5. This slightly elevated temperature non-uniformity may be the result of multiple compounding factors beyond those evaluated in the section 4.2.2 predictive model. Specifically, slight flow maldistributions (discussed further in section 6.1.1), thermal shortcut losses within the manifold, and imperfect thermocouple solder joints (inconsistent thermal contact resistance across measurement locations), may all play a role on overall measured temperature uniformity.

4.5.2. Pressure drop uncertainty

Uncertainty propagation was also computed for pressure drop results. Once again, Reynolds number uncertainty could be calculated identically to the method described in section 4.5.1 using equations 4-2, 4-3, and 4-4. Pressure drop uncertainty is straight forward, as provided by the instrumentation specification sheets of the pressure transducers. However, pressure drop uncertainty was dependent upon the measurement range. Logical statements were used to determine which pressure transducer device measurement was applied from the three parallel

pressure transducers. Pressure drop k-factor and Darcy friction factor could be calculated from measured values as follows:

$$k_{air} = \frac{2\Delta P_{imp}}{\rho_f(T, P)v^2} = \frac{\Delta P_{imp}\rho_f(T, P)}{8} \left(\frac{\pi N_j^2 D_j^2}{\dot{V}_{stp}\rho_{f,stp}} \right)^2 \quad 4-11$$

$$f_{air} = \frac{k_{air}D_j}{L_{eq}} = \frac{\Delta P_{imp}\rho_f(T, P)D_j}{8 \left(2L + 2H + \frac{S}{\sqrt{2}} \right)} \left(\frac{\pi N_j^2 D_j^2}{\dot{V}_{stp}\rho_{f,stp}} \right)^2 \quad 4-12$$

$$k_{liq} = \frac{2\Delta P_{imp}}{\rho_f(T, P)v^2} = \frac{\Delta P_{imp}}{8\rho_f(T, P)} \left(\frac{\pi N_j^2 D_j^2}{\dot{V}} \right)^2 \quad 4-13$$

$$f_{liq} = \frac{k_{liq}D_j}{L_{eq}} = \frac{\Delta P_{imp}D_j}{8\rho_f(T, P) \left(2L + 2H + \frac{S}{\sqrt{2}} \right)} \left(\frac{\pi N_j^2 D_j^2}{\dot{V}} \right)^2 \quad 4-14$$

where, ΔP_{imp} , T , P , D_j , \dot{V} , \dot{V}_{stp} , L , and H are all measured parameters with uncertainty applied. S , N_j , and $\rho_{f,stp}$ are all constants. L_{eq} is the equivalent flow path length and was defined as the centerline flow path length from the inlet of a jet nozzle to the outlet of the nearest return port, $L_{eq} = \left(2L + 2H + \frac{S}{\sqrt{2}} \right)$. Once again, air flow rate was measured on a mass flow basis as standard volumetric flow rate while liquid flow was measured as true volume flow, resulting in slightly different expressions shown above. Fluid density was determined from property tables using an average of inlet and outlet temperature and absolute pressure measurements. Geometric parameters D_j and H were measured and discussed in section 4.1.3, and uncertainty was determined using standard deviations for each parameter. However, jet nozzle length, L , was not measured so an uncertainty of $\pm 30\%$ of the as-designed nozzle length was assumed. Measurement uncertainty could be propagated to k-factor and Darcy friction factor using the following equations.











$$U_k^2 = U_{\Delta P_{imp}}^2 \left(\frac{\partial k}{\partial \Delta P_{imp}} \right)^2 + U_{\dot{V}}^2 \left(\frac{\partial k}{\partial \dot{V}} \right)^2 + U_{D_j}^2 \left(\frac{\partial k}{\partial D_j} \right)^2 + U_H^2 \left(\frac{\partial k}{\partial H} \right)^2 + U_P^2 \left(\frac{\partial k}{\partial P} \right)^2 + U_T^2 \left(\frac{\partial k}{\partial T} \right)^2 \quad 4-15$$

$$U_f^2 = U_{\Delta P_{imp}}^2 \left(\frac{\partial f}{\partial \Delta P_{imp}} \right)^2 + U_{\dot{V}}^2 \left(\frac{\partial f}{\partial \dot{V}} \right)^2 + U_{D_j}^2 \left(\frac{\partial f}{\partial D_j} \right)^2 + U_H^2 \left(\frac{\partial f}{\partial H} \right)^2 + U_L^2 \left(\frac{\partial f}{\partial L} \right)^2 + U_P^2 \left(\frac{\partial f}{\partial P} \right)^2 + U_T^2 \left(\frac{\partial f}{\partial T} \right)^2 \quad 4-16$$

Uncertainty propagation was once again performed in Engineering Equation Solver and accounted for all measured parameters. Pressure and temperature measurement uncertainty had a negligible effect on pressure loss coefficient and Darcy friction factor uncertainty. Generally, jet diameter uncertainty had the greatest effect on propagated uncertainties for Reynolds number, pressure loss coefficient, and Darcy friction factor. For air tests, uncertainty was often dominated by geometric parameters with moderate effects from flow rate and pressure drop at low flow rates. For liquid tests, geometric parameter uncertainty still played a major role on propagated uncertainties, but flow rate uncertainty became dominant at low flow rates. For all data, Reynolds number uncertainty was $\pm 3.2\%$ on average for air and $\pm 10.8\%$ on average for water testing. Pressure loss coefficient uncertainty was, on average, $\pm 12.5\%$ and $\pm 25.4\%$ for air and water respectively. Average Darcy friction factor uncertainty was found to be $\pm 13.7\%$ and $\pm 26.3\%$ for air and water respectively. Part C01 exhibited the greatest level of uncertainty for all parameters, which can be attributed to that configuration having the greatest jet diameter variation. Exemplary uncertainty values are included in section 6.1.

Table 4-9 shows the relative contributions of different measurements on Reynolds number and Darcy friction factor uncertainty for the adiabatic pressure drop tests. Once again, measured variables which are not accounted for in Table 4-9 had a negligible effect on downstream propagated uncertainties. The provided values are representative of average uncertainty contributions across all test sections and flow conditions. Similar to the heat transfer tests, Reynolds number uncertainty was dominated by flow rate measurements (86% contribution) for liquid tests and roughly evenly contributed by flow rate and geometry uncertainty for air test. Other factors had a negligible effect on Reynolds number uncertainty. The same observations made in section 4.5.1 on Reynolds number uncertainty contributions for heat transfer tests could be repeated here for the adiabatic pressure drop tests. For air tests, Darcy friction factor uncertainty was dominated by geometry effects (73% contribution) including jet diameter, jet height, and jet nozzle length uncertainties. Darcy friction factor measurement fidelity could, thus, be significantly improved through more exact impingement part fabrication. Flow rate measurement and pressure drop measurement each had a modest impact on friction factor uncertainty. Once again, the contribution of flow rate is higher for the liquid experiments, contributing 59% of friction factor uncertainty on average across adiabatic pressure drop tests with water. Impinging jet geometry still contributed significantly (35%) to friction factor measurement uncertainty with water. Pressure drop measurement proved sufficiently accurate, contributing only 5.5% of the propagated friction

Table 4-9: Measurement contribution to propagated uncertainties for pressure drop tests

Measurement	Relative Contribution to Uncertainty			
	Reynolds Number		Darcy Friction Factor	
	Air	Water	Air	Water
Flow Rate	44.0% 	86.2% 	11.7% 	59.4% 
Geometry (D_j , H , L)	55.9% 	13.1% 	72.9% 	35.1% 
Pressure Drop	0.0%	0.0%	14.8% 	5.5% 
Fluid State (T_{in} , T_{out} , P_{in})	0.1%	0.8%	0.6%	0.0%

factor uncertainty. For both air and water, the measured fluid state (temperature and absolute pressure) had an insignificant effect on friction factor uncertainty.

CHAPTER 5. Heat Transfer Results, Discussion, and Correlation

Development

Steady-state heat transfer testing was conducted on all nine impingement device configurations provided with a range of flow rates and heat loads. Testing was performed using air (233 distinct test points) water (211 distinct test points) and a dielectric fluorocarbon fluid Fluorinert FC3283 (82 distinct test points). This chapter will discuss the results of those tests and will establish a predictive correlation based upon the collected data.

5.1. Results

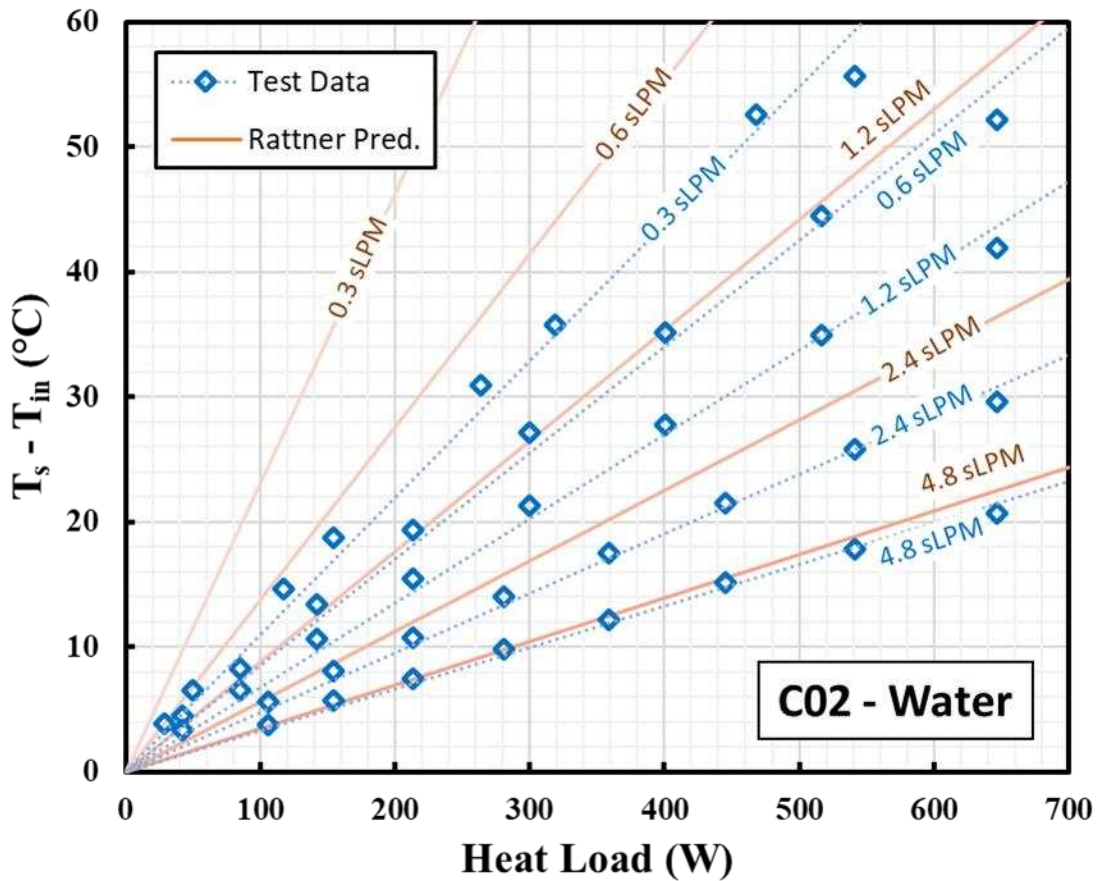


Figure 5-1: Exemplary test data for water tests with the CO2 impingement part at all nominal flow rates and heat loads. Prediction lines using Rattner’s correlation are provided for reference.

Steady state heat transfer testing of the nine impingement geometries, across three test fluids and myriad flow rates and heat loads, produced 526 distinct test results. An exemplary subset of that collected data is provided in Figure 5-1 for the C02 geometry configuration tested with water only. The prescribed heat load is given on the x axis with the resulting measured surface-to-inlet temperature difference on the y axis. Each of the 40 datapoints (blue diamonds) represents a single test point, similar to the 6 test points provided in Figure 4-37. Surface temperature (T_s) was calculated as the average of the surface thermocouple measurements as discussed in section 4.5.1.

The 40 experiments were conducted across five nominal flow rates ranging from 0.3 sLPM up to 4.8 sLPM. A linear regression (dotted blue line) has been fit through each data sub-set that was recorded at the same nominal flow rate. The slope of this line represents the thermal resistance between the target surface and the inlet fluid. Thus, a shallower slope indicates a lower thermal resistance and consequently a higher heat transfer coefficient. Note that, as expected, there is no dramatic or obvious trend between heat load and the measured thermal resistance. Of course, the heat load will affect how fluid properties change along the flow pathway, but this effect is expected to be minor. As such, the data indicate that a heat flux independent heat transfer correlation should be sufficient for characterizing the system performance. This is typically the case for single phase convection systems.

Importantly, the nominal flow rates listed in Figure 5-1 are shown only to provide easy visual categorization of the otherwise arbitrary looking data. The actual flow rate of each individual point may vary (sometimes significantly) from the nominal value shown. For example, the nominal 4.8 sLPM test points were actually conducted, on average, at 5.00 sLPM and ranged from 4.90 up to 5.14 sLPM across the 8 test points. Actual measured flow rate values were recorded and consistently used in any subsequent calculations for each test point. The solid orange lines

were constructed using Rattner’s Nusselt number correlation [44]. During testing, these prediction lines served as a guide for the facility operator to estimate facility temperatures and to select appropriate heat loads accordingly. Here, they are provided to serve as a reference for how similar experimental results were to the predicted values. Some experimental values were very close to the Rattner predictions, whereas others deviated significantly. In the case of part C02 water testing, the 4.8 sLPM data aligned very well with the Rattner prediction, while the 0.3 sLPM prediction greatly underpredicts the measured heat transfer performance demonstrated in this study.

The maximum heat load tested in this study was approximately 650 Watts (40 W cm^{-2}), limited by the 700W power supply limit and reduced as a result of line losses. The maximum surface-to-inlet temperature difference was generally maintained below 60°C and the fluid inlet condition ranged from 18°C up to 58°C . The surface-to-inlet thermal resistance (R_{s-in}) ranged from $7.3 \text{ }^\circ\text{C W}^{-1}$ down to $0.33 \text{ }^\circ\text{C W}^{-1}$ for air, from $0.13 \text{ }^\circ\text{C W}^{-1}$ down to $0.018 \text{ }^\circ\text{C W}^{-1}$ for water, and from $0.49 \text{ }^\circ\text{C W}^{-1}$ down to $0.095 \text{ }^\circ\text{C W}^{-1}$ for FC3283. Water, as expected, dramatically outperformed the other fluids.

Using the data shown in Figure 5-1 and similar data collected for all nine impingement geometries, the average heat transfer coefficient could then be calculated for each test. The resulting heat transfer coefficients are shown in Figure 5-2a using the same exemplary data subset (C02 – water). The heat transfer coefficient was calculated using the log mean temperature difference (LMTD) as follows:

$$htc = \frac{Q}{A_s \cdot LMTD} \quad 5-1$$

where,

$$LMTD = \frac{\Delta T1 - \Delta T2}{\ln\left(\frac{\Delta T1}{\Delta T2}\right)} \quad 5-2$$

Here, $\Delta T1$ and $\Delta T2$ are defined as:

$$\Delta T1 = T_s - T_{in} \quad 5-3$$

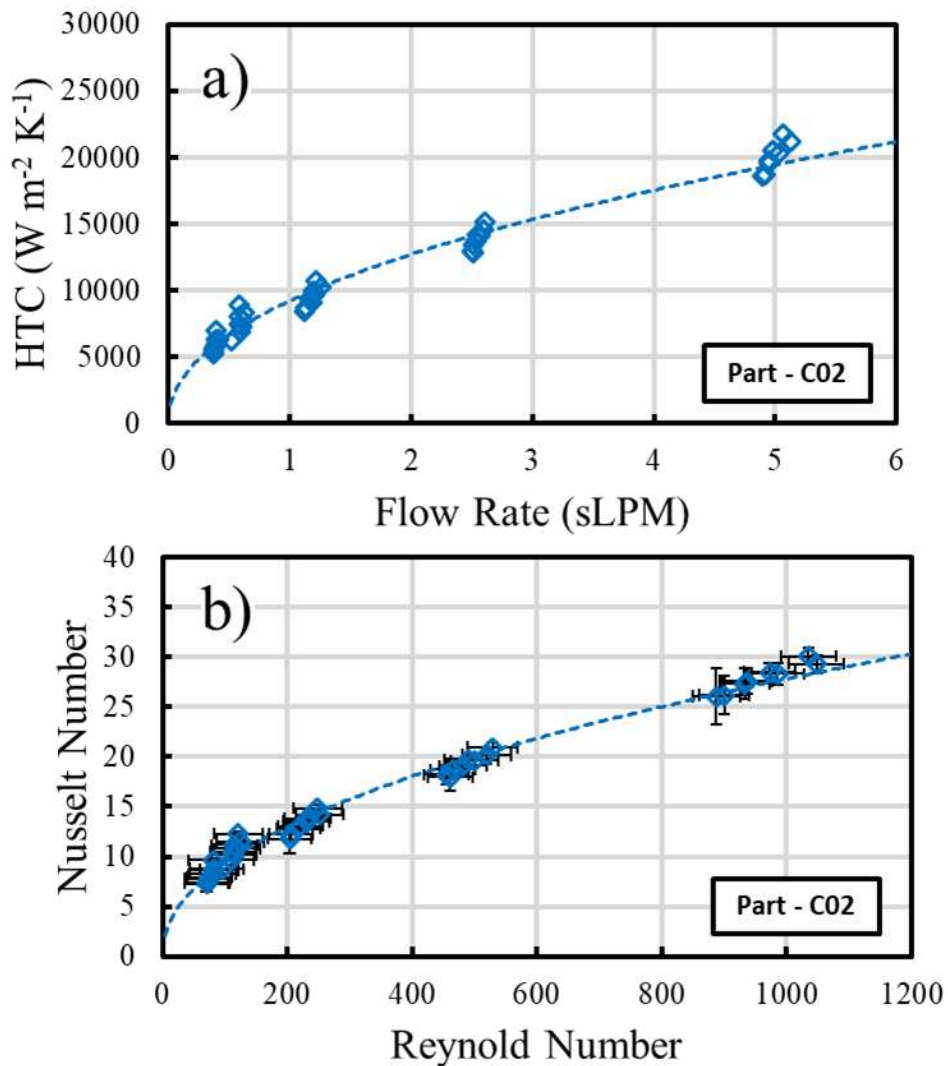


Figure 5-2: Exemplary steady-state heat transfer results for part C02 with water. a) heat transfer coefficient varying with standard flow rate. b) Nusselt number varying with Reynolds number.

$$\Delta T_2 = T_s - T_{out} \quad 5-4$$

where h_{tc} represents the heat transfer coefficient, Q represents the heat load, and A_s represents the wetted surface area of the target impingement surface (40 mm × 40 mm). T_{in} is the fluid inlet temperature as measured when it enters the impingement device. T_{out} is the fluid outlet temperature, measured at the device exit. T_s is the average surface temperature as measured by the thermocouples embedded into the surrogate heater.

The data in Figure 5-2a are clustered about the five nominal water flow rates. A power law regression was fit through the data, represented by the dashed blue line. Heat transfer coefficients in excess of 20,000 W m⁻² K⁻¹ were recorded with the C02 geometry configuration. Notably, the data span a range of heat transfer coefficients at approximately the same flow rates. This is an effect of both measurement uncertainty and fluid temperature changes from test to test. The same dataset in Figure 5-2a can be nondimensionalized as Nusselt number versus Reynolds number where Nusselt number (Nu) is calculated as follows:

$$Nu = \frac{h_{tc} \cdot D_j}{k_f} \quad 5-5$$

And Reynolds number (Re) is defined as,

$$Re = \frac{\rho_f v_j D_j}{\mu_f} \quad 5-6$$

The fluid properties k_f , ρ_f , and μ_f are thermal conductivity, density, and dynamic viscosity of the fluid, respectively. Fluid properties are determined using temperature and pressure measurements at the inlet of the impingement device. Instead using inlet-outlet averaged temperatures and

pressures does not result in significant property changes but correlation formulation using inlet properties resulted in slightly better fit. v_j denotes the mean jet velocity at the jet nozzle, calculated as:

$$v_j = \frac{4\dot{V}_{in}}{N_j^2 \pi D_j^2} \quad 5-7$$

where \dot{V}_{in} is the actual volumetric flow rate into the impingement device and N_j^2 is the total number of jets in the impingement array, as described in Table 4-1. Note that \dot{V}_{in} is not the same as what is plotted on the x axis of Figure 5-2a which is standard volumetric flow rate. Standard volumetric flow rate (\dot{V}_{stp}) is, in fact, a volume representation mass flow rate (\dot{m}) such that:

$$\dot{m} = \dot{V}_{in,stp} \rho_{f,stp} = \dot{V}_{in} \rho_{f,a}, \quad \dot{V}_{in,stp} = \dot{V}_{in} \frac{\rho_{f,a}}{\rho_{f,stp}} \quad 5-8$$

where $\rho_{f,a}$ represents actual fluid density while $\rho_{f,stp}$ is a constant representing fluid density at some standard condition. In this case, the standard condition was taken as 101 kPa at 21.1°C, to remain consistent with the specifications of the Kelly Pneumatic air mass flow meter.

Figure 5-2b presents the exemplary CO₂ – water dataset plotted as Nusselt number versus Reynolds number. Note that the Reynolds number values are relatively spread out compared to their flow rate counter parts. This is a consequence of changing fluid properties (viscosity and density) from test to test. The changing fluid properties are resultant of changing fluid temperatures. For example, during the highest flow rate subgroup in this data subset (nominally 4.8 sLPM), the inlet water temperature was 32 °C on average but ranged from 29 °C up to 35 °C across the eight tests. Error bars have been selectively included in this figure and are typical for water tests. Absolute Reynolds number uncertainty is shown to be fairly consistent; however, at

low Reynolds numbers, this accounts for substantial relative uncertainty, as noted in section 4.5.1. Once again, a power law regression was fit through the data, as represented by the blue dashed line. Nusselt number for this particular subset of the data, varied with Reynolds number as:

$$Nu \propto Re^{0.47} \quad 5-9$$

This same procedure was repeated for the complete dataset to calculate heat transfer coefficients, Reynolds number, and Nusselt number for all 526 data points. Heat transfer coefficient and Nusselt number results for the entire dataset are plotted in Figure 5-3, segregated by working fluid. Green circles represent air data, blue diamonds represent water data, and yellow squares represent FC3283. This labeling convention is maintained for subsequent figures in this section. Figure 5-3a provides heat transfer coefficients plotted against jet Reynolds number, while Figure 5-3b presents Nusselt number plotted against the same. The dashed lines in each figure are provided to aid in visualizing the data trend. Note that these dashed lines are not power-law regression curves fit through the data (which would fail to account for the varying geometries), but rather constant-exponent power law trends such that:

$$Nu \propto htc \propto Re^{0.57} \quad 5-10$$

with variable multiplier coefficients which were manually selected for each line. In Figure 5-3a the dashed lines are used to provide a visual clue of the data trend for each individual working fluid. Conversely, in Figure 5-3b the dashed lines are used to bound the full dataset while still indicating the general trend. The exponent of 0.57 was taken from a regression of the full dataset, which will be discussed later in this chapter. Average relative uncertainties for Reynolds number were $\pm 3.3\%$, $\pm 22\%$, and $\pm 20\%$ for air, water, and FC3283 respectively. Average relative Nusselt

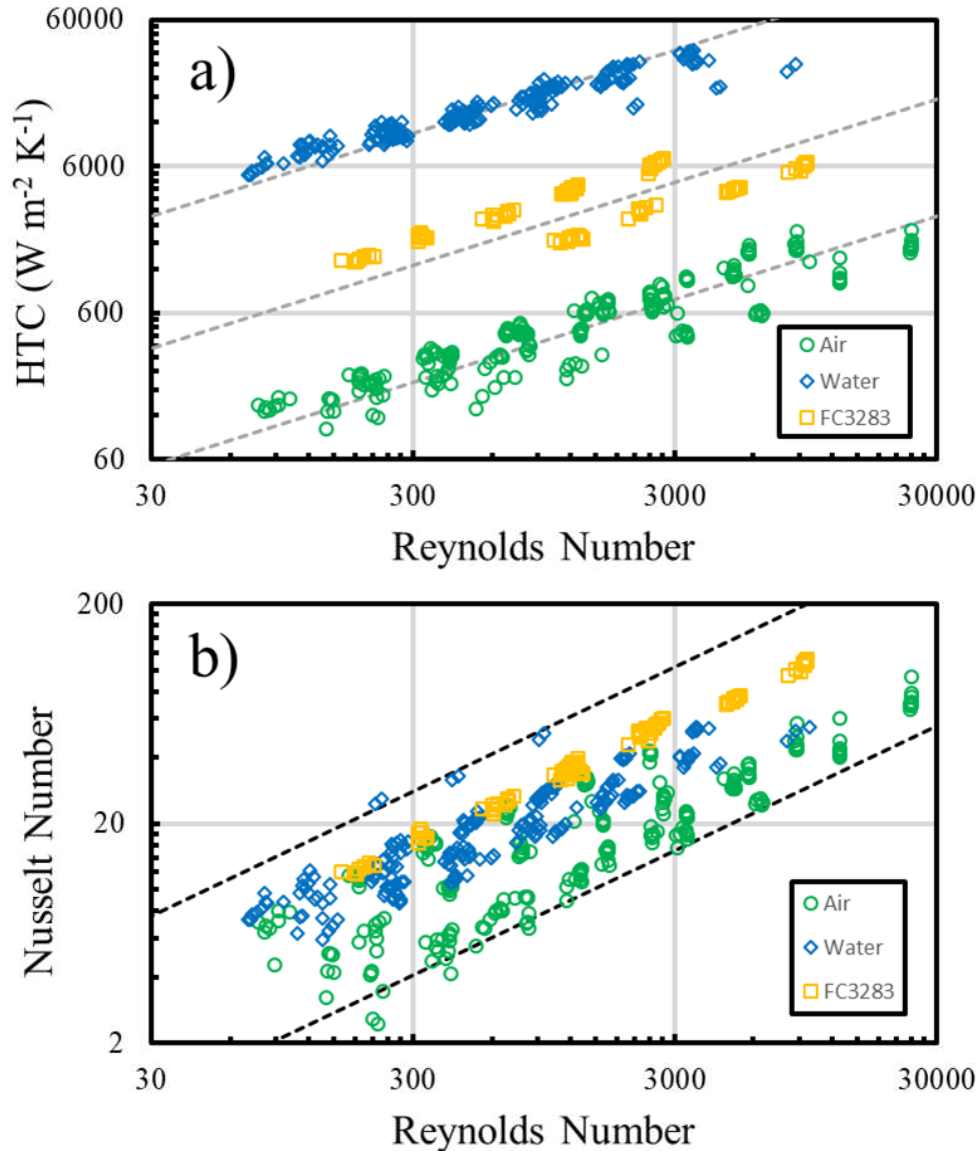


Figure 5-3: Complete steady-state heat transfer data set with all nine geometry configurations and three working fluids. a) heat transfer coefficient vs. Reynolds number, b) Nusselt number vs. Reynolds number.

number uncertainties were $\pm 5.2\%$, $\pm 4.5\%$, and $\pm 4.2\%$ for air, water, and FC3283 respectively.

Uncertainty was not uniform across all test points. Additional data, including error bars for the complete dataset are provided in Appendix F.

Air data spanned the widest range of Reynolds numbers, reaching from 77 to 24,000 and achieved Nusselt numbers from 2.5 up to 93. The maximum heat transfer coefficient measured

with air was $2,200 \text{ W m}^{-2} \text{ K}^{-1}$ with a minimum heat transfer coefficient of $97 \text{ W m}^{-2} \text{ K}^{-1}$. Water was tested at Reynolds numbers spanning from 71 up to 8,700 over which Nusselt numbers from 5.9 up to 55 were achieved. Water tests by far resulted in the highest heat transfer coefficients with a minimum htc of $5,200 \text{ W m}^{-2} \text{ K}^{-1}$ and a maximum of $38,000 \text{ W m}^{-2} \text{ K}^{-1}$. FC3283 data spanned a range of Reynolds numbers from 160 up to 9,600 and achieved the highest Nusselt numbers, reaching from 12 up to 110. The minimum and maximum recorded heat transfer coefficients for FC3283 were $1,300 \text{ W m}^{-2} \text{ K}^{-1}$ and $6,800 \text{ W m}^{-2} \text{ K}^{-1}$, respectively. The highest Reynolds numbers and highest Nusselt numbers were achieved with part C09. The highest heat transfer coefficients were achieved with parts C03 and C06. This can be primarily attributed to the small total jet cross-sectional area—thus, high jet velocities—in combination with the small jet size of nominally 0.6 mm. For reference, Murshed provides ranges of typical overall heat transfer coefficients for different fluid mediums and cooling modes [80] which have been reconstructed in Figure 5-4. Results from this investigation are shown by yellow bars. The reported heat transfer coefficients from this study greatly outperform the high-end typical values of forced convection for similar fluids. Heat transfer for return jet impingement with air rivals water cooling under conventional forced convection techniques, despite air having dramatically inferior thermal properties. Water return jet impingement data exhibited heat transfer coefficients which are competitive with two-phase water cooling techniques according to the typical ranges provided by Murshed [80]. Recall that relatively large jet diameters of 0.6 mm and larger were used in this study in order to ensure hole roundness and manufacturing consistency. Reduced jet sizes are achievable and can further expand the heat transfer coefficients beyond those exhibited here.

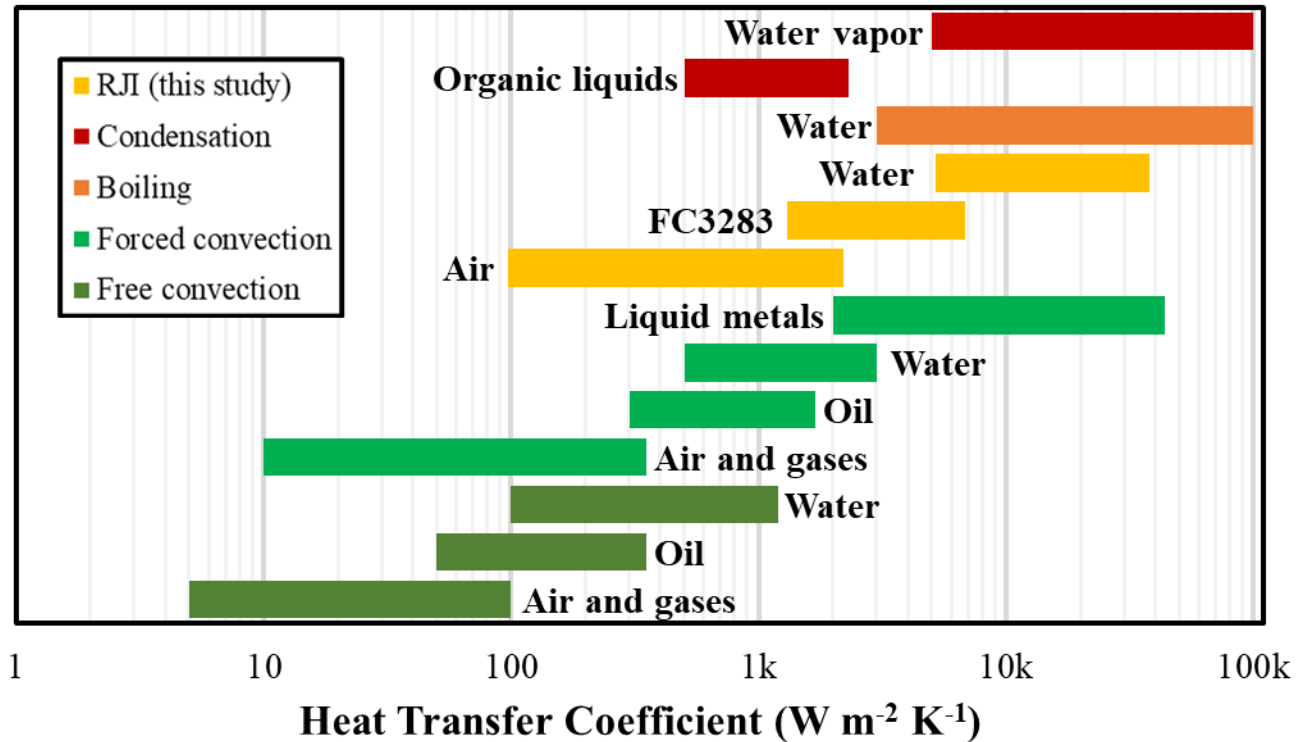


Figure 5-4: Comparison of typical heat transfer coefficient values [80] to experimental results from this study.

A brief note on FC3283 data:

The test facility experienced pressure instabilities during FC3283 data collection which were not present when testing with either water or air. These instabilities were observable as substantial noise in both digital and analog pressure measurements. Sometimes, in the case of excessive instability, tubing in the test facility would visibly vibrate. Cavitation and pump slip present two possible explanations; however, the cause of these pressure instabilities is yet undetermined. Regardless of the cause, the presence of intense pressure fluctuations during testing calls into question the results for the FC3283 test data. Constant pressure fluctuation could disrupt fluid boundary layers from forming, thus likely improving heat transfer performance. As such, FC3283 data was not considered when formulating a heat transfer correlation to describe the impingement system. However, despite the presence of these pressure instabilities the FC3283

data appear to match nicely with air and water data and present an important contribution to this investigation by confirming the Prandtl number dependence of heat transfer performance of the impingement cooling system. Thus, FC3283 data have been retained in this report and are still presented here. The reader, though, should be aware of the testing anomaly and consider the data appropriately.

5.2. Correlation Development and Fit

One of the primary objectives of this investigation is to develop a useful correlation for predicting the heat transfer performance of jet impingement arrays with interspersed fluid extraction ports. In this section, such a correlation is formulated, presented, and validated against the experimental data.

The following equation was considered to describe the Nusselt relationship of the impingement heat transfer system:

$$Nu = aRe^bPr^cK_G \quad 5-11$$

where,

$$K_G = \left(\frac{S}{D_j}\right)^d \left(\frac{H}{D_j}\right)^e \quad 5-12$$

Thus,

$$Nu = aRe^bPr^c \left(\frac{S}{D_j}\right)^d \left(\frac{H}{D_j}\right)^e \quad 5-13$$

Re is the jet Reynolds number and Pr is the fluid Prandtl number. K_G is a unitary parameter for describing the geometry effects. S, H, and D_j represent the geometric parameters as described in

Table 4-1. The coefficients a, b, c, d, and e are all fit parameters which can be adjusted to best fit the data. This equation represents a power-law fit of the data while accounting for fluid properties, flow rate, and the key geometric parameters which were varied in this investigation. The same equation form was used by Huber and Viscanta [20] and a similar form was implemented by Rattner [44].

Equation 5-13 can be reformatted into a linear equation as follows:

$$\ln(Nu) = \ln(a) + b \ln(Re) + c \ln(Pr) + d \ln\left(\frac{S}{D_j}\right) + e \ln\left(\frac{H}{D_j}\right) \quad 5-14$$

In this form a multiple linear regression could be used to determine the best fit values for the parameters a, b, c, d, and e which maximized the coefficient of determination. The resulting Nusselt number correlation is as follows:

$$Nu = 1.126 Re^{0.567} Pr^{0.330} \left(\frac{S}{D_j}\right)^{-0.755} \left(\frac{H}{D_j}\right)^{-0.119} \quad 5-15$$

This regression fits the data with a coefficient of determination of $r^2 = 0.962$. Correlation predicted Nusselt number is plotted against experimentally measured Nusselt number in Figure 5-5a. Once again, the data are segregated by working fluid, following the same labeling convention as before. The root mean square error (RMSE) between data and regression was 3.6 and the mean absolute deviation (MAD) was 10.3%, where MAD is defined as:

$$MAD = \frac{\sum_i^N \text{abs}\left(\frac{Nu_{pred,i} - Nu_{exp,i}}{Nu_{pred,i}}\right) \cdot 100\%}{N} \quad 5-16$$

The solid black bars in Figure 5-5 represent $\pm 25\%$ error boundaries. 92.6% of the data fits within these error limits with the greatest deviation occurring among low-flow rate air tests. For comparison, both Rattner's correlation and Huber and Viscanta's correlation were tested against the experimental data from this investigation. Rattner predicted Nusselt number versus experimental data is given in Figure 5-5b and Huber and Viscanta's prediction is provided in Figure 5-5c. Each pre-existing correlation matches the data fairly well. Rattner's correlation produces a mean absolute deviation of 31.8% and is well centered. 60.8% of the Rattner-predicted data falls within the $\pm 25\%$ error limits. Huber and Viscanta's correlation achieves a slightly better MAD of 28.5%, but tends to underpredict the experimental data. The $\pm 25\%$ bounds contain only 45.1% of the dataset. The tendency to underpredict may be, in part, a result of thermal shortcut losses being more active in the Huber and Viscanta study than in this investigation; however, the manifold architecture is not described in that study. Both the Rattner and the Huber and Viscanta correlations manage to predict approximately 90% of the data within $\pm 50\%$ of experimental results. This presents a promising result while simultaneously highlighting the need for the experimental work conducted in this study. None of the three studies diverge significantly, indicating broad-scale consistency and reliability in the measurements taken. Meanwhile, the inability of prior works to closely predict the data in the present study may emphasize the importance that isolating impingement geometry from manifold geometry has on producing accurate experimental results.

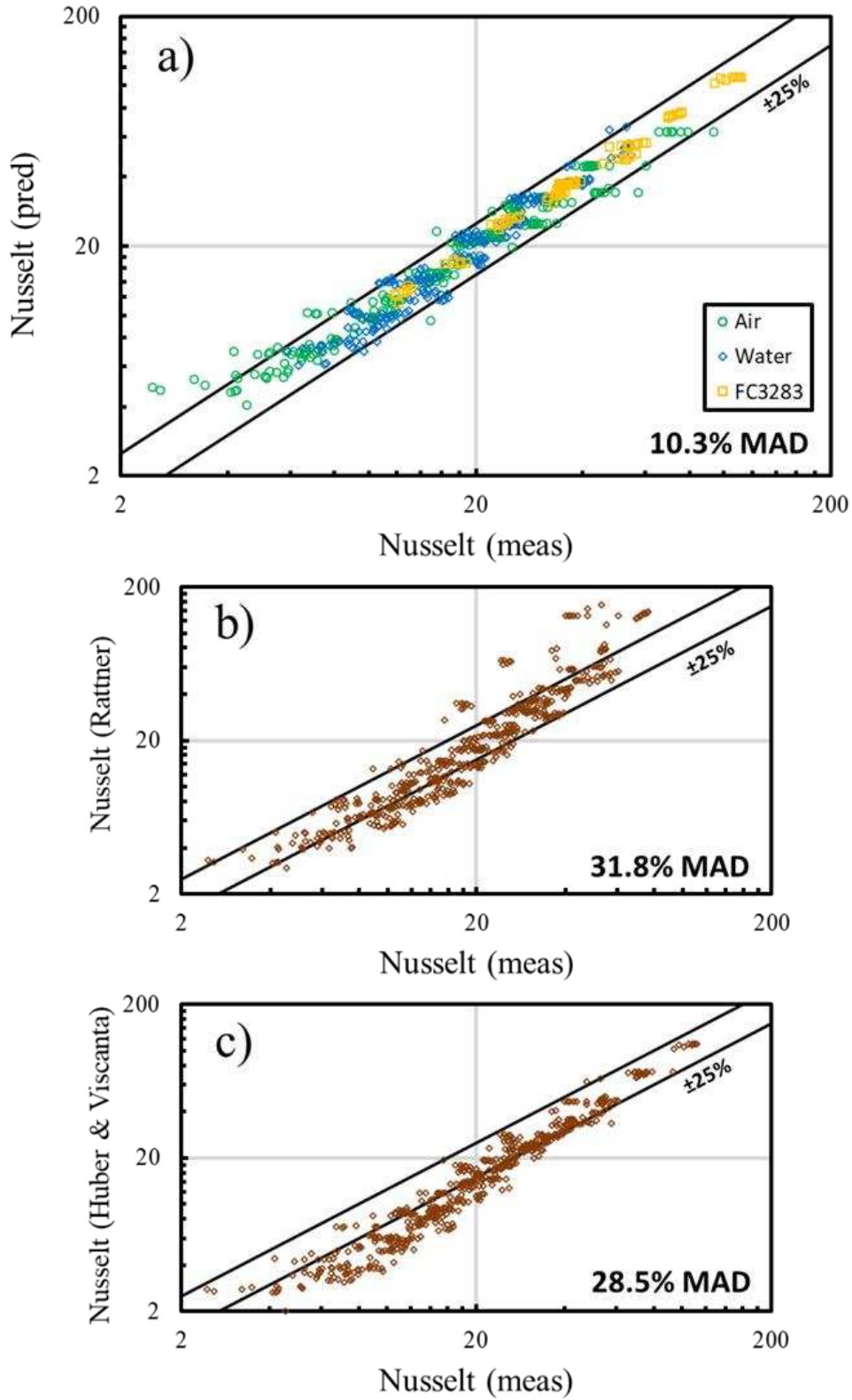


Figure 5-5: Complete steady-state heat transfer dataset; correlation-predicted Nusselt number plotted against measured Nusselt number. a) Present study correlation; b) Rattner correlation [44]; c) Huber and Visaonta correlation [20].

A more exhaustive account of correlation fit is provided in Table 5-1 which reports the fraction of predicted data captured within various error limits from 5% up to 50% for this work and both prior studies. The results have been color-coordinated to provide a better visual representation with green values containing more of the data (better) and red values containing less (worse).

Many previous investigations have correlated Reynolds number to Nusselt number using a power-law model for single impinging jets and for conventional jet arrays. The proposed Reynolds number exponent of 0.567 from this work is within the range of published values from a litany of prior conventional impingement investigations, which have reported Reynolds number exponents ranging from 0.46 up to 0.78 [11,21–31]. Notably, the RJI study by Wei et al. [52] reports a Reynolds number exponent of 0.57, in good agreement with the results provided here.

One notable result involves the dependence of Nusselt number on geometric parameters S/D_j and H/D_j . The best-fit exponents for non-dimensional spacing and non-dimensional height were -0.755 and -0.119, respectively. This result is remarkably similar to the values published by Huber and Viscanta which were -0.725 and -0.123, respectively. This presents a very promising

Table 5-1: Deviation between correlation predicted Nusselt number and experimental Nusselt number data

Dev	Percent Fit		
	This Work	Rattner	Huber & Viscanta
±5%	37.6%	14.3%	5.5%
±10%	62.4%	26.4%	11.8%
±15%	77.8%	37.1%	19.6%
±20%	86.5%	48.5%	27.8%
±25%	92.6%	60.8%	45.1%
±30%	96.2%	69.0%	58.0%
±40%	98.1%	82.1%	74.7%
±50%	98.9%	89.7%	90.5%

result, noting the consistency in geometry dependence between the two independent studies. Figure 5-6 presents a visual representation of the geometry dependence in the form of a contour map. The contours are of the geometric parameter K_G , as described in equation 5-12. Higher values of K_G will result in higher Nusselt numbers. As expected, Low S/D_j values and low H/D_j values produce a higher K_G , with S/D_j being the much stronger performance predictor of the two. The as-fabricated geometric parameters of all nine impingement configurations are overlain onto Figure 5-6 for reference.

Prandtl number was found to correlate to Nusselt number as $Nu \propto Pr^{0.33}$. It was an expected result that Nusselt number would vary with the cube root of Prandtl number. This finding maintains consistency not only with the prior jet impingement studies with interspersed fluid

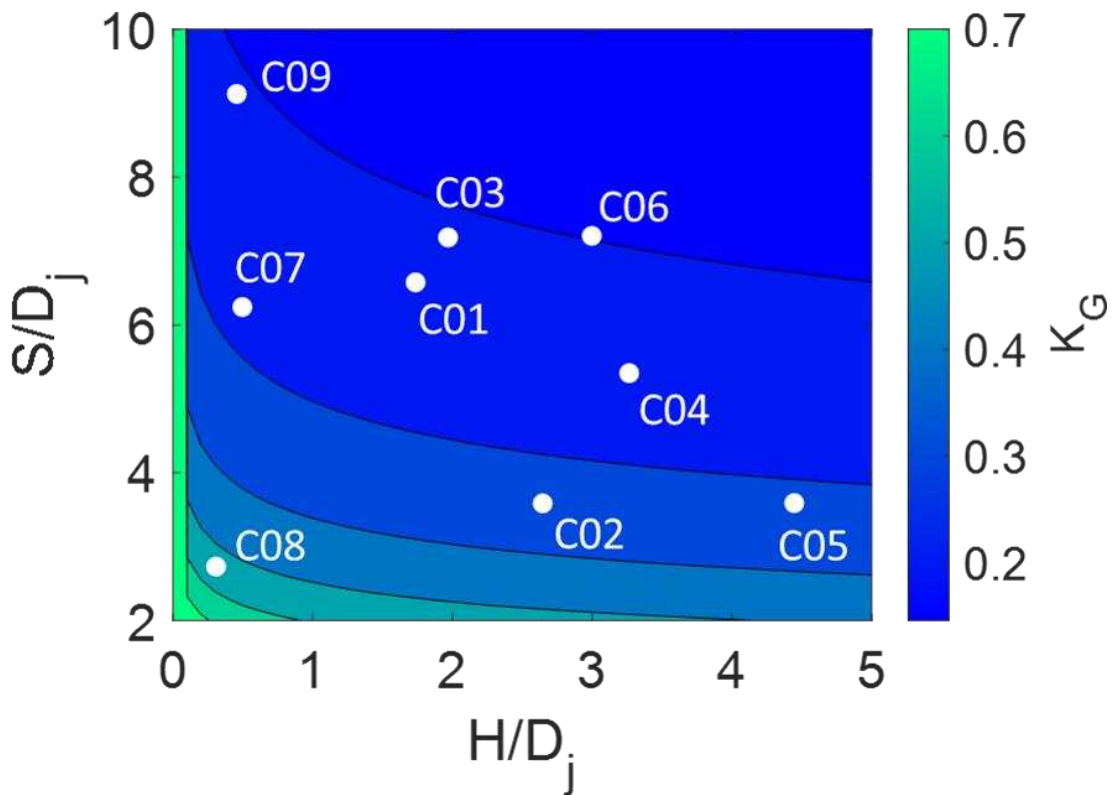


Figure 5-6: Response surface of geometric parameters spacing (S/D_j) and height (H/D_j) on Nusselt geometry factor K_G .

extraction, but also with many other convection correlations presented in the literature (including the Sieder-Tate correlation [81]) and, of course, with the analytical solution of laminar convection across a flat isothermal surface [82]. This analytical backing provides the reason for which a Prandtl number exponent of one-third was selected by Huber and Viscanta [20] in their novel return jet impingement study despite having a lack of experimental data at varying Prandtl numbers. Rattner [44] similarly demonstrated a Prandtl number near one-third empirically, indicating a consistent result across all heat transfer correlations for jet impingement cooling with interspersed fluid removal which have ever been formulated in the known body of literature. Overall, this study supports and improves upon the original return jet impingement heat transfer correlation formulated by Huber and Viscanta [20]. It validates the terms of their correlation while improving the fit through updated coefficients determined in combination with the intentional elimination of manifold effects.

Given that the Prandtl dependence was found to be approximately a cube root, the Colburn J factor offers a convenient method for comparing data across the different working fluids. The Colburn J factor for heat transport is calculated as follows:

$$J = \frac{Nu}{Re \cdot Pr^{1/3}} \quad 5-17$$

Substituting the power law correlation from this work gives:

$$J = \frac{1.126 Re^{0.567} Pr^{0.33} \left(\frac{S}{D_j}\right)^{-0.755} \left(\frac{H}{D_j}\right)^{-0.119}}{Re \cdot Pr^{1/3}} \quad 5-18$$

$$J \approx \frac{1.126 K_G}{Re^{0.433}} \quad 5-19$$

Colburn J factor is plotted against Reynolds number for each impingement device configuration in Figure 5-7, Figure 5-8, and Figure 5-9. The same labeling convention as before is used to distinguish between fluid types. The solid black line plotted through each dataset is constructed using the Nusselt correlation from this study as provided in equation 5-19.

Overall, the correlation appears to match the data trend well for all nine part configurations. Parts C03, C06, and C09 appear to exhibit modest Colburn factor underprediction at high Reynolds number values. These three parts, along with C07 were tested at the highest Reynolds number values, each with peak Reynolds numbers exceeding 8000, indicating that extrapolation to Reynolds numbers beyond the range tested may trend towards gradual underprediction. Low-Reynolds number (≤ 500) laminar water data, as with parts C03, C04, and C07, appears to be slightly underpredicted by the correlation. The greatest deviations seem to occur among low Reynolds number air tests on parts C01 and C05. Despite the pressure fluctuations which occurred during FC3283 testing, the data for those tests lie very close to the prediction curve for the C01 and C09 configurations.

The data show no obvious or dramatic inflection points to indicate transition between laminar and turbulent flow. The correlation provides a smooth prediction through laminar and turbulent flow regimes. As such, it was deemed unnecessary to develop separate correlations to accommodate the different flow regimes. The proposed correlation can be applied towards laminar, turbulent, and transitional flow.

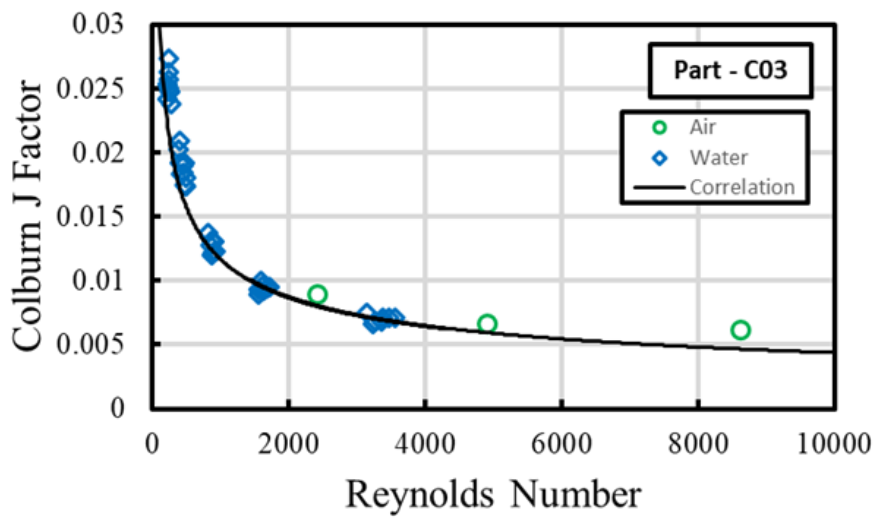
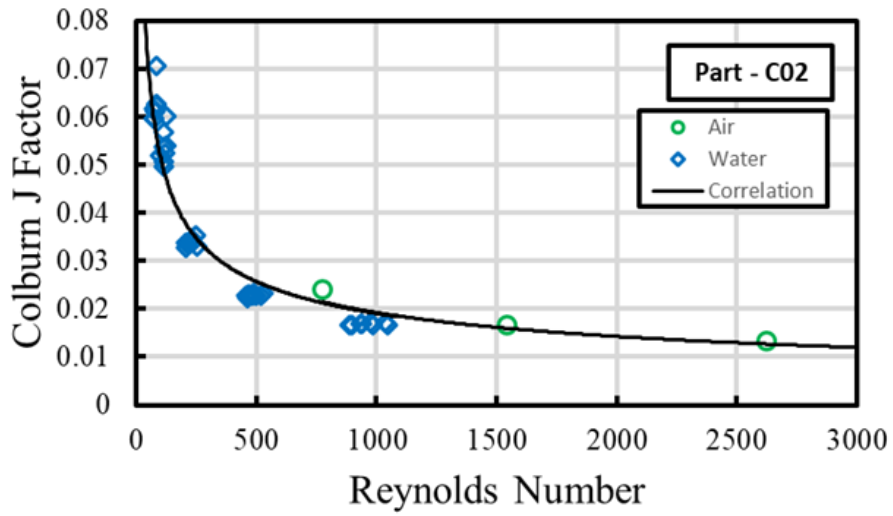
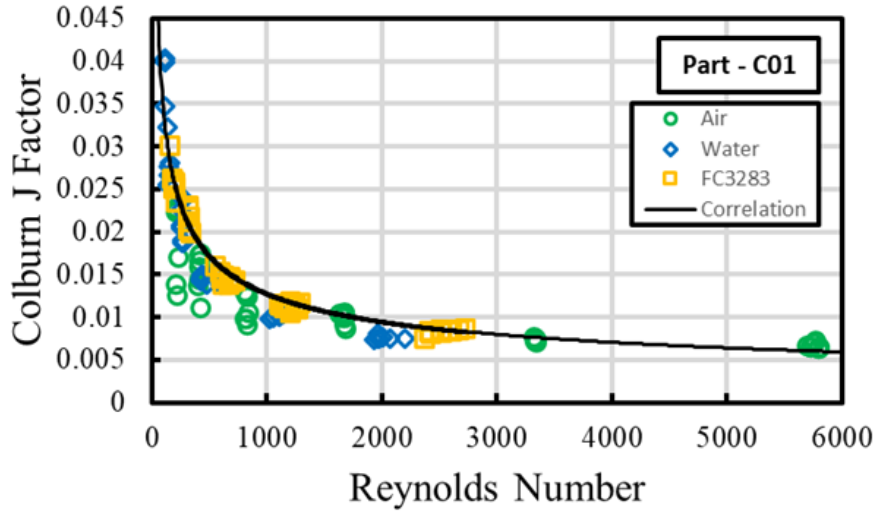


Figure 5-7: Steady-state heat transfer data: Colburn J factor vs Reynolds number for configurations C01, C02, C03

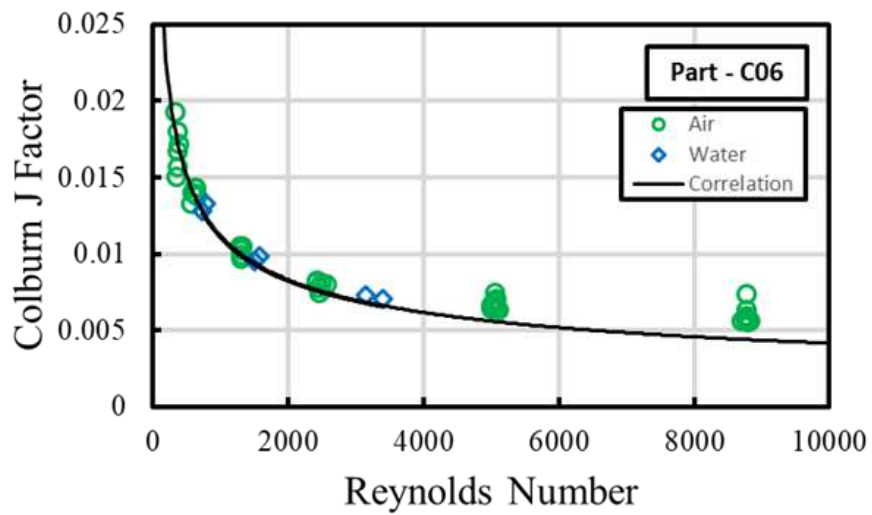
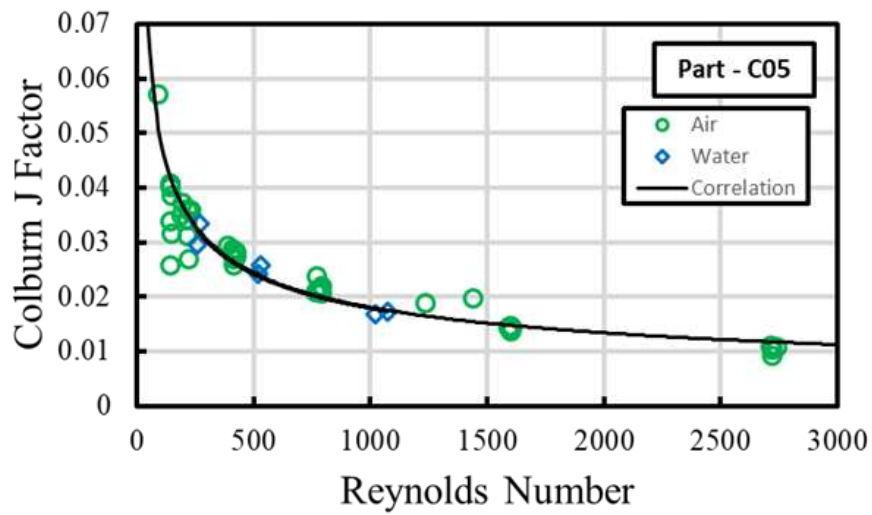
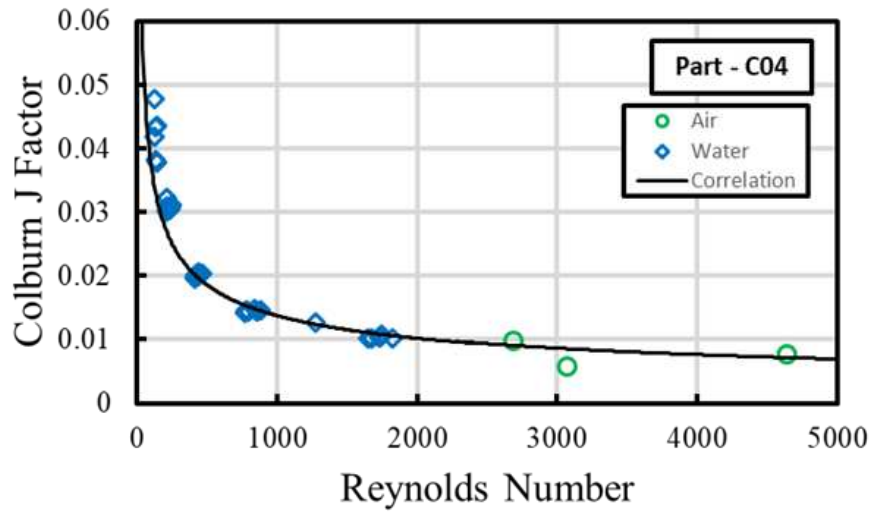


Figure 5-8: Steady-state heat transfer data: Colburn J factor vs Reynolds number for configurations C04, C05, C06

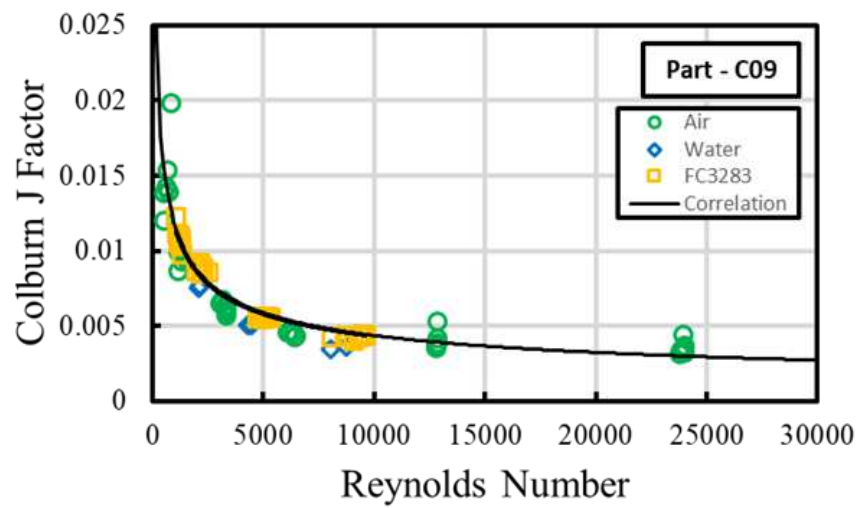
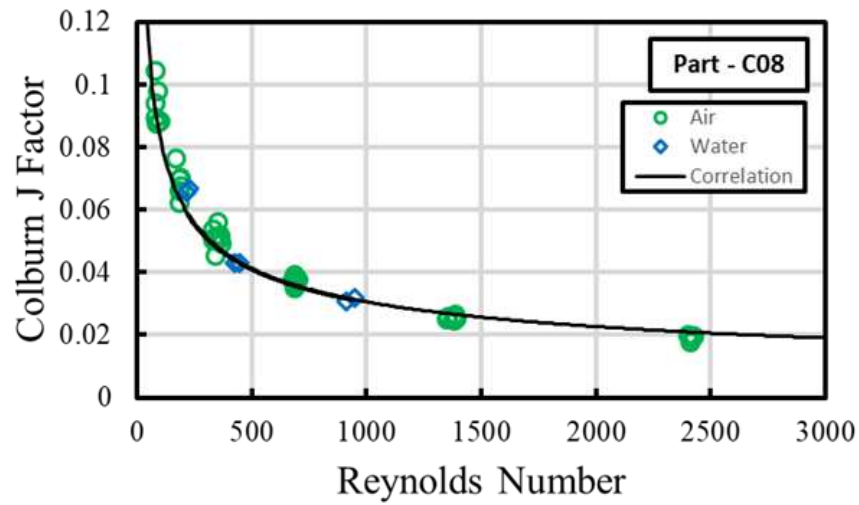
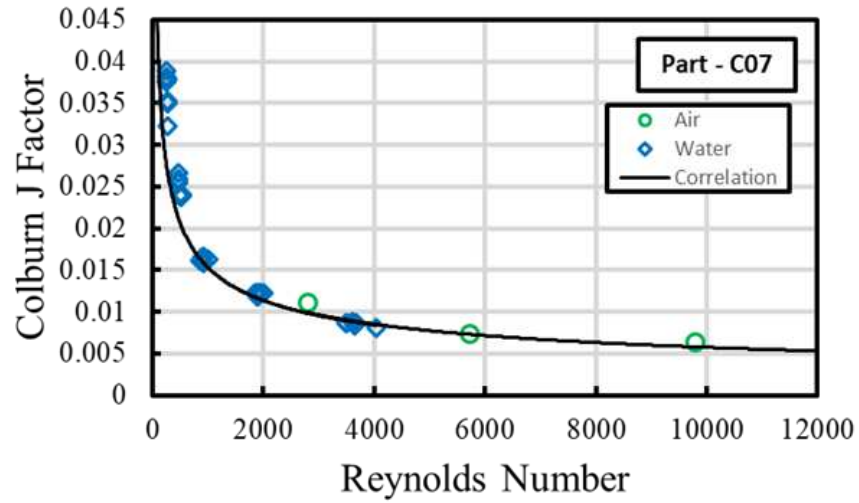


Figure 5-9: Steady-state heat transfer data: Colburn J factor vs Reynolds number for configurations C07, C08, C09

One of the most important results shown in these figures is that the correlation predicts the data well across the three very different working fluids. This is despite dramatic differences in density, viscosity, conductivity, and compressibility. Although only air and water data were used in formulating the correlation, FC3283 data are well predicted, regardless. The result is a robust and diversely applicable correlation which can likely be accurately applied to many different fluid types.

Figure 5-10 displays all nine of the same prediction curves shown in Figure 5-7 through Figure 5-9, without the data. These curves are supplied to provide a visual comparison between each of the different geometry configurations on a constant scale. A higher Colburn factor curve will translate to higher Nusselt number at the same Reynolds number. This is not to be confused

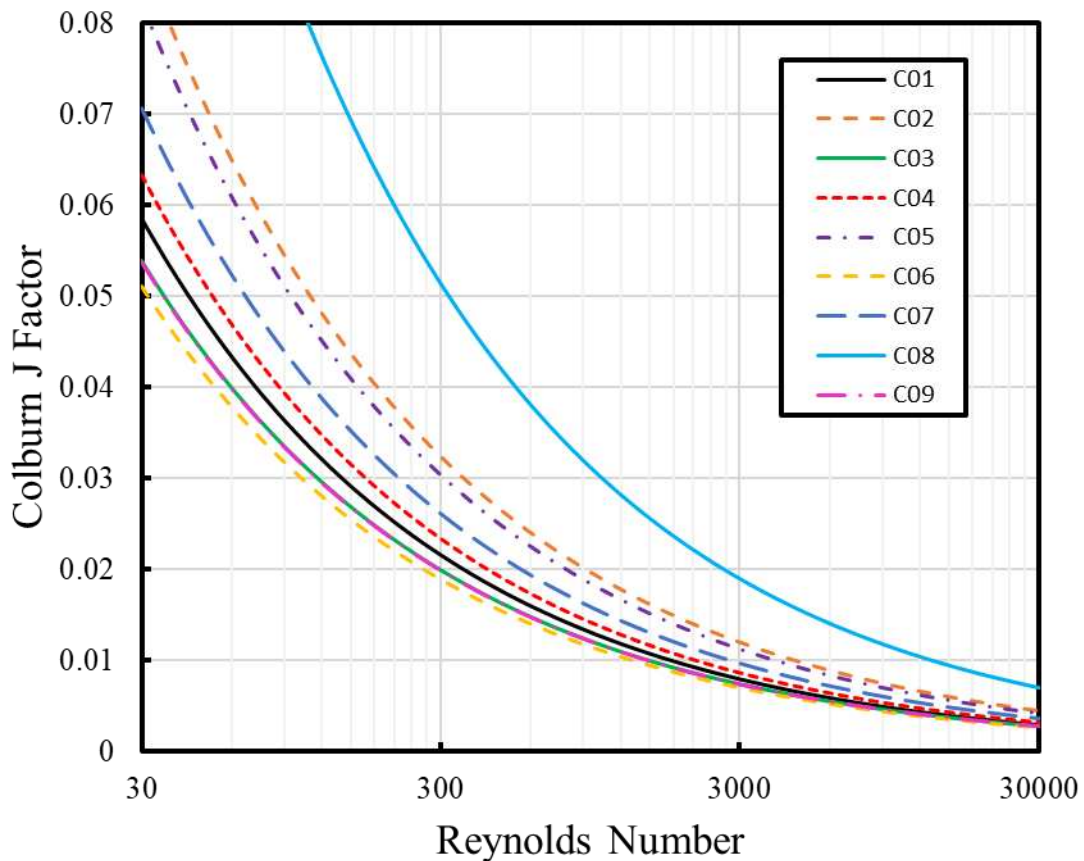


Figure 5-10: Colburn J factor correlation curves for each impingement geometry C01 thru C09

for a performance metric. The cooling performance will depend on what metrics are important to the user. For example, the C08 configuration can achieve the greatest Nusselt number at a given Reynolds number; however, C08 requires a dramatically higher flow rate to achieve the same Reynolds number than the C09 configuration. This results in much higher heat transfer coefficients, which can be achieved using C09 than C08 on a per flow rate basis. Different applications may prioritize heat transfer coefficient, pressure drop, flow rate, pumping power, jet size (manufacturability) differently, resulting in different optimal solutions.

Finally, all 526 data points can be compared simultaneously in a single plot if the data are first normalized by geometric parameters. Reformating equation 5-19 as:

$$\frac{J}{K_G} \approx \frac{1.126}{Re^{0.433}} \quad 5-20$$

allows for the heat transfer results to be compared as a function of Reynolds number only. The outcome is plotted in Figure 5-11 as geometry-normalized Colburn factor versus Reynolds number. Once again, the fluid color coordination is maintained, and the solid black line represents the correlation plotted through the data. Figure 5-11 provides a concise overview of all data and their relationship to the proposed correlation.

The proposed Nusselt number correlation provides robust prediction of the heat transport performance of impinging jet arrays with interspersed fluid extraction. The correlation spans laminar, turbulent, and transitional flow regimes, including Reynolds numbers ranging from approximately 70 to 24,000. Impingement array geometries incorporating $2.7 \leq S/D_j \leq 9.1$ and $0.31 \leq H/D_j \leq 4.4$ are correlated. Prandtl numbers from 0.7 to 21 were included in the investigation. A strong fit with a MAD of 10.3% was found across all geometries, fluids, and flow conditions

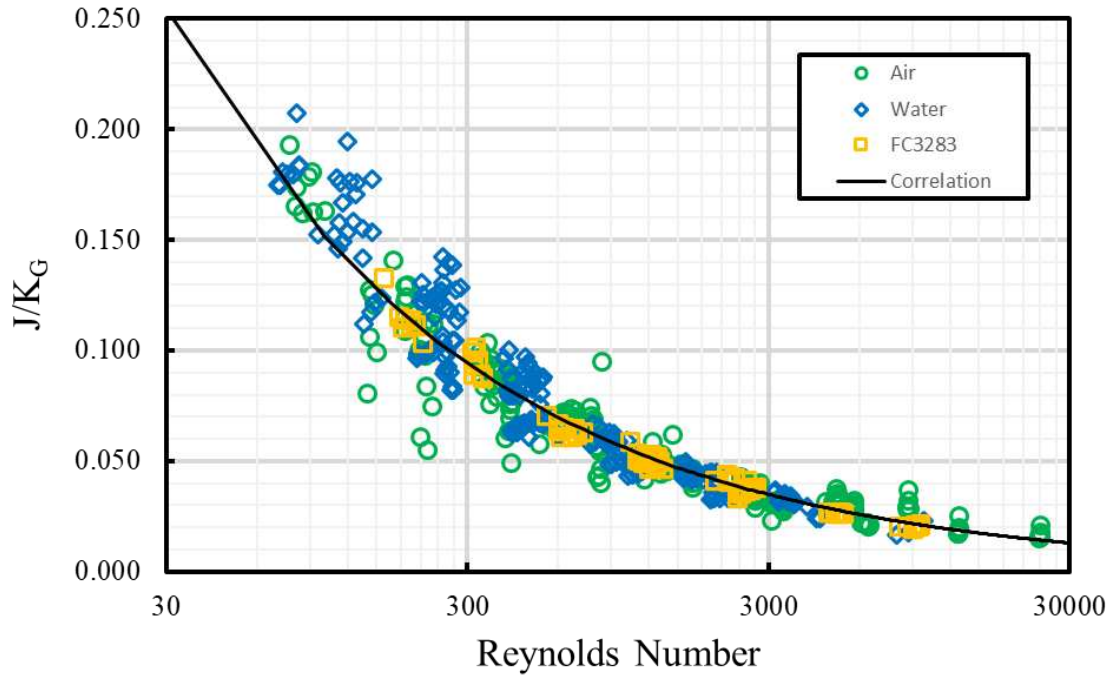


Figure 5-11: Complete heat transfer dataset; geometry-normalized Colburn J factor vs Reynolds Number

tested, which represent the most diverse set of conditions and the most expansive dataset tested on return-jet impingement geometries to date. The proposed Nusselt correlation is summarized below:

$$Nu = 1.126Re^{0.567}Pr^{0.330}\left(\frac{S}{D_j}\right)^{-0.755}\left(\frac{H}{D_j}\right)^{-0.119} \quad 5-21$$

$$for, \quad 70 \leq Re \leq 24,000, \quad 0.7 \leq Pr \leq 21$$

$$and, \quad 2.7 \leq \left(\frac{S}{D_j}\right) \leq 9.1, \quad 0.31 \leq \left(\frac{H}{D_j}\right) \leq 4.4$$

CHAPTER 6. Pressure Drop Results, Discussion, and Correlation

Development

Adiabatic pressure drop testing was conducted for each jet impingement device. This chapter will discuss pressure drop experimental results which were used to establish a predictive correlation for pressure losses through an impingement array with interspersed fluid extraction.

6.1. Results

Pressure drop tests were conducted on all nine jet impingement parts as per the test procedure described in the previous section. An exemplary subset of the resulting data is provided in Figure 6-1 for the C01 geometry configuration. Figure 6-1 shows the experimental adiabatic pressure drop versus standard volumetric flow rate for two water tests (blue diamonds) and two air tests (green circles). The displayed pressure drop values were recorded between the P3 and P2 instrumentation ports as depicted in Figure 4-5, and, thus, they closely represent the pressure drop for the impingement section only, discounting manifold flow restrictions.

The Figure 6-1a plot depicts the results on a linear scale, highlighting the approximately quadratic behavior of the data while accentuating the different pressure drop and flow rate ranges which were tested for the two different flow media. Data for the two separate air tests align nearly on top of one another, as to be indistinguishable in the Figure 6-1 plots despite being taken independently, at different times with several heat transfer tests conducted in between them. The same is true for the two distinct water tests, with slightly more variation apparent due to varying fluid temperatures between each test. Figure 6-1b provides the same data on a log-log scale for a clearer view of each dataset.

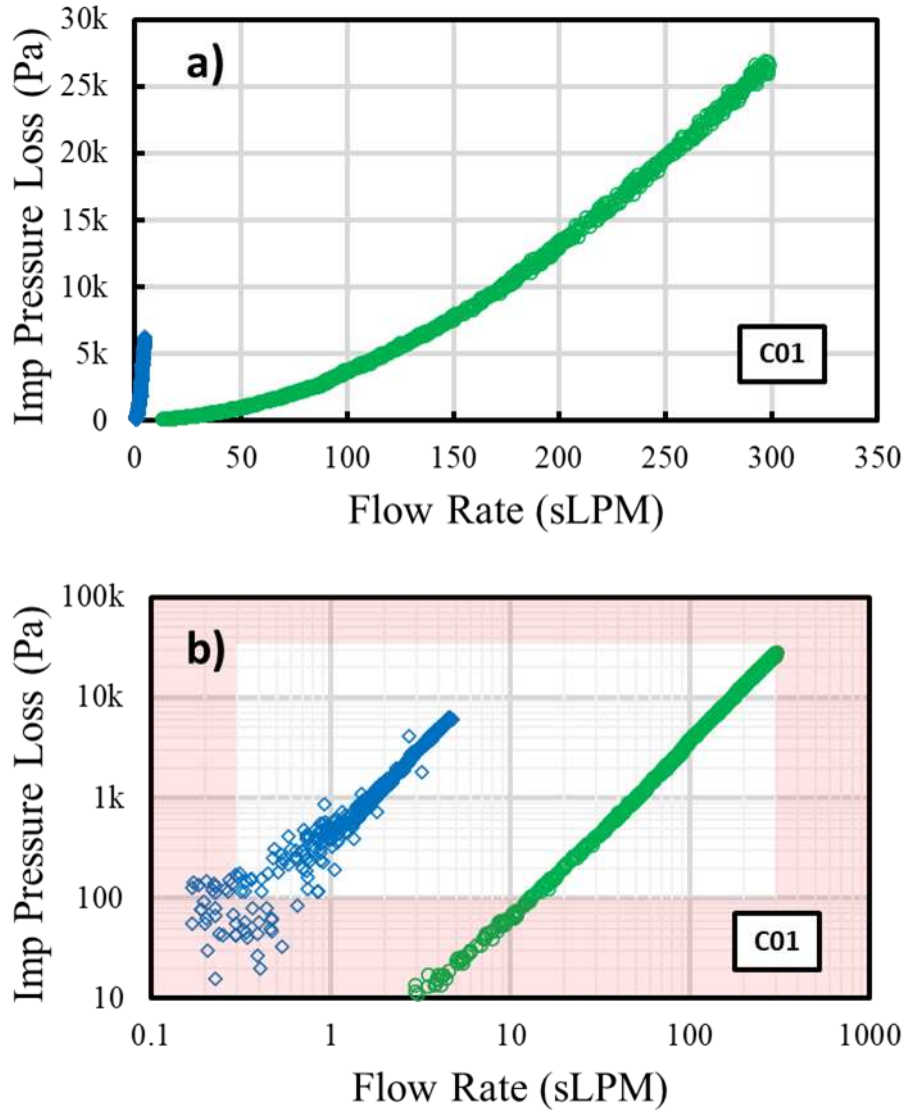


Figure 6-1: Exemplary pressure drop data for part C01 with water and air. a) linear plot of raw data b) log plot of raw data with excluded data shown in red

Also shown in Figure 6-1b is a data exclusion zone highlighted in red. Any data collected within the exclusion zone was cropped from the resulting dataset for subsequent correlation construction due to high levels of measurement uncertainty outside of the included data range. This was done for all tests on all part configurations. The data exclusion zone was constructed considering the measurement limitations of the pressure drop and flow rate instrumentation hardware used in these tests. Pressure drop instrumentation allowed for accurate measurement

from roughly 0.1 kPa up to 34.5 kPa (0.015 to 5 psi) as per the measurement ranges provided by the pressure drop transducers discussed in section 4.3.1. Any data collected outside of this pressure range were excluded, marking the upper and lower exclusion boundaries shown in Figure 6-1. The published measurement range for the liquid flow meter was from 0.3 LPM to 19 LPM, thus any liquid data taken outside of this range were excluded as well. However, liquid test flow rates never approached the 19 LPM upper limitation, making that boundary functionally irrelevant. The left exclusion boundary in Figure 6-1 reflects the lower measurement limit for liquid flow rate. Finally, the air flow meter can accommodate flow rates up to 300 sLPM, thus marking the right exclusion boundary in Figure 6-1. The air flow meter manufacturers claim a measurement accuracy of 2% of the reading down to 2.5 sLPM. In all cases, the lower pressure drop limitation was reached at a flow rate of greater than 2.5 sLPM, making this lower limitation functionally irrelevant.

One notable result apparent in Figure 6-1b is the difference in measurement noise between air tests and water tests at the low measurement range. This can be partially accounted for by the different flow rate measurement instrumentation. The liquid flow meter offers poorer low range accuracy than the air flow meter. Also, its paddle wheel design with Hall effect rotational measurement results in reduced accuracy of the paddle wheel angular speed as the number of rotations in the measurement period are reduced. For the low end of the measurement range, at 0.3 LPM, the paddle wheel rotates at only 1.8 Hz. The frequency measurement period was chosen dynamically by the Keysight 34972A data acquisition system. Another factor which contributes to the increased uncertainty of water pressure drop tests at the low measurement range is the presence of pressure perturbations in the liquid test facility. Liquid flow coming from the pump and passing through the pipes in the liquid test facility causes slight vibrations, thus increasing the pressure drop measurement noise floor relative to the air pressure drop tests. This results in generally higher

pressure drop measurement noise throughout the water tests regardless of flow rate, causing less reliable pressure drop measurement at the low end of the measurement range.

Figure 6-2 provides error bars for the exemplary C01 data sets with both air and water, based on uncertainty propagation discussed in section 4.5.2. Here, measured impingement pressure drop is plotted against jet Reynolds number, calculated as defined in equation 5-6. Impingement

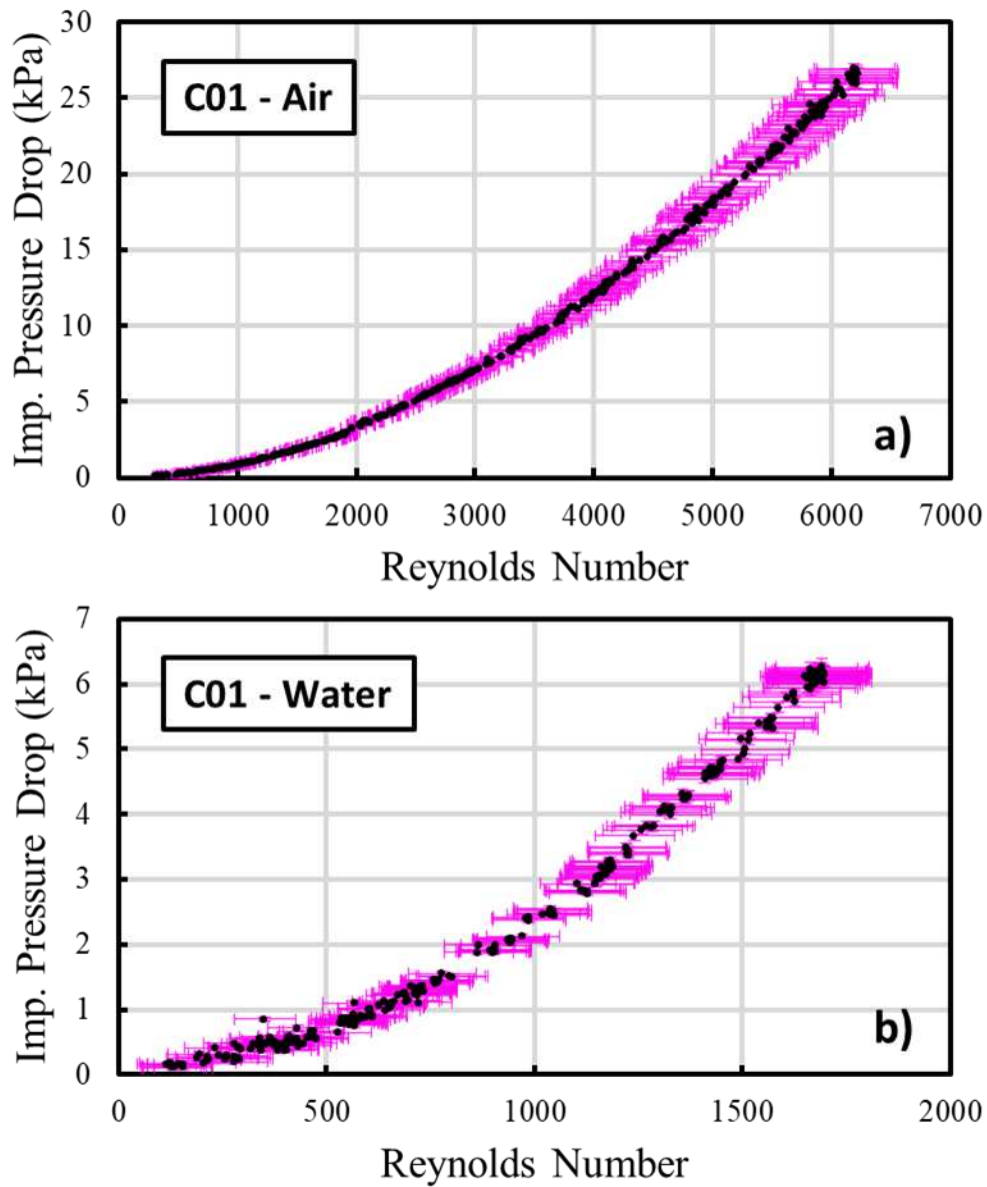


Figure 6-2: Exemplary adiabatic pressure drop data with error bars for part C01 with a) air and b) water.

pressure drop error bars are small enough that they are difficult to detect in Figure 6-2. However, pressure drop uncertainty does become significant at very low pressure drop measurements, with a minimum uncertainty of ± 34 Pa. Figure 6-2a shows that relative Reynolds number uncertainty was fairly constant for the air tests because the flow rate measurement device reports measurement accuracy within 2% of the measured value. Conversely, water tests exhibited fairly constant absolute Reynolds number uncertainty as can be seen in Figure 6-2b by the much more consistently sized error bars. This occurred because the liquid flow rate measurement device reports a measurement accuracy of 1% of full scale measurement. The result was much higher relative uncertainties at low flow rates for water than for air. This is consistent with the Reynolds number uncertainty reported in Chapter 5. The C01 impingement device had the greatest uncertainty. As was previously discussed, this can be attributed primarily to jet diameter uncertainty being highest with that test section. Thus, the uncertainty for all other impingement devices was less than that shown in Figure 6-2.

Pressure drop data for all nine geometry configurations have been compiled into Figure 6-3. Air data are shown in Figure 6-3a) with water data shown in Figure 6-3b). In cases where multiple pressure drop experiments were performed with the same impingement part and fluid medium, only the first conducted test is presented in Figure 6-3 for clarity. The curves plotted through each data set represent simple quadratic regressions. All nine impingement configurations were tested with air and seven of the nine configurations were tested with water, excluding parts C05 and C08. Impingement configuration C06 exhibited the greatest pressure drop on a per-flow basis while part C08 exhibited the least. In order of greatest pressure drop to least, the nine geometry configurations performed as follows—C06, C03, C09, C07, C01, C04, C05, C02, C08—

with both air and water tests resulting in the same ranking order. Considered in terms of ideal pumping power calculated as:

$$W_{p,ideal} = \dot{V}\Delta P_{imp} \quad 6-1$$

where \dot{V} represents the volume flow rate, part C06 required approximately 36 times higher pumping power than the C08 configuration. Recalling the heat transfer results from Chapter 5, part C08 produced one of the lowest heat transfer coefficients of all parts on a per flow rate basis (see additional heat transfer figures in appendix H). However, the highest heat transfer coefficients tested (parts C06 and C09) were only about two to three times greater than those produced by the lowest performing parts (C02, C05, C08). Thus, the disparity in pumping power is dramatically greater than the disparity in heat transfer, suggesting that low pressure drop geometry configurations with moderately reduced thermal performance (C08) may be preferable for producing the greatest cooling performance per pumping power requirement. These tradeoffs in thermal and hydrodynamic performance will be discussed in greater detail in Chapter 7.

Across the 25 adiabatic pressure drop tests performed, Reynolds numbers were investigated ranging from 90 to 22,000. Part C09 tests with air contributed the highest Reynolds number and Part C02 tests with water contributed the lowest.

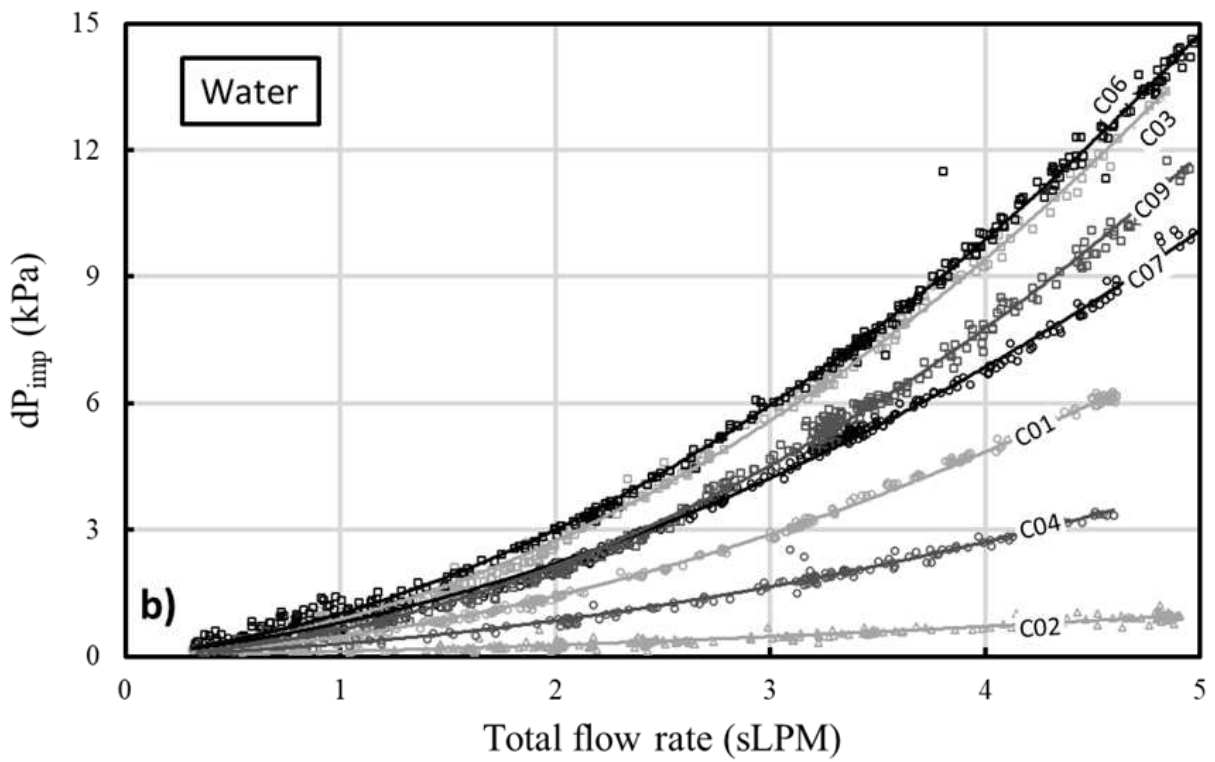
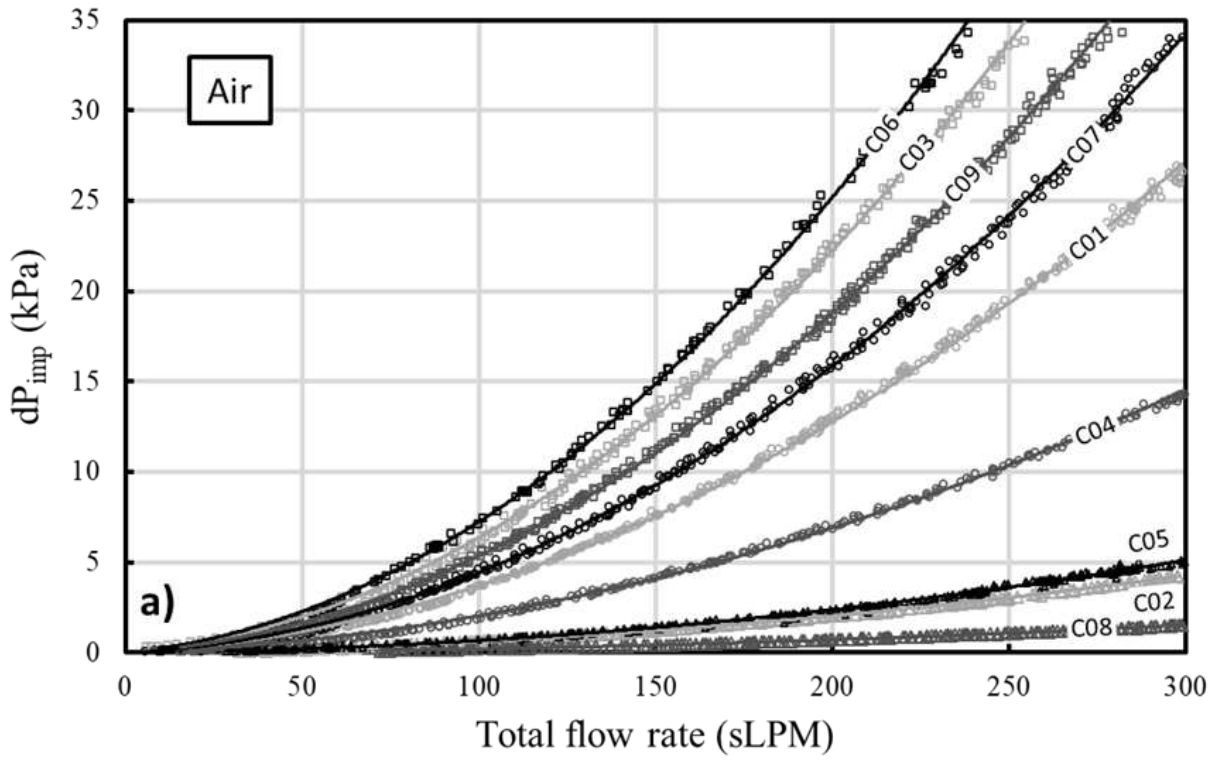


Figure 6-3: Pressure vs flow rate raw data for water and air with all part configurations

6.1.1. Manifold pressure drop contribution

As was previously discussed in section 4.1, the impingement test sections for this study were designed for minimal header pressure drop in order to promote flow uniformity and to maximize the measurement fidelity of impingement section pressure drop. Referring to Figure 4-5, impingement pressure drop was measured via the P2 and P3 measurement ports to provide the most direct possible measurement of impingement region pressure drop. Recall that the P2 measurement port is located directly at the inlet of a single impinging jet while the P3 measurement port is located directly at the outlet of a single impingement return port. Inlet header pressure drop was measured via the P1 and P2 measurement ports, and outlet header pressure drop was measured via the P3 and P4 measurement ports. With this method, it was possible to separate the contribution of total device pressure drop by inlet header, outlet header, and impingement region. However, a key assumption must be made that the pressure at P2 is representative of the impingement inlet pressure at every impinging jet location throughout the array. Similarly, it is assumed that the P3 measurement is representative of outlet pressure at every return port location throughout the array. These assumptions are true when the inlet and outlet header pressure drops are negligible. Thus, the best possible measurement of the impingement region will occur when impingement pressure drop is dominant. Conversely, large header pressure drop will induce greater uncertainty which is difficult to quantify.

Exemplary header and impingement pressure drop data are provided for the C08 part configuration with air in Figure 6-4. Figure 6-4a provides the raw pressure drop data for the inlet header, outlet header, and impingement region. Quadratic regression curves were fit through the data and stacked on one another to compose Figure 6-4b, which provides a clear representation of the fraction of pressure drop contributed by each flow section. For the C08 configuration,

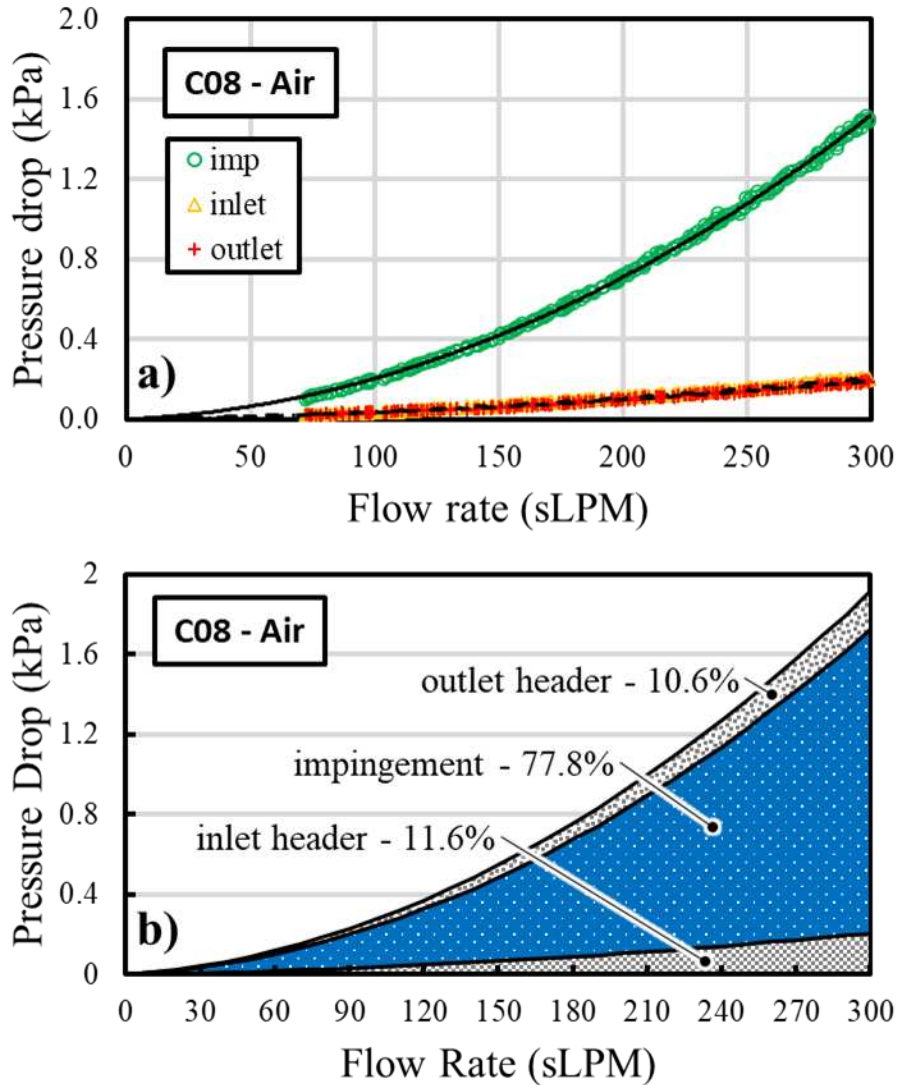


Figure 6-4: Exemplary header pressure drop fraction for part C08 with air, a) raw data with quadratic regression curves, b) stacked proportional pressure drop from regression curves.

approximately 78% of the total device pressure drop could be attributed to the impingement region with inlet and outlet headers contributing the remainder of pressure drop in roughly equal shares. Proportions were calculated as the ratio of the individual areas shown in Figure 6-4b to the total area. This was done by integrating the quadratic regressions for each flow section from 0 to 300 sLPM. For C08, impingement region pressure drop was roughly 7 times greater than inlet header pressure drop, indicating well distributed flow and good measurement fidelity.

Table 6-1 provides impingement pressure drop fractions for all nine test geometries. Parts C01 through C07 all achieved impingement pressure drop fractions greater than 85%. Thus, impingement pressure drop was dominant for all parts except for C09 which had only 23% of total pressure drop contributed by the impingement region. This is a surprising result considering that part C09 had the smallest fraction of impinging jet total cross-sectional area to header cross-sectional area of only 1.3%. This means that the combined cross-sectional area of all 16 jets in the C09 impinging array was only 1.3% of the inlet header cross-sectional area. This result brings into question the flow uniformity and pressure drop measurement fidelity of the C09 test section. Additional testing with an updated manifold design for the C09 geometry is recommended for future investigations. The uniform flow distribution assumption and the port P2 and P3 assumptions can be considered accurate for all other part configurations.

Table 6-1: Fraction of test section pressure drop attributed to impingement region for all test sections. The remainder of pressure drop is from inlet and outlet header sections.

Part num.	Imp. pressure drop fraction
C01	97.3%
C02	89.5%
C03	93.2%
C04	96.4%
C05	86.2%
C06	96.6%
C07	94.8%
C08	77.8%
C09	22.7%

6.2. Correlation Development and Fit

A primary objective of this work is to develop a useful predictive correlation for characterizing the pressure drop of single-phase flow through impinging jet arrays with

interspersed fluid extraction ports across a wide range of geometric and fluid parameters. In this section, the experimental data presented will be correlated to key parameters to accomplish that objective. A predictive equation will be established for quickly and easily calculating the pressure drop through such devices. Recall that the separation of impingement array pressure drop from the pressure drop in manifolds and other ancillary fluid pathways is of critical importance. As such, the correlations presented in this section will attempt to reflect flow restriction in the impingement array only (jet nozzles, return nozzles, and impingement region). In practical application, designers of return jet impingement devices should independently account for manifold pressure drop effects specific to their selected flow routing architecture. Both the impingement array component and the manifold component are necessary to produce an accurate characterization of total device pressure drop performance.

6.2.1. Constant k-factor evaluation

The relationship between frictional pressure losses and fluid flow for single-phase incompressible flow through the impingement array can be described by the Darcy-Weisbach equation:

$$\Delta P_{imp} = \frac{1}{2} \rho v_j^2 \left(f \frac{L_{eq}}{D_j} \right) \quad 6-2$$

where ρ is the fluid density, v_j is the mean jet velocity, D_j is the jet diameter, L_{eq} is the equivalent flow path length, and f represents the Darcy friction factor. In this case the equivalent flow path length was taken to be the sum of the nozzle lengths, jet heights, and the center-to-center distance between a jet and the nearest return port:

$$L_{eq} = 2L + 2H + \frac{S}{\sqrt{2}} \quad 6-3$$

For flow systems without a flow path length or where the flow cross-sectional geometry varies along the path length, it can be convenient to converge the geometric term $\left(f \frac{L_{eq}}{D_j}\right)$ into a single flow loss coefficient, k , also described as the k-factor, such that:

$$k = f \frac{L_{eq}}{D_j} = \frac{\Delta P_{imp}}{\frac{1}{2} \rho v_j^2} \quad 6-4$$

Both a k-factor approach and a friction factor approach were considered for correlation development.

Figure 6-5 once again presents the exemplary dataset from part C01. Two adiabatic pressure drop tests with air are represented by green circles and two water pressure tests are represented by blue diamonds. Here, in Figure 6-5a, experimental pressure drop through the impingement array is plotted against the flow kinetic energy term, $\frac{1}{2} \rho v_j^2$. The slope of this plot, then, represents the k-factor.

As a first-order approximation, a constant k-factor approach can be considered under the assumption that the k-factor is only weakly dependent on flow parameters (fluid properties and flow rate). The data in Figure 6-5a exhibits nearly linear behavior, indicating that a constant k-factor may be able to reasonably characterize the impingement pressure drop. The yellow line in Figure 6-5a represents a constant k-factor of 1.6 and correlates well with the data ($R^2 = 0.98$, $RSME = 0.95$ kPa, $MAD = 13.9\%$). A best fit k-factor was taken for each impingement configuration and the resulting values are tabulated in Table 6-2 along with corresponding fit statistics. Best fit k-factors were calculated by taking a linear regression of each individual test (25 in total as per Table 4-7).

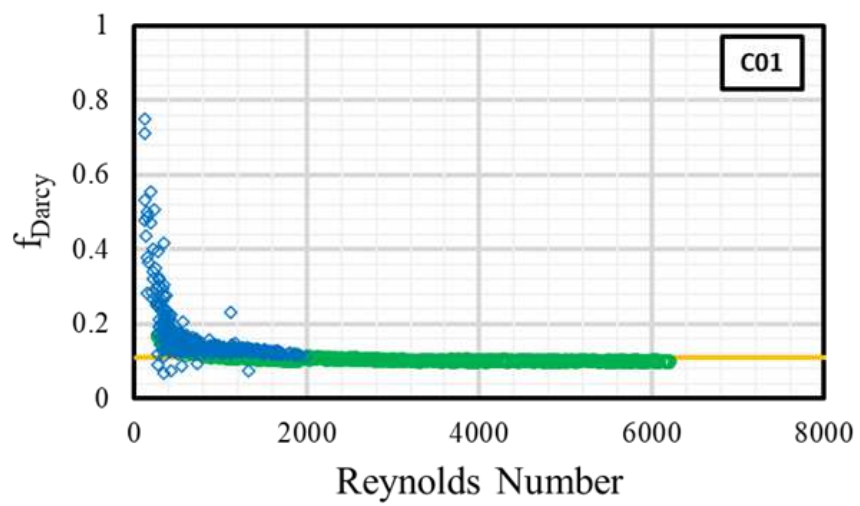
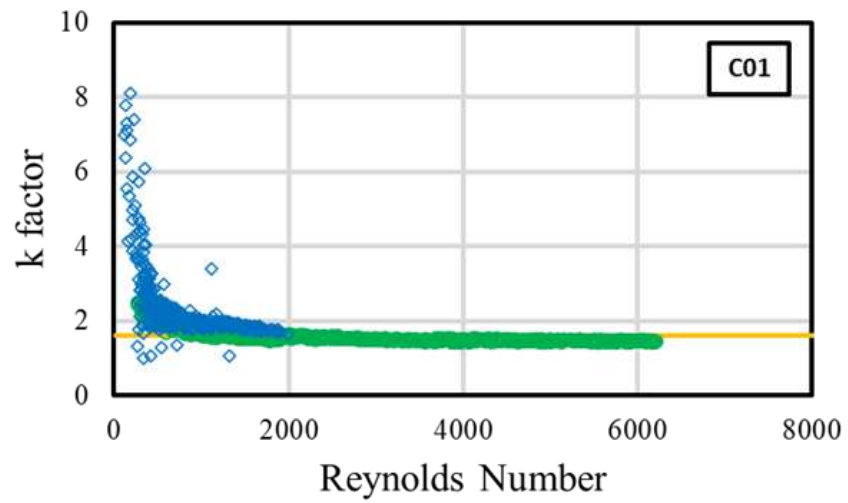
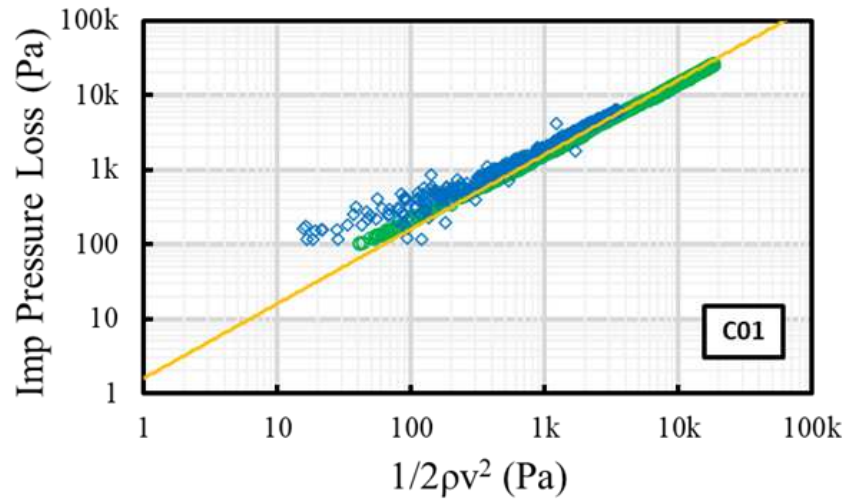


Figure 6-5: Exemplary C01 pressure data. a) pressure drop vs kinetic energy, b) k-factor, c) Darcy friction factor

In cases where more than one test was conducted for a single geometry/fluid combination, the resulting slopes were averaged to produce a single k-factor representative of both tests. This resulted in two best fit k-factors for each geometry configuration (one for water, one for air) except for parts C05 and C08 for which no water data was taken. These k-factors were then similarly averaged to produce a single k-factor for each impingement device considering both water and air experiments. This method was employed rather than producing a single linear regression for each combined air and water dataset to avoid biasing the results by the varying sizes of each dataset. For example, if an air test on part C01 contained 500 data points while a water test contained only 300 data points, the resulting regression would be unfairly biased towards the air data. By averaging the k-factors, equal consideration was given to air and water data regardless of the number of repetitions or the size of each test.

By evaluating statistical metrics (R^2 , RSME, MAD) a constant k-factor approach appears to provide strong predictive agreement with the impingement pressure drop data. Applying a best fit constant k-factor to each geometry configuration allows for prediction of the data across all 25 tests with a worst case mean absolute deviation of 28.8% ($R^2 = 0.966$), which occurred on part C02. A constant k-factor approach can provide a reasonable prediction for impingement pressure

Table 6-2: Best fit k-factors

Part Config.	Const k-Factor (Air)	Const k-Factor (Water)	Const k-Factor (Overall)	R^2	MAD	RMSE (kPa)
C01	1.45	1.75	1.60	0.983	13.9%	0.95
C02	2.26	2.45	2.35	0.966	28.8%	0.14
C03	1.72	2.16	1.94	0.955	27.5%	1.41
C04	1.73	2.08	1.91	0.974	21.8%	0.50
C05	2.75	-	2.75	0.993	10.6%	0.13
C06	2.15	2.43	2.29	0.989	14.1%	0.93
C07	2.23	2.96	2.60	0.946	26.0%	1.98
C08	2.38	-	2.38	0.991	8.1%	0.04
C09	0.85	0.78	0.81	0.980	15.5%	1.13

drop, independent of jet Reynolds number, assuming a correlation relating impingement geometry to k-factor can be established.

Figure 6-5b and c consider the exemplary C01 dataset in terms of k-factor versus Reynolds number and Darcy friction factor versus Reynolds number, respectively. Here the constant k-factor established by Figure 6-5a is carried over and represented once again by a yellow line. The same has been converted to a constant Darcy friction factor for Figure 6-5c using equation 6-4 above. Considering this interpretation of the data, it becomes apparent that, despite good overall fit, a constant k-factor approach fails to capture the sharp incline of k-factor at low Reynolds numbers. The high confidence of fit can be explained by considering that far more data points were taken at high Reynolds numbers than at low ones. For the C01 configuration, for example, only 30% of all data taken were below a Reynolds number of 1000, creating a bias in fit statistics where a good fit is held at high Reynolds numbers. Still, for approximating pressure drop of turbulent flow through an impingement array with interspersed fluid extraction, implementing a constant k-factor offers a promising predictive method. In the next section, a correlational approach for Reynolds number dependent friction coefficients will be evaluated.

6.2.2. Reynolds number dependence

Here, the dependence of flow loss coefficient on Reynolds number will be evaluated. The Reynolds dependency is easiest to see in Figure 6-6 which presents a single air pressure drop test on the C01 geometry as k-factor versus Reynolds number. Here, the transition from laminar to turbulent flow is much more apparent and presents a very intriguing result. The plot has been segmented into 5 distinct regions where the telltale signs of laminar-to-turbulent transition can be seen not just once, but in several locations. Figure 6-7 provides a typical laminar-turbulent transition profile in terms of friction factor versus Reynolds number from Everts and Meyer [83].

This same behavior is seen most easily in Figure 6-6 surrounding a Reynolds number of 2000, in the transition between turbulent region 2 and turbulent region 3. This distinct profile, as expected, suggests a transition from laminar to turbulent flow around $Re = 2000$. However, similar behavior is visible around the 500, 1200, and 4000 Reynolds number marks. These regions are marked in Figure 6-6 and linear trends imposed over top of the data aid in the visualization of each transition

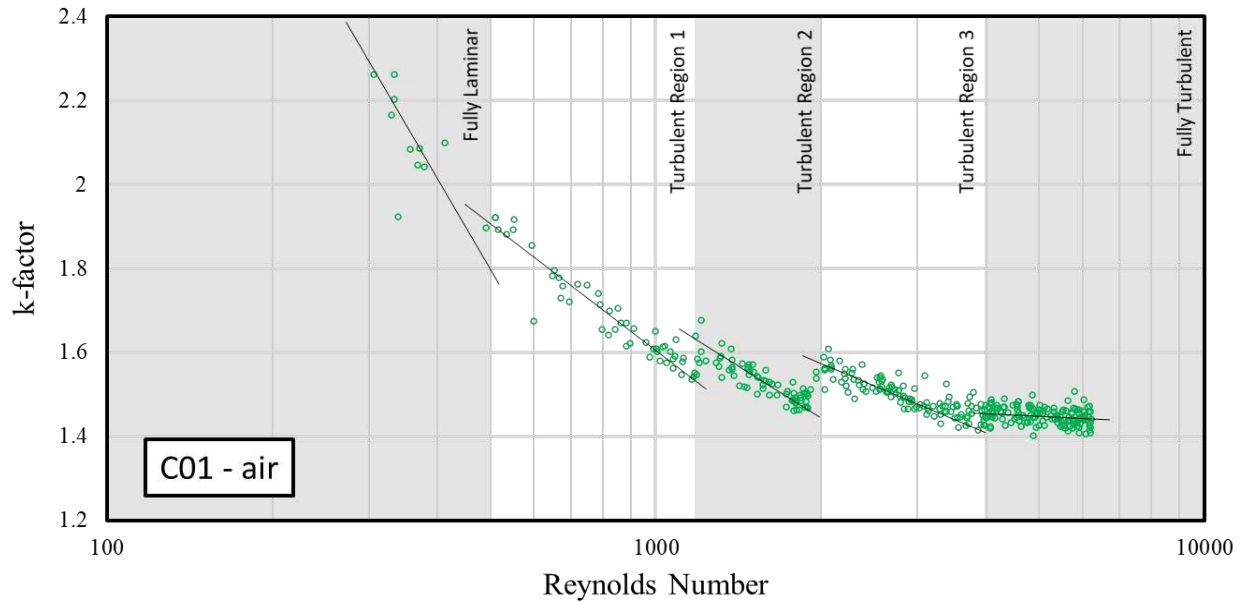


Figure 6-6: Laminar and turbulent flow regimes within C01 air pressure drop test data

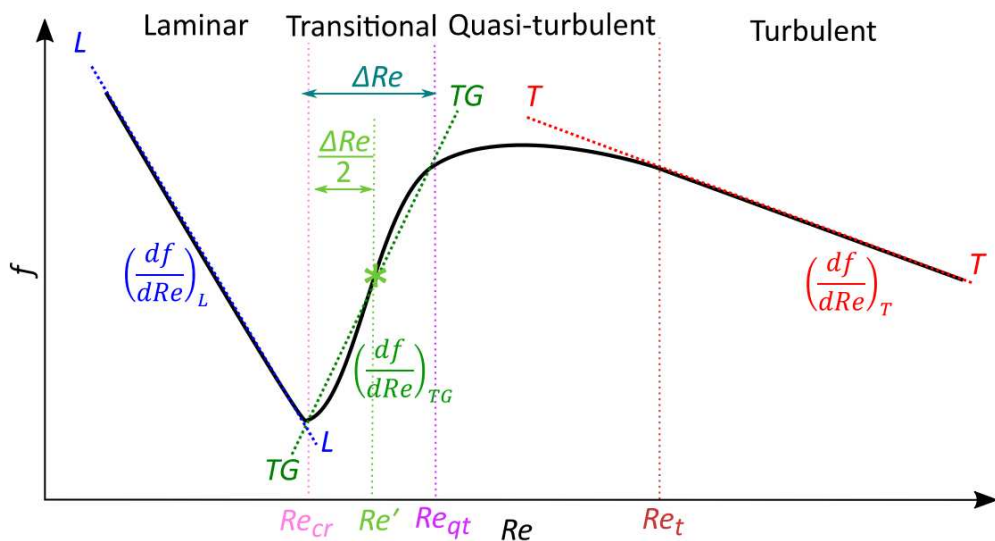


Figure 6-7: Schematic of typical laminar-turbulent transition profile [83].

point. Note that the transition at $Re = 500$ is indistinct due to a lack of data in that region; however, water tests for the same part configuration contain much more data in that region and more clearly indicate the transition. This interesting behavior suggests that the complex impingement flow path can be segmented into multiple, distinct regions which undergo turbulent transition at different stages. For example, the wall jet region may become turbulent before the free jet does.

From the data, it is apparent that the full impingement flow path generally remains laminar below a jet Reynolds number of 500, where the first transition occurs. Above that point, it seems likely that jet-to-jet interaction plays a role in early-onset turbulent transition. As fluid moves along the wall jet, away from the stagnation point, the velocity decreases as the wall jet height grows and the flow expands radially outward. This causes a reduction in local Reynolds number along the flow path length until the fluid reaches a halfway point between the jet nozzle and return nozzle. At that point, the flow is forced to contract again as it converges towards the return port. The fluid accelerates, now increasing the local Reynolds number. Additionally, as the fluid moves away from the jet stagnation point, it begins to interact with adjacent jets at the periphery of its imposed unit cell. As one quarter the flow from a single jet accelerates towards an adjacent return port, it is met by the imperfectly symmetrical flow of three nearby jets. This highly chaotic collision likely produces turbulence in the flow entering the return port well before turbulence occurs in the jet nozzle. Figure 6-8 offers a simple schematic which proposes where different turbulent regions may occur at different points along the impingement flow path. Considering Figure 6-8, Reynolds number increases from one diagram to the next, moving downward. Initially, at low jet Reynolds numbers (as calculated by equation 5-6), laminar flow persists throughout the entire flow path,

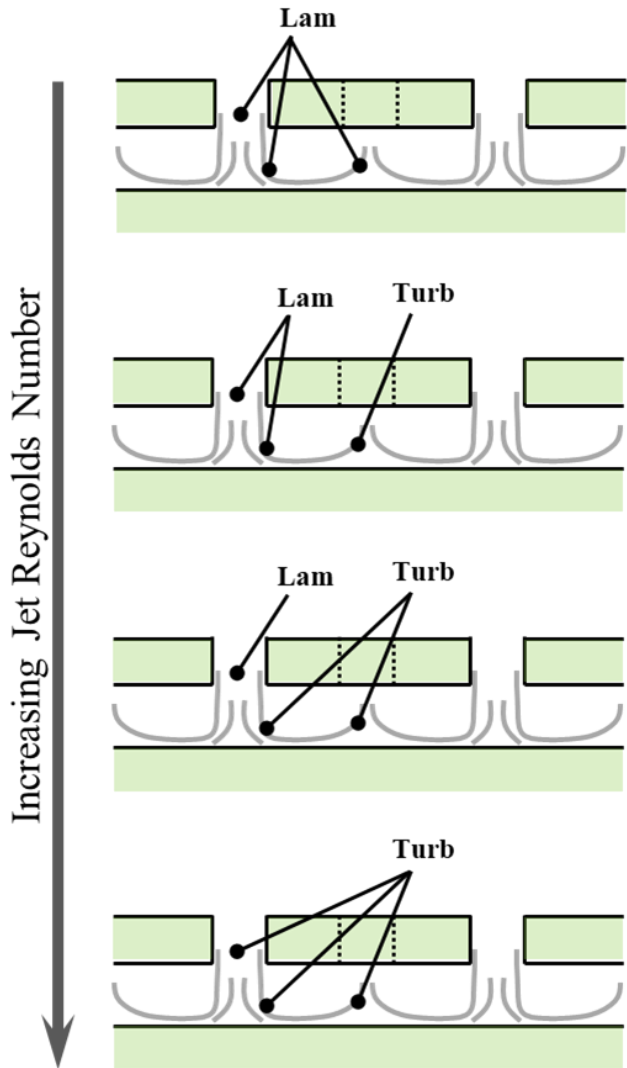


Figure 6-8: Schematic of potential laminar and turbulent regions within impingement flow pathway

indicated by the top schematic. At high jet Reynolds numbers (bottom schematic), turbulence is experienced over the entire flow path. At some intermediate jet Reynolds number, the collision between adjacent jets may trigger turbulence at that interface which propagates downstream while flow upstream from that point remains laminar. This is indicated by the second figure. That condition would persist until another critical jet Reynolds number is reached such that turbulence is triggered in the high velocity wall jet and propagates downstream from there. The experiments conducted in this investigation do not allow for local flow observation to support or contradict this

proposed behavior. However, an early non-impinging jet study by McNaughton and Sinclair identifies similar semi-turbulent regions in liquid jets in short cylindrical vessels with flow transition points at Reynolds numbers of 300, 1000, and 3000 [84]. Further investigation of this phenomenon, either through computational simulations or large-scale experiments where localized flow observations are possible, would be valuable for better characterizing the complex laminar-turbulent transition points identified by this work.

The identification of four distinct laminar-to-turbulent transition points in the return jet impingement flow process, presents an important discovery. However, detailed characterization of each flow transition is unnecessary for developing a useful pressure drop correlation, one of the primary objectives of this investigation. Even a constant k-factor approach offers decent predictive capacity for practical pressure loss calculations. It is clear that some Reynolds number dependency should be accounted for in developing a more authentic flow restriction correlation; however, capturing each flow transition in detail for a wide range of impingement geometries is both very difficult and inadequately rewarding. The difficulty comes from the fact that these flow transitions do not consistently occur at identical Reynolds numbers across part geometries. Instead, this work will propose an approach which divides the flow into only three primary regions, creating a smooth, piecewise function that adequately addresses each.

The three primary regions considered were a fully laminar region given $Re \leq 500$, a fully turbulent region given $Re > 4000$, and a transitional region comprising $500 < Re \leq 4000$ which accounts for the various regions where both laminar and turbulent flow zones are present. A correlation for Darcy friction factor was considered of the form:

$$f_{Darcy} = \begin{cases} Re_t^b Re_l^{1-b} f_G Re^{-1}, & 0 < Re \leq Re_l \\ Re_t^b f_G Re^{-b}, & Re_l < Re \leq Re_t \\ f_G, & Re > Re_t \end{cases} \quad 6-5$$

where, Re_l and Re_t represent the laminar and turbulent Reynolds number transition points of 500 and 4000 respectively. The leading coefficients of Re_t^b and $Re_t^b Re_l^{1-b}$ were set to provide continuity in the function such that the separate piecewise components intersect neatly at the transitional Reynolds numbers. A Reynolds number exponent of -1 was chosen for the laminar section which has been well established for laminar flow systems. In the fully turbulent regime, a constant friction factor is proposed. The coefficients b and f_G are fit parameters where f_G is a function of impingement array geometry.

$$f_G = f\left(\frac{S}{D}, \frac{H}{D}\right) \quad 6-6$$

An equation of similar form was considered for correlating k-factor rather than Darcy friction factor. However, the Darcy friction factor resulted in a slightly better fit than a k-factor correlation, so only the friction factor correlation is presented here. Fit parameters b and f_G were determined by maximizing the sum of R^2 values for all impingement geometry configurations. The best overall

Table 6-3: Best-fit values for f_G correlation fit parameter for all nine impingement geometries.

Part Config.	Best Fit f_G	R^2	MAD
C01	0.10	0.998	10.5%
C02	0.14	0.990	11.4%
C03	0.12	0.984	17.9%
C04	0.11	0.995	11.3%
C05	0.14	0.993	8.4%
C06	0.13	0.998	8.9%
C07	0.19	0.983	20.4%
C08	0.27	0.998	4.2%
C09	0.06	0.980	16.9%
Overall		0.990	12.3%

fit was found for $b = 0.232$ and for the values of f_G provided in Table 6-3. Notably, the best-fit Reynolds number exponent, b , found in this investigation is similar to the Reynolds number exponent of -0.25 proposed by the Blasius equation for turbulent flow in circular pipes. Given $b = 0.232$, $Re_l = 500$, and $Re_t = 4000$, the proposed Darcy friction factor correlation can be presented as follows:

$$f_{Darcy} = \begin{cases} 810f_G Re^{-1}, & 0 < Re \leq 500 \\ 6.86f_G Re^{-0.232}, & 500 < Re \leq 4000 \\ f_G, & Re > 4000 \end{cases} \quad 6-7$$

Also provided in Table 6-3 are fit statistics for each geometry configuration. These can be compared to the fit statistics provided in Table 6-2 to see how incorporating Reynolds number dependence has improved correlation fit. All R^2 values are now greater than 0.98 and the largest mean absolute deviation is 20.4%.

Figure 6-9 revisits the exemplary C01 dataset which now includes the empirical correlation from equation 6-7 with f_G set to 0.1 as per Table 6-3. The resulting trend follows the data much

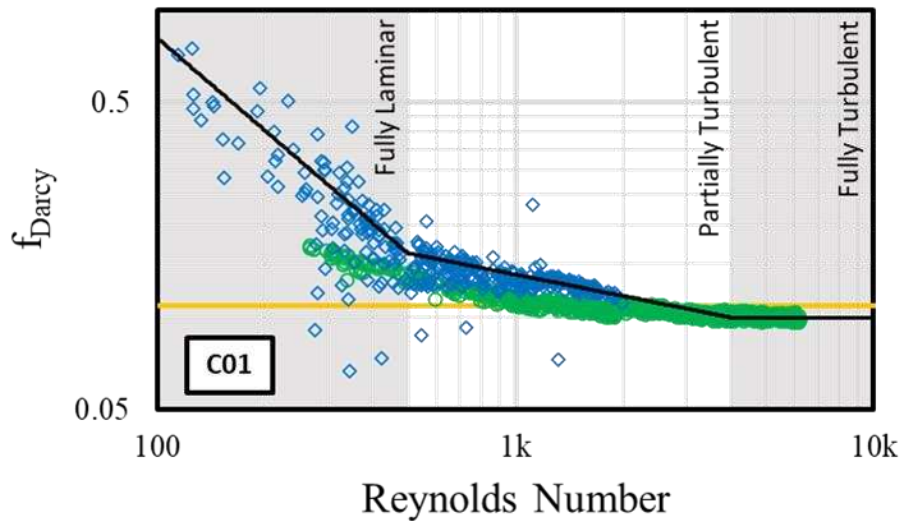


Figure 6-9: Darcy friction factor with exemplary correlation curve fit for part C01

more closely than the constant k-factor approach. Now, given an equation which can correlate f_G to key impingement geometric parameters, S/D_j and H/D_j , a broad empirical correlation for impingement array pressure drop can be formed.

6.2.3. Geometric dependence

Power law and quadratic equation forms were considered for correlating f_G . The following equations present each of these options.

$$f_G = C_1 \left(\frac{S}{D_j} \right)^{C_2} \left(\frac{H}{D_j} \right)^{C_3} \quad 6-8$$

$$f_G = C_0 + C_1 \left(\frac{S}{D_j} \right) + C_2 \left(\frac{S}{D_j} \right)^2 + C_3 \left(\frac{H}{D_j} \right) + C_4 \left(\frac{H}{D_j} \right)^2 + C_5 \left(\frac{SH}{D_j^2} \right)^2 \quad 6-9$$

Other polynomial forms were considered with more or fewer terms. Other terms included SH/D_j^2 , S/H , H/S , L/D_j , and L/D_j^2 . Regressions were performed with equations 6-8 and 6-9 to determine best-fit values for the C_i coefficients. The resulting power law and quadratic correlations for f_G are as follows:

$$f_G = 0.471 \left(\frac{S}{D_j} \right)^{-0.746} \left(\frac{H}{D_j} \right)^{-0.092} \quad 6-10$$

$$f_G = 0.311 + 0.00315 \left(\frac{S}{D_j} \right) - 0.00288 \left(\frac{S}{D_j} \right)^2 - 0.0887 \left(\frac{H}{D_j} \right) + 0.00831 \left(\frac{H}{D_j} \right)^2 + 0.000295 \left(\frac{SH}{D_j^2} \right)^2 \quad 6-11$$

Figure 6-10 compares the proposed power law and quadratic equations for f_G to the best fit values from Table 6-3. The black triangles were calculated using equation 6-10, and the orange X's were calculated using equation 6-11. The power law regression fits the data with a coefficient of determination of only $R^2 = 0.55$ while the quadratic regression achieved $R^2 = 0.94$. P-values for each of the coefficients in the power law regression were also quite high, with the smallest p-value being 0.12. For the quadratic regression, all coefficients exhibited a p-value less than 0.05 except for the constant term which had a p-value of 0.076. Overall, the quadratic regression exhibited much better agreement with best fit f_G values than the power law regression. Thus, it is proposed that equation 6-11 be used for correlating impingement array geometric parameters to frictional pressure loss.

A contour map of equation 6-11 is provided in Figure 6-11 overlain with the nine test geometries. Part C08 exhibited the highest geometric friction coefficient, despite contributing the lowest pressure drop on a per flow rate basis. Several of the part geometries (C01, C02, C03, C04,

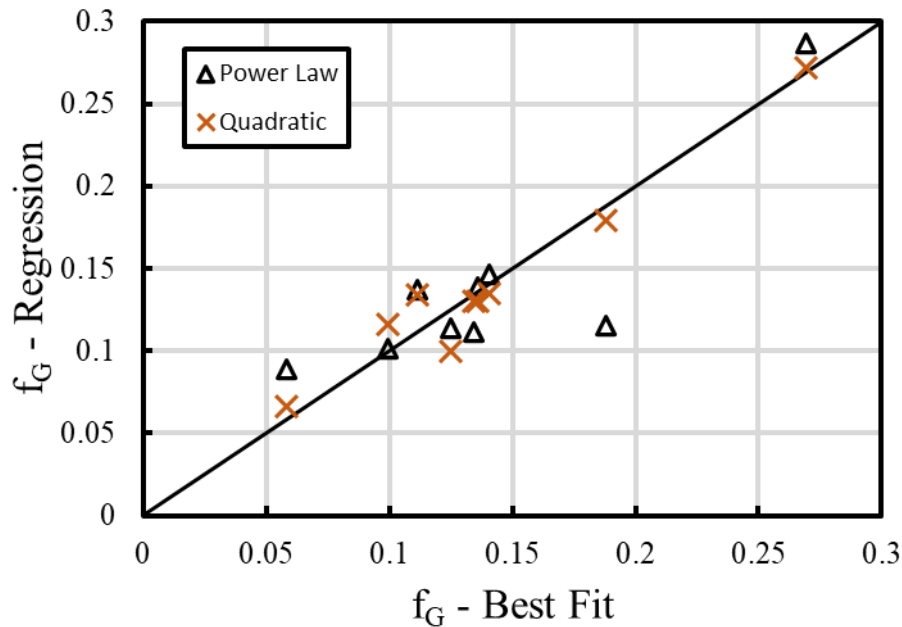


Figure 6-10: Regression goodness of fit for Darcy friction factor geometry coefficient f_G

C05, C06) exhibited comparable friction coefficients while only the impingement geometries with low jet height to diameter ratios (C07, C08, C09) diverged significantly, indicating that H/D_j is the dominant predictive factor for determining impingement friction factor. Notably, in Figure 6-11, the upper right region indicating high H/D_j and S/D_j ratios is patterned off in red where the quadratic correlation predicts a rapid increase in f_G . It is highly unlikely that this represents an authentic characterization of the geometry-dependent flow restriction behavior of an impingement array, but rather is an artifact of the curve fitting approach. It is not recommended to extrapolate pressure drop correlations into or beyond the region considered in Figure 6-11. More diverse geometries should be tested to compose a better characterization of the geometry space.

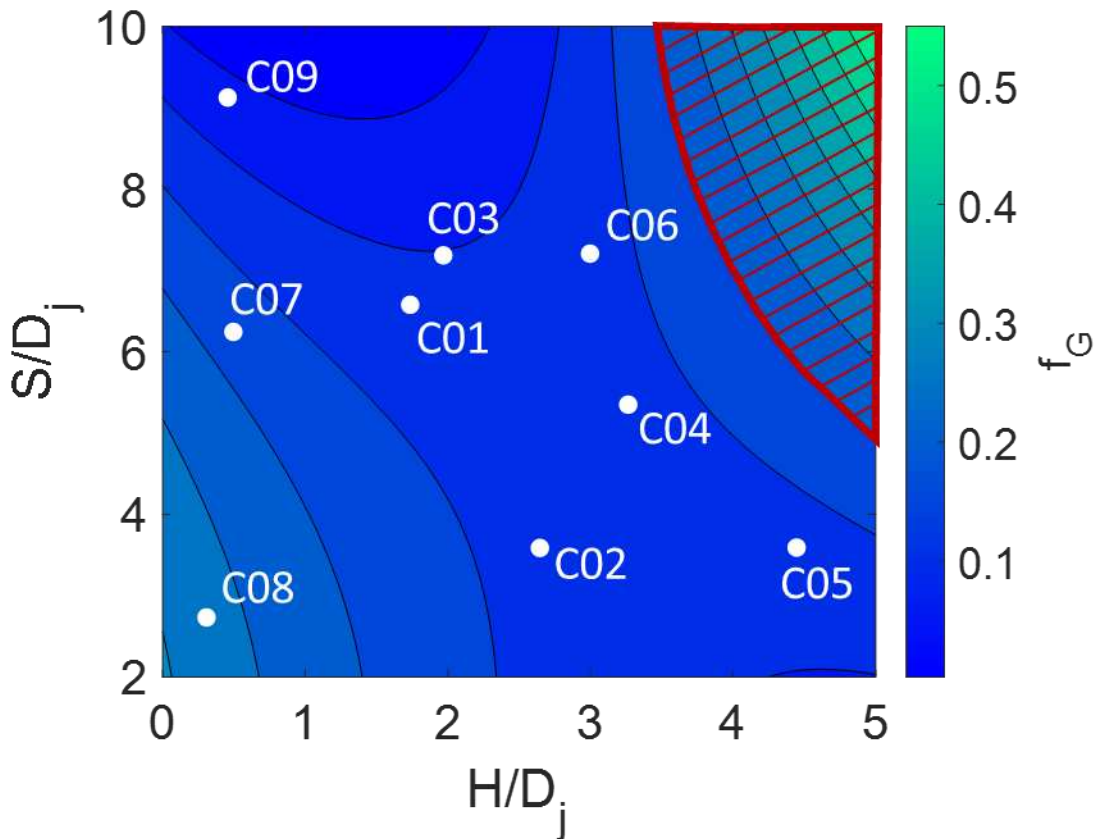


Figure 6-11: Contour map of friction factor geometric coefficient f_G

6.2.4. Goodness of fit

The Darcy friction factor correlation from equation 6-7 was used in conjunction with the quadratic regression expressed in equation 6-11 and compared to the experimental data. These two equations are consolidated into the following proposed flow loss correlation for return jet impingement arrays:

$$f_{Darcy} = \begin{cases} 810f_G Re^{-1}, & 0 < Re \leq 500 \\ 6.86f_G Re^{-0.232}, & 500 < Re \leq 4000 \\ f_G, & Re > 4000 \end{cases}$$

$$f_G = 0.311 + 0.00315 \left(\frac{S}{D_j}\right) - 0.00288 \left(\frac{S}{D_j}\right)^2 - 0.0887 \left(\frac{H}{D_j}\right) + 0.00831 \left(\frac{H}{D_j}\right)^2 + 0.000295 \left(\frac{SH}{D_j^2}\right)^2 \quad 6-12$$

Figure 6-12, Figure 6-13, and Figure 6-14 depict experimental Darcy friction factor values for all 25 adiabatic pressure drop tests, segregated by impingement geometry. The black line overlaying the data on each figure represents the proposed equation 6-12 correlation. Also present is a solid yellow line which once again represents the constant k-factor approach where best-fit flow loss coefficients are used from Table 6-2. Finally, the purple line was constructed using Rattner's k-factor correlation [44]. The proposed correlation follows the data trend well, incorporating both air and water tests across all nine impingement geometries. Rattner's correlation has a tendency to underpredict the experimental data. It also tends to remain mostly constant well into very low Reynolds numbers despite the correlation having been originally developed for fully laminar flow with Reynolds numbers below 500.

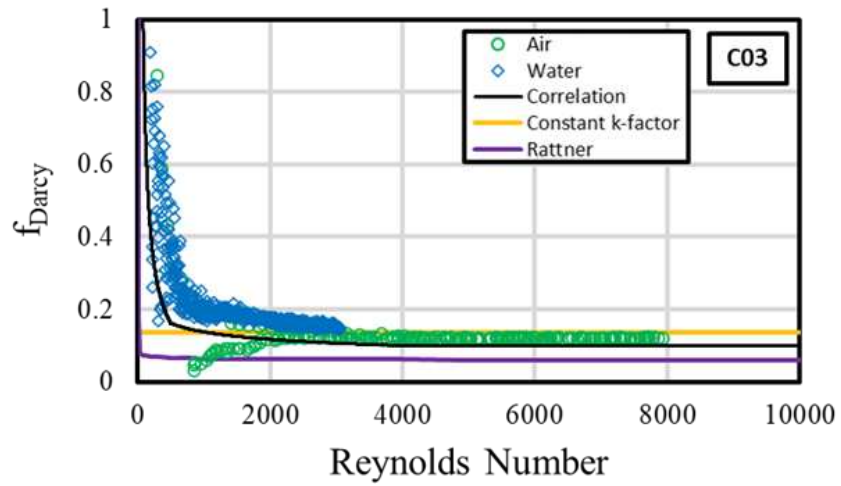
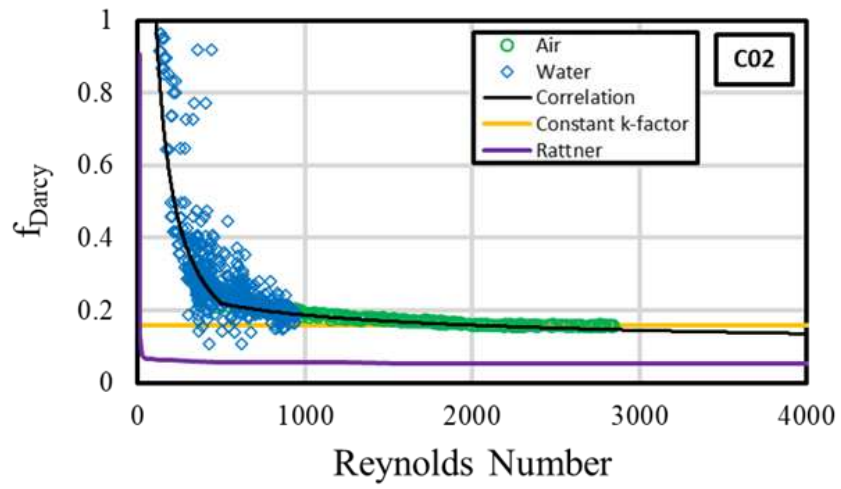
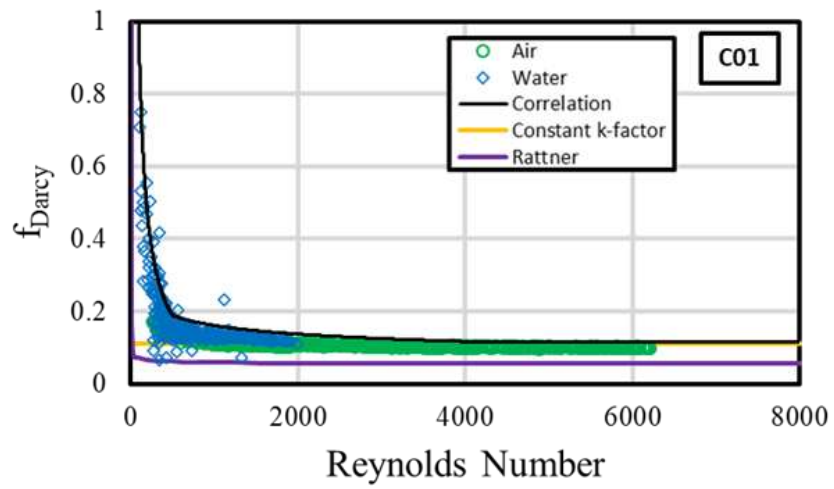


Figure 6-12: Darcy friction factor experimental data with proposed correlation and Rattner correlation for C01, C02, C03

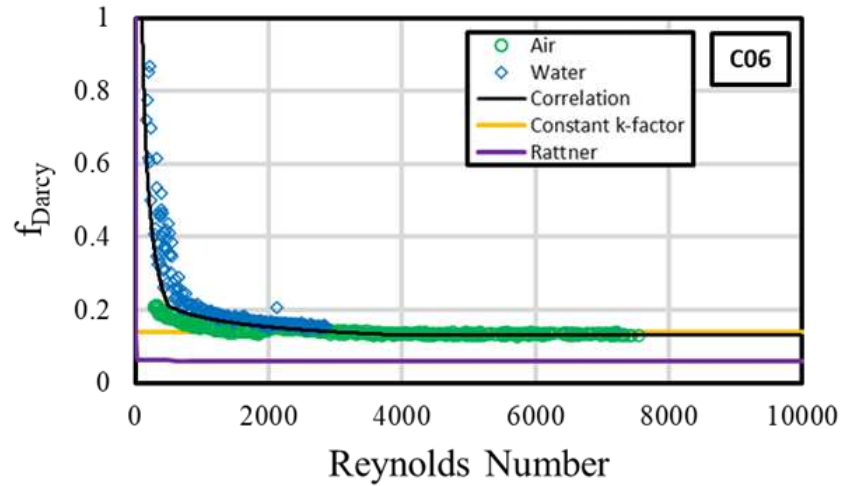
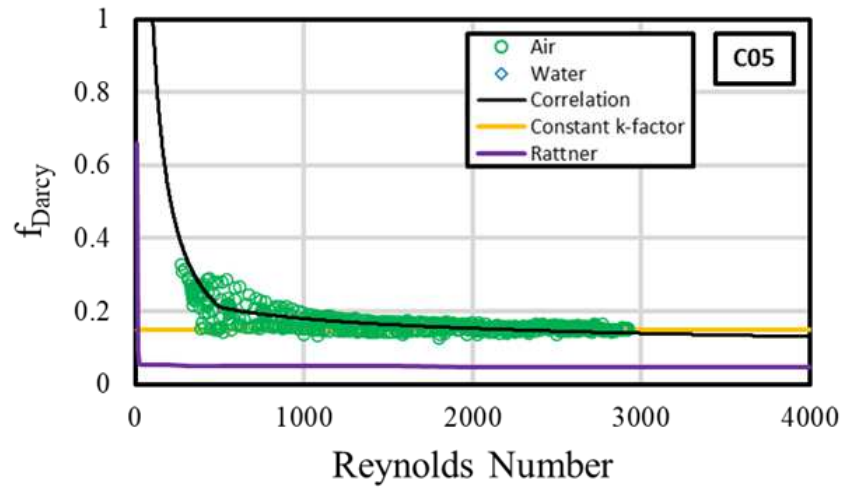
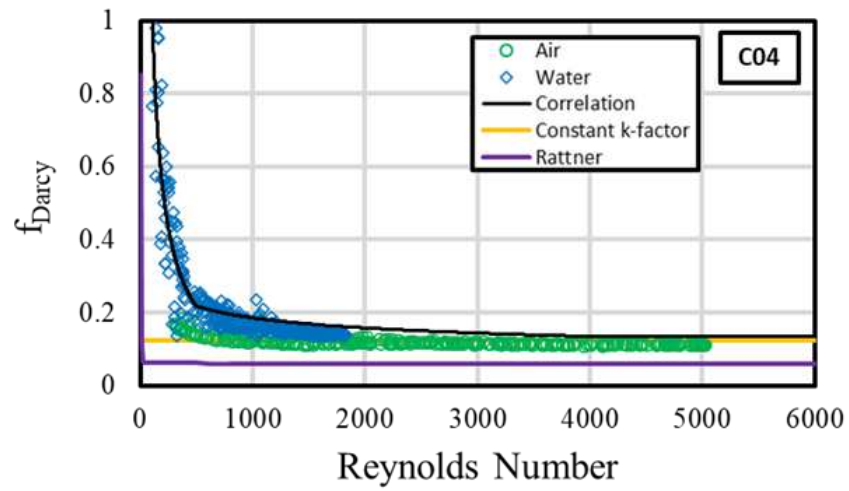


Figure 6-13: Darcy friction factor experimental data with proposed correlation and Rattner correlation for C04, C05, C06

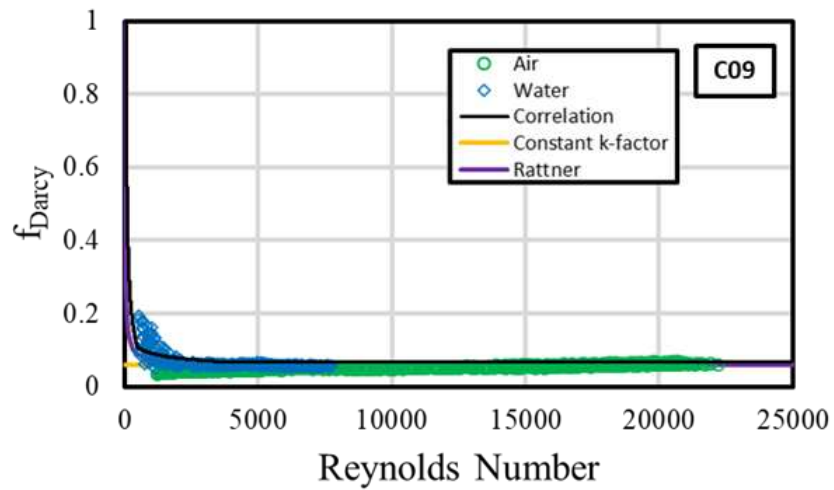
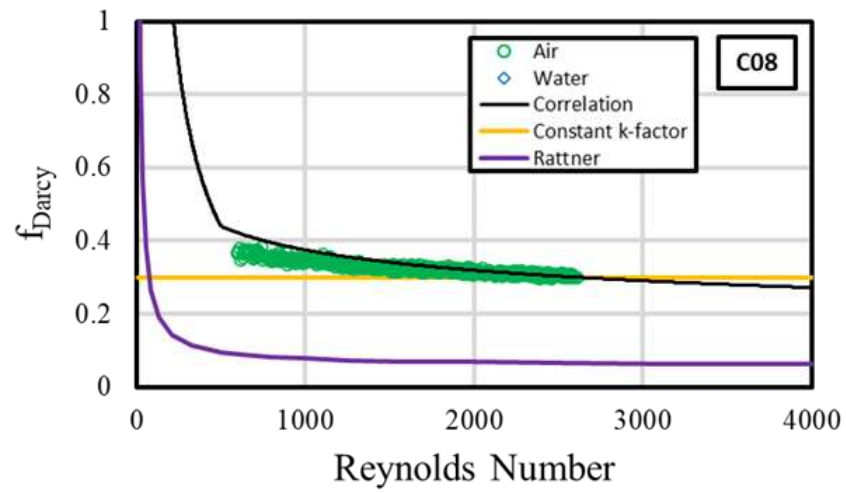
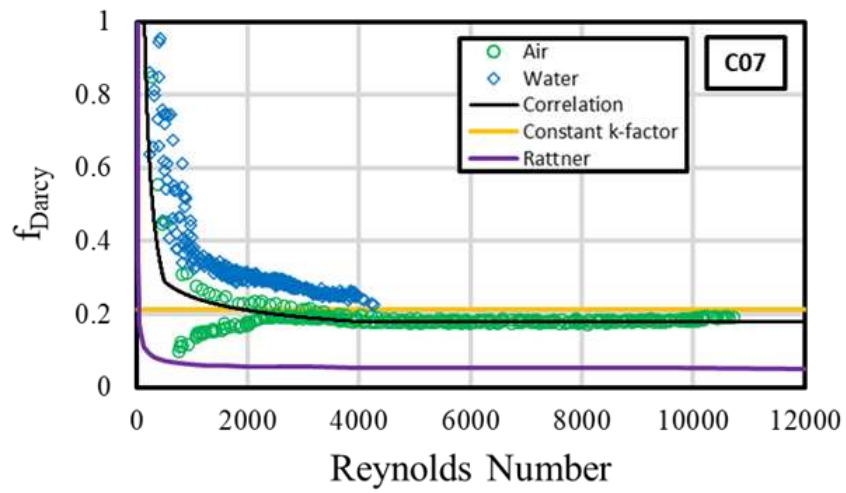


Figure 6-14: Darcy friction factor experimental data with proposed correlation and Rattner correlation for C07, C08, C09

The Darcy friction factors calculated using equation 6-12 were used to predict experimental pressure drop values. Experimental and correlation predicted pressure drop values are compared in Figure 6-15. The solid black lines represent $\pm 50\%$ error bounds in which approximately 94% of the data lie. Fit statistics are provided for each individual impingement configuration as well as for the overall data set in Table 6-4. The proposed correlation fits the experimental data with a mean absolute deviation of 19.5% and a coefficient of determination of 0.95. As can be seen in Table 6-5, 70% of predicted values fit within $\pm 25\%$ of the experimental results. The C03 impingement configuration resulted in the lowest individual coefficient of determination of 0.82 and the highest MAD of 31.0%.

A broad view of the proposed Darcy friction factor correlation is provided in Figure 6-16 as a log-log plot of Darcy friction factor versus Reynolds number for variable impinging array

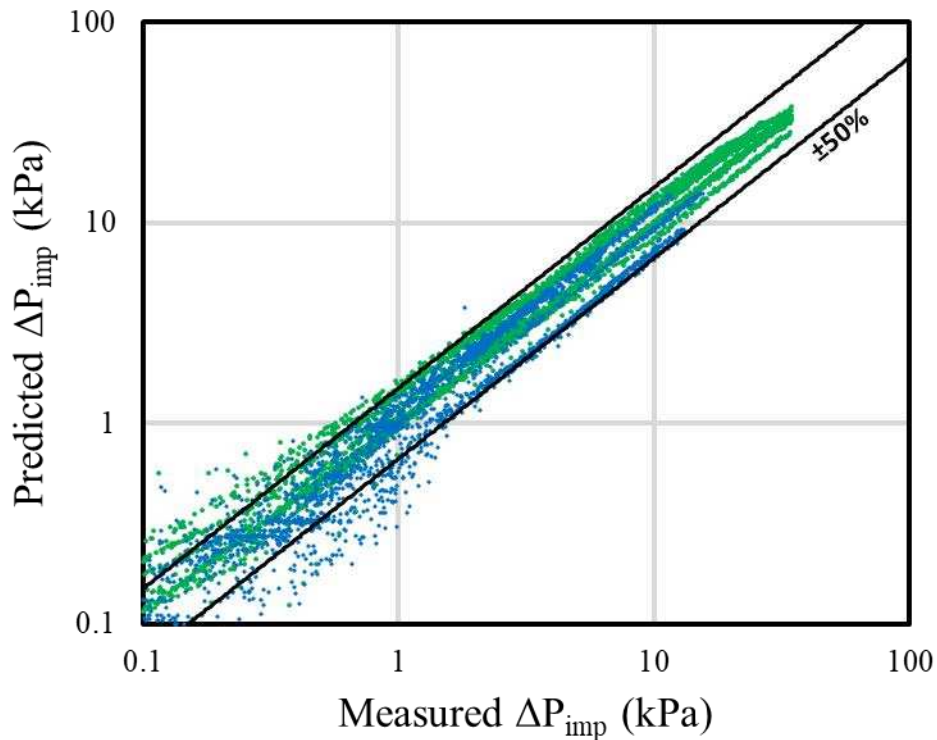


Figure 6-15: Correlation predicted pressure drop compared to experimental values for all datasets

Table 6-4: Friction factor geometric parameter f_G for each impingement configuration as calculated by equation 6-12

Part Config.	Corr. f_G	R^2	MAD
C01	0.12	0.952	27.4%
C02	0.14	0.985	11.2%
C03	0.10	0.823	31.0%
C04	0.13	0.925	22.0%
C05	0.13	0.987	7.9%
C06	0.13	0.996	9.3%
C07	0.18	0.977	21.0%
C08	0.27	0.997	4.6%
C09	0.07	0.945	28.5%
Overall		0.950	19.5%

Table 6-5: Overall fit statistics for the proposed pressure drop correlation against experimental data

Dev	Percent Fit
±5%	23.8%
±10%	37.5%
±15%	47.7%
±20%	62.0%
±25%	69.7%
±30%	78.4%
±40%	90.7%
±50%	94.4%

geometries. Figure 6-16a depicts the proposed correlation provided by equation 6-12 as applied towards each of the nine test geometries. Figure 6-16b provides a multiple friction factor curves at a single jet nondimensional jet spacing of 4 with variable nondimensional jet heights ranging from 0.5 to 4. Similarly, Figure 6-16c shows multiple curves for a single nondimensional jet height of two with five distinct jet spacings ranging from 3 to 7 jet diameters. Figure 6-16 can be considered as analogous to a Moody diagram for internal pipe flow. Notably, the impingement array geometric parameters of S/D_j and H/D_j modify the nondimensional pressure losses through the jet array in a similar way as pipe relative surface roughness does in pipe flow. Reduced jet spacings and reduced jet heights have an analogous effect to increasing pipe roughness. As Reynolds number increases to fully turbulent flow, the friction factor rapidly becomes independent of Reynolds number and only affected by flow path geometry, similar to very rough pipe flow. This seems to be a reasonable comparison considering the tortuous flow path inherent in return jet impingement geometries, marked rapid flow turning and by numerous jets colliding with one other along multiple interfaces. A more compact jet arrangement (reduced jet height and spacing) intuitively increases jet interaction with adjacent jets and with the wall.

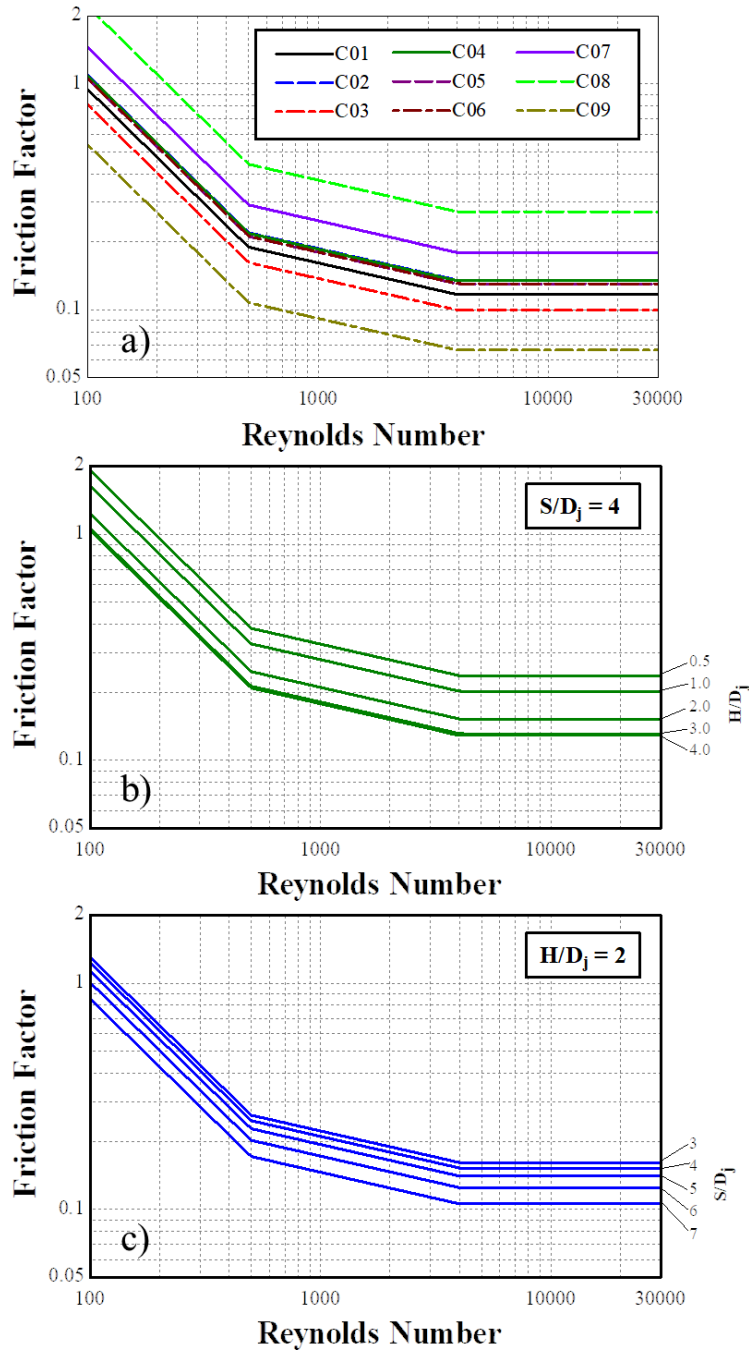


Figure 6-16: Log-log plots of Darcy friction factor correlation at various impinging array geometries, a) nine test geometries, b) constant jet spacing and variable jet height, c) constant jet height and variable jet spacing

In contrast with conventional pipe flow, friction factor in the laminar flow region is dependent on jet geometry, and not only on Reynolds number. This can likely be explained by the scale of flow disturbance and by the imperfect symmetry of jet interactions. In conventional rough pipe flow addressed by the Moody diagram, the maximum pipe roughness is on the order of $1/20^{\text{th}}$ of the pipe hydraulic diameter. Geometry changes made to the return jet flow path described in this study are on the same order of magnitude as the jet diameter itself. This could be compared to increasing roughness in a pipe until it resembles an entirely different flow path with bulk flow turning and repeated expansions and contractions. In this way, the flow described in this study is well outside the typical parameters covered by conventional rough pipe flow.

Experimental pressure drop data is plotted against jet Reynolds number in Figure 6-17, Figure 6-18, and Figure 6-19 for further comparison with the proposed correlation. Air and water data are presented for all 25 adiabatic pressure tests spanning the nine impingement configurations. The data are segregated by geometry and fluid type. The solid black lines in each figure represent predicted pressure drop values as calculated by the proposed Darcy friction factor correlation. Once again, the solid purple lines were produced using Rattner's k-factor correlation. The comparison plots in these figures provide a practical visualization of the goodness of fit between empirical correlation and experimental data. Generally, predicted pressure drop can be seen to track well with experimental data with the greatest disparity appearing in the C03 geometry configuration.

In this Chapter, a predictive correlation for impingement array pressure drop has been proposed which covers a wide range of key geometric parameters. The proposed correlation exhibits strong agreement with experimental data for both air and water tests. Reynolds number dependence was investigated, and five distinct flow regions were identified which are

characterized by a combination of distinct laminar and turbulent flow regimes. The proposed correlation accounts for Reynolds number dependence by establishing a reduced set of three flow zones. A Reynolds number exponent of -1 was considered for fully laminar flow present at $Re \leq 500$ to remain consistent with well-established properties of frictional losses in laminar flow. High Reynolds number turbulent flow at $Re > 4000$ was characterized by a constant friction factor dependent on geometry only, consistent with the experimental data. Finally, an intermediate Reynolds number region from 500 to 4000 was established to provide a cumulative characterization of the three flow regions therein identified as partially laminar and partially turbulent. A friction factor geometry coefficient was established to account for the S/D_j and H/D_j impingement array geometric parameters. Standard multivariable regressions were explored in order to establish a suitable equation for predicting the friction factor geometry coefficient and a quadratic model was reported to produce the closest fit to experimental data. The correlation proposed in equation 6-12 of this work can be used by impingement designers to predict pressure drop in impingement arrays with interspersed flow extraction ports across a wide range of geometries, fluids, and flow parameters.

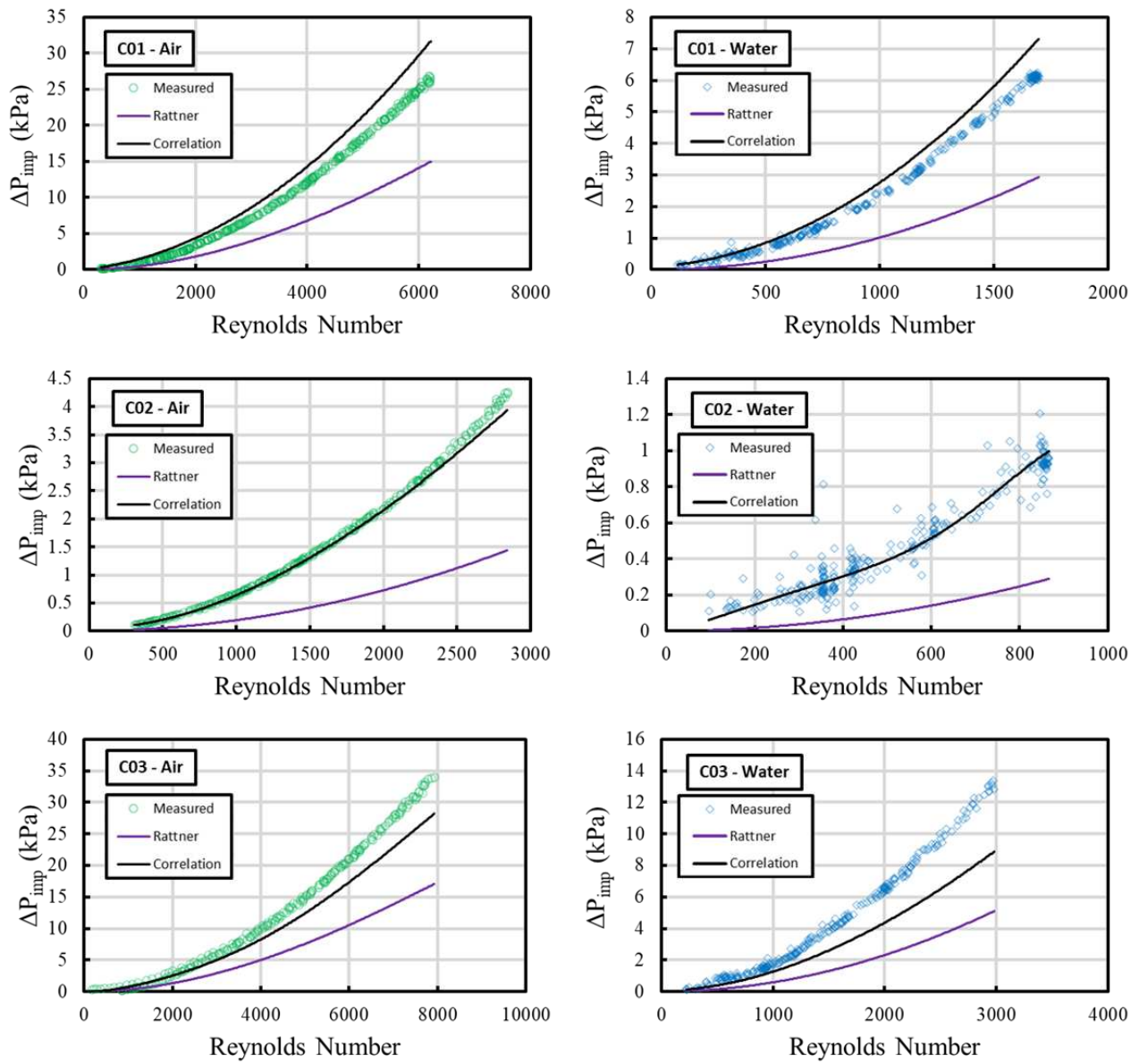


Figure 6-17: Predicted and experimental pressure drop for C01, C02, C03

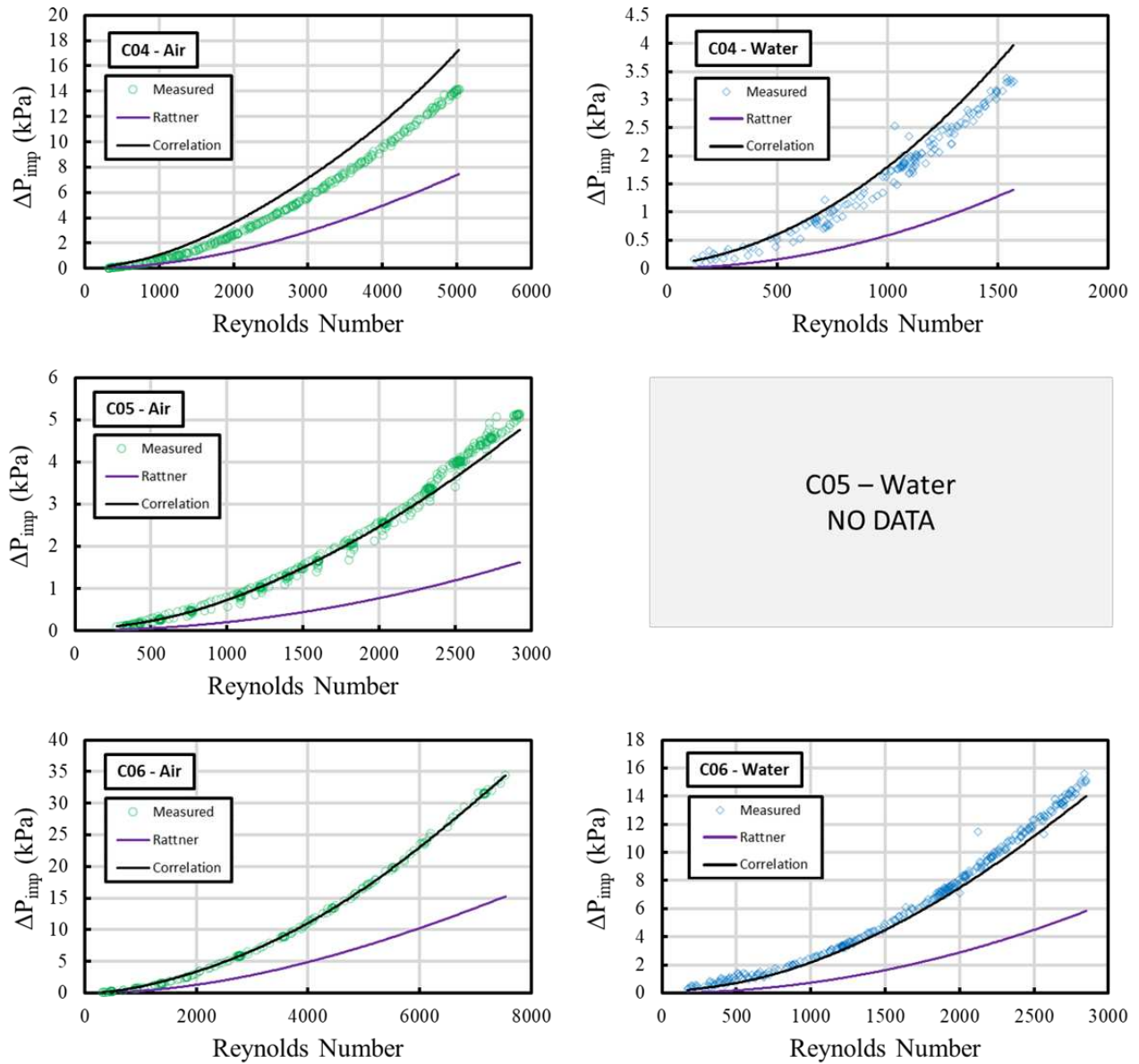


Figure 6-18: Predicted and experimental pressure drop for C04, C05, C06

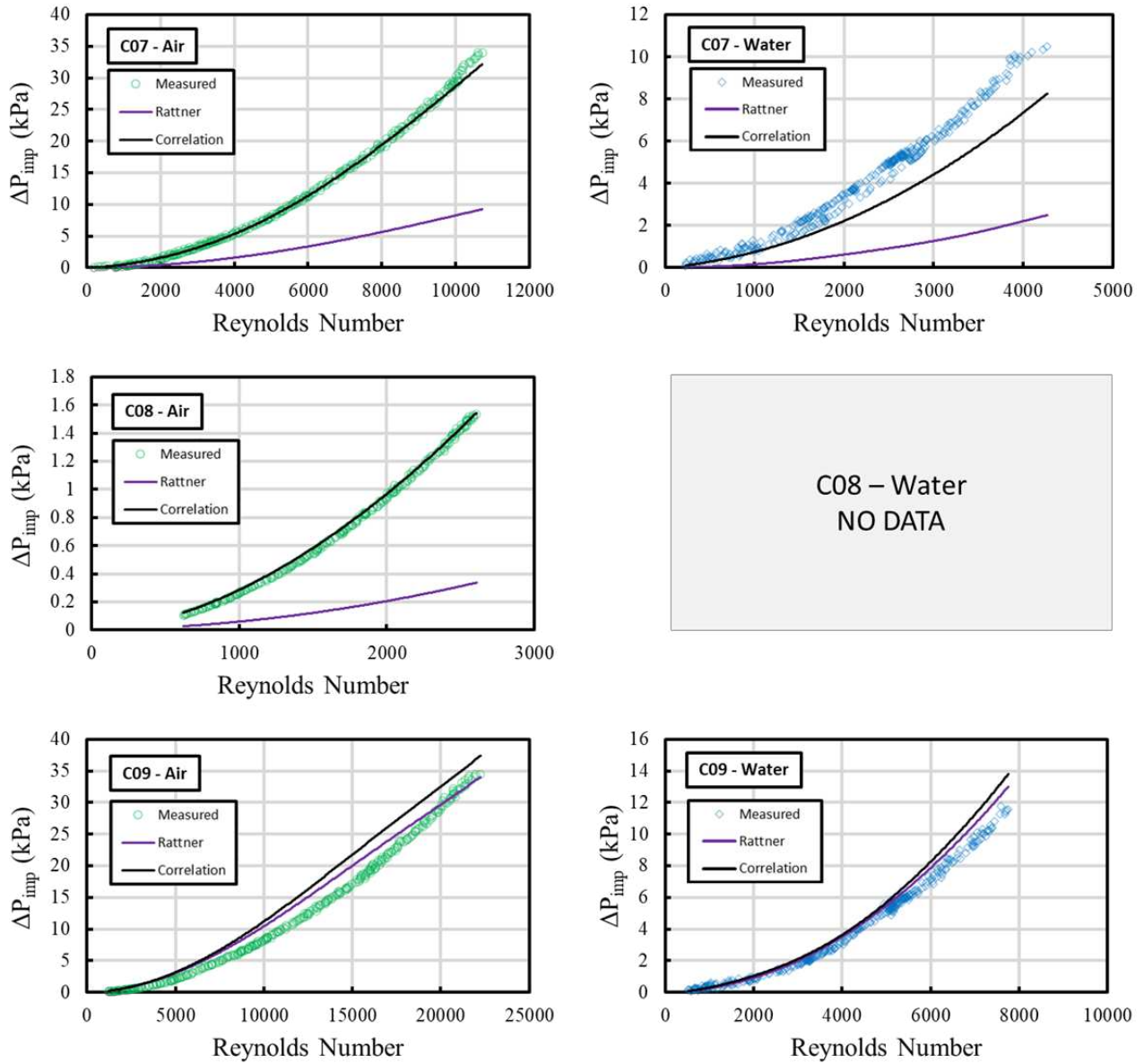


Figure 6-19: Predicted and experimental pressure drop for C07, C08, C09

CHAPTER 7. Optimization Study

This chapter has been composed to explore the combined heat transfer and pressure drop performance of return jet impingement cooling structures based on the combined results from Chapters 5 and 6. A case study was considered which is representative of a real-world application of return jet impingement cooling. Cooling integrated circuits presents one useful application of jet impingement cooling, so a typical microelectronics package was considered like the one shown in Figure 7-1. The microelectronics package consists of an integrated circuit (IC) which is made up of one or more (typically silicon) dice, shown in black. Only a single die is included in the representative package in Figure 7-1. The IC is attached to a printed circuit board (PCB) via an array of solder connections (not shown). A metallic case, also referred to as the internal heat spreader (IHS), is attached to the top side of the IC. The IHS is fabricated from an electrically and thermally conductive material, typically copper, and serves multiple purposes by 1) acting as a physical barrier to protect the delicate silicon IC beneath, 2) providing protection from

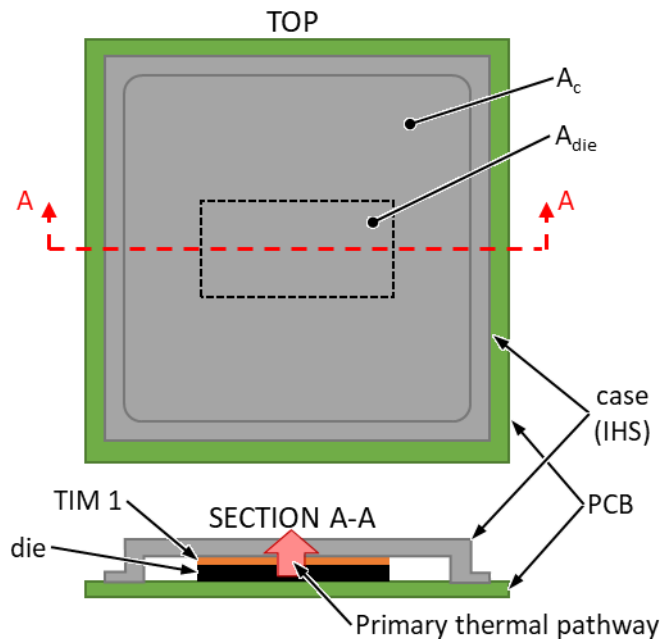


Figure 7-1: Microchip package schematic

electromagnetic interference, and 3) spreading heat generated by the IC to a greater area for removal. Good thermal contact is made between the IHS and silicon die via a thermal interface material (TIM) designated in orange as TIM 1 in Figure 7-1. The TIM improves thermal contact by filling in any air gaps between the two connecting surfaces and can be made of a variety of materials [85]. A heat load, designated as the IC thermal design power (TDP), is produced by die and conducts through the electronics package where it is removed across an area, A_c , at the top side of the package. Typically, a heatsink would be attached to the top surface of the IHS via a second thermal interface material (TIM 2). For this case study, the IHS serves as the impingement target with direct fluid contact over the surface area, A_c . Thus, TIM 2 is not required. The heat load is assumed to be uniformly spread across the target surface, producing a uniform heat flux, q'' , where:

$$q'' = \frac{TDP}{A_c} \quad 7-1$$

Coolant delivery is assumed to be uniformly distributed across the target surface as well and the resulting chip case temperature can be calculated, discounting local spatial temperature variations. Microchip manufacturers often publish specifications for either a maximum chip case temperature or a maximum junction temperature which must be maintained. To simplify the impingement cooling case study, a maximum case temperature was selected at $T_c = 80^\circ\text{C}$, which is a high but reasonable temperature for modern central processing units (CPUs). For example, the 11th generation Intel Core i7-11700K processor has a maximum junction temperature of 100°C with a 125 W TDP [86]. Maintaining a case temperature of 80°C would require a maximum junction-to-case thermal resistance of 0.16 K W^{-1} , which is easily achievable when using modern indium-

silver TIM materials [87]. Junction-to-case thermal resistance and maximum case temperature are not provided.

The objective of this case study is to evaluate what impact geometry, fluid, flow, and heat load characteristics have on the overall cooling performance of a return jet impingement array. Two critical performance metrics were identified to quantify cooling proficiency, ideal coefficient of performance (COP) and effectiveness, ε . The ideal COP is a measure of how energetically efficient the cooling system is, calculated as:

$$COP = \frac{TDP}{W_p} = \frac{q''}{W_p''} = \frac{TDP}{\dot{V}\Delta P_{imp}} = \frac{q''}{\dot{V}''\Delta P_{imp}} \quad 7-2$$

where, W_p is the ideal pumping power required to provide flow to the cooling system. W_p'' represents pumping power normalized by the target cooling area, A_c . \dot{V} is the total volumetric flow rate of fluid through the impingement device, and ΔP_{imp} is the pressure drop experience in the impingement region only, discounting pressure drop in manifolds and other ancillary flow regions. For $COP > 1$, more thermal energy is removed from the target package than mechanical energy is expended in order to removed it, which is advantageous. A COP value much greater than unity is preferred for an efficient cooling solution. This definition of COP is idealized and only for the impingement array. When designing an impingement cooling system, an actual COP should be calculated by considering other flow losses and pumping losses elsewhere in the system (e.g., pump efficiency, piping losses, manifold losses). \dot{V}'' is similarly normalized by target area such that $\dot{V}'' = \frac{\dot{V}}{A_c}$. Normalizing heat load, flow rate, and pumping power by target area is convenient for applying the case study analysis to an electronics package of arbitrary size. Effectiveness is calculated as:

$$\varepsilon = \frac{TDP}{\dot{m}c_p(T_c - T_{in})} = \frac{q''}{\dot{G}c_p(T_c - T_{in})} \quad 7-3$$

where, \dot{m} represents total mass flow rate through the device and \dot{G} represents the mass flow rate normalized by target area. T_{in} is the fluid temperature at the inlet of the impingement device, and T_c is the case temperature of the target surface. The fluid heat capacity, c_p , is taken from property tables at the average of inlet and outlet fluid temperature. An effectiveness equal to unity is ideal. The relative importance of each performance metric may differ from system to system depending on other system characteristics and the specific application. For example, in systems where power delivery is constrained or otherwise costly, impingement efficiency may be prioritized over effectiveness. Conversely, consider a liquid impingement system where the size of an ambient-coupled heat exchanger is critically important. In that system, maximizing impingement effectiveness would allow for higher fluid outlet temperature, thus reducing the required size of the heat exchanger. In that case, high effectiveness may be more valuable than high efficiency.

For this case study, first the effect of S/D_j and H/D_j geometric parameters on cooling performance were investigated. The case temperature was set at $T_c = 80^\circ\text{C}$ and the fluid inlet temperature was set at $T_{in} = 30^\circ\text{C}$ to represent a hot ambient environment. A jet diameter of 0.3 mm was somewhat arbitrarily selected and held as constant. Heat loads of 10 W cm^{-2} for air and 500 W cm^{-2} for water were somewhat arbitrarily selected and held constant. The effects of varying jet size and heat load will be evaluated separately. S/D_j and H/D_j parameters were varied from 2 to 8 and from 0.2 to 5 respectively.

The analytical case study model was built in Engineering Equation Solver (EES) [71]. The heat transfer coefficient and Nusselt number required to maintain the 80°C case temperature set point were calculated by:

$$Nu_{req} = \frac{htc_{req}D_j}{k_f} \quad 7-4$$

$$htc_{req} = \frac{q''}{LMTD} \quad 7-5$$

$$LMTD = \frac{(T_c - T_{in}) - (T_c - T_{out})}{\ln\left(\frac{T_c - T_{in}}{T_c - T_{out}}\right)} \quad 7-6$$

The required Nusselt number was used in conjunction with the proposed Nusselt correlation from equation 5-21 to calculate a required Reynolds number. Subsequently, a required flow rate for maintaining the 80°C case temperature was calculated from Reynolds number by:

$$\dot{G} = \frac{\dot{m}}{A_c} = \frac{\rho\dot{V}}{A_c} = \frac{N_j^2 \mu Re \pi D_j}{4A_c} = \frac{\mu \pi Re}{4\left(\frac{S}{D_j}\right)^2 D_j} \quad 7-7$$

N_j is the total number of jets and is calculated as:

$$N_j^2 = \frac{A_c}{S^2} \quad 7-8$$

Outlet fluid temperature was solved iteratively along with flow rate using an energy balance.

$$T_{out} = T_{in} + \frac{q''}{\dot{G}c_p} \quad 7-9$$

Finally, pressure drop was calculated using equations 6-3, 6-4, and 6-12. All fluid properties were calculated using property tables built into Engineering Equation Solver and pressure/temperature state points averaged between fluid inlet and outlet. Note that an actual value for target surface

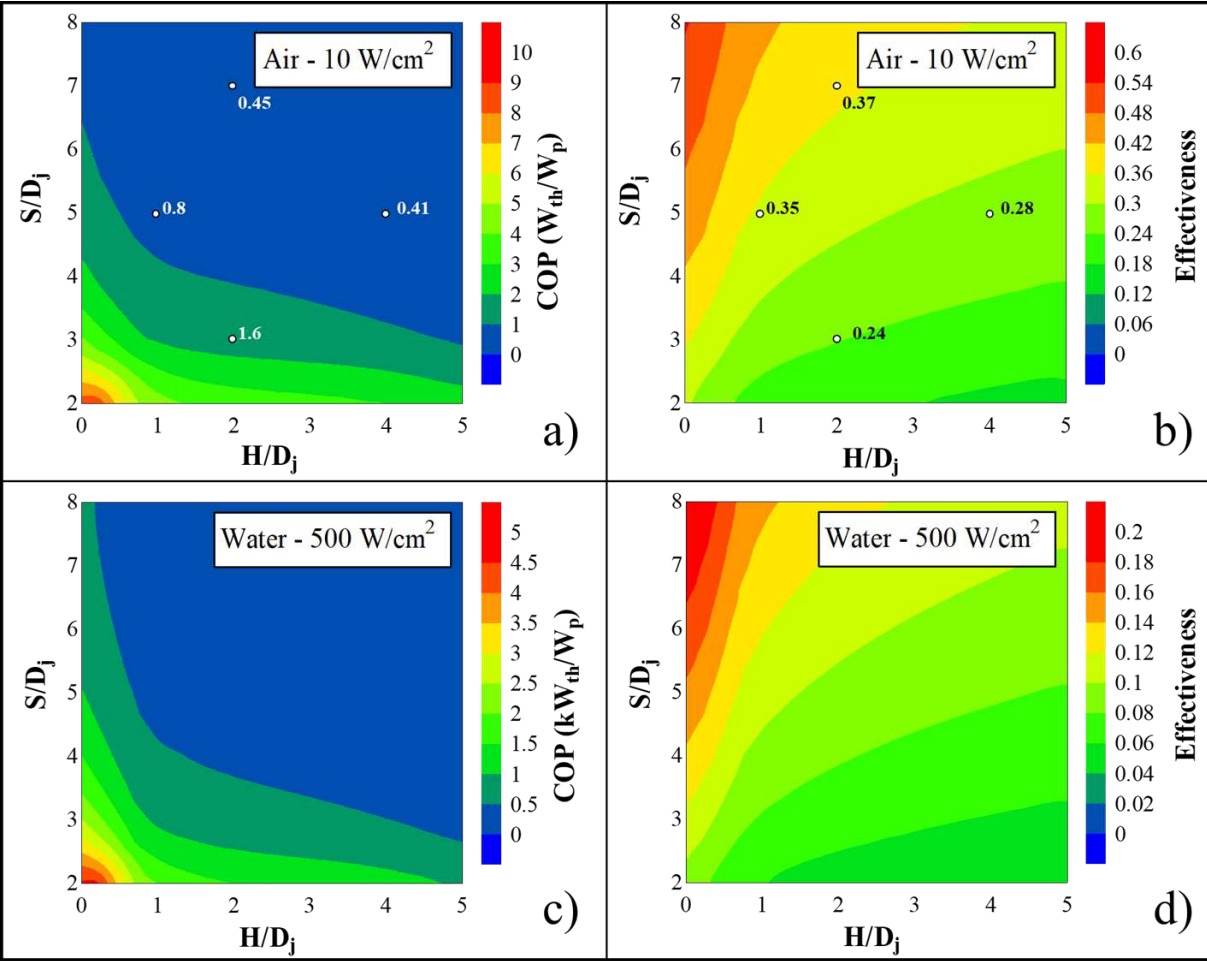


Figure 7-2: Contour maps of coefficient of performance (COP) and effectiveness for water and air at variable geometry configurations. Constant parameters: $D_j = 0.3$ mm, $dT = 50$ C. a) Air COP at 10 W/cm², b) air effectiveness at 10 W/cm², c) water COP at 500 W/cm², d) water effectiveness at 500 W/cm².

area, A_c , is not needed for any of the computations as all relevant parameters are normalized by the target surface area, making the analysis applicable to an electronic package of arbitrary size.

Figure 7-2 provides contour maps of COP and effectiveness across the geometry space. Figure 7-2a and Figure 7-2b show COP and effectiveness respectively for air, while Figure 7-2c and Figure 7-2d present the same metrics for water. Several key discoveries can be made from these geometric case study results. First, air and water follow the same basic trends. Both COP and effectiveness increase as H/D_j is reduced, indicating that low jet height-to-diameter ratios result in the best all-around cooling performance. For example, consider the air case with a constant S/D_j

of 5. COP increases by a factor of 1.9 from 0.41 to 0.80 when H/D_j is reduced from 4 to 1 and effectiveness similarly increases by 24% from 0.28 to 0.35 over the same range. These specific points are indicated in Figure 7-2a and b for clarity. The same trend persists for different jet spacings and for water. It is important to recognize that the minimum nondimensional jet height tested was 0.3 and that further reduction in jet height may become problematic. The behavior shown in Figure 7-2 may not extend to very low jet heights. One potential inhibiting factor at low jet height to diameter ratios could be unsurmountable pressure changes in the wall jet caused by high wall-jet velocities. This can be easily seen for incompressible flow by equating volumetric flow rate at the jet nozzle (v_j) to the volumetric flow rate moving radially outward from the jet (V_H):

$$\begin{aligned} \dot{V} &= v_j A_j = v_H A_H \\ A_j &= \frac{\pi D_j^2}{4}; \quad A_H = \pi D_j H \\ v_H &= v_j \frac{A_j}{A_H} = \frac{v_j}{4(H/D_j)} \end{aligned} \tag{7-10}$$

Key flow areas, A_j and A_H , and other relevant geometries are designated in Figure 7-3 which provides a labeled schematic of a single impinging jet produced via CFD under arbitrary geometric and flow conditions for qualitative purposes only. Color contours in Figure 7-3 are proportional to fluid velocity with red indicating high velocity and blue indicating low velocity flow. For $H/D_j < 0.25$, equation 7-10 shows that the mean radial velocity outward from the jet exit (v_H) is greater than the mean jet velocity at the nozzle (v_j). Furthermore, the wall jet height, h , may account for only a fraction of the available jet height, H . Wall jet height is a function of radial distance from the jet stagnation point as well as geometric and flow parameters. In the arbitrary case depicted in

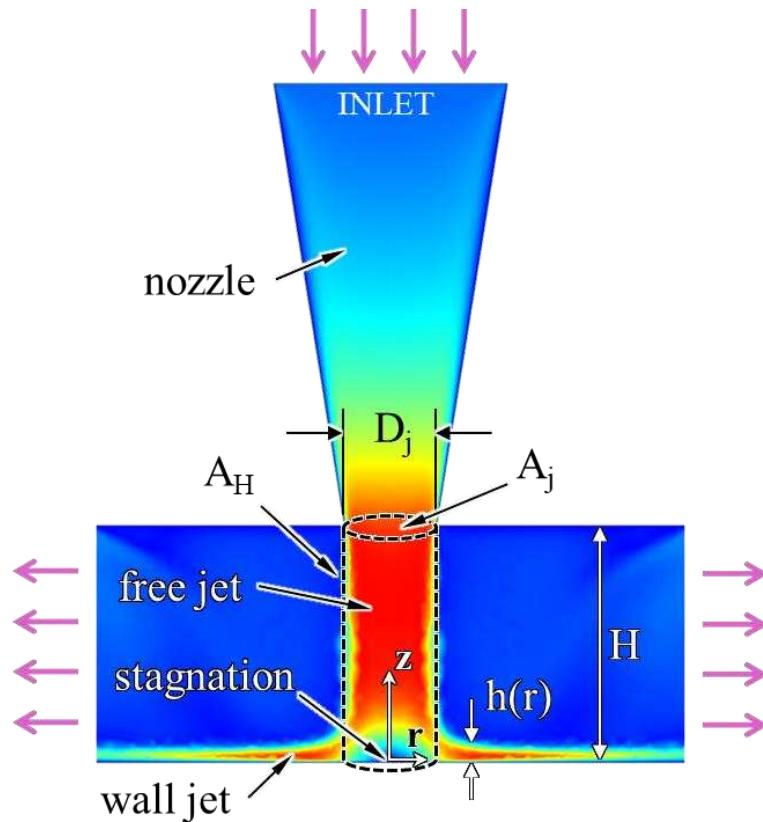


Figure 7-3: Single impinging jet schematic.

Figure 7-3, the wall jet height is less one-tenth of the jet height, H , indicating that the velocity in the wall jet (v_h) could be an order of magnitude greater than the mean radial velocity (v_H). As a result, reducing jet height further can rapidly and dramatically increase wall jet velocity and consequently, wall jet pressure drop. In the case of gaseous working fluids, this may even result in choked flow. In either case, extraordinary wall jet pressure drop at very low jet height-to-diameter ratios will become debilitating and the correlations proposed in this work should not be used to predict performance below the tested region of $H/D_j = 0.3$.

COP and effectiveness follow opposite trends with jet spacing variation; low S/D_j results in optimal COP performance but poor effectiveness while high S/D_j produces improved effectiveness but declining efficiency. Consider, for example, the air case with a constant jet height of $H/D_j = 2$ and variable nondimensional jet spacing from 3 to 7. As jet spacing is increased from

3 to 7, COP decreases by 72% from 1.6 to 0.45 while effectiveness improves by 53% from 0.24 to 0.37. These specific points are indicated in Figure 7-2a and b for clarity. Although only a single heat flux is shown here for each fluid, the same geometric performance trends hold true for varying heat loads. It is also important to recognize that large jet spacing will increase local spatial thermal gradients across the target surface, which should be considered during impingement design. Broadly, it can be concluded that the best impingement cooling performance can be achieved by minimizing jet height and by using jet spacing as a tuning knob to shift between more efficient and more effective solutions, as needed for the target application.

Figure 7-2 can also be used to examine how the required fluid flow rate varies with impinging jet height and spacing parameters. Consider the formulation of effectiveness provided in equation 7-3 which relates effectiveness to heat flux, inlet and case temperatures, fluid heat capacity, and mass flux. In Figure 7-2, heat flux and temperature differential are held constant and fluid heat capacity only varies slightly over the range of fluid temperatures. Thus, essentially all variation in effectiveness can be inversely attributed to variations in impingement mass flux, \dot{G} . As effectiveness increases in Figure 7-2b and d, flow rate decreases proportionately, approaching a minimum value as effectiveness approaches unity. For example, in the air case, at a nondimensional jet height of 0.5 and nondimensional jet spacing of 7, an effectiveness of 0.45 is achieved with a flow rate of 22 sLPM cm⁻². At $H/D_j = 4$, $S/D_j = 3$, an effectiveness of only 0.22 is achieved at 46 sLPM cm⁻². Note that effectiveness and flow rate change inversely by the same proportion. Thus, Figure 7-2b and d can be used to determine how changes in geometry effect the required impingement flow rate.

Also consider the magnitudes of effectiveness and COP as they compare between water and air. The maximum effectiveness shown for air is around 0.6, while the same is only about 0.2

for water. This would seem to suggest that air cooling results in generally higher effectiveness than water, however, this is only true at the particular heat loads which were arbitrarily selected for Figure 7-2. As will be shown later in this case study, effectiveness increases with reduced heat flux, so it is only true to say that air cooling at 10 W cm^{-2} is generally more effective than water cooling at 500 W cm^{-2} and no broad conclusions can be drawn comparing the two fluids. By contrast, a much more definitive comparison can be drawn in terms of COP. Note that COP is presented in different units for Figure 7-2a (W_{th}/W_p) than for Figure 7-2c (kW_{th}/W_p) where the Watt unit subscripts th and p indicate thermal power and pumping power, respectively. Consider a comparison between air and water COP in Figure 7-2a and c using a high-COP geometry of $H/D_j = 0.5$ and $S/D_j = 2.5$. The ideal COPs for this case would be 3.63 and 1855 for air and water respectively. Thus, the COP for water is approximately 500 times greater than that of air. Like effectiveness, COP will vary depending on heat flux however, the difference is so stark and persists over such a wide disparity in heat flux that it is fair to conclude that water jet impingement cooling results in dramatically higher efficiency than air impingement cooling.

The next step in this case study continues to evaluate the effect of geometry on efficiency and effectiveness performance metrics. The same analysis was performed with varying jet diameter instead of jet height and spacing. Heat load and temperature constraints were kept the same as before ($q''_{air} = 10 \text{ W cm}^{-2}$, $q''_{water} = 500 \text{ W cm}^{-2}$) and, once again, required flow rate was computed to satisfy the $T_c = 80^\circ\text{C}$ set point with a fluid inlet temperature of $T_{in} = 30^\circ\text{C}$. Non-dimensional jet height was set to $H/D_j = 0.5$ to enhance performance while being reasonably manufacturable and within the bounds of the empirical study. Three non-dimensional jet spacings were evaluated to represent a high efficiency ($S/D_j = 2.5$), a high effectiveness ($S/D_j = 8$), and an intermediate ($S/D_j = 5$) solution.

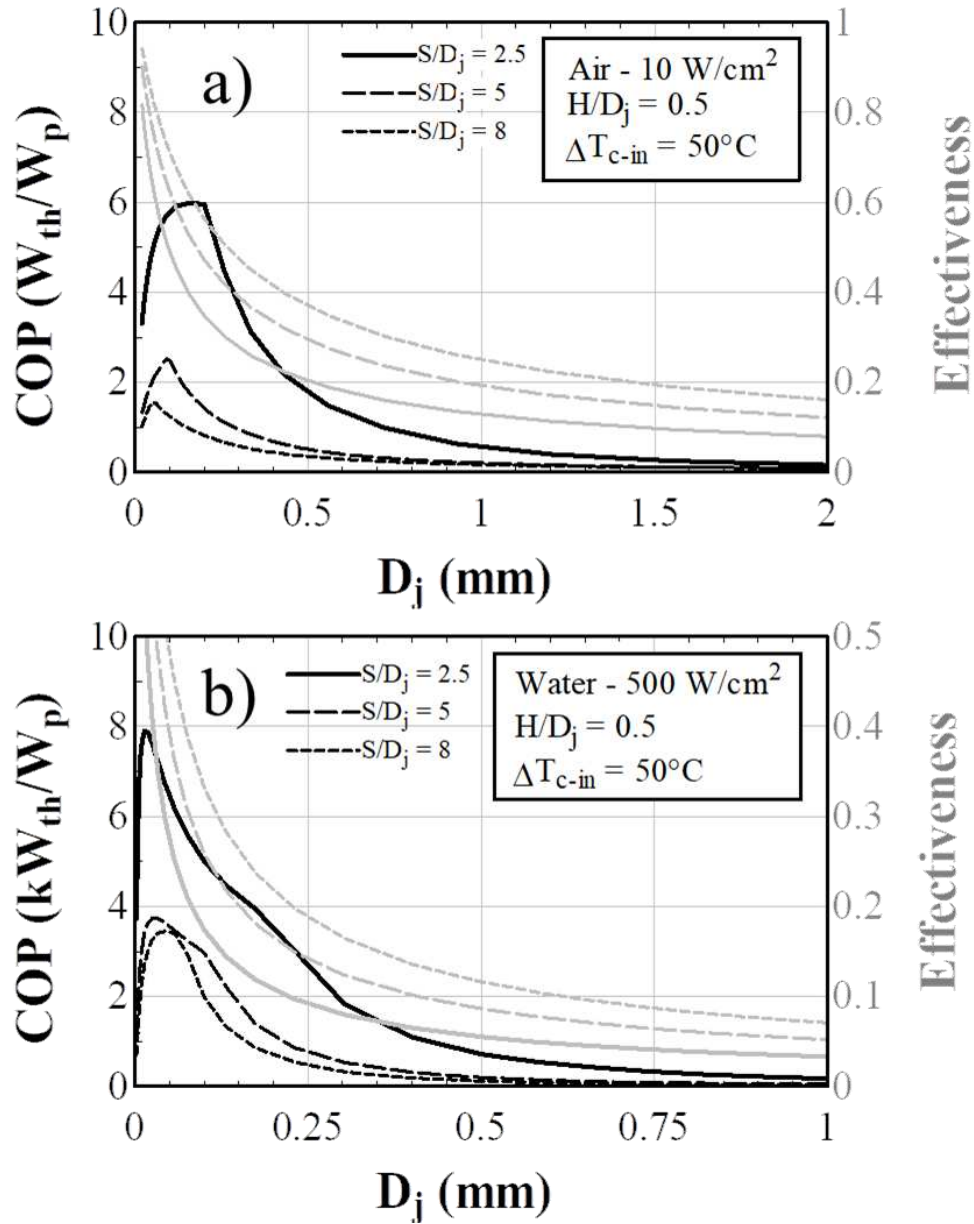


Figure 7-4: COP and effectiveness variation with jet diameter at $H/D_j = 0.5$ and variable S/D_j . a) air at 10 W/cm^2 , b) water at 500 W/cm^2 .

Figure 7-4 presents case study results for varying jet orifice diameter, segregated by fluid type. COP is shown in black, and effectiveness is shown in grey with the line type (solid, long-dashed, short-dashed) representing the jet spacing in ascending order. Once again, the presented units for COP differ by a factor of 1000 between the air case study and the water case study results. Impingement cooling effectiveness increases as jet size is reduced and eventually approaches unity

as the jet diameter approaches zero. The previously identified relationships between jet spacing and cooling performance hold true as jet diameter is varied, i.e., low jet spacing results in consistently higher COP and consistently poorer effectiveness independent of jet diameter. Cooling efficiency offers an interesting relationship with jet diameter. COP increases as jet diameter is reduced until it reaches a maximum at some critical jet diameter. After this point, COP then declines toward zero as jet size is reduced further. The optimal jet diameter varies depending on fluid properties, jet spacing, and heat flux. Intriguingly, in the case of air impingement, the optimal jet diameter decreases with increasing jet spacing; however, the opposite is true for the case study results with water. For air, these critical jet diameters occurred at 160 μm , 97 μm , and 51 μm for jet spacings of 2.5, 5, and 8 respectively. Meanwhile, for the water case, they occurred at 15 μm , 28 μm , and 43 μm for S/D_j of 2.5, 5, and 8 respectively. All six optimal jet diameters and their corresponding values for COP are tabulated in Table 7-1. The critical jet diameters discovered in this study are low enough that they are likely only relevant to microfluidic and nanofluidic impingement devices.

To understand the presence of COP maxima, consider that heat load was held constant in this stage of the case study, meaning that the COP changes shown in Figure 7-4 are driven by changes in pumping power only. As jet size decreases, pumping power decreases to a minimum then reverses direction and increase as jet size is further reduced. Fluid heat capacity, and case-to-inlet temperature difference are also held constant meaning that changes in effectiveness are driven by changes in flow rate only. As jet size is reduced, the required flow rate to maintain the case temperature set

Table 7-1: Optimal jet diameter values corresponding to Figure 7-4.

Fluid (-)	S/D_j (-)	D_j (μm)	COP (W/W)
Air	2.5	160	6.0
Air	5	97	2.5
Air	8	51	1.6
Water	2.5	15	7900
Water	5	28	3700
Water	8	43	3400

point decreases continuously, approaching the minimum possible flow rate as jet diameter approaches zero. Because flow rate will never drop below the minimum required to carry the applied heat load away, COP will not continue toward infinity as flow rate is reduced. In fact, a theoretical maximum COP can be calculated as:

$$COP_{max} = \frac{q''}{W''_{p,min}} \quad 7-11$$

$$W''_{p,min} = 8k \left(\frac{q''}{c_p \Delta T_{c-in}} \right)^3 \frac{(S/D_j)^4}{(\rho\pi)^2} \quad 7-12$$

where 100% effectiveness is assumed. A derivation for equation 7-12 is supplied in appendix E. In this form, it is much easier to recognize some of the relationships involved. In Figure 7-4, the heat flux, jet spacing, and temperature differential are all held constant and fluid properties (heat capacity and density), offer little variation. Given a constant k-factor for impingement pressure drop, ideal COP would continue to rise as jet size was reduced until it would reach COP_{max} at a jet diameter of zero. If this were the case, no optimal jet diameter would occur. Instead, k-factor rapidly increases towards infinity as jet diameter (and consequently Reynolds number) approaches zero, thus driving COP back down and producing the maxima depicted in Figure 7-4.

After exploring the effects of impingement geometry on cooling performance, the impact of varying heat load was similarly investigated. The case study analysis was performed in the same way as before, but now with fixed geometries. Jet diameter was fixed at 0.3 mm; small, for increased performance, but still manufacturable and larger than the critical jet diameter for all of the base cases. Non-dimensional jet height remained at 0.5 and two jet spacing configurations—high efficiency ($S/D_j = 2.5$) and a high effectiveness ($S/D_j = 8$)—were considered. The target case temperature was still set at 80°C with a fluid inlet temperature of 30°C. The resulting flow rate,

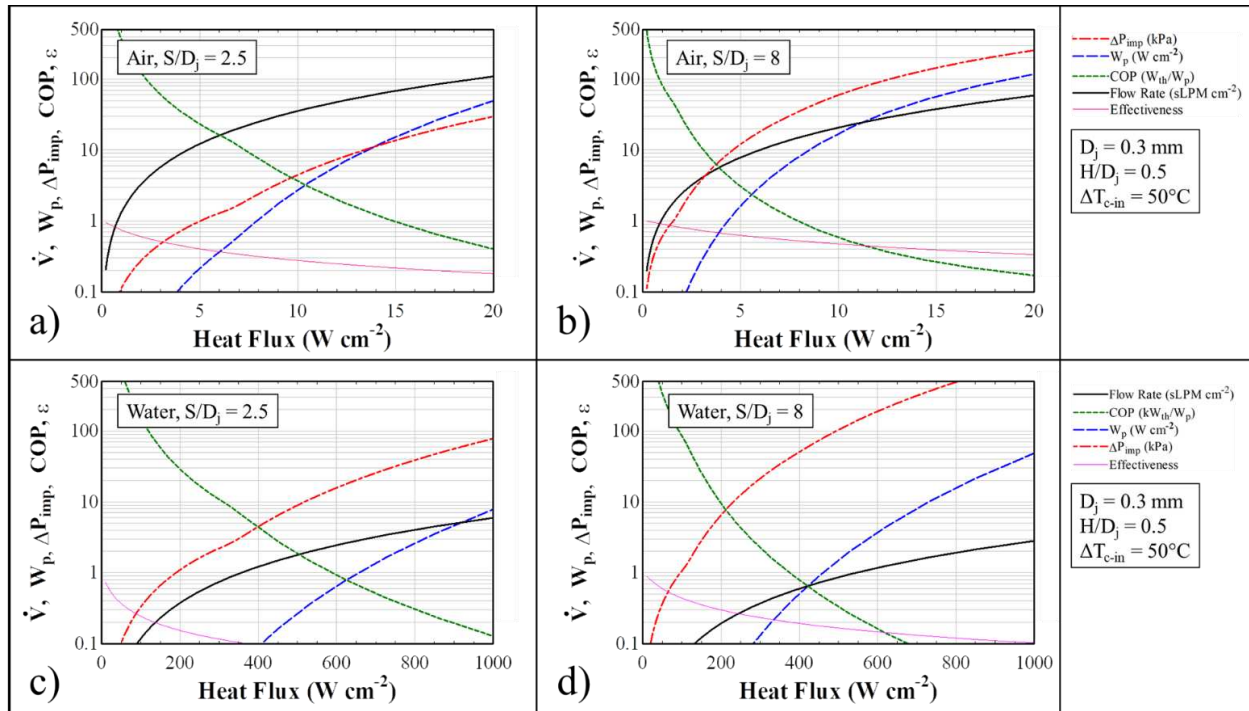


Figure 7-5: Effect of heat flux on key performance parameters: Flow rate, pumping power, pressure drop, COP, and effectiveness. a) Air at 10 W cm⁻² and S/D_j = 2.5, b) air at 10 W cm⁻² and S/D_j = 8, c) water at 500 W cm⁻² and S/D_j = 2.5, d) water at 500 W cm⁻² and S/D_j = 8.

pressure drop, pumping power, COP and effectiveness were calculated over a range of heat loads. For air, heat flux was varied from 0.2 up to 20 W cm⁻², and for water it was varied from 10 up to 1000 W cm⁻². The case study modeling results are provided in Figure 7-5 where a) represents a high efficiency configuration with air, b) represents a high effectiveness configuration with air, c) represents a high efficiency configuration with water, and d) represents a high effectiveness configuration with water. Once again, units for COP differ by factor of 1000 between water and air. Several broad, and often predictable trends can be drawn from Figure 7-5. As heat flux increases, naturally, flow rate must increase in accommodation, thus increasing both pressure drop and pumping power in tandem. Pumping power increases at a faster rate than heat load, resulting in diminishing COP as heat flux inclines. This result is consistent with the behavior apparent from equations 7-11 and 7-12 which indicate that pumping power increases at a rate proportional to the

cube of heat flux. Effectiveness similarly diminishes as heat flux increases and approaches unity at a heat flux of zero.

Several comparisons can be drawn between the results for different fluid and spacing configurations. Impingement cooling with water is, predictably, dramatically more energetically efficient than with air. For air, in order to achieve an ideal COP greater than 1—meaning more energy is removed from the target package than is expended driving the air—the heat load must be kept below approximately 15 W cm^{-2} . Further reducing jet diameter and height would allow for higher heat flux packages to be cooled efficiently. By contrast, for water, it is easily reasonable to efficiently cool packages well in excess of 1 kW cm^{-2} . This is apparent by considering the square and cubic inverse relationships that fluid density and heat capacity have with pumping power, shown in equation 7-12. For water cooled impingement devices, pressure drop is likely to become a limiting factor far before pumping power does. In all but very high heat flux applications, the pumping power required to operate a water-cooled impingement device is so low that overall system efficiency will likely be dominated by other system components, thus the effectiveness of the impingement device will likely serve as a much more important metric in most water-cooled applications. Conversely, air-cooled applications are more likely to benefit from efficiency-optimized geometries. This would result in high jet spacing applied towards water impingement devices and low jet spacing applied towards air impingement devices. Other fluids, including dielectrics like FC3283, could be similarly analyzed.

Analyzing the dependence of cooling performance on heat flux in this case study deserves a discussion on what heat fluxes are of interest to the target application. As was mentioned previously, heat fluxes were chosen somewhat arbitrarily for this case study. In actuality, the heat fluxes were chosen to reflect a realistic and observable range for each fluid. The air-cooled

configurations could not be analyzed out to hundreds of Watts per square centimeter because it would result in outrageous and unachievable flow rates and pressure drops while pushing Reynolds number well outside of the bounds of the proposed correlations. Similarly, if water were analyzed only up to only tens of Watts per square centimeter, the results would rely entirely on correlation results below the minimum tested Reynolds numbers and the calculated pressure drops and flow rates would be minuscule. The analysis could be shifted by altering jet diameter, jet height, and fluid inlet temperature, but keeping those constant seemed more useful for making comparisons. As a result, the two very different heat flux ranges would seem to cover very different applications, and at this stage it is useful to provide some definition.

Consider, for example the AMD EPYC 7H12 microprocessor. The 7H12 has a maximum TDP of 280 W, a die area of 10.1 cm², and a package area of 44.1 cm² [88,89]. In most cooling applications, a heat spreader will be attached to the microchip package, further expanding the usable cooling footprint. For this example, consider a heat spreader with an area of 81 cm², which is reasonable. For this one microprocessor, the average heat flux at the target surface could be 28, 6.3, or 3.5 W cm⁻² jetting on the die, lid, or external heat spreader respectively. Local heat fluxes on the die could be an order of magnitude higher [90]. Of course, heat spreading introduces more thermal resistances which can detract from the benefits gained by reducing heat flux. However, considering the remarkable improvements in impingement COP and effectiveness that can be gained by spreading the heat from 28 W cm⁻² down to 3.5 W cm⁻², well designed heat spreading solutions can result in dramatic net performance gains. This highlights the important role that thermally efficient heat spreading can have on developing efficient impingement cooling solutions, especially with air. By employing heat spreading methods a cooling system designer can

manufacture tradeoffs between compactness and cooling performance. In other electronics cooling packages such as high-power laser diodes, 1 kW cm^{-2} heat fluxes are realistic [91].

Finally, this case study considers a static geometry and static heat load but with variable flow rate and case temperature. This phase of the case study offers a more practical view of how a fixed-design impingement device would perform at cooling an electronics package as the supplied flow rate changes. The same analysis was performed in reverse such that flow rate was the model input and the case temperature was calculated as the output. Input flow rate was varied from 0 to 100 sLPM cm^{-2} for air and from 0 to 5 sLPM cm^{-2} for water. Heat loads were again set at 10 W cm^{-2} and 500 W cm^{-2} for air and water respectively. Jet diameter was 0.3 mm and non-dimensional jet height was 0.5 . Once again, a high-efficiency spacing of $S/D_j = 2.5$ and a high-effectiveness spacing of $S/D_j = 8$ were evaluated. Figure 7-6 presents the resulting inlet, outlet, and case temperatures for air and water and for both spacing configurations. Inlet temperature is held constant at 30°C . The case temperature is represented by a solid black line for the high-efficiency case and by a solid grey line for the high-effectiveness case. Immediately, a clear difference can be seen between the two jet spacing configurations. The high-effectiveness variant ($S/D_j = 8$) achieves the 80°C target at approximately 50-60% of the flow rate of the high-efficiency variant ($S/D_j = 2.5$). For the air case, this is apparent as the black line crosses the 80°C temperature target at a flow rate of 36 sLPM cm^{-2} while the grey line crosses at a flow rate of 21 sLPM cm^{-2} . Furthermore, by increasing flow rate, the high effectiveness solution can achieve much lower case temperatures; for example, reaching a case temperature of only 48°C at 100 sLPM cm^{-2} air flow rate compared to 57°C for the high-efficiency geometry. However, this apparent performance improvement comes at a steep cost of energy efficiency. By cross referencing Figure 7-5, it can be seen that the high effectiveness solution requires approximately 6 times more pumping power to

achieve the 80°C case temperature for both air and water. This is apparent when comparing where the blue dashed lines cross the 10 W cm⁻² mark for air. For S/D_j = 2.5, 2.76 W cm⁻² of ideal pumping power are required while 17.3 W cm⁻² are required for S/D_j = 8. For air, the difference in pumping power (~15 W cm⁻²) is very substantial compared to the cooling load of 10 W cm⁻². As a result, selecting a high effectiveness configuration could be intolerable to an energy sensitive system. For water, however, this difference is so small (~1 W cm⁻²) that it only represents ~0.2% of the target heat load and is thus likely inconsequential to the overall system performance. By choosing the high effectiveness configuration, the impingement outlet temperature can be raised from 34°C to 38°C and provide expanded temperature lift which could be beneficial elsewhere in the system.

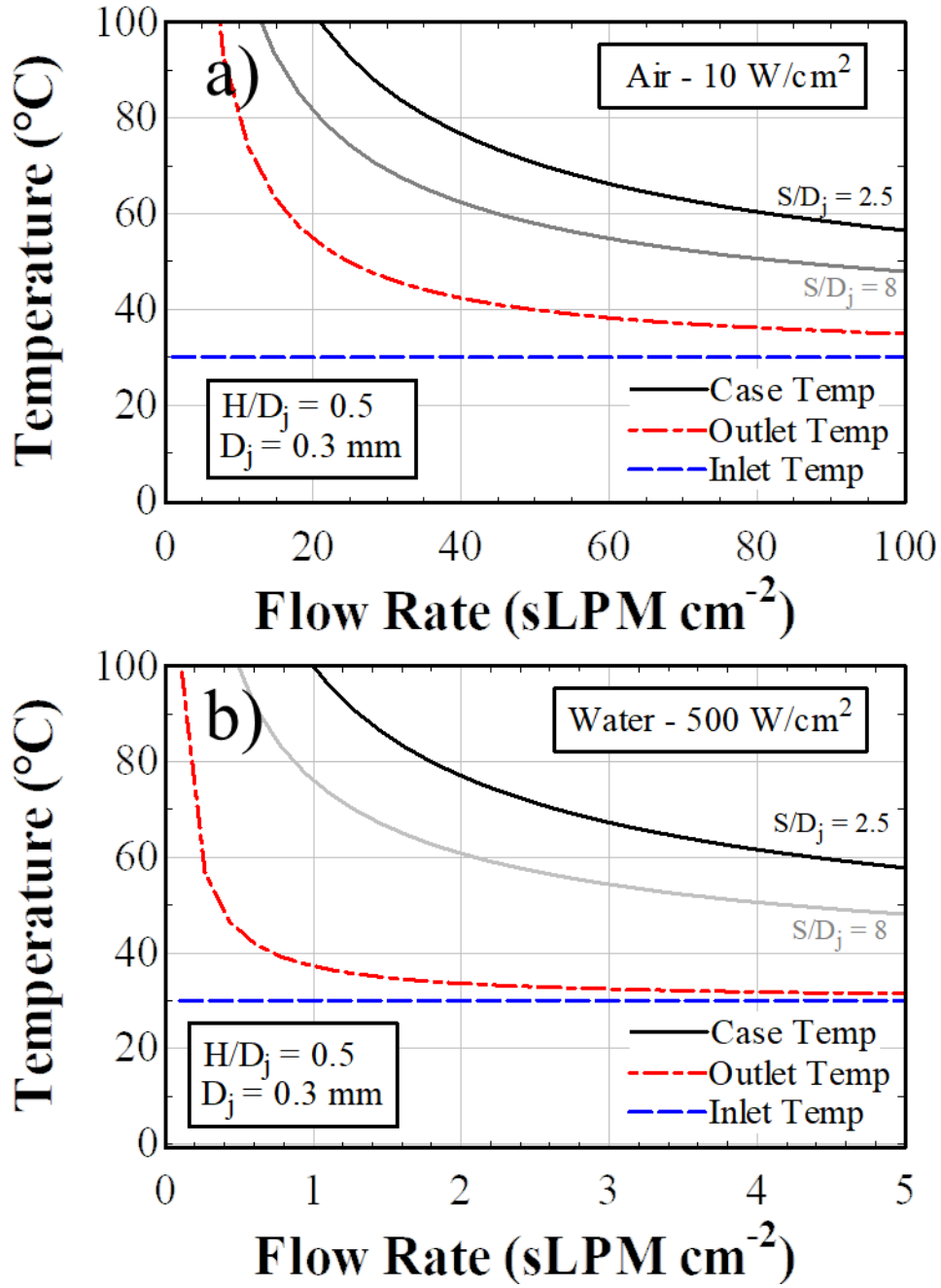


Figure 7-6: Effect of flow rate on chip case temperature for constant geometry and heat load. a) air at 10 W cm⁻², b) water at 500 W cm⁻²

In this chapter, a case study was performed which applied the empirical heat transfer and pressure drop correlations developed in this work to a model cooling application. Several key discoveries are summarized below:

- Low non-dimensional jet height results in the best overall performance in terms of both COP and effectiveness. Wherever it is manufacturable, this work would suggest a working jet height for return jet impingement designs of 0.5. Lower jet heights should be considered with awareness that behavior may deviate from predictions.
- Low spacing-to-diameter ratios provide optimal efficiency while high spacing-to-diameter ratios promote high effectiveness. Non-dimensional jet spacing offers a design tool which can allow designers to generate an impingement solution which prioritizes efficiency or effectiveness to best meet the needs of a specific application.
- An optimal jet diameter exists for any given configuration of other geometric parameters, fluid parameters, and heat flux. Generally, reducing jet diameter has a net positive effect on both efficiency and effectiveness.
- Effectiveness and COP can be dramatically improved by reducing the heat flux at the impingement target. This marks the importance of effective heat spreading solutions on elevating the performance of an impingement cooling design and offers a tradeoff between package size and cooling performance.

CHAPTER 8. Conclusions and Recommendations

The current research effort has investigated the thermal and hydrodynamic performance of a novel jet impingement architecture with interspersed fluid extraction. An in-depth review of all known return jet impingement studies in the open literature revealed an acute need for generalized and experimentally validated heat transfer and pressure drop correlations, among other key gaps in the literature. The current effort addresses those gaps by proposing novel Nusselt and Darcy friction factor correlations for impinging arrays with interspersed fluid extraction.

As part of this investigation, a proof-of-concept study was initially performed. This study established a single return jet impingement geometry and a fabrication method. Preliminary heat transfer and pressure drop experiments were performed on the POC geometry to establish viability of the cooling solution and to inform subsequent studies on the challenges to overcome and improvements that could be made. The POC investigation established viability of the cooling solution while solidifying the necessity for improved correlations. Preliminary heat transfer and pressure drop data were compared with previously established correlations which highlighted the need for better correlation development. One key discovery from the POC study involved decoupling the impinging array geometry from manifold effects. Manifolding architectures have proved to be very diverse among the very few distinct studies on return jet impingement. It was determined that high-confidence generalized correlations for return jet impingement, independent of manifold construction, could not be composed unless effects from the manifold architecture could be sufficiently isolated or minimized. A concerted effort would be needed to isolate the impingement array. This discovery led to an improved test section geometry designed expressly for the purpose of manifold-agnostic correlation development.

Nine new test sections were designed and fabricated in an expanded investigation. Each test section incorporated a unique combination of jet height (H/D_j) and jet spacing (S/D_j) parameters with the same improved manifolding architecture. The improved manifold was designed to greatly reduce flow loss and flow turning immediately upstream and downstream of the impingement region. Additionally, pressure measurement ports were integrated into the new device much closer to the impinging array. The new impingement devices were tested in a custom-designed facility under various flow and heat load conditions with water, air, and a dielectric fluorocarbon fluid. Each test section was evaluated for heat transfer performance and pressure losses. Experiments incorporated Reynolds numbers ranging from 70 to 24,000, Prandtl numbers from 0.7 to 21, and impingement geometries including $2.7 \leq S/D_j \leq 9.1$ and $0.31 \leq H/D_j \leq 4.4$. This represents the most comprehensive study to date on return jet impingement in terms of those parameters, experimental or otherwise.

Very high heat transfer coefficients were achieved during heat transfer testing, as high as $2,200 \text{ W m}^{-2} \text{ K}^{-1}$ for air, $38,000 \text{ W m}^{-2} \text{ K}^{-1}$ for water, and $6,800 \text{ W m}^{-2} \text{ K}^{-1}$ for FC3283. The thermal performance established in this study solidifies the viability of return jet impingement techniques for various cooling applications. The heat transfer data were used to establish an empirical correlation which relates Nusselt number to Reynolds number, Prandtl number, jet height (H/D_j), and jet spacing (S/D_j). Nusselt number was found to vary with Reynolds number raised to the power of 0.57 and with Prandtl number raised to the power of one-third. By evaluating geometry dependence, it was determined that low values for nondimensional jet spacing and jet height could produce the highest Nusselt number. The proposed correlation exhibited strong agreement with experimental results, exhibiting a mean absolute deviation of 10.3% and representing 92% of the data within $\pm 25\%$. This study also served to support the correlation formulated by Huber and

Viscanta [20] in their novel 1994 return jet impingement investigation. It expands on the types of fluids tested and updates the coefficients for improved fit to the present study which has intentionally separated the impingement array from upstream and downstream manifold effects.

Pressure drop experiments uncovered multiple distinct flow regimes present in the impinging structure, including fully laminar flow, fully turbulent flow, and multiple semi-turbulent regions where some parts of the flow path were turbulent and others were laminar. Dealing with each flow regime made developing a single continuous correlation challenging, so a simplified reduced-order piecewise Darcy friction factor correlation was proposed which still accounts for the changes in flow regime to a suitable level for practical engineering applications. For the fully laminar flow regime, which was broadly present at Reynolds numbers below 500, friction factor is proportional to Reynolds number to the power of -1. At high Reynolds numbers, friction factor dependency on Reynolds number was very weak, and so a constant friction factor was used for fully turbulent flow where $Re > 4000$. In the semi turbulent flow range, a best fit was found with a Reynolds number exponent equal to -0.232. A polynomial regression was proposed for capturing geometric effects within the jet spacing and height bounds of the correlation. The Darcy friction factor correlation reasonably predicts the experimental data with a mean absolute deviation of 19.5%. 70% of the experimental data fit within 25% of correlation predicted values.

The proposed correlations were utilized in a case study to determine the broader effects of variable impingement design performance using efficiency and effectiveness metrics in a practical context. The case study involved an analytical model of an exemplary microelectronics package cooled by return jet impingement. It was discovered that reducing non-dimensional impinging jet height results in the highest effectiveness and efficiency while altering non-dimensional jet spacing will promote either better efficiency or better effectiveness. High jet spacing to diameter ratios

amplify cooling effectiveness while low jet spacing to diameter ratio favor cooling efficiency instead. It was determined that an optimum jet diameter could be found for any particular impingement configuration which maximizes cooling efficiency for that design. Minimizing heat flux has a profound positive effect on both cooling effectiveness and cooling efficiency. This highlights the importance of quality heat spreading in the microelectronics package has on constructing an economical return jet impingement cooling solution. The best return jet impingement design will depend on the application, including system priorities, manufacturability, and cooling demands. The included case study offers compendious guidance to inform such designs.

In brief, this study:

- Constructed a novel return jet impingement design
- Proposed general empirical correlations for Nusselt number and Darcy friction factor over the broadest range of fluid, flow, and geometric parameters to date
- Established strong correlational agreement and comparison to prior correlations in the literature
- Conducted a practical case study for RJI applied towards electronics cooling
- Offers key design guidance for developing high-performing impingement cooling solutions

8.1. Recommendations for Future Research

The current investigation focused on a limited subset of the most important impingement geometry parameters, namely jet height and spacing. It is recommended that follow-up research on this subject expand upon this work in the following ways:

- Impinging jet arrays with interspersed fluid extraction should be investigated in cooperation with various surface area enhancement techniques. Prior studies have demonstrated the remarkable value of surface structures for greatly enhancing heat transfer performance for single impinging jets and conventional arrays [35,92]; however, application towards RJI arrays has been, so far, overlooked.
- There were several impinging jet geometric parameters which were held constant during this study to reduce the number of test geometries needed. Further investigation on the effects of these parameters would offer a valuable contribution to the current body of work. Namely, jet length (L/D_j), return orifice size (D_r/D_j), jet cone angle (ϕ_j), and return cone angle (ϕ_r), should be investigated further.
- Alternate, more complex geometric parameters beyond those listed above could also be evaluated. For example, nozzle shape [93], jet impact angle [94,95], and jet confinement architecture [96] may offer non-obvious but substantial performance enhancements when applied towards return jet impinging arrays.
- A future investigation which evaluates the pressure loss, thermal shortcut losses, flow distribution uniformity, and spatial footprint of several different RJI manifold strategies would be critically important for aiding impingement design. Although this investigation provides clear guidance for impingement array design, manifold architecture is non-trivial, varies greatly, and can have a profound impact on overall device performance. A comprehensive review of known RJI manifold designs, including qualitative benefits and drawbacks of each, would be valuable for informing design. Furthermore, quantitative guidance for predicting flow uniformity and pressure and flow losses for these designs would be exceptionally beneficial for practical design.

- More in-depth evaluation of the various flow regimes present in the return jet impingement flow path is also recommended. The current work only identifies the existence of multiple semi-turbulent flow regimes and their approximate Reynolds number onset points for a particular geometry. A follow-up flow visualization or CFD investigation focused on this aspect could better illuminate the phenomenon and provide clear distinction for when and where flow transitions occur.
- This study relies heavily on additive manufacturing of the impingement test sections using vat-photopolymerization fabrication techniques to produce the complex internal geometries necessary for this work. One downside with this approach is inherent variability which can occur both from part-to-part and temporally with a single impingement device. Modern commercial SLA 3D printers can produce complex microfluidic pathways with remarkable accuracy; however, at the scales considered in this study, printing precision remains to be a formidable challenge. The as-printed geometry of devices like those used in this study, fabricated by photo stereolithography, is highly dependent on a large number of often difficult-to-control parameters. For example, modest variations in ambient temperature, humidity, laser spot size, age of the photopolymer resin, curing time, cure depth, contaminants, cleaning procedures, and more can have measurable effects on the final dimensions of key geometric parameters. As a result, it is difficult to repeatably produce microfluidic devices with consistent performance. A follow-up study should investigate the repeatability of 3D printed return jet impingement devices and explore methods for improving part-to-part consistency.

- Similarly, the material and geometric parameters of a single 3D printed microfluidic device are subject to change throughout the lifetime of the part. Thermal stresses during operation can cause both temporary and permanent changes to key geometries in the form of recoverable thermal expansion and non-recoverable warpage. In some cases, cracking may even occur. Part erosion, clogging, and fouling can also play a role similar to other heat exchanger devices. Specific to photopolymers, continued curing in ambient light can result in gradual changes in material properties and even in severe embrittlement of the printed part. These temporally relevant parameters and their impact on bulk test section performance should be investigated in depth in a future study.

REFERENCES

- [1] Liu, Z., and Feng, Z., 2011, “Numerical Simulation on the Effect of Jet Nozzle Position on Impingement Cooling of Gas Turbine Blade Leading Edge,” *Int. J. Heat Mass Transf.*, **54**(23), pp. 4949–4959.
- [2] Sarkar, A., Nitin, N., Karwe, M. V, and Singh, R. P., 2004, “Fluid Flow and Heat Transfer in Air Jet Impingement in Food Processing,” *J. Food Sci.*, **69**(4), pp. CRH113-122.
- [3] Wajs, J., Mikielewicz, D., Fornalik-Wajs, E., and Bajor, M., 2019, “High Performance Tubular Heat Exchanger with Minijet Heat Transfer Enhancement,” *Heat Transf. Eng.*, **40**(9–10), pp. 772–783.
- [4] Ditri, J., Cadotte, R., McNulty, M., Hahn, J., and Luppia, D., 2015, “Embedded Cooling of High Heat Flux Electronics Utilizing Distributed Microfluidic Impingement Jets,” *Proc. of the ASME 13th ICNMM*.
- [5] Bandhauer, T. M., Hobby, D. R., Jacobsen, C., and Sherrer, D., 2018, “Thermal Performance of Micro-Jet Impingement Device With Parallel Flow, Jet-Adjacent Fluid Removal,” *ASME 2018 16th International Conference on Nanochannels, Microchannels, and Minichannels*, American Society of Mechanical Engineers, Dubrovnik.
- [6] Brunswiler, T., Rothuizen, H., Fabbri, M., Kloter, U., Michel, B., Bezama, R. J., Natarajan, G., and Ieee, 2006, “Direct Liquid Jet-Impingement Cooling with Micron-Sized Nozzle Array and Distributed Return Architecture,” *2006 Proc. 10th Intersoc. Conf. Therm. Thermomechanical Phenom. Electron. Syst. Vols 1 2*, pp. 196–203.
- [7] Ndao, S., Lee, H. J., Peles, Y., and Jensen, M. K., 2012, “Heat Transfer Enhancement from Micro Pin Fins Subjected to an Impinging Jet,” *Int. J. Heat Mass Transf.*, **55**(1–3), pp. 413–421.
- [8] Bandhauer, T. M., and Bevis, T. A., 2016, “High Heat Flux Boiling Heat Transfer for Laser Diode Arrays,” (50343), p. V001T04A002.
- [9] Escher, W., Brunswiler, T., Michel, B., and Poulikakos, D., 2010, “Experimental Investigation of an Ultrathin Manifold Microchannel Heat Sink for Liquid-Cooled Chips,” *J. Heat Transfer*, **132**(8), pp. 81402–81410.
- [10] Narumanchi, S., Mihalic, M., Kelly, K., Eesley, G., and Ieee, 2008, “Thermal Interface Materials for Power Electronics Applications,” *2008 11th Ieee Intersociety Conference on Thermal and Thermomechanical Phenomena in Electronic Systems, Vols 1-3*, Ieee, New York, pp. 395–404.
- [11] Martin, H., 1977, “Heat and Mass Transfer between Impinging Gas Jets and Solid Surfaces,” *Adv. Heat Transf.*, **13**, pp. 1–60.

- [12] Jambunathan, K., Lai, E., Moss, M. A., and Button, B. L., 1992, “A Review of Heat Transfer Data for Single Circular Jet Impingement,” *Int. J. Heat Fluid Flow*, **13**(2), pp. 106–115.
- [13] Zuckerman, N., and Lior, N., 2006, “Jet Impingement Heat Transfer: Physics, Correlations, and Numerical Modeling,” *Adv. Heat Transf.*, **39**, pp. 565–631.
- [14] Jing, Q., Zhang, D., and Xie, Y., 2018, “Numerical Investigations of Impingement Cooling Performance on Flat and Non-Flat Targets with Dimple/Protrusion and Triangular Rib,” *Int. J. Heat Mass Transf.*, **126**, pp. 169–190.
- [15] Natarajan, G., and Bezama, R. J., 2007, “Microjet Cooler with Distributed Returns,” *Heat Transf. Eng.*, **28**(8–9), pp. 779–787.
- [16] Maddox, J. F., Knight, R. W., and Bhavnani, S. H., 2015, “Local Thermal Measurements of Impinging Liquid Jets with Angled Confining Wall for Power Electronics Cooling,” *Proc. of the ASME 13th ICNMM*.
- [17] Glanzer, E., and Michna, G., 2016, “Novel Jet Impingement Array Geometries through 3D Printed Manifolds.”
- [18] Robinson, A. J., Tan, W., Kempers, R., Colenbrander, J., Bushnell, N., and Chen, R., 2017, “A New Hybrid Heat Sink with Impinging Micro-Jet Arrays and Microchannels Fabricated Using High Volume Additive Manufacturing,” *Annu. IEEE Semicond. Therm. Meas. Manag. Symp.*, pp. 179–186.
- [19] Sung, M. K., and Mudawar, I., 2008, “Single-Phase Hybrid Micro-Channel/Micro-Jet Impingement Cooling,” *Int. J. Heat Mass Transf.*, **51**(17–18), pp. 4342–4352.
- [20] Huber, A. M., and Viskanta, R., 1994, “Effect of Jet-Jet Spacing on Convective Heat Transfer to Confined, Impinging Arrays of Axisymmetric Air Jets,” *Int. J. Heat Mass Transf.*, **37**(18), pp. 2859–2869.
- [21] Liu, X., Lienhard, J. H., and Lombarda, J. S., 1991, “Convective Heat Transfer by Impingement of Circular Liquid Jets,” *J. Heat Transfer*, **113**(3), pp. 571–582.
- [22] Tie, P., Li, Q., and Xuan, Y., 2011, “Investigation on the Submerged Liquid Jet Arrays Impingement Cooling,” *Appl. Therm. Eng.*, **31**(14–15), pp. 2757–2763.
- [23] Michna, G. J., Browne, E. A., Peles, Y., and Jensen, M. K., 2011, “The Effect of Area Ratio on Microjet Array Heat Transfer,” *Int. J. Heat Mass Transf.*, **54**(9–10), pp. 1782–1790.
- [24] Wolf, D. H., Viskanta, R., and Incropera, F. P., 1990, “Local Convective Heat Transfer from a Heated Surface to a Planar Jet of Water with a Nonuniform Velocity Profile,” *J. Heat Transfer*, **112**(4), pp. 899–905.
- [25] Womac, D. J., Incropera, F. P., and Ramadhyani, S., 1994, “Correlating Equations for Impingement Cooling of Small Heat Sources With Multiple Circular Liquid Jets,” *J. Heat Transfer*, **116**(2), pp. 482–486.

- [26] Elison, B., and Webb, B. W., 1994, "Local Heat Transfer to Impinging Liquid Jets in the Initially Laminar, Transitional, and Turbulent Regimes," *Int. J. Heat Mass Transf.*, **37**(8), pp. 1207–1216.
- [27] Garimella, S. V., and Rice, R. A., 1995, "Confined and Submerged Liquid Jet Impingement Heat Transfer," *J. Heat Transfer*, **117**(4), pp. 871–877.
- [28] Li, C. Y., and Garimella, S. V., 2001, "Prandtl-Number Effects and Generalized Correlations for Confined and Submerged Jet Impingement," *Int. J. Heat Mass Transf.*, **44**(18), pp. 3471–3480.
- [29] Fabbri, M., and Dhir, V. K., 2005, "Optimized Heat Transfer for High Power Electronic Cooling Using Arrays of Microjets," *J. Heat Transfer*, **127**(7), pp. 760–769.
- [30] Robinson, A. J., and Schnitzler, E., 2007, "An Experimental Investigation of Free and Submerged Miniature Liquid Jet Array Impingement Heat Transfer," *Exp. Therm. Fluid Sci.*, **32**(1), pp. 1–13.
- [31] Meola, C., 2009, "A New Correlation of Nusselt Number for Impinging Jets," *Heat Transf. Eng.*, **30**(3), pp. 221–228.
- [32] Webb, B. W., and Ma, C. F., 1995, "Single-Phase Liquid Jet Impingement Heat Transfer," *Adv. Heat Transf.*, **26**(C), pp. 105–217.
- [33] Shukla, A., and Dewan, A., 2017, "Flow and Thermal Characteristics of Jet Impingement: Comprehensive Review," *Int. J. Heat Technol.*, **35**(1), pp. 153–166.
- [34] Brakmann, R., Chen, L., Weigand, B., and Crawford, M., 2015, "Experimental and Numerical Heat Transfer Investigation of an Impinging Jet Array on a Target Plate Roughened by Cubic Micro Pin Fins," *Vol. 5A Heat Transf.*, p. V05AT11A002.
- [35] Ndao, S., Peles, Y., and Jensen, M. K., 2014, "Effects of Pin Fin Shape and Configuration on the Single-Phase Heat Transfer Characteristics of Jet Impingement on Micro Pin Fins," *Int. J. Heat Mass Transf.*, **70**, pp. 856–863.
- [36] Ndao, S., Peles, Y., and Jensen, M. K., 2012, "Experimental Investigation of Flow Boiling Heat Transfer of Jet Impingement on Smooth and Micro Structured Surfaces," *Int. J. Heat Mass Transf.*, **55**(19–20), pp. 5093–5101.
- [37] Browne, E. A., Michna, G. J., Jensen, M. K., and Peles, Y., 2010, "Experimental Investigation of Single-Phase Microjet Array Heat Transfer," *J. Heat Transfer*, **132**(4), p. 041013.
- [38] Bhunia, A., Chen, C. L., and Asme, 2010, "LIQUID MICRO-JET ARRAY IMPINGEMENT COOLING FOR LARGE AREA SYSTEMS," *Imece2009 Proc. Asme Int. Mech. Eng. Congr. Expo. - 2009 Adv. Aerosp. Technol.*, pp. 11–17.
- [39] Bhunia, A., and Chen, C. L., 2011, "On the Scalability of Liquid Microjet Array

- Impingement Cooling for Large Area Systems,” *J. Heat Transfer*, **133**(6), p. 64501.
- [40] Onstad, A. J., Elkins, C. J., Moffat, R. J., and Eaton, J. K., 2009, “Full-Field Flow Measurements and Heat Transfer of a Compact Jet Impingement Array With Local Extraction of Spent Fluid,” *J. Heat Transfer*, **131**(8), pp. 082201-1–8.
- [41] Hoberg, T. B., Onstad, A. J., and Eaton, J. K., 2010, “Heat Transfer Measurements for Jet Impingement Arrays with Local Extraction,” *Int. J. Heat Fluid Flow*, **31**(3), pp. 460–467.
- [42] Han, Y., Lau, B. L., Zhang, H., and Zhang, X., 2014, “Package-Level Si-Based Micro-Jet Impingement Cooling Solution with Multiple Drainage Micro-Trenches,” *2014 IEEE 16th Electronics Packaging Technology Conference (EPTC)*, IEEE, pp. 330–334.
- [43] Husain, A., Al-Azri, N. A., Al-Rawahi, N. Z. H., and Samad, A., 2016, “Comparative Performance Analysis of Microjet Impingement Cooling Models with Different Spent-Flow Schemes,” *J. Thermophys. Heat Transf.*, **30**(2), pp. 466–472.
- [44] Rattner, A. S., 2017, “General Characterization of Jet Impingement Array Heat Sinks With Interspersed Fluid Extraction Ports for Uniform High-Flux Cooling,” *J. Heat Transfer*, **139**(8), pp. 82201–82211.
- [45] Sharma, C. S., Tiwari, M. K., Zimmermann, S., Brunswiler, T., Schlottig, G., Michel, B., and Poulidakos, D., 2015, “Energy Efficient Hotspot-Targeted Embedded Liquid Cooling of Electronics,” *Appl. Energy*, **138**, pp. 414–422.
- [46] Rhee, D. H., Yoon, P. H., and Cho, H. H., 2003, “Local Heat/Mass Transfer and Flow Characteristics of Array Impinging Jets with Effusion Holes Ejecting Spent Air,” *Int. J. Heat Mass Transf.*, **46**(6), pp. 1049–1061.
- [47] Tiwei, T., Oprins, H., Cherman, V., Van der Plas, G., De Wolf, I., Beyne, E., and Baelmans, M., 2017, “High Efficiency Direct Liquid Jet Impingement Cooling of High Power Devices Using a 3D-Shaped Polymer Cooler,” *2017 IEEE International Electron Devices Meeting (IEDM)*, IEEE, pp. 32.5.1-32.5.4.
- [48] Wei, T. W., Oprins, H., Cherman, V., De Wolf, I., Beyne, E., Yang, S., and Baelmans, M., 2018, “3D Printed Liquid Jet Impingement Cooler: Demonstration, Opportunities and Challenges,” *Proceedings - Electronic Components and Technology Conference*, pp. 2389–2396.
- [49] Wei, T., Oprins, H., Cherman, V., Yang, S., De Wolf, I., Beyne, E., and Baelmans, M., 2018, “Experimental Characterization of a Chip Level 3D Printed Microjet Liquid Impingement Cooler for High Performance Systems,” *IEEE Trans. Components, Packag. Manuf. Technol.*, **PP**(c), pp. 1–1.
- [50] Wei, T., Oprins, H., Cherman, V., De Wolf, I., Beyne, E., and Baelmans, M., 2018, “NOZZLE ARRAY SCALING EFFECTS ON THE THERMAL/HYDRAULIC PERFORMANCE OF LIQUID JET IMPINGEMENT COOLERS FOR HIGH PERFORMANCE ELECTRONIC APPLICATIONS,” *International Heat Transfer*

Conference 16, Begellhouse, Connecticut, pp. 3631–3638.

- [51] Wei, T., Oprins, H., Cherman, V., Qian, J., De wolf, I., Beyne, E., and Baelmans, M., 2018, “High Efficiency Polymer Based Direct Multi-Jet Impingement Cooling Solution for High Power Devices,” *IEEE Trans. Power Electron.*, **PP**(c), p. 1.
- [52] Wei, T. W., Oprins, H., Cherman, V., Van der Plas, G., De Wolf, I., Beyne, E., and Baelmans, M., 2019, “Experimental Characterization and Model Validation of Liquid Jet Impingement Cooling Using a High Spatial Resolution and Programmable Thermal Test Chip,” *Appl. Therm. Eng.*, **152**(January), pp. 308–318.
- [53] Wei, T., Oprins, H., Cherman, V., Beyne, E., and Baelmans, M., 2019, “Conjugate Heat Transfer and Fluid Flow Modeling for Liquid Microjet Impingement Cooling with Alternating Feeding and Draining Channels,” *Fluids*, **4**(3), p. 145.
- [54] Wei, T.-W., Oprins, H., Cherman, V., De Wolf, I., Van der Plas, G., Beyne, E., and Baelmans, M., 2019, “Thermal Analysis of Polymer 3D Printed Jet Impingement Coolers for High Performance 2.5D Si Interposer Packages,” *2019 18th IEEE Intersociety Conference on Thermal and Thermomechanical Phenomena in Electronic Systems (ITherm)*, IEEE, Las Vegas, NV, United states, pp. 1243–1252.
- [55] Wei, T. W., Oprins, H., Cherman, V., De Wolf, I., Beyne, E., and Baelmans, M., 2019, “First Demonstration of a Low Cost/Customizable Chip Level 3D Printed Microjet Hotspot-Targeted Cooler for High Power Applications,” *Proc. - Electron. Components Technol. Conf.*, **2019-May**, pp. 126–134.
- [56] Wei, T. W., Oprins, H., Cherman, V., Yang, Z., Rivera, K., Van Der Plas, G., Pawlak, B. J., England, L., Beyne, E., and Baelmans, M., 2020, “Demonstration of Package Level 3D-Printed Direct Jet Impingement Cooling Applied to High Power, Large Die Applications,” *Proc. - Electron. Components Technol. Conf.*, **2020-June**, pp. 1422–1429.
- [57] Wei, T., Oprins, H., Cherman, V., Beyne, E., and Baelmans, M., 2020, “Low-Cost Energy-Efficient On-Chip Hotspot Targeted Microjet Cooling for High- Power Electronics,” *IEEE Trans. Components, Packag. Manuf. Technol.*, **10**(4), pp. 577–589.
- [58] Wei, T. W., Oprins, H., Fang, L., Cherman, V., De Wolf, I., Beyne, E., and Baelmans, M., 2020, “Nozzle Scaling Effects for the Thermohydraulic Performance of Microjet Impingement Cooling with Distributed Returns,” *Appl. Therm. Eng.*, **180**(February), p. 115767.
- [59] Wei, T. W., Oprins, H., Cherman, V., Beyne, E., and Baelmans, M., 2020, “Experimental and Numerical Investigation of Direct Liquid Jet Impinging Cooling Using 3D Printed Manifolds on Lidded and Lidless Packages for 2.5D Integrated Systems,” *Appl. Therm. Eng.*, **164**(June 2019), p. 114535.
- [60] Wei, T., Oprins, H., Cherman, V., Yang, Z., Rivera, K. C., Plas, G. Van Der, Pawlak, B. J., England, L., Beyne, E., and Baelmans, M., 2021, “Experimental and Numerical Study of 3-D Printed Direct Jet Impingement Cooling for High-Power, Large Die Size Applications,”

- IEEE Trans. Components, Packag. Manuf. Technol., **11**(3), pp. 415–425.
- [61] Royne, A., and Dey, C. J., 2006, “Effect of Nozzle Geometry on Pressure Drop and Heat Transfer in Submerged Jet Arrays,” *Int. J. Heat Mass Transf.*, **49**(3–4), pp. 800–804.
- [62] Colucci, D. W., Viskanta, R., and Lafayette, W., 1996, “Effect of Nozzle Geometry on Local Convective Heat Transfer to a Confined Impinging Air Jet,” *Exp. Therm. Fluid Sci.*, **1777**(96), pp. 71–80.
- [63] Dede, E. M., 2010, “Multiphysics Optimization, Synthesis, and Application of Jet Impingement Target Surfaces,” pp. 1–7.
- [64] Kjar, A., and Huang, Y., 2019, “Application of Micro-Scale 3D Printing in Pharmaceuticals,” *Pharmaceutics*, **11**(8), p. 390.
- [65] Manufactur3D, 2018, “3D Printing Technology Choice: FDM v/s SLA v/s SLS” [Online]. Available: <https://manufactur3dmag.com/3d-printing-technology-choice-fdm-v-s-sla-v-s-sls/>.
- [66] Au, A. K., Bhattacharjee, N., Horowitz, L. F., Chang, T. C., and Folch, A., 2015, “3D-Printed Microfluidic Automation,” *Lab Chip*, **15**(8), pp. 1934–1941.
- [67] Hipolite, W., 2014, “Autodesk Begins Taking Orders for Their Ember 3D Printer,” 3DPrint.com [Online]. Available: <https://3dprint.com/28250/autodesk-ember-3d-printer/>.
- [68] Gong, H., Beauchamp, M., Perry, S., Woolley, A. T., and Nordin, G. P., 2015, “Optical Approach to Resin Formulation for 3D Printed Microfluidics,” *Rsc Adv.*, **5**(129), pp. 106621–106632.
- [69] Hobby, D., Walker, T., Rattner, A., Jacobsen, C., Sherrer, D., and Bandhauer, T., 2019, “Comparison of Experimental and Computational Heat Transfer Characterization of Water Jet Impingement Array with Interspersed Fluid Extraction,” *Heat Transf. Eng.* (In Rev.
- [70] 2015, “COMSOL Multiphysics.”
- [71] Klein, S., 2018, “Engineering Equation Solver.”
- [72] Idel’chik, I. E., 2005, “Handbook of Hydraulic Resistance,” Jaico Publishing House.
- [73] Crane, 1982, *Flow of Fluids Through Valve Fittings and Pipes*, Crane Co, New York.
- [74] Kakac, S., Shah, R., and Aung, W., 1987, *Handbook of Single-Phase Convective Heat Transfer*, Wiley-Interscience.
- [75] Lasance, C. J. M., 2001, “The Thermal Conductivity of Unfilled Plastics,” *Electron. Cool.* [Online]. Available: <https://www.electronics-cooling.com/2001/05/the-thermal-conductivity-of-unfilled-plastics/>.
- [76] Lytle, D., and Webb, B. W., 1994, “AIR-JET IMPINGEMENT HEAT-TRANSFER AT

- LOW NOZZLE PLATE SPACINGS,” *Int. J. Heat Mass Transf.*, **37**(12), pp. 1687–1697.
- [77] 3D Systems, 2020, “Accura ® Xtreme™ Data Sheet.”
- [78] McMaster-Carr, “Ultra-Thin Aerogel Pipe Insulation Sheet - 9590K12” [Online]. Available: <https://www.mcmaster.com/9590K12/>.
- [79] Davis, R., and John, P., 2018, “Application of Taguchi-Based Design of Experiments for Industrial Chemical Processes,” *Statistical Approaches With Emphasis on Design of Experiments Applied to Chemical Processes*, InTech.
- [80] Murshed, S. M. S., 2016, “Introductory Chapter: Electronics Cooling — An Overview,” *Electronics Cooling*, InTech, pp. 8–10.
- [81] Sieder, E. N., and Tate, G. E., 1936, “Heat Transfer and Pressure Drop of Liquids in Tubes,” *Ind. Eng. Chem.*, **28**(12), pp. 1429–1435.
- [82] Bergman, T., Lavine, A., Incropera, F., and Dewitt, D., 2011, “External Flow,” *Fundamentals of Heat and Mass Transfer*, John Wiley & Sons, Inc., pp. 437–441.
- [83] Everts, M., and Meyer, J. P., 2018, “Relationship between Pressure Drop and Heat Transfer of Developing and Fully Developed Flow in Smooth Horizontal Circular Tubes in the Laminar, Transitional, Quasi-Turbulent and Turbulent Flow Regimes,” *Int. J. Heat Mass Transf.*, **117**, pp. 1231–1250.
- [84] McNaughton, K. J., and Sinclair, C. G., 1966, “SUBMERGED JETS IN SHORT CYLINDRICAL FLOW VESSELS,” *J. Fluid Mech.*, **25**, pp. 367-+.
- [85] Gwinn, J. P., and Webb, R. L., 2003, “Performance and Testing of Thermal Interface Materials,” **34**, pp. 215–222.
- [86] Intel Ark, “Intel Core I7-11700K Processor,” Intel Ark [Online]. Available: <https://ark.intel.com/content/www/us/en/ark/products/212047/intel-core-i711700k-processor-16m-cache-up-to-5-00-ghz.html>.
- [87] Wei, J., 2008, “Challenges in Cooling Design of CPU Packages for High-Performance Servers,” *Heat Transf. Eng.*, **29**(2), pp. 178–187.
- [88] 2020, “EPYC 7H12 - AMD,” WikiChip [Online]. Available: <https://en.wikichip.org/wiki/amd/epyc/7h12>.
- [89] 2020, “AMD EPYC 7H12,” X86 CPUS’ Guid. [Online]. Available: <https://www.x86-guide.net/en/cpu/AMD-EPYC-7H12-cpu-no7748.html>.
- [90] Mahajan, R., Chiu, C. P., and Chrysler, G., 2006, “Cooling a Microprocessor Chip,” *Proc. Ieee*, **94**(8), pp. 1476–1486.
- [91] Anderson, C., Richey, J., Fish, M., and Bandhauer, T., 2021, “Peak Temperature Mitigation

- of a Multimicrochannel Evaporator Under Transient Heat Loads,” *J. Electron. Packag.*, **143**(4).
- [92] Huang, X., Yang, W., Ming, T., Shen, W., and Yu, X., 2017, “Heat Transfer Enhancement on a Microchannel Heat Sink with Impinging Jets and Dimples,” *Int. J. Heat Mass Transf.*, **112**, pp. 113–124.
- [93] Attalla, M., Maghrabie, H. M., Qayyum, A., Al-Hasnawi, A. G., and Specht, E., 2017, “Influence of the Nozzle Shape on Heat Transfer Uniformity for In-Line Array of Impinging Air Jets,” *Appl. Therm. Eng.*, **120**, pp. 160–169.
- [94] Li, W., Xu, M., Ren, J., and Jiang, H., 2016, “Experimental Investigation of Local and Average Heat Transfer Coefficients Under an Inline Impinging Jet Array, Including Jets With Low Impingement Distance and Inclined Angle,” *J. Heat Transfer*, **139**(1), p. 012201.
- [95] Ingole, S. B., and Sundaram, K. K., 2016, “Experimental Average Nusselt Number Characteristics with Inclined Non-Confined Jet Impingement of Air for Cooling Application,” *Exp. Therm. Fluid Sci.*, **77**, pp. 124–131.
- [96] Ashforth-Frost, S., and Jambunathan, K., 1996, “Effect of Nozzle Geometry and Semi-Confinement on the Potential Core of a Turbulent Axisymmetric Free Jet,” *Int. Commun. Heat Mass Transf.*, **23**(2), pp. 155–162.

APPENDICES

A CFD approach for POC investigation

Computational fluid flow and heat transfer simulations were performed for this jet impingement configuration to explore local jet hydrodynamics and the heat transfer distribution on the target surface within the unit-cell domain shown in Figure 1-3. Simulation results can be applied to assess the impingement region pressure drop for the jet impingement manifold and serve as a theoretical reference for heat transfer measurements.

Steady incompressible flow finite element simulations were performed using COMSOL 5.2a [70]. Laminar flow was assumed for all cases because peak jet Reynolds numbers were less than 1500. Constant fluid properties were assumed (water at 34°C), which is applicable for lower heat flux cases. The solved governing equations neglect viscous dissipation and pressure work effects, as was justified for similar jet impingement conditions in an earlier investigation [44].

$$\nabla \cdot \vec{u} = 0 \quad (\text{A-1})$$

$$\rho \vec{u} \cdot \nabla \vec{u} = -\nabla p + \mu \nabla^2 \vec{u} \quad (\text{A-2})$$

$$\rho c_p \vec{u} \cdot \nabla T = k \nabla^2 T \quad (\text{A-3})$$

The governing equations were discretized with 2nd and 3rd order finite elements (2nd order for pressure, 3rd order for velocity and temperature). A streamwise stabilization term was applied in the discretized equations, the magnitude of which reduces as mesh is refined.

The studied simulation domain represents a single unit cell in an infinite array of injection and return ports. The domain contains a quarter of an injection and return port and the impingement zone underneath. The sides of the domain are modeled as symmetry planes. The target surface is a constant heat flux surface. The upper wall and jet boundaries were modeled as no-slip and

adiabatic (owing to the low thermal conductivity of the plastic manifold). The fluid inlet into the domain was assumed to have uniform velocity and temperature. The outlet port to the return plenum was modeled as an outflow boundary with zero gage pressure.

The simulations were evaluated at the nominal jet flow rates studied in experiments. Simulation results were analyzed to determine the pressure drop in the inlet ports, jet zone, and return ports. Nusselt numbers were also evaluated for each flow rate based on the temperature difference between the fluid inlet and the average surface temperature:

$$\text{Nu} = \frac{1}{(\bar{T}_s - T_{in})} \frac{q'' D_j}{k_f} \quad (\text{A-4})$$

For each flow rate case, three meshes were evaluated: 35,700 cells (average cell size $\Delta = 34.9 \mu\text{m}$), 179,000 cells ($\Delta = 20.4 \mu\text{m}$), and 491,000 ($\Delta = 14.6 \mu\text{m}$). An image of a representative meshed unit cell is provided in Figure 3-14. Apparent mesh convergence was found for all derived pressure drop parameters, except for the return port pressure drop for the two highest flow rate cases. The relative change in all pressure drop parameters was $< 3\%$ between the two finer meshes (except for the return-port pressure drop in the two highest flow rate cases). Oscillatory convergence was found for some of the Nusselt number calculations, but the range in Nusselt numbers was less than 4% for the three considered meshes.

B POC Heat Transfer Experimental vs CFD Discrepancy

There are numerous factors that may contribute to the discrepancy between experimental and computational impingement heat transfer results. One possibility comes from the basic assumption that the measured temperatures at the inlet and outlet of the device (Figure 3-2a) serve as a good approximation for inlet and outlet conditions at the simulation boundary (Figure 1-3b). As was previously stated, Bunschwiler et al. discussed the impact of thermal shortcut losses in a return jet impingement architecture. They showed significant heat transfer between the warm fluid in the exit manifold and the cool fluid in the inlet manifold, leading to preheating of the jets and reduced performance [6]. A conservative, simplified analytical model was used to estimate the shortcut thermal resistance through the channel walls. It was determined that, at all flow rate and heat load conditions tested, the maximum potential for fluid preheating by thermal shortcut losses was always either within the limits of experimental error or less than 1% of the total temperature differential used for Nusselt number calculation. From this result, it is unlikely that thermal shortcut losses had a meaningful effect on the experimental results.

Another possible factor that may account for the difference in CFD and experimental heat transfer trends is the degree of flow distribution uniformity from jet to jet. The CFD simulation assumes a perfect repeating unit cell populates the full impingement array. In the physical setup, some jets may receive more flow than others based on position in the array and flow restriction in the manifolds. Inconsistent jet profiles could contribute to the stray in experimental results from the idealized computational arrangement. Similarly, because of the 90° change in flow direction from the manifold branches to the jet nozzle, the assumption of uniform velocity profile at the injection port may be markedly invalid. Upstream fluid momentum perpendicular to the axial jet

direction may cause jets to impact the target surface at an angle other than 90° , thus significantly changing local boundary layer formation at the point where the jet impacts the surface. A reduced-order flow prediction model could potentially be used to account for these flow distribution effects. However, by adjusting manifold design to reduce the presence of maldistribution, further analytical accommodation may become either unnecessary or, at least, less complex. For this reason, the authors propose further development in the area of manifold architecture to minimize the impact of flow routing scheme on local impinging jet formation.

A few additional possibilities that may account for divergence of simulation and experimental results include the constant fluid property assumption in simulations, increased thermal leakage at reduced flow rates, and conjugate heat transfer effects impacting the uniform heat flux assumption at the target surface. Regardless of the specific causes, it is imperative that they be identified and accounted for, either in model or experiment, before next steps are taken to formulate a large dataset for correlational development and validation.

C Ancillary Model Uncertainty Propagation Sample Calculation

Assume a device-scale pressure drop is measured to be 30 ± 1 kPa and the ancillary pressure drop is calculated to be 20 kPa. If the ancillary model predicts actual pressure drop to within $\pm 25\%$, then the ancillary pressure drop can be estimated as 20 ± 5 kPa. Equation C.1 could then be used to estimate the impingement region pressure drop.

$$\Delta P_{imp} = \Delta P_{meas} - \Delta P_{anc} = 30 - 20 = 10 \text{ kPa} \quad \text{C-1}$$

Uncertainty propagation can be used to estimate the impingement region uncertainty:

$$U_{imp} = \sqrt{\left(\frac{\partial \Delta P_{imp}}{\partial \Delta P_{meas}}\right)^2 U_{meas}^2 + \left(\frac{\partial \Delta P_{imp}}{\partial \Delta P_{anc}}\right)^2 U_{anc}^2} \quad \text{C-2}$$

Where,

$$\frac{\partial \Delta P_{imp}}{\partial \Delta P_{meas}} = 1, \quad \frac{\partial \Delta P_{imp}}{\partial \Delta P_{anc}} = -1 \quad \text{C-3}$$

Thus,

$$U_{imp} = \sqrt{U_{meas}^2 + U_{anc}^2} = \sqrt{1^2 + 5^2} = \pm 5.1 \quad \text{C-4}$$

From this, the impingement region pressure drop can be estimated as 10 ± 5.1 kPa. In this example, because a large portion (two-thirds) of the total pressure drop is attributed to the ancillary regions, the estimate for pressure drop in the impingement region is highly uncertain. Clearly, the uncertainty is dominated by model inaccuracy rather than by measurement inaccuracy, meaning that uncertainty cannot be improved by using better instrumentation.

D Thermal Shortcut Losses

A first order, conservative approximation was made by assuming a plane wall conduction thermal resistance network through the channel walls. The thermal resistance, R_{th} , is then given by equation D-1:

$$R_{th} = \frac{1}{hc_{cold}A} + \frac{L}{kA} + \frac{1}{hc_{hot}A} \quad D-1$$

The channel wall thickness, L , is 0.45 mm and the total cross-sectional area of the conduction path, A , is equal to the total surface area for convection and is roughly 540 mm². The thermal conductivity of the cured photopolymer used to construct the impingement device is unknown however, like most plastics, it can be assumed to be less than 0.5 W m⁻¹ K⁻¹ [34]. In the interest of making a worst-case estimate, a thermal conductivity of 0.5 W m⁻¹ K⁻¹ was used to calculate a minimum thermal resistance. The cold-side heat transfer coefficient, h_c , and the hot side heat transfer coefficient, h_h , were assumed to be the same and calculated using a Nusselt number equal to 4.79 for laminar flow in a rectangular channel of 3:1 aspect ratio with uniform heat flux boundary condition [35]. This yielded a heat transfer coefficient of 2700 W m⁻² K⁻¹. The resulting total thermal resistance is then approximately 3.1 K W⁻¹. At all flow rate and heat load conditions tested, the maximum potential for fluid preheating by this estimate of thermal shortcut losses was always either within the limits of experimental error or less than 1% of the total temperature differential used for Nusselt number calculation.

E Derivations for select equations in Chapter 7

The following is a derivation for equation 7-11 and 7-12 in the CHAPTER 7 optimization study. The maximum COP achievable for a given return jet impingement arrangement can be defined by the minimum possible pumping power required to reject a prescribed heat load as follows:

$$COP_{max} = \frac{q''}{W''_{p,min}} \quad \text{E-1}$$

The minimum ideal pumping power can then be defined as:

$$W''_{p,min} = \dot{V}''_{min} \Delta P \quad \text{E-2}$$

where, \dot{V}''_{min} is the minimum flow rate capable of removing the applied heat load and ΔP is the pressure drop associated with that flow rate. The minimum allowable flow rate can be defined by an energy balance:

$$q'' = \dot{G} c_p (T_c - T_{in}) \quad \text{E-3}$$

$$\dot{V}''_{min} = \frac{\dot{G}}{\rho} = \frac{q''}{\rho c_p (T_c - T_{in})} \quad \text{E-4}$$

where, it is assumed that the fluid outlet temperature reaches the case temperature, T_c . Pressure drop can be calculated as:

$$\Delta P = \frac{1}{2} k \rho V_{j,min}^2 \quad \text{E-5}$$

with minimum jet velocity defined as:

$$V_{j,min} = \frac{\dot{V}_{min}}{A_{j,tot}} \quad \text{E-6}$$

$$A_{j,tot} = \frac{\pi D_j^2}{4} N_j^2 \quad \text{E-7}$$

For a square array of evenly spaced jets, the number of jets can be determined by the area and spacing as follows:

$$N_j^2 = \frac{A_c}{S^2} \quad \text{E-8}$$

Equations E-7 and E-8 may be substituted into equation E-6 to give:

$$V_{j,min} = \frac{4S^2}{\pi D_j^2} \frac{\dot{V}_{min}}{A_c} = \frac{4S^2}{\pi D_j^2} \dot{V}_{min}'' \quad \text{E-9}$$

Substituting E-4 into E-9 and E-9 into E-5 then gives:

$$V_{j,min} = \frac{4S^2}{\pi D_j^2} \frac{q''}{\rho c_p (T_c - T_{in})} \quad \text{E-10}$$

$$\Delta P = \frac{1}{2} k \rho \left(\frac{4S^2}{\pi D_j^2} \frac{q''}{\rho c_p (T_c - T_{in})} \right)^2 \quad \text{E-11}$$

Equations E-4 and E-11 can be combined into equation E-2 to form the following expression for pumping power:

$$W_{p,min}'' = \left(\frac{q''}{\rho c_p (T_c - T_{in})} \right) \frac{1}{2} k \rho \left(\frac{4S^2}{\pi D_j^2} \frac{q''}{\rho c_p (T_c - T_{in})} \right)^2 \quad \text{E-12}$$

Finally, reorganizing equation E-12 gives:

$$W_{p,min}'' = 8k \left(\frac{q''}{c_p \Delta T_{c-in}} \right)^3 \frac{(S/D_j)^4}{(\rho \pi)^2} \quad \text{E-13}$$

which is presented as equation 7-12 in CHAPTER 7.

F Heat Transfer Uncertainty Data

The following are select graphs containing uncertainty data from section 5.1 as per the methodology provided in section 4.5.1. Figure F-8-1 contains bilateral relative uncertainties for all calculated Reynolds numbers and Nusselt numbers from heat transfer experiments.

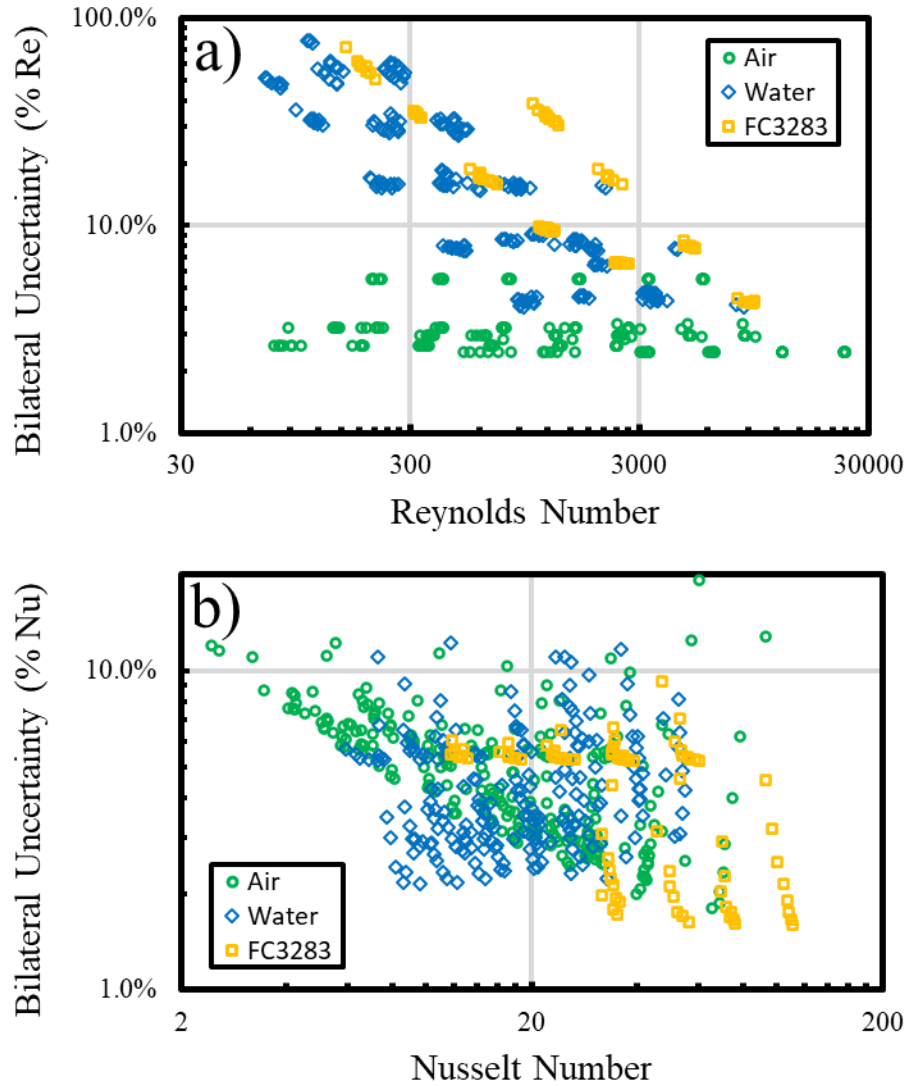


Figure F-8-1: Percentage bilateral uncertainty for all heat transfer data points; a) Reynolds number, b) Nusselt number.

Figure F-8-2 provides the same data as in Figure 5-3b but segregated by fluid type and with error bars applied to all data points. All errors are identical to those provided in Figure F-8-1.

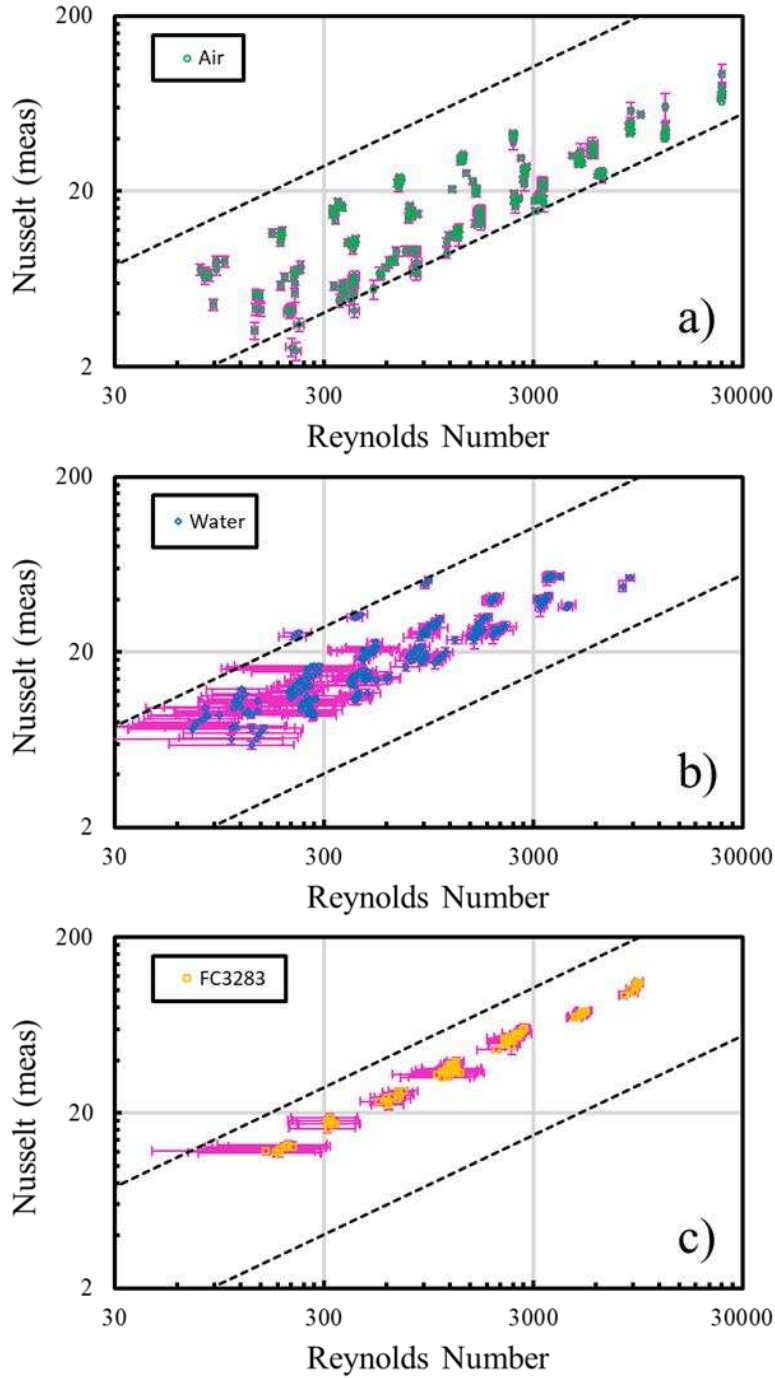


Figure F-8-2: Nusselt vs Reynolds number data for all heat transfer tests with error bars.

G Target Surface Temperature Measurement Procedure

This section discusses how spatially averaged surface temperature measurements were calculated for the Chapter 5 analysis. For each heat transfer test point, three temporally averaged surface temperature measurements were taken at the TT-S1, TT-S3, and TT-S4 measurement locations described in Figure 4-37. Temporal averaging was done as discussed in section 4.4.1. Combining the spatial measurement locations with temporally averaged temperature data resulted in three points of the following form:

$$(X, Y, T) \qquad \text{G-1}$$

For brevity, TT-S1, TT-S3, and TT-S4 may be shortened to simply S1, S3, and S4. X and Y temperature probe coordinates may be obtained from Figure 4-37 where the origin is set at the center. Coordinates for S1, S3, and S4 are then $(12, -12, T1)$, $(12, 12, T3)$, and $(-8, -8, T4)$ respectively. These three points can then be used to form two vectors on a plane.

$$\overrightarrow{S12} = \langle 0, 24, T2 - T1 \rangle \qquad \text{G-2}$$

$$\overrightarrow{S13} = \langle -20, 4, T3 - T1 \rangle$$

Taking the cross product of these two vectors yields a normal vector which can be used to formulate an equation for the temperature-spatial plane.

$$\vec{n} = \langle a, b, c \rangle = \overrightarrow{S12} \times \overrightarrow{S13} = \begin{vmatrix} \vec{i} & \vec{j} & \vec{k} \\ 0 & 24 & T2 - T1 \\ -20 & 4 & T3 - T1 \end{vmatrix} \quad \text{G-3}$$

$$= \langle -20T1 - 4T2 + 24T3, 20T1 - 20T2, 480 \rangle$$

Where the equation for the plane becomes:

$$a(X - X1) + b(Y - Y1) + c(T - T1) = 0 \quad \text{G-4}$$

$$T(X, Y) = T1 - \frac{a(X - 12) + b(Y + 12)}{c} \quad \text{G-5}$$

The resulting equation can then be used to approximate the temperature anywhere on the square 40 mm by 40 mm target surface. The center point temperature on this plane, T(0,0), represents the spatially averaged temperature and which was used to produce a single representative measurement. One final adjustment was made to the resulting temperature value to correct for additional conduction thermal resistance between the thermocouple locations and the actual target surface. As was previously mentioned, the thermocouples were embedded at a depth of 0.9 mm below the target surface. Thus, thermal resistance in the thin layer of copper between the measurement probes and the top surface was accounted for using simple linear conduction such that:

$$T_{adj} = T(0,0) - \frac{(0.9 \text{ mm})}{\left(0.4 \frac{\text{W}}{\text{mm}\cdot\text{K}}\right) \cdot (40 \text{ mm})^2} q = T(0,0) - 0.0014q \quad \text{G-6}$$

where, 0.4 represents the thermal conductivity in the copper and 40^2 is the area of the target surface. This final adjusted temperature was used for all surface temperature measurements resulting in a single temporally and spatially averaged value adjusted for probe depth. Although the conduction thermal resistance through this portion of copper is small, it results in greater than a 0.5°C temperature adjustment at high heat loads. Notably, contact resistance between the thermocouple and the copper was neglected under the assumption of a perfect solder joint as no tests were done which could determine the quality of that connection

H Additional Graphs of Chapter 5 Heat Transfer Data

This appendix contains additional figures of heat transfer data from Chapter 5.

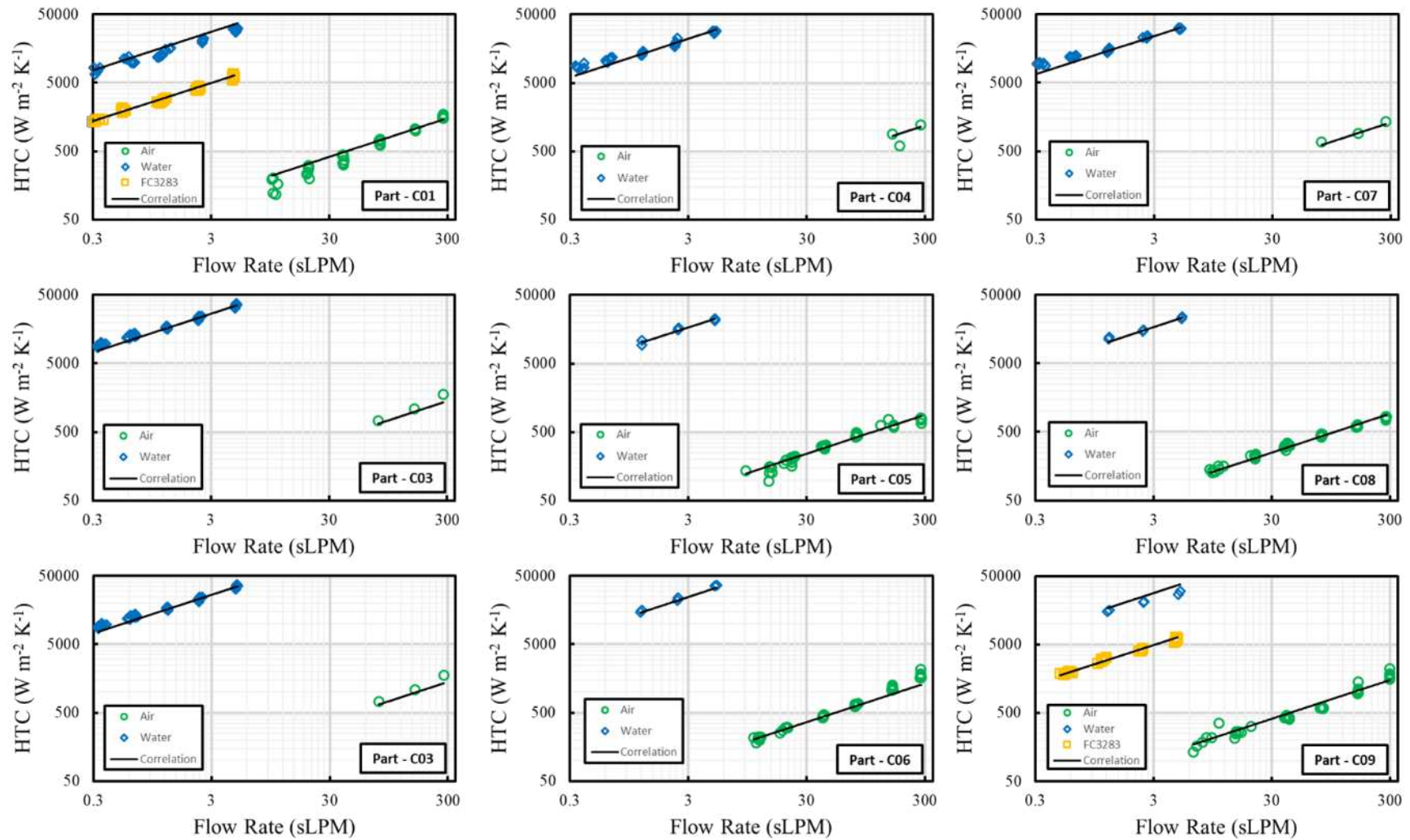


Figure H-8-3: Heat transfer coefficient vs flow rate for all heat transfer tests segregated by part number and fluid type.

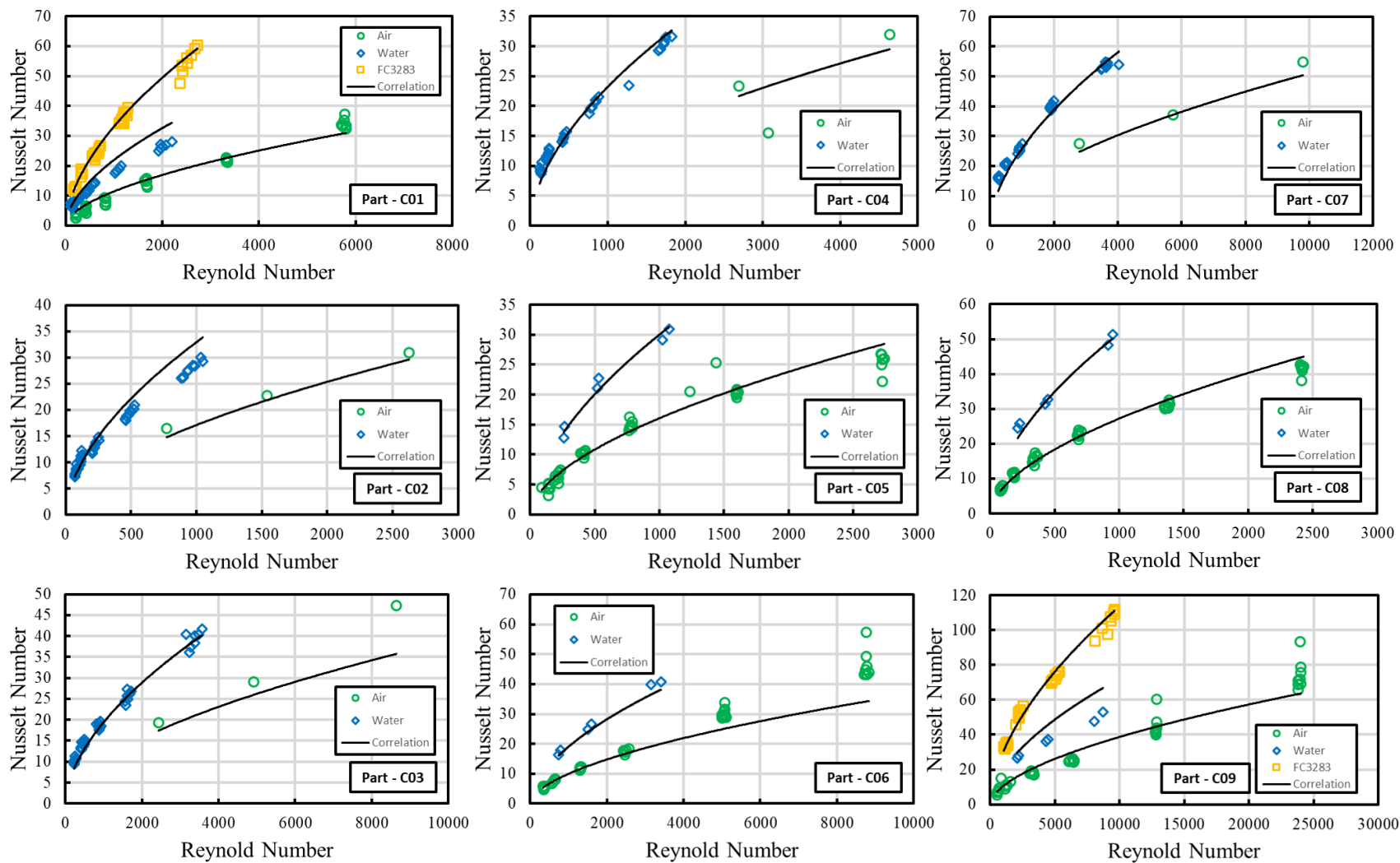


Figure H-8-4: Nusselt number vs Reynolds number data for all heat transfer tests segregated by part number and fluid type.